UNIVERSITY OF CALIFORNIA,
IRVINE

Transgenic Expression of Nitrogenase Iron Proteins

DISSERTATION

submitted in partial satisfaction of the requirements
for the degree of

DOCTOR OF PHILOSOPHY

in Chemistry

by

Caleb J. Hiller

Dissertation Committee:
Professor Yilin Hu, Chair
Professor Markus Ribbe
Professor Thomas Poulos

2018

Dedication

To

my God, my family, my friends, and my colleagues.

I appreciate your help and support.

Table of Contents

List of Figures viii

List of Tables xii

List of Abbreviations xiii

Acknowledgments xv

Curriculum Vitae xvii

Abstract of the Dissertation xix

Chapter 1 Introduction to Nitrogenase 1

1.1 General Introduction 2

1.2 Characterization of Nitrogenase – An Introduction of Characterization Techniques 5

1.2.1 Anaerobic Techniques 5

1.2.2 X-ray Crystallography 6

1.2.3 X-ray Absorption (XAS) and Emission (XES) Spectroscopies 7

1.2.4 Electron Paramagnetic Resonance (EPR) Spectroscopy 9

1.2.5 Mössbauer Spectroscopy 10

1.3 The Functional Components of Nitrogenase 11

1.3.1 Structural Description of the Catalytic Component of Nitrogenases 12

1.3.1.1 EPR Spectroscopy of the FeS Clusters of *Av*NifDK 17

1.3.2 Structural Description of Component 2 – The Reductase Component 19

1.3.2.1 Characterization of the $[Fe_4S_4]$ cluster of the Nitrogenase Fe Protein 23

1.3.2.2 EPR Analysis of the Fe Proteins 23

1.3.2.3 Reduction Potential of Fe Proteins 25

1.3.2.4 Nucleotide-induced Conformational Changes of *Av*NifH 28

1.3.3 Structural Description of the *Av*NifH/*Av*NifDK Complex 31

1.4 The Biosynthesis of the Metalloclusters of *Av*NifDK 33

1.4.1 The Ex Situ Biosynthesis of the M-cluster 34

1.4.1.1 Formation of 2Fe and 4Fe Clusters 36

1.4.1.2 Formation of L-cluster 36

1.4.1.3 Mo and Homocitrate Insertion into the L-cluster 38

1.4.1.4 Transfer of M-cluster to the Active Site on *Av*NifDK 39

1.4.2 The In Situ Biosynthesis of the P-cluster 40

1.4.2.1 Synthesis of the P-cluster Precursor (P^P-cluster) 41

1.4.2.2 Conversion of the P^P-cluster to the P-cluster 43

1.5 The Multiple Functions *Av*NifH 44

1.5.1 Nitrogenase Cofactor Maturation 45

1.5.2 Electron Transfer in Nitrogenase 48

1.5.3 Interconversion of CO_2 and CO 50

1.6 Conclusion and Aims of the Dissertation 51

1.7 Acknowledgments 52

Section 1 Characterization of Fe Protein Homologs – The Physiological Functions 53

Chapter 2 Tuning Electron Flux through Nitrogenase with Methanogen Iron Protein Homologs 57

2.1 Introduction 58

2.2 Results and Discussion 59

2.2.1 Expression and Characterization of *Ma*NifH and *Ma*VnfH 59

2.2.2 EPR Spectroscopy of Fe Protein Homologs 60

2.2.3 Cross-reactivities of the Catalytic and Reductase Components 61

2.2.4 Homology Modeling and In Silico Docking 62

2.2.5 Substrate Trapping Using *Ma*VnfH/*Av*VnfDGK Complex 63

2.3 Summary and Conclusion 66

2.4 Materials and Methods 66

2.4.1 Experimental Section 66

2.4.2 Cell Growth and Protein Purification 67

2.4.3 SDS-PAGE Analysis and Molecular Mass Determination 67

2.4.4 Iron Determination. 68

2.4.5 EPR Analysis 68

2.4.6 P-Cluster Maturation Assays 69

2.4.7 Enzymatic Assays 69

2.4.8 Docking Analyses 70

2.4.9 Catalytic Complexes 70

2.4.10 Assembly Complexes 73

2.4.11 Evaluation of Complexation Affinities 74

2.5 Supplemental Tables and Figures 75

2.6 Acknowledgments 84

2.7 Contributions 84

Chapter 3 Evaluation of the Catalytic Relevance of the CO-Bound States of V-Nitrogenase 85

3.1 Introduction 86

3.2 Results and Discussion 87

3.2.1 Generating a Singly-bound and Multi-bound CO State on *Av*VnfDGK 87

3.2.2 Quantification of CO on *Av*VnfDGK 88

3.2.3 *Ma*VnfH/*Av*VnfDGK Hybrid Produces Hi-CO conformation 89

3.2.4 Catalytic Relevance of the Hi-CO State Using *Ma*VnfH/*Av*VnfDGK Complex 91

3.2.5 Effects of CO Binding to *Av*VnfDGK by Addition of N_2 93

3.3 Summary and Conclusion 94

3.4 Materials and Methods 95

3.4.1 Experimental Section 95

3.4.2 Cell Growth and Protein Purification. 95

3.4.3 Activity Assays of V-nitrogenase 96

3.4.4 Generation of the CO-bound V-nitrogenase 96
3.4.5 Quantification of the Cofactor-bound CO in V-nitrogenase 97
3.4.6 Turnover Experiments of the CO-bound V-nitrogenase 97
3.4.7 GC-MS Experiments of the CO-bound V-nitrogenase 98
3.4.8 EPR Analysis of the CO-bound V-nitrogenase 98
3.5 Supplemental Tables and Figures 99
3.6 Supplemental Discussion 101
3.7 Acknowledgments 102
3.8 Contributions 103

Chapter 4 The MgADP-Bound Crystal Structure of the Vanadium Nitrogenase Iron Protein from *Methanosarcina acetivorans* 104
4.1 Introduction 105
4.2 Results and Discussion 107
4.3 Materials and Methods 111
4.3.1 Cell Growth and Purification 111
4.3.2 Crystallization and Data Collection 111
4.3.3 Structure Solution and Refinement 112
4.4 Acknowledgments 112
4.5 Contributions 112

Chapter 5 Continued Work toward Characterizing the Physiological Roles of Fe Protein Homologs of Nitrogenase 113
5.1 Introduction 114
5.2 Theoretical Docking Model 115
5.3 Expression and Characterization of Fe Protein Homologs 117
5.3.1 Characterization of the [Fe_4S_4] Cluster Using EPR Spectroscopy 118
5.3.2 Cross-reactivities of the Fe Protein Homologs with *Av*NifDK 121
5.3.3 M-cluster Maturation 123
5.4 Materials and Methods 124
5.4.1 Experimental Section 124
5.4.2 Cell Growth and Protein Purification 124
5.4.3 SDS-PAGE Analysis 125
5.4.4 Iron Determination 125
5.4.5 EPR Analysis 125
5.4.6 Enzymatic Assays 125
5.4.7 M-cluster Maturation Assay 126
5.4.8 Docking Calculations 126
5.5 Acknowledgments 126
5.6 Contributions 126

Section 2 Characterization of Fe Protein Homologs – The Adventitious Function of the Fe Protein to Reduce CO_2 and CO 127

Chapter 6 Ambient Conversion of CO_2 to Hydrocarbons by Biogenic and Synthetic [Fe_4S_4] clusters 130
6.1 Introduction 131
6.2 Results and Discussion 132
6.2.1 Reduction of CO_2 and CO by Protein-bound [Fe_4S_4] Clusters 132
6.2.2 Reduction of CO_2 and CO by Synthetic [Fe_4S_4] Clusters 136
6.2.3 Proposed Reaction Pathway of CO_2 Reduction Catalyzed by the [Fe_4S_4] Cluster 138
6.3 Summary and Conclusion 143
6.4 Materials and Methods 144
6.4.1 Experimental Section 144
6.4.2 Cell Growth and Protein Purification 145
6.4.3 Redox Potential Determination 145
6.4.4 Assays of CO- and CO_2-reduction with Fe Proteins 146
6.4.5 Assays of CO Oxidation with Fe Proteins 147
6.4.6 Assays of CO- and CO_2-reduction with $[Fe_4S_4]^{Syn}$ Clusters and SmI_2 147
6.4.7 Assays of CO- and CO_2-reduction with $[Fe_4S_4]^{Syn}$ and Eu^{II}-DTPA 148
6.4.8 Quantification of CO and CO_2 149
6.4.9 Quantification of Hydrocarbons 149
6.4.10 Gas Chromatography–mass spectrometry (GC–MS) Analysis 150
6.4.11 Density Functional Theory Calculations 150
6.5 Supplemental Results 152
6.5.1 DFT Calculations 152
6.5.1.1 Transition States for the Steps of C-C Bond Formation 152
6.5.1.2 Other Considered Reaction Pathways Involving Protonation of the Cluster Sulfur Atoms 152
6.5.1.3 Coordination of CO_2 to the Cluster 154
6.6 Supplemental Tables and Figures 155
6.7 Supplemental Discussion 162
6.7.1 Fe Protein (Fe_4S_4) vs. Nitrogenase (Cofactor) 162
6.7.1.1 Fe Protein vs. Nitrogenase 162
6.7.1.2 Fe_4S_4 Cluster vs. Cofactor 164
6.7.2 Fe_4S_4 Cluster vs. Other Fe/S-based Catalysts 165
6.7.2.1 Fe_4S_4 Cluster vs. Synthetic FeS-based Catalysts 165
6.7.2.2 Fe_4S_4 Cluster vs. Fe/S-containing Precipitates 166
6.7.3 Fe_4S_4 Cluster vs. Non-Fe/S Catalysts 167
6.7.3.1 Fe_4S_4 Cluster vs. Homogeneous Non-Fe/S Catalysts 167
6.7.3.2 Fe_4S_4 Cluster vs. Heterogeneous Non-Fe/S Catalysts 168
6.8 Acknowledgments 169
6.9 Contributions 169
Chapter 7 Structural Implications for the Formation of Hydrocarbons from CO_2 and CO by Nitrogenase Iron Proteins 170
7.1 Introduction 171
7.2 Electron Paramagnetic Resonance (EPR) Spectroscopy 172

7.3 Comparison of the CO_2 and CO Reduction Capabilities of *Av*NifH, *Ma*NifH, and *Dv*NifH 173
7.4 Crystal Structures of *Dv*NifH 174
7.5 Role of Cluster Location and Accessibility 175
7.6 Characterization of *Ma*VnfH 177
7.7 Crystal Structures of *Ma*VnfH 178
7.8 The Cluster Location and Accessibility of *Ma*VnfH 179
7.9 EPR Spectroscopy of *Ma*VnfH 180
7.10 Summary and Conclusion 182
7.11 Supplemental Tables and Figures 184
7.12 Materials and Methods 186
7.12.1 Experimental Section 186
7.12.2 Cell Growth and Protein Purification 187
7.12.3 Assays of CO- and CO_2-reduction with Fe Proteins 187
7.12.4 Crystallization and Data Collection 187
7.13 Contributions 189

References 190

List of Figures

Figure 1.1 The crystal structure of *Av*NifDK at 1 Å resolution (PDB code: 3U7Q). 14

Figure 1.2 The crystal structure of *Av*VnfDGK at 1.35 Å resolution (PDB code: 5N6Y). 16

Figure 1.3 The characteristic *S* = 3/2 EPR signal of the M-cluster bound to *Av*NifDK. 18

Figure 1.4 The characteristic EPR signal and structural changes of the P-cluster on *Av*NifDK. .19

Figure 1.5 The crystal structure of *Av*NifH with MgADP bound at 2.15 Å resolution (PDB code: 1FP6). 21

Figure 1.6 EPR spectra of *Av*NifH in the IDS-oxidized ($[Fe_4S_4]^{2+}$, A), DT-reduced ($[Fe_4S_4]^{1+}$, B), and Eu^{II}-reduced all-ferrous states ($[Fe_4S_4]^{0}$, C). 24

Figure 1.7 EPR spectra of *Av*NifH bound with nucleotides in the DT-reduced ($[Fe_4S_4]^{1+}$) State. 25

Figure 1.8 Summary of the midpoint reduction potentials (E_m) for the Fe proteins from *A. vinelandii*. 27

Figure 1.9 Structural comparison of nucleotide-free and nucleotide-bound *Av*NifH, both as free proteins and in complex with *Av*NifDK. 30

Figure 1.10 The crystal structure of the ADP·AlF_4^- stabilized *Av*NifH/*Av*NifDK complex at 3 Å resolution (PDB code: 1N2C). 33

Figure 1.11 A schematic representation of the M-cluster biosynthetic pathway. 35

Figure 1.12 Structural comparison of the proposed L-cluster structure to the M-cluster. 38

Figure 1.13 The crystal structure cartoon of *Av*NifEN at 2.4 Å resolution (PDB code: 3PDI). ...39

Figure 1.14 A schematic representation of the P-cluster biosynthetic pathway.....42

Figure 1.15 *In vitro* maturation of the first P-cluster requires Δ*nifH Av*NifDK, *Av*NifH, MgATP, and DT. 43

Figure 1.16 Summary of the *in vitro* maturation of the L-cluster to the M-cluster. 47

Figure 1.17 A depiction of the MgATP-dependent electron transfer (ET) from *Av*NifH to *Av*NifDK. 50

Figure 2.1 EPR features of the Fe proteins. 61

Figure 2.2 Interactions between the Fe Protein and its catalytic partner. 62

Figure 2.3 Capture of CO on the *Ma*VnfH/*Av*VnfDGK hybrid. 65

Figure 2.4 Functions of the nitrogenase Fe protein. 77

Figure 2.5 Nitrogenase-encoding operons of *M. acetivorans* and sequence alignment of Fe proteins. 78

Figure 2.6 Purification of M. acetivorans Fe Proteins. 79

Figure 2.7 Docking between component proteins in catalytic complexes. 80

Figure 2.8 Comparison of the affinities between the component proteins in various catalytic complexes. 81

Figure 2.9 Docking between component proteins in an assembly complex. 81

Figure 2.10 Interactions between the Fe protein and its assembly partner. 82

Figure 2.11 Comparison of product profiles of a given or altered nitrogenase complex upon variation of electron fluxes. 83

Figure 3.1 EPR spectra of CO-bound *Av*VnfDGK. 88

Figure 3.2 *Av*VnfDGK/*Av*VnfH activities. 90

Figure 3.3 Relevance of the CO-bound states of *Av*VnfDGK to C–C coupling. 92

Figure 3.4 Relevance of the CO-bound states of *Av*VnfDGK to N_2 reduction. 94

Figure 3.5 Schematic presentations of (A) molybdenum (*nif*-encoded) and (B) vanadium (*vnf*-encoded) nitrogenases. 99

Figure 3.6 Proposed CO binding modes to the V-cluster. 100

Figure 3.7 EPR spectra of (A) *Av*VnfDGK and (B) V-cluster-deficient *Av*VnfDGK protein incubated with and without 2.6 atm CO in the presence of Eu^{II}-DTPA. 101

Figure 4.1 A depiction of the MgATP-dependent electron transfer (ET) from *Av*NifH to *Av*NifDK. 106

Figure 4.2 The crystal structure of *Ma*VnfH with MgADP bound at 1.70 Å resolution. 108

Figure 5.1 Energy landscape and binding efficiency plots used to determine the affinity and specificity markers. 117

Figure 5.2 SDS-PAGE of select Fe protein homologs. 118

Figure 5.3 EPR spectra of Fe protein homologs in the IDS-oxidized ($[Fe_4S_4]^{2+}$, A), DT-reduced ($[Fe_4S_4]^{1+}$, B), Eu^{II}-reduced all-ferrous states ($[Fe_4S_4]^{0}$, C), and the observed all-ferrous signal observed in the DT-reduced state ($[Fe_4S_4]^{1+}$, D). 120

Figure 5.4 Interactions of the Fe proteins with *Av*NifDK. 122

Figure 6.1 Reduction of CO_2 and CO by protein-bound $[Fe_4S_4]$ clusters. 133

Figure 6.2 Formation of hydrocarbons in reactions of CO_2- and CO-reduction by protein-bound and synthetic $[Fe_4S_4]$ clusters. 136

Figure 6.3 Proposed reaction pathway of CO_2 reduction catalyzed by the $[Fe_4S_4]$ cluster. 139

Figure 6.4 Alternative reaction pathway of CO_2 reduction catalyzed by the $[Fe_4S_4]$ cluster. . 142

Figure 6.5 Reduction of CH_2O to CH_4 by synthetic $[Fe_4S_4]$ cluster. 143

Figure 6.6 Product distribution of CO_2 reduction in the presence of increasing amounts of reductant. 155

Figure 6.7 Titration of product yield versus CO concentration. 156

Figure 6.8 Redox properties of protein-bound $[Fe_4S_4]$ clusters. 156

Figure 6.9 Reduction of CO to hydrocarbons by protein-bound $[Fe_4S_4]$ clusters using dithionite as a reductant. 157

Figure 6.10 Structures of protein-bound and synthetic $[Fe_4S_4]$ clusters. 157

Figure 6.11 Formation of hydrocarbons by $[Fe_4S_4]^{Syn}$ and Fe-containing controls. 158

Figure 6.12 Structures of the catalyst and proton source for DFT calculations. 158

Figure 6.13 Transition states for the proposed mechanisms. 159

Figure 6.14 Cumulative reaction energies of CO_2 reduction pathways catalyzed by the $[Fe_4S_4]$ cluster. 160

Figure 6.15 Protonation of the [Fe_4S_4] cluster. 161

Figure 6.16 Reaction mechanism starting with the protonation of one of the S atoms of the [Fe_4S_4] cluster. 161

Figure 6.17 Examples of endothermic proton or electron/proton transfer reactions to the sulfur atoms of the [Fe_4S_4] cluster. 162

Figure 7.1 Structure of the synthetic [Fe_4S_4] clusters. 171

Figure 7.2 EPR spectra of *Dv*NifH in the IDS-oxidized ([Fe_4S_4]$^{2+}$, A), DT-reduced ([Fe_4S_4]$^{1+}$, B), Eu^{II}-reduced all-ferrous states ([Fe_4S_4]^{0}, C). 173

Figure 7.3 Comparative CO_2 (A) and CO (B) Reduction Assays of Fe Protein Homologs. 174

Figure 7.4 The crystal structure of *Dv*NifH at 2.8 Å resolution. 175

Figure 7.5 Comparison of the location of the [Fe_4S_4] cluster of *Dv*NifH and *Ma*NifH to *Av*NifH. 176

Figure 7.6 Cluster Accessibility comparison of *Av*NifH, *Ma*NifH, and *Dv*NifH. 177

Figure 7.7 Reduction of CO_2 and CO by Fe Protein Homologs. 178

Figure 7.8 The 1.81 Å and 1.75 Å crystal structures of *Ma*VnfH in the DT-reduced ([Fe_4S_4]$^{1+}$, A) and Eu^{II}-DTPA-reduced states ([Fe_4S_4]^{0}, B), respectively. 179

Figure 7.9 Comparison of the location of the [Fe_4S_4] cluster of *Av*NifH and *Ma*VnfH and accessibility to the FeS cluster of *Ma*VnfH. 180

Figure 7.10 EPR spectra of *Ma*VnfH in the IDS-oxidized ([Fe_4S_4]$^{2+}$, A), DT-reduced ([Fe_4S_4]$^{1+}$, B), Eu^{II}-reduced all-ferrous states ([Fe_4S_4]^{0}, C), and the observed all-ferrous signal observed in the DT-reduced state ([Fe_4S_4]$^{1+}$, D). 182

List of Tables

Table 1.1 Designation and Functions of the *nif*- Gene Products.....4

Table 1.2 The protein names and designations for the two-component systems of the Mo-, V-, and Fe-only nitrogenase systems. 12

Table 1.3. Select Fe protein crystal structures with corresponding PBD codes and resolutions. 22

Table 1.4 EPR Features and Signals Generated by the Fe proteins from *A. vinelandii*. 24

Table 2.1 Substrate ‑ reducing activities of various nitrogenase complexes. 75

Table 2.2 Summary of docking calculations. 76

Table 4.1 Data Collection and Refinement Statistics for the MgADP-bound *Ma*VnfH Structure. 109

Table 5.1 The Fe protein homologs, protein designations, and affinity and specificity markers. 115

Table 5.2 Metals analysis of the Fe protein homologs.....118

Table 5.3 Interactions of the Fe proteins with *Av*NifDK.....123

Table 5.4 The comparative effectiveness of the Fe protein homologs to synthesize the M-cluster, represented as a percent to *Av*NifH. 124

Table 7.1 Data Collection and Refinement Statistics for the *Av*NifH^{0} and *Ma*NifH^{1C} Structures. 184

Table 7.2 Data Collection and Refinement Statistics for the *Dv*NifH Structure in the DT-reduced state.....185

Table 7.3 Data Collection and Refinement Statistics for the *Ma*VnfH Structures in the DT-reduced $[Fe_4S_4]^{1+}$ and Eu^{II}-DTPA-reduced $[Fe_4S_4]^{0}$ states. 186

List of Abbreviations

$[Fe_4S_4]$	Four iron four sulfur
A. vinelandii (*Av*)	*Azotobacter vinelandii*
C. phaeobacteroides (*Cp*)	*Chlorobium phaeobacteroides*
C_2H_2	Acetylene
C_2H_4	Ethylene
C_2H_6	Ethane
C_3H_6	Propene
C_3H_8	Propane
C_4H_{10}	Butane
C_4H_8	Butene
CH_4	Methane
CO	Carbon monoxide
CO_2	Carbon dioxide
D. vulgaris (*Dv*)	*Desulfovibrio vulgaris*
DMF	Dimethylformamide
DT	Dithionite
e^-	Electron
E. coli	*Escherichia coli*
$E^{0'}$	Standard reduction potential
ENDOR	Electron nuclear double resonance
EPR	Electron paramagnetic resonance
ESEEM	Electron spin echo envelope modulation
ET	Electron transfer
Eu^{II}-DTPA	Europium (II) diethylenetriaminepentaacetic acid
EXAFS	Extended X-ray absorption fine structure
Fe-only nitrogenase	Iron-only nitrogenase
FeS	Iron sulfur
FID	Flame ionization detector
G. uraniireducens (*Gu*)	*Geobacter uraniireducens*
GC	Gas chromatography
GC-MS	Gas chromatography mass spectrometry
H^+	Proton
hr	Hour
ICP-OES	Inductively coupled plasma optical emission spectroscopy
IDS	Indigo disulfonite
kDa	kiloDalton
L	Liter

LN_2	Liquid nitrogen
M	Molar
M-cluster	Iron molybdenum cofactor
M. acetivorans (*Ma*)	*Methanosarcina acetivorans*
M. maripaludis (*Mmp*)	*Methanococcus maripaludis*
M. palustris (*Mp*)	*Methanosphaerula palustris*
MgADP	Magnesium adenosine diphosphate
MgATP	Magnesium adenosine triphosphate
min	Minute
Mo-nitrogenase	Molybdenum nitrogenase
NMF	N-methylformamide
NMR	Nuclear magnetic resonance
Od_λ	Optical density at a particular wavelength
P_i	Inorganic phosphate
P^P-cluster	P-cluster precursor
rpm	Rotations per minute
SAXS	Small-angle X-ray scattering
SDS-PAGE	Sodium dodecyl sulfate polyacrylamide gel electrophoresis
SmI_2	Samarium (II) iodide
Tris	Tris-(hydroxymethyl)-amino methane
UV/Vis	Ultraviolet-visible
V-cluster	Iron vanadium cofactor
V-nitrogenase	Vanadium nitrogenase
v/v	Volume/volume
w/v	Weight/volume
XAS	X-ray absorption spectroscopy

Acknowledgments

It is inevitably impossible to fully acknowledge the help that one receives from others while they chart their way through a doctoral program. A small conversation or thought can spark a thought that later yields a new result. Also, they are also countless individuals who teach ways to improve your laboratory technique, and who make future work possible. Thanks also need to be given to those whose encouragement help you continue when times are difficult. I, therefore, say thank you to all that I have interacted with through the course of my work.

Special thanks are given to Professor Yilin Hu and Professor Markus Ribbe, who have been my advisors over the course of my doctorate. Their knowledge and experience has provided key insights in project development and my success.

Thanks are due to my dissertation committee – Professor Yilin Hu (chair), Professor Markus Ribbe, and Professor Tom Poulos – who helped make this dissertation better and challenged me to expect more from myself.

Thanks to my advancement committee – Professor Mike Green (chair), Professor Andy Borovik, Professor Celia Goulding, Professor Tom Poulos, and Professor Rob Spitale – for not giving up on me.

Thanks to the postdoctoral students who provided expertise in their respective fields: Dr. Aaron Fay, Dr. Nate Sickerman, Dr. Jared Wiig, Dr. Chi Chung (CC) Lee, Dr. Kazuki Tanifuji, Dr. Martin Stiebritz, Dr. Andrew Jasniewski, and Dr. Wonchull Kang. I especially want to thank Aaron, Nate, and Jared for training me when I first began work in the lab, CC for helping me get through advancement, and Andrew for helping me with my dissertation.

Thanks my fellow in-lab graduate students for going through this process with me: Dr. Johannes (Joe) Rebelein, Megan Newcomb, Lee Rettberg, Jasper Liedtke, Matty Rasekh, and Joe Solomon.

Thanks are given to the Poulos and Borovik labs for allowing me to send protein crystals with them to the synchrotron. I also want to again thank Lee Rettberg and Alec Follmer (Poulos lab) for teaching me how to solve crystal structures.

Thanks to my fellow graduate students, who have supported me with their friendship and expertise. Together we learned, taught, and decompressed.

Thanks to my family and friends for their love and encouragement. I wouldn't have made it through this program with your support. Special thanks are given to my parents. You are wonderful and wise people. I am especially grateful for your counsel.

Thanks also to John Wiley and Sons for permission to include Chapter 2 and Chapter 3 in my dissertation, which were published in Chemistry A European Journal and Angewandte, respectively. I'd also like to that the Nature Publishing Group for allowing me to publish Chapter 6 in my dissertation, which was originally published in Nature Catalysis. Financial Support was provided by the Hellman Fellowship (to Yilin Hu), and NSF Career grant (CHE-1651398), and an NSF grant (CHE-1608926), in addition to grants provided by collaborators.

Curriculum Vitae

Caleb Hiller

Education

Ph.D. – Chemistry, University of California, Irvine, 2018
Advisors: Professor Yilin Hu and Professor Markus Ribbe
G.P.A. – **3.99**

M.S. – Chemistry, Brigham Young University, 2010
G.P.A. – **4.00**

B.S. – Chemistry, Brigham Young University, 2007
Graduated Magna Cum Laude
G.P.A. – **3.97**

Study Abroad, Brigham Young University Jerusalem Center for Near Eastern Studies, 2007

Experience

Research Assistant, University of California, Irvine, 2018
Teaching Assistant, University of California, Irvine, 2018
Taught lecture or laboratory courses at least one quarter per year
Chemistry Teacher, Bingham High School, 2011-2014
Taught general chemistry for Bingham High and dual-enrollment chemistry for Salt Lake Community College
Research Assistant, Brigham Young University, 2007-2010
Teaching Assistant, Brigham Young University, 2007-2010

Publications

- **Hiller, C. J.**; Lee, C. C.; Stiebritz, M. T.; Rettberg, L.; Hu, Y. Strategies towards capturing nitrogenase substrates and intermediates via controlled alteration of electron fluxes. *Chem. Eur. J.* (2018) doi: 10.1002/chem.201803735
- [*]Stiebritz, M. T.; [*]**Hiller, C. J.;** [*]Sickerman, N. S.; [*]Lee, C. C.; Tanifuji, K.; Ohki, Y.; Hu, Y. Ambient Conversion of CO2 to Hydrocarbons by Biogenic and Synthetic $[Fe_4S_4]$ clusters. *Nat. Catal.* **1**, 444–451 (2018). [[*]First authorship shared].
- Lee, C. C.; Wilcoxen, J.; **Hiller, C. J.**; Hu, Y. Evaluation of the Catalytic Relevance of the CO-bound States of V-Nitrogenase. *Angew. Chem., Int. Ed. Engl.* **57**, 3411–3414 (2018).
- [*]**Hiller, C. J.;** [*]Stiebritz, M. T.; [*]Lee, C. C.; Liedtke, J.; Hu, Y. Tuning Electron Flux through Nitrogenase with Methanogen Iron Protein Homologues. *Chem. Eur. J.* **23**, 16152–16156 (2017). [[*]First authorship shared].

Scholarships and Awards

Stanley and Leona Goates Research Award, Brigham Young University
Full Tuition Academic Scholarship, Brigham Young University
Robert C. Byrd Academic Scholarship Recipient, State of Utah
Undergraduate Research Award Recipient, Brigham Young University
Valedictorian, Viewmont High School

Skills

Fluent in Spanish

Affiliations and Volunteer Work

Phi Kappa Phi National Honor Society Member
Full-time Missionary, Bahia Blanca, Argentina
Eagle Scout

Abstract of the Dissertation

Transgenic Expression of Nitrogenase Iron Proteins

By

Caleb J. Hiller

Doctor of Philosophy in Chemistry

University of California, Irvine, 2019

Professor Yilin Hu, Chair

The iron (Fe) protein is one of two components involved in the biological fixation of dinitrogen (N_2) to bioavailable ammonia (NH_3) by nitrogenase. The physiological roles of the Fe protein include transferring electrons to the catalytic component and assisting in the bioassembly of the two metalloclusters found within the catalytic component. The Fe protein has also been shown to adventitiously reduce CO_2. The goal of this work has been to heterologously express and characterize Fe protein homologs according to their physiological and adventitious functions. This dissertation is divided into two sections, comprising multiple chapters, based on these functions.

Section 1 begins by comparing the molybdenum (Mo-) and vanadium (V-) nitrogenase Fe proteins from *Methanosarcina acetivorans* (*Ma*NifH and *Ma*VnfH, respectively) to the Fe proteins from the model organism *Azotobacter vinelandii* (*Av*NifH and *Av*VnfH, respectively). Characterization includes comparing the size of the proteins, the behavior of the $[Fe_4S_4]$ cluster of the protein, and the ability of the homologs to assist in the bioassembly of the catalytic component's metalloclusters. Next, there is a discussion about a hybrid nitrogenase system, created by pairing *Ma*VnfH with the catalytic component of *A. vinelandii*, which resulted in the

ability to trap the alternate V-nitrogenase substrate, CO, on the catalytic cofactor. Also included are a brief chapter that reports the MgADP-bound crystal structure of *Ma*VnfH and a miscellaneous chapter, which contains preliminary results regarding the characterization of five additional Mo-nitrogenase Fe protein homologs.

The first chapter of Section 2 reports that *Ma*NifH is able to reduce CO_2 beyond CO and also generate hydrocarbons, which is further than the *A. vinelandii* counterparts. Consequently, a CO reduction assay was created, and this section focuses on the ability of Fe protein homologs to reduce both CO_2 and CO. It was determined that CO_2 and CO reduction is an intrinsic property of $[Fe_4S_4]$ clusters. The final chapter compares the product profiles of different Fe protein homologs and compares the crystal structures of these Fe proteins to gain insights into what may cause these differences.

Chapter 1 Introduction to Nitrogenase

1.1 General Introduction

Nitrogen (N) is an element found in some of the most fundamental building blocks of life – including deoxyribonucleic acid (DNA), ribonucleic acid (RNA), and proteins – and is therefore an essential element of life. Dinitrogen (N_2) is the elemental form of nitrogen and comprises ~78% of the Earth's atmosphere. It is, however, a relatively stable molecule because of the strong triple bond (bond dissociation energy of 945 kJ/mol) that binds the two nitrogen atoms together and most organisms do not have the necessary machinery to convert N_2 into usable forms such as ammonia (NH_3), in a process known as nitrogen fixation.[1] Humans have developed an industrial method, known as the Haber-Bosch process, that has allowed them to generate NH_3 from N_2, and that NH_3 has been used as a N source in fertilizers to increase food production and support an ever-growing population. The Haber-Bosch process requires high temperatures (400-500 °C) and pressures (150-250 atm) and a series of transition metal catalysts so that N_2 can react with dihydrogen (H_2) to form NH_3 as shown in Equation 1.[2]

$$N_2 + 3H_2 \xrightarrow[400\text{-}500\ ^\circ C]{150\ atm} 2NH_3 \quad (1)$$

A certain class of organisms known as diazotrophs can also carry out nitrogen fixation, but do so biologically because they contain genes that encode for an enzymatic system called nitrogenase.[3,4] Nitrogenase can convert N_2 to NH_3 under ambient temperatures and pressures as shown in the following equation (Equation 2):

$$N_2 + 8H^+ + 16MgATP + 8e^- \longrightarrow 2NH_3 + H_2 + 16MgADP + 16P_i \quad (2)$$

where MgATP is magnesium adenosine triphosphate, MgADP is magnesium adenosine diphosphate, and P_i is inorganic phosphate. The ability to perform this reaction under ambient conditions is one advantage to the method that diazotrophs use over the Haber-Bosch process. A

second advantage is the ability to use water as a proton source, instead of H_2, which is often generated by steam methane reforming – another process that requires high temperatures (700-1100 °C) and metal-based catalysts. However, the nitrogen fixation method utilized by diazotrophs also has its disadvantages, e.g. it requires large amounts of cellular energy in the form of MgATP, which also makes it an energy-intensive method to generate NH_3. Despite this disadvantage, nitrogenase has been studied since at least the early 1900's in an effort to understand how nitrogenase carries out the reduction of N_2 under ambient conditions, with the hopes that the knowledge gained will be translatable to industrial techniques.

Several forms of nitrogenase have been identified in diazotrophs, and these proteins are differentially expressed depending on the availability of certain transition metals during growth.[5,6] The molybdenum-dependent nitrogenase (Mo-nitrogenase) is considered to be the most efficient at N_2 reduction and is favorably expressed in the bacteria and archaea that contain multiple nitrogenase systems when molybdenum (Mo) is present.[3–5] The Mo-nitrogenase from *Azotobacter vinelandii* (*A. vinelandii*) is the most extensively characterized nitrogenase system and is encoded by the nitrogen fixation (*nif*) operon.[3,4,7] Table 1.1 contains an abbreviated list of selected "essential" Mo-nitrogenase genes, gene products, and functions of these gene products. In the absence of Mo, other nitrogenases, termed "alternative nitrogenases" are expressed. These alternative nitrogenase systems include the vanadium-dependent (V-nitrogenase) and iron-only nitrogenase (Fe-only nitrogenase) and are encoded by the *vnf* and *anf* genes, respectively.[5,6] These alternative nitrogenase systems are less well characterized than the Mo-nitrogenase.

Table 1.1 Designation and Functions of the *nif*- Gene Products. This table is adapted from reference 7.

Gene	Protein Code	Function	Reference
nifU	NifU	NifU is a scaffold protein involved in the assembly of small FeS clusters.	8–10
nifS	NifS	NifS is involved in sulfur mobilization to NifU for the assembly of small FeS clusters.	8–13
nifB	NifB	NifB mediates a radical SAM-dependent carbide insertion concomitant to L-cluster formation.	14
nifE, N	NifEN	NifEN is a scaffold protein used for M-cluster maturation.	15–18
nifH	NifH	NifH has three physiological roles: it mediates ATP-dependent electron transfer to the catalytic component, is involved in P-cluster biosynthesis, and acts as a Mo and homocitrate insertase in M-cluster maturation.	3,16,19–23
nifZ	NifZ	NifZ is involved in the step-wise maturation of P-cluster.	23,24
nifD, K	NifDK	NifDK catalyzes the reduction N_2. Hydrocarbon formation is likely adventitious.	3,4

One major goal of nitrogenase research is to heterologously express nitrogenase genes in plants so that they have the functional machinery required to produce bioavailable NH_3 from N_2, thereby generating their own nitrogen-fixed "fertilizer" which would facilitate growth to help feed the growing population. To date, a functioning nitrogenase system has not been expressed in a heterologous host; however, efforts have gone into the expression of individual nitrogenase genes (Table 1.1) in *Escherichia coli* (*E. coli*).[25] *E. coli* is not a diazotroph; however, it is a well-studied organism with a rapid growth phase, therefore providing an excellent system to work with. Hu and co-workers were able to successfully express a nitrogenase gene product, NifB, from a methanogenic organism in *E. coli* in the first step to heterologous nitrogenase expression.[25] Based on that approach, the work outlined is this dissertation is focused on the expression and characterization of another nitrogenase gene product, NifH, in *E. coli*.

This chapter will discuss many important aspects about nitrogenase research, including the techniques used to characterize nitrogenase proteins, protein structure and characterization, and the assembly and characterization of the metal cofactors found within nitrogenase proteins. An emphasis will be placed on the role of one these nitrogenase proteins, the Fe protein or NifH, as it has been the focus of my work.

1.2 Characterization of Nitrogenase – An Introduction of Characterization Techniques

1.2.1 Anaerobic Techniques

Nitrogenase consists of several metalloproteins, which are sensitive to dioxygen (O_2) – a major component of the atmosphere. While diazotrophs have methods to protect nitrogenase proteins from O_2, care must be taken to prevent this gas from interacting with these proteins while they are being studied. During the purification process, harvested cells are placed under vacuum and back-filled with an inert gas like argon (Ar) to remove O_2 from the buffer-cell suspension, typically through the use of glass or metal vacuum-gas manifolds, known as Schlenk lines. Additionally, a sacrificial oxygen scavenger, like sodium dithionite ($Na_2S_2O_4$, DT), is added to the buffer-cell suspension to further protect the metallocluster from degradation. After purification, the protein is frozen and stored under liquid nitrogen (LN_2) to prevent oxygen exposure. When it is time to assess the reactivity of nitrogenase proteins, these proteins can be thawed under anaerobic conditions on a Schlenk line and monitored for their ability to carryout particular reactions.

Even though nitrogenase is best known for its ability to reduce N_2, it can also reduce other substrates, including but not limited to acetylene (C_2H_2), carbon monoxide (CO), and protons (H^+). A standard nitrogenase assay involves the addition of two nitrogenase gene

products (NifDK and NifH) and a reductant (typically DT) to a gaseous substrate of choice (note that Ar is used as the headspace gas in the proton reduction assays). Protocols have been established for the experimental set-up, detection, and analysis of the resulting products.

1.2.2 X-ray Crystallography

Two functioning proteins are required for nitrogenase catalysis, in the case of the Mo-nitrogenase they are the heterotetrameric $\alpha_2\beta_2$ catalytic component (NifDK) and the homodimeric γ_2 reductase component (NifH).[3,4] In addition to these proteins, other nitrogenase proteins are involved in cofactor synthesis, act as chaperones, and play roles in regulating nitrogenase activity.[7] One goal of nitrogenase research is to understand how these proteins perform their functions and also how they interact with the other nitrogenase proteins. The three-dimensional protein structures that X-ray crystallography provides bring insights into how these reactions are performed and how the various components interact by providing a snapshot of the protein under certain conditions.

As the name implies, crystals of the protein(s) of interest are required to obtain the three-dimensional structure of the protein(s). This involves use of highly purified protein and often screening a variety of chemical conditions that range in chemical composition, concentration, pH, and methods of crystallization. It is not uncommon that years pass before the proper conditions to crystallize a protein are identified. Once crystals have been obtained, they are soaked in a cryoprotectant, mounted on a circular holder called a loop, and generally frozen in LN_2 to await analysis. For analysis, the crystal-containing loop is mounted on the X-ray diffractometer, whereupon highly focused X-rays are shot at the crystal while a simultaneous stream of LN_2 cools the crystal to prevent it from being destroyed by the high-powered X-rays. In order to have the possibility to obtain a crystal structure, the crystal needs to diffract the X-

rays. A detector collects this diffraction pattern, and the corresponding intensities. The crystal is then rotated and another diffraction pattern is obtained. This process is continued until enough images of the diffraction pattern have been captured so that a three-dimensional representation of the electron density of the protein can be determined, and is dependent on the symmetry of the crystal. Next, a computational model of the protein is generated and compared to the electron density map, and a process of refinement occurs to the end that the model fits the experimental data, as monitored by statistical parameters to ensure the quality of the refinement.

Commercial diffractometers provide the ability to screen crystals and determine whether they diffract, but often result in lower-resolution data. To obtain higher-resolution data, crystals are sent to a synchrotron facility, which has the ability to generate a more intense X-ray beam. Higher resolution data results in structures represented by more accurate protein folds and amino acid location, the position of cofactors, and insights into the potentially charged residues on the surface of the protein. If proteins are not co-crystallized together, the X-ray structures can be used to model the interactions that may exist between two protein components.

1.2.3 X-ray Absorption (XAS) and Emission (XES) Spectroscopies

X-ray absorption spectroscopy (XAS) is a spectroscopic technique typically carried out at synchrotron facilities because intense X-ray beams are required to collect data. This technique targets a particular element, typically Fe in the case of nitrogenase, and can provide precise bonding metrics between atoms of the complex FeS clusters found within the proteins. This technique requires concentrated protein solutions that are mixed with a cryoprotectant, to prevent the formation of ice crystals, prior to freezing the sample and sample holder in in LN_2. During analysis, samples are placed in a cryostat at cryogenic temperatures (usually between 4 and 77 K) where they are irradiated by the X-ray source. Core electrons from the target atom are excited

and ejected because of the high energy X-rays. Absorption also generates a photoelectron, which subsequently scatters off nearby atoms. During sample collection, the energy of the X-rays is varied and the absorption/scattering events are detected in a variety of ways depending on the design of the experiment. The data are then analyzed and processed to provide the bonding metrics for the target atom. XAS is typically most effective when used in conjunction with other techniques. For instance, because XAS does not provide information leading to the three-dimensional structure, the information can be better interpreted if there is a corresponding crystal structure. Another caveat to XAS is that it only provides average information regarding the experiment; so pure protein samples and well-designed experiments that take into account the multiple-cluster proteins are required to yield beneficial results.

Like XAS, X-ray emission spectroscopy (XES) is an element specific technique; however, it provides information about the electronic configuration of an element rather than the bonding metrics. In the general sense in XES, a core electron is ionized from a target atom by a high-energy X-ray source, resulting in a 'core hole' where the electron used to be. An electron in a higher energy level is able to drop down to fill the core hole, and in the process emits light in the form of fluorescence. Depending on the construction of the experiment and the type of electron that fills the core hole, the fluorescent emission data can be analyzed and interpreted to determine the type of bond that the target element makes. Interpretation of XES data typically relies on creating model systems to compare the experimental data of an unknown system to that of known systems. This was the first technique used to determine that the interstitial atom in the nitrogenase cofactor was indeed a carbide (C^{4-}) atom and not a nitride (N^{3-}) or oxide (O^{2-}) as many predicted.[26]

1.2.4 Electron Paramagnetic Resonance (EPR) Spectroscopy

Transition metals play important roles in metalloprotein biochemistry.[27–29] Of particular relevance to nitrogenase, transition metals can support multiple oxidation states, so they can be used in electron transfer reactions as well as chemical transformations, that ultimately results in the reduction of N_2 to NH_3.[30–32] Electron paramagnetic resonance (EPR) spectroscopy is a technique used in nitrogenase research to monitor the oxidation states of the FeS cluster-containing proteins.

EPR spectroscopy detects the presence of unpaired electrons by irradiating a sample with microwaves and then simultaneously applying and varying the strength of a magnetic field on the sample. In the absence of a magnetic field, the spin states of electrons orbiting atoms are degenerate ($m_s = \pm 1/2$). However, when a magnetic field is applied, electrons must either align themselves parallel or anti-parallel to the field, and as a result the energies are no longer degenerate. As the strength of the magnetic field increases, the energy difference between the spin states also increases. Resonance occurs when the energy of the microwaves is equal to the difference in energy of the two now non-degenerate orbitals, caused by adjusting the strength of the magnetic field, and the electron will flip its spin to the higher energy state by the absorption of a photon – resulting in the observance of a signal. Because the measured signal is sensitive to the electronic and nuclear environment, as the clusters are cycled through different oxidation states that change the number of unpaired electrons, the different characteristic signals for the cluster are obtained. Each cluster has a characteristic line-shape and *g*-values that correspond to a particular oxidation state. This technique has been used as a diagnostic tool to track the formation of cluster, monitor cluster transfer, observe changes in the oxidation states of proteins, and in response to substrate binding.[16,18]

EPR spectroscopy can also be used to more extensively probe the electron-nuclear interactions in paramagnetic systems and give information regarding the identity of the nuclei that interact with the unpaired electron. The techniques that provide this information are known as electron nuclear double resonance (ENDOR) and electron spin echo envelope modulation (ESEEM), and despite being able to provide similar information, these two techniques are quite different. In ENDOR experiments, the EPR spectrometer is fitted with a radio frequency generator and receiver that can interact with the paramagnetic sample and perform a nuclear magnetic resonance (NMR) experiment. When conventional EPR resonance and the NMR resonance occur simultaneously, the electron spin flip caused by EPR can be coupled to the nuclear spin flip of the NMR and can be used to probe the electron-nuclear interactions of nuclei near the paramagnetic atoms. These types of experiments are useful for substrate-bound interactions between the substrate and cofactor. In ESEEM experiments, a paramagnetic sample with magnetic nuclei is placed in an external magnetic field and precisely timed microwave radiation pulses irradiate the sample and allow for the electron-nuclear interactions to be probed. ESEEM studies tend to be more effective for samples when the nucleus of interest is weakly coupled to or more distant from the paramagnetic center.

1.2.5 Mössbauer Spectroscopy

Mössbauer spectroscopy is a technique primarily used in metallobiochemistry to determine the oxidation state, spin state and local coordination environment of a metallocofactor. This technique utilizes the recoilless nuclear absorption and emission of gamma rays (γ-rays) to characterize metal complexes. While this technique can be used with a wide variety of elements, Fe is the most studied element biologically because of the prevalence of Fe-containing proteins, and is especially useful for nitrogenase research. ^{57}Fe-containg samples are prepared and frozen,

and later analyzed at cryogenic temperatures in a cryostat. ^{57}Co, used as a radiation source to irradiate the sample, has a half-life of 270 days and decays to a metastable ^{57}Fe state via electron capture. γ-emissions from the source can be used to excite ^{57}Fe nuclei in the sample, which ultimately can be used to provide information about the local environment around the Fe in the sample by providing information known as a chemical shift, quadrupole splitting, and magnetic hyperfine splitting (if a magnetic field is applied). Computations and simulations often accompany Mössbauer experiments as a way to support the data. One of the difficulties in using this technique is the low natural abundance of ^{57}Fe, often resulting in expensive experiments to get the needed ^{57}Fe incorporated into the protein of interest.

1.3 The Functional Components of Nitrogenase

Nitrogenase is a two-component system that involves a catalytic component, responsible for the reduction of N_2 to NH_3, and a reductase component, which delivers electrons to the catalytic component and is essential for catalysis (Table 1.2).[33,34] During the span of nitrogenase research, the terminology used to refer to the two components has evolved. For instance, the catalytic component from the Mo-nitrogenase of *A. vinelandii* has been referred to as the catalytic component, component 1, *Av*I, dinitrogenase, Mo-nitrogenase, Mo-protein, and the MoFe protein; while the reductase component, typically referred to as the Fe protein, has also been referred to as the reductase component, component 2, *Av*II, and dinitrogenase reductase. The naming system has been further complicated because of the "alternative nitrogenase systems. While the reductase components for the V-nitrogenase and Fe-only nitrogenase are still generally referred to as Fe proteins, the catalytic components are referred to as V-nitrogenase or VFe protein and the Fe-only nitrogenase or FeFe-protein, respectively. Most recently, there has been a transition to designate the proteins as the gene products for clarity, with the *nif*-, *vnf*-, and

anf-genes referring to the Mo-, V-, and Fe-only nitrogenase systems, respectively. This is the system that I have chosen as the primary method to refer to specific proteins throughout this dissertation, such that the catalytic components from the Mo- and V- nitrogenase systems are referred to as NifDK and VnfDGK, respectively; and the Fe proteins are designated as NifH and VnfH, respectively. If the components are being referred to in a more general sense, components 1 and 2 are generally referred to as the catalytic components and Fe proteins, respectively. Because nitrogenase proteins were used from a variety of organisms in this work, an italicized prefix is included with the protein designation to specify the organism of origin. For example, the Mo-nitrogenase Fe protein from *A. vinelandii* is encoded by the *nifH* gene and the gene product is designated *Av*NifH.

Table 1.2 The protein names and designations for the two-component systems of the Mo-, V-, and Fe-only nitrogenase systems.

	Component 1 **Catalytic Component**	**Component 2** **Reductase Component**
Mo-Nitrogenase	MoFe protein NifDK *Av*I Dinitrogenase	Fe protein NifH *Av*II Dinitrogenase reductase
V-Nitrogenase	VFe protein VnfDGK	Fe protein VnfH
Fe-only Nitrogenase	FeFe protein AnfDGK	Fe protein AnfH

1.3.1 Structural Description of the Catalytic Component of Nitrogenases

The Mo-nitrogenase from *A. vinelandii* (*Av*NifDK) is the best characterized nitrogenase system. The *nifD* and *K* genes encode for a heterotetrameric $\alpha_2\beta_2$ protein that is ~230 kDa in size (Figure 1.1A). *Av*NifDK houses two different complex metalloclusters clusters in each αβ-dimer that are essential for electron transfer and substrate turnover, designated as the P- and M-clusters (Figure 1.1B and C, respectively).[26,35–37] The P-cluster is a $[Fe_8S_7]$ cofactor that facilitates

electron transfer to the M-cluster and is positioned at the α/β interface ~10 Å below the surface of the protein and is bound by 3 cysteine residues from each subunit ($Cys^{\alpha62}$, $Cys^{\alpha88}$, $Cys^{\alpha154}$, $Cys^{\beta70}$, $Cys^{\beta95}$, and $Cys^{\beta153}$). The cluster appears as two [Fe_4S_3] cubane cluster units that share a common vertex, a μ_6-sulfide (Figure 1.1B). The M-cluster is a [$MoFe_7S_9C$-(R)-homocitrate] cluster that is responsible for substrate reduction and this cluster is buried ~10 Å below the surface of the protein in the α subunit ~14 Å from the P-cluster (Figure 1.1A). The cluster appears as two partial cubanes, a [Fe_4S_3] and a [$MoFe_3S_3$], with a μ_6-insterstitial carbide coordinated in the central cavity, and additionally is bridged by three μ_2-sulfides designated as "belt sulfides" (Figure 1.1C).[7,26,35–37] The Mo atom is further coordinated to (*R*)-homocitrate by the 2-hydroxy and 2-carboxy groups from the homocitrate, and the M-cluster is anchored to the protein by two amino acid residues: $Cys^{\alpha275}$ at the Fe-capped end and $His^{\alpha442}$ at the Mo-capped end (Figure 1.1C).[7] The assembly of these two clusters will be provided in Section 1.4.

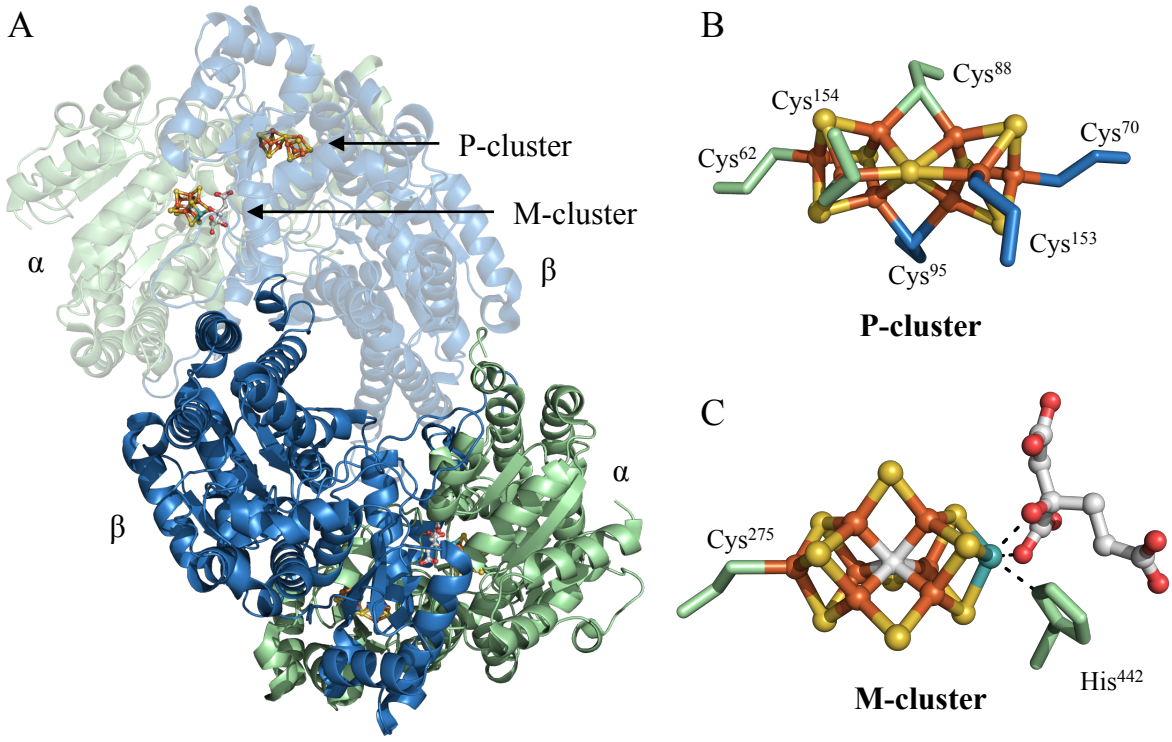

Figure 1.1 The crystal structure of *Av*NifDK at 1 Å resolution (PDB code: 3U7Q). (**A**) Crystal structure cartoon of *Av*NifDK with the metalloclusters highlighted. (**B**) A zoomed-in view of the P-cluster cofactor from *Av*NifDK. (**C**) A zoomed-in view of the M-cluster cofactor from *Av*NifDK. The NifD and NifK subunits are represented in green and blue, respectively. Atoms are colored as follows: Fe, rust; S, yellow; Mo, cyan; C, light gray; O, red. PyMOL was used to generate this figure.[38]

The *A. vinelandii* V-nitrogenase catalytic component, *Av*VnfDGK, is encoded by *vnfDGK* and forms a heterohexameric protein ($\alpha_2\beta_2\gamma_2$) ~244 kDa in size.[5,39,40] The exact function of the additional γ subunit is still unknown, but it has been proposed that it may be involved in transferring V-cluster to the apo-enzyme based on sequence similarity to proposed cofactor chaperones from *A. vinelandii* and *Klebsiella pneumoniae*.[41,42] AvVnfDGK is highly homologous to *Av*NifDK, but a recent crystal structure of *Av*VnfDGK has shed light on some key differences (Figure 1.2A).[40] Like *Av*NifDK, *Av*VnfDGK houses two types of metalloclusters necessary for electron transfer and substrate turnover designated as the P*-cluster (Figure 1.2B) and V-cluster (Figure 1.2C). Prior to the recent crystal structure, the P*-cluster in *Av*VnfDGK

and the P-cluster in *Av*NifDK were believed to have different structures, due in part to spectroscopic differences between the species.[40,43] However, the VnfDGK structure reveals that the P^*-cluster indeed appears as an $[Fe_8S_7]$ cluster positioned between the VnfD and K subunits via six cysteine residues ($Cys^{\alpha 49}$, $Cys^{\alpha 75}$, $Cys^{\alpha 138}$, $Cys^{\beta 31}$, $Cys^{\beta 56}$, and $Cys^{\beta 115}$) and the overall cluster structure is remarkably similar to the P-cluster of *Av*NifDK (Figure 1.1B and Figure 1.2B).[40] The V-cluster is a $[VFe_7S_8C(CO_3)$-(*R*)-homocitrate] cluster that is buried in the α subunit ~15 Å from the P^*-cluster, and like the M-cluster, is anchored to the protein scaffold by two residues, $Cys^{\alpha 257}$ and $His^{\alpha 423}$, on the Fe- and V-capped ends, respectively. The overall shape and structure of the V-cluster core is similar to that of M-cluster, but with three differences: the Mo is replaced by a V atom, the average V-Fe distance of 2.77 Å to the closest three Fe centers in the cluster is slightly longer than the analogous 2.69 Å Mo-Fe distance in the M-cluster, and one of the "belt" μ_2-sulfides sulfide ligands has been replaced by a CO_3^{2-} moiety.[40] Currently there is no definitive source or function of the carbonate ligand identified in the crystal structure.

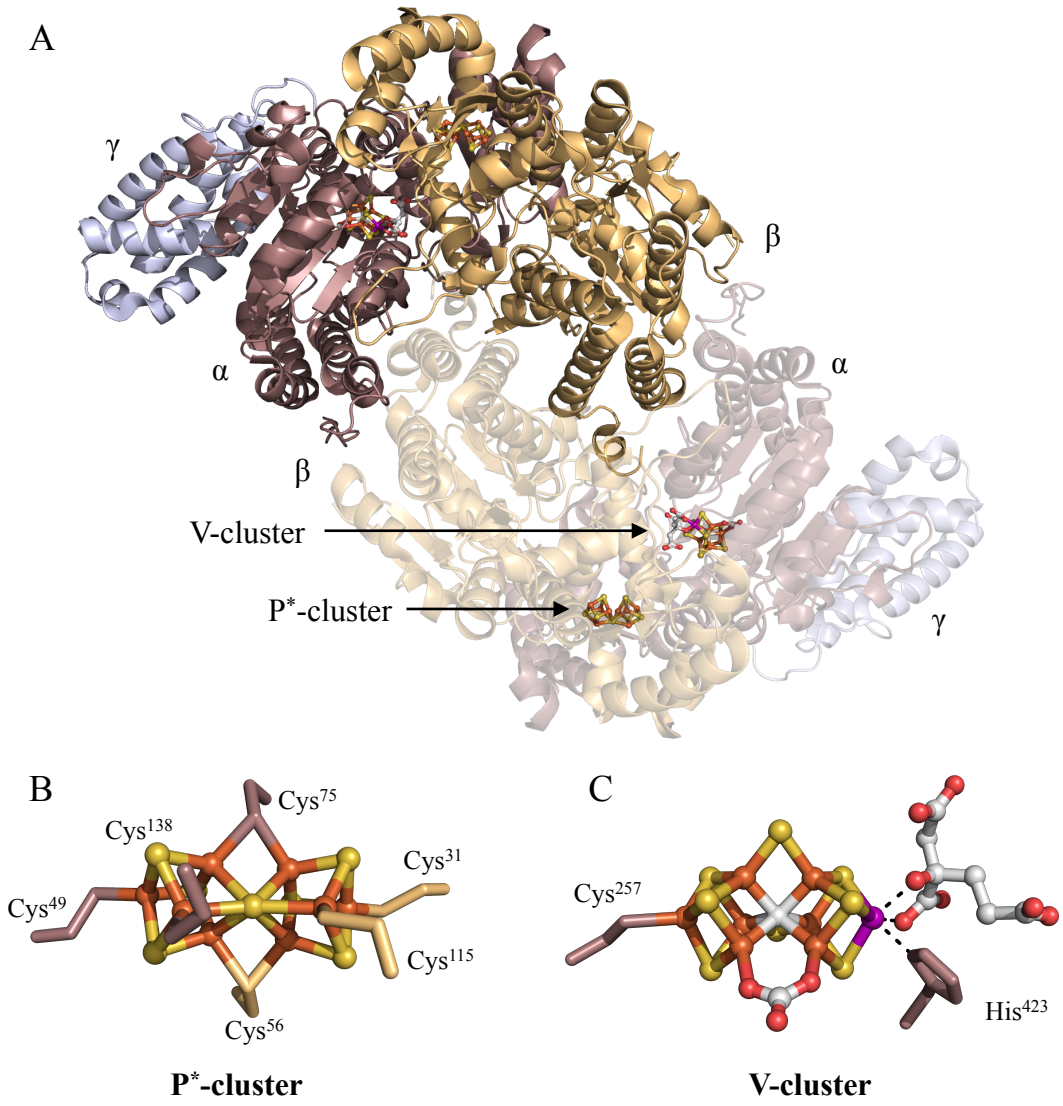

Figure 1.2 The crystal structure of *Av*VnfDGK at 1.35 Å resolution (PDB code: 5N6Y). (**A**) Crystal structure cartoon of *Av*VnfDGK with the metalloclusters highlighted. (**B**) A zoomed-in view of the P*-cluster from *Av*VnfDGK. (**C**) A zoomed-in view of the V-cluster cofactor from *Av*VnfDGK. The VnfD, VnfG, and VnfK subunits are represented in violet, blue, and orange, respectively. Atoms are colored as follows: Fe, rust; S, yellow; V, purple; C, light gray; O, red. PyMOL was used to generate this figure.[38]

The *A. vinelandii* Fe-only nitrogenase catalytic component, *Av*AnfDGK, is encoded by *anfDGK* and forms a heterohexameric protein ($\alpha_2\beta_2\gamma_2$) ~250 kDa in size. Characterization of this protein is somewhat limited. To date, a crystal structure of *Av*AnfDGK has not yet been determined; however, XAS, EPR, and Mössbauer spectroscopy of AnfDGK from *Rhodobacter*

capsulatus (*R. capsulatus*) suggests that the protein contains FeS clusters similar to those of the P/P* - and the M/V-clusters of the Mo- and V-nitrogenases, respectively. It is therefore proposed that the catalytic cofactor of AnfDGK would be structurally similar to the M/V-clusters, but exclusively contain Fe. Additional work is needed to further characterize this protein.

1.3.1.1 EPR Spectroscopy of the FeS Clusters of *Av*NifDK

The FeS clusters of the nitrogenase catalytic components are arguably the most interesting aspect of nitrogenase, and are unique to the nitrogenase enzyme system. The M- and P-clusters can cycle between different oxidation states as electrons are shuttled between them, and understanding electron flow is a formidable task. EPR spectroscopy lends itself well to monitoring the changes in oxidation states, as characteristic signals or the disappearance of signal is associated with each cluster and its oxidation states. The EPR signals of the Mo-nitrogenase system are the best characterized and will be summarized in this section. The analogous clusters of the alternative nitrogenase systems can also be analyzed using EPR spectroscopy, however, they will not be addressed here in detail.

As mentioned in the previous section, *Av*NifDK is an $\alpha_2\beta_2$ heterotetramer that contains one P- and one M- cluster in each αβ dimer. The *Av*NifDK-bound M-cluster displays a characteristic $S = 3/2$ EPR signal (Figure 1.3) at $g = 4.7$, 3.7, and 2.0 in the presence of excess dithionite (DT).[3] This cluster has been shown to undergo a reversible one-electron oxidation process, which results in the disappearance of the $S = 3/2$ signal.[3] The M-cluster has also been successfully extracted from the protein into organic solvents, such as N-methylformamide (NMF) and dimethylformamide (DMF).[44] The EPR signal of the extracted M-cluster displays a similar, albeit broader, features than its protein-bound counterpart.[44,45] This unique signal has been crucial for the study of M-cluster biosynthesis.[7] In one study, the appearance of the

characteristic $S = 3/2$ signal on the scaffold protein *Av*NifEN indicated that M-cluster was fully synthesized outside of the active site of *Av*NifDK (see Section 1.4).[16,18] More advanced EPR techniques, such as ENDOR, have also been used to characterize signals associated with the M-cluster and to identify intermediate species.[46]

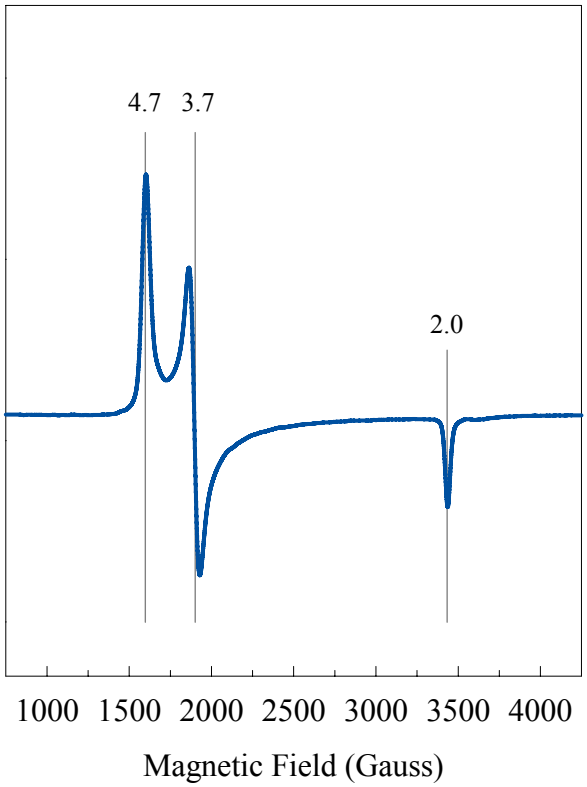

Figure 1.3 The characteristic *S* = 3/2 EPR signal of the M-cluster bound to *Av*NifDK. The *g*-values are observed at 4.7, 3.7, and 2.0 in excess DT, indicated by vertical lines. Conditions: four scans were run at 10 K with a microwave power of 50 mW and a microwave frequency of 9.62 GHz.

The P-cluster primarily shuttles electrons from *Av*NifH to the M-cluster, and three oxidation states of the P-cluster have been identified, designated as the P^N, P^{1+}, and P^{Ox} states, respectively.[47–49] In the presence of excess DT, the P-cluster occupies the P^N, all-ferrous diamagnetic state and does not exhibit an EPR signal. Addition of the oxidant indigo disulfonate (IDS), results in the two-electron oxidization of P-cluster to the P^{Ox} state, which exhibits an $S = 3$ or 4 spin state, reflected in an EPR signal with $g = 11.8$ (Figure 1.4A).[47–49] Concomitant with the

oxidation of the P^N (Figure 1.4B) to P^{Ox} (Figure 1.4C) state, the cluster attains a more open conformation, as observed by crystallography.[35,50,51] It has been proposed that the cluster conformational change may allow for the two-electron reduction to occur; however, further studies are required to definitively address this issue. This change in the EPR signal with respect to the redox state and cluster conformation has also been used to study the stepwise synthesis of the P-cluster in NifDK.[7]

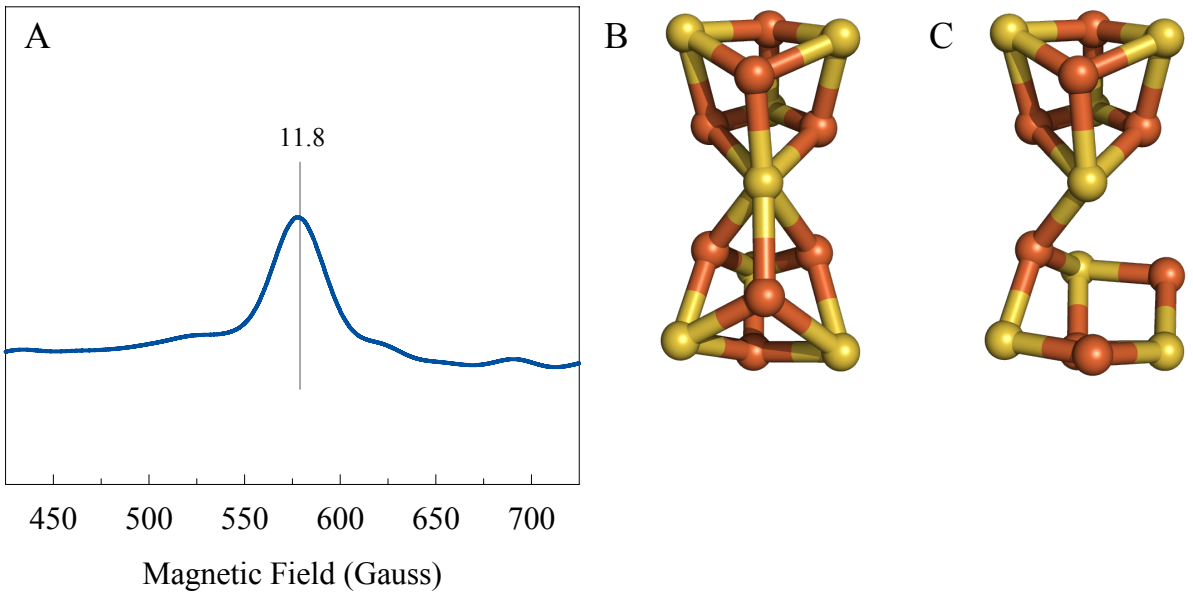

Figure 1.4 The characteristic EPR signal and structural changes of the P-cluster on *Av*NifDK. (**A**) The g = 11.8 EPR signal of the P-cluster that reflects an S = 3 or 4 spin state. Conditions: ten scans were run at 10 K with a microwave power of 50 mW and a microwave frequency of 9.62 GHz. The crystal structure representations of the P^N (**B**) and P^{Ox} (**C**) states of the P-cluster (PDB code: 3U7Q). The clusters are shown as ball-and-stick. Atoms are colored as follows: Fe, rust; S, yellow.

1.3.2 Structural Description of Component 2 – The Reductase Component

The *A. vinelandii* Mo-nitrogenase reductase component, *Av*NifH, is encoded by the *nifH* gene and forms a homodimer (γ_2) approximately 60 kDa in size (Figure 1.5A and B). The protein contains a nucleotide-binding site in each subunit and a $[Fe_4S_4]$ cluster positioned at the subunit interface of the protein near the surface by the Cys^{97} and Cys^{132} residues from each subunit (Figure 1.5C).[52] The $[Fe_4S_4]$ cluster can support three oxidation states, $[Fe_4S_4]^0$, $[Fe_4S_4]^{1+}$, and

$[Fe_4S_4]^{2+}$, and the crystal structures of the proteins in different oxidation states have been solved.[53] The protein crystal structures in the different oxidation states do not vary greatly, despite solution-state experiments that suggest otherwise.[3,53] This difference may be due to either oxidation reactions that occur during the crystallization process or to photoreduction of the metallocluster during data collection. *Av*NifH also binds MgATP, one in each subunit, in a W Walker's A motif protein fold, found between residues 9 and 16.[52,54] Several *Av*NifH structures have been solved that have a nucleotide bound in this location (Table 1.3), and they show minor conformational changes between the nucleotide-bound and unbound states.[53] However, experimental results suggest that the structures of the protein and the $[Fe_4S_4]$ cluster are dynamic in the presence of nucleotides, and these dynamics are better reflected in the crystal structures of the *Av*NifH/*Av*NifDK complex (Section 1.3.3).

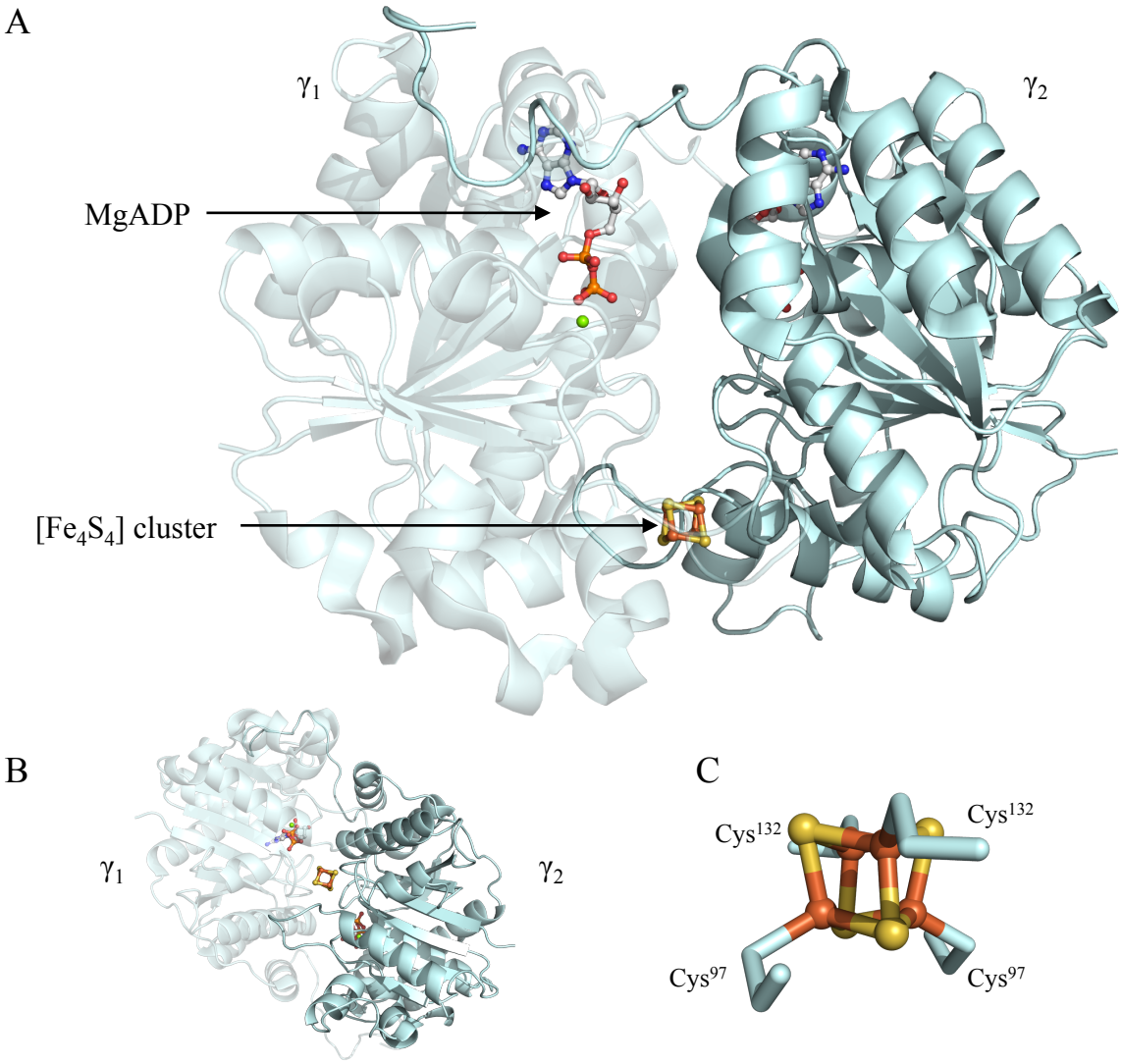

Figure 1.5 The crystal structure of *Av*NifH with MgADP bound at 2.15 Å resolution (PDB code: 1FP6). (**A**) Crystal structure cartoon of *Av*NifH with the metallocluster and nucleotides highlighted. (**B**) A 90° rotation of the *Av*NifH crystal structure, with a view down the two-fold rotation axis. (**C**) Ball-and-stick representation of the [Fe_4S_4] cluster of *Av*NifH. Atoms are colored as follows: Fe, rust; S, yellow; C, white; N, blue; O, red; Mg, green. PyMOL was used to generate this figure.[38]

Table 1.3. Select Fe protein crystal structures with corresponding PBD codes and resolutions.

Protein	PDB code:	Resolution (Å)	Reference
NifH	1G5P	2.2	55
VnfH	[a]	2.2	56
NifH with $[Fe_4S_4]^0$ cluster	1G1M	2.25	55
NifH + MgADP	1FP6	2.15	57
ΔL127-NifH + MgATP	2C8V	2.5	58
ΔL127-NifH + NifDK + MgATP	1G21	3.0	59
NifH + NifDK + MgAMP·AlF_4^-	1N2C	3.0	34
NifH + NifDK + MgADP	2AFI	3.1	33

[a]at the time of writing, the PDB code was not yet released

Until recently, only crystal structures of the Mo-nitrogenase Fe protein were published, but spectroscopic characterization of the reductases from the V- and Fe-only nitrogenases, *Av*VnfH and *Av*AnfH, respectively, were known.[5] EPR and XAS suggested that the $[Fe_4S_4]$ clusters of the alternative nitrogenase Fe proteins behaved similarly to *Av*NifH; and the sequence similarity of the three Fe proteins suggested a similar overall protein structure.[53] The first structure of *Av*VnfH with MgADP bound was published in 2018. The protein is encoded by the *vnfH* gene and forms a homodimer (γ_2) approximately 60 kDa in size, not dissimilar to *Av*NifH, and shares a 91% sequence homology with that protein. As predicted from spectroscopic and biochemical characterizations, the overall structures of the ADP-bound *Av*VnfH and *Av*NifH structures have a high degree of structural homology, with structural alignment of the ADP-bound Fe proteins having a root-mean-squared deviation of 0.3 Å for all atoms.[56] *Av*VnfH, like *Av*NifH, also contains a nucleotide-binding site in each subunit and a bridging $[Fe_4S_4]$ cluster, bound by the Cys^{98} and Cys^{133} residues from each subunit.[54] Unfortunately, at the time of writing, the PDB code was not yet released and so a figure is not included.

1.3.2.1 Characterization of the [Fe_4S_4] cluster of the Nitrogenase Fe Protein

Fe proteins perform three known physiological functions: 1) it mediates the ATP-dependent electron transfer to the catalytic component, 2) it assists in the biosynthesis of the P-cluster on *Av*NifDK, and 3) it serves as a molybdenum and homocitrate insertase for M-cluster maturation.[21,22,60,61] In addition, Hu and coworkers showed that *Av*NifH and *Av*VnfH could also perform the seemingly adventitious interconversion CO_2 to CO.[62] In all of these capacities the [Fe_4S_4] cluster plays a pivotal role for activity and is sensitive to reaction conditions.[3,53] Substantial effort has gone into the characterization of this FeS cluster, both spectroscopically and biochemically, and the results are summarized in the section below.

1.3.2.2 EPR Analysis of the Fe Proteins

The [Fe_4S_4] cluster of *A. vinelandii* Fe proteins can occupy three oxidation states: $[Fe_4S_4]^0$, $[Fe_4S_4]^{1+}$, and $[Fe_4S_4]^{2+}$, but only the $[Fe_4S_4]^{1+/2+}$ oxidation states are thought to be physiologically relevant.[3,63] The [Fe_4S_4] cluster of the Fe protein, like most nitrogenase metalloclusters, is oxygen-sensitive and so is generally handled in the presence of the reductant and oxygen scavenger DT. Under these conditions the $[Fe_4S_4]^{1+}$ state is readily accessible and exists as a mixture of a $S = 1/2$ and $S = 3/2$ species (Figure 1.6B), with the rhombic $S = 1/2$ signal being the major component (*g*-values of 2.04, 1.93, and 1.84).[64,65] However, chemical additives to the protein solution can alter the ratio of the $S = 1/2$ and $S = 3/2$ species.[66] The cluster can be chemically oxidized to the $[Fe_4S_4]^{2+}$ state by addition of indigo disulfonate (IDS), resulting in diamagnetic cluster with an overall $S = 0$ spin state, as determined by Mössbauer spectroscopy, which does not show a signal in the EPR spectrum (Figure 1.6A).[3] The "all ferrous" $[Fe_4S_4]^0$ state is generated by addition of a strong reductant, such as titanium (III) citrate or europium (II) diethylenetriaminepentaacetic acid (Eu^{II}-DTPA), and the EPR spectrum displays a $g = 15.9$

resonance in parallel-mode, consistent with an $S = 4$ species (Figure 1.6C).[67–70] The Fe proteins from the alternative nitrogenases, *Av*VnfH and *Av*AnfH, also exhibit similar EPR signals and cluster behavior as observed for *Av*NifH, and some of this information is summarized in Table 1.4.[65]

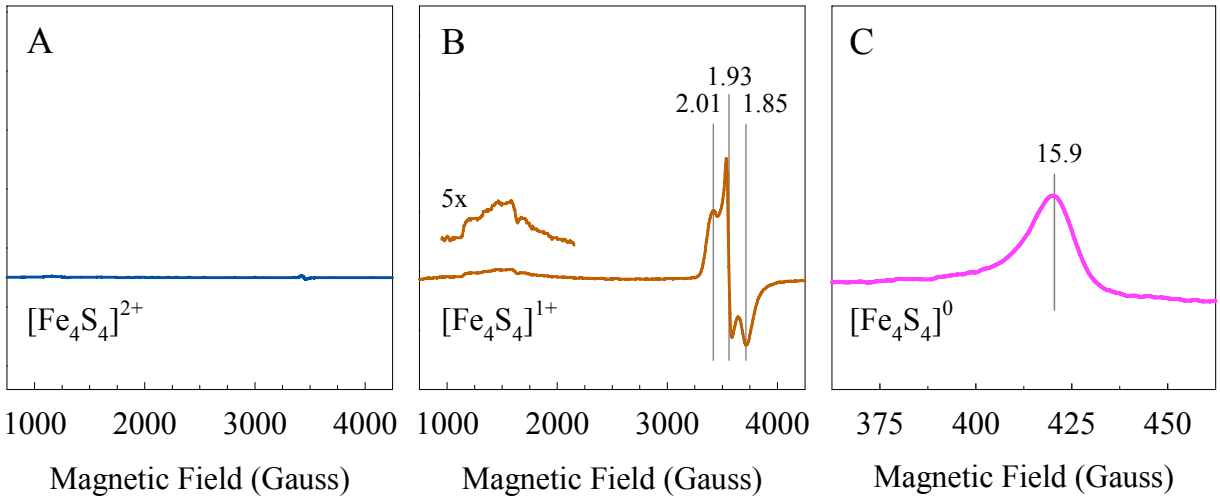

Figure 1.6 EPR spectra of *Av*NifH in the IDS-oxidized ($[Fe_4S_4]^{2+}$, A), DT-reduced ($[Fe_4S_4]^{1+}$, B), and Eu^{II}-reduced all-ferrous states ($[Fe_4S_4]^{0}$, C). The *g*-values are indicated by vertical lines. IDS = indigo disulfonate, DT = dithionite, Eu^{II}-DTPA = europium (II) diethylenetriaminepentaacetic acid. Conditions: four scans were run at 10 K with a microwave power of 50 mW and a microwave frequency of 9.62 GHz.

Table 1.4 EPR Features and Signals Generated by the Fe proteins from *A. vinelandii*.

Protein	Oxidation State	Nucleotide-bound	Spin State	Line-shape	*g*-values		
*Av*NifH	$[Fe_4S_4]^{2+}$	-	$S = 0$	Featureless		-	
	$[Fe_4S_4]^{1+}$	Nucleotide-free	$S = 1/2, 3/2$	Rhombic	2.01	1.93	1.85
	-	ATP-bound	$S = 1/2$	Axial	2.03	1.91	
	-	ADP-bound	$S = 1/2$	Axial	2.02	1.92	
	$[Fe_4S_4]^{0}$	-	$S = 4$			15.9	
*Av*VnfH	$[Fe_4S_4]^{2+}$	-	$S = 0$	Featureless		-	
	$[Fe_4S_4]^{1+}$	Nucleotide-free	$S = 1/2, 3/2$	Rhombic	2.00	1.93	1.84
		ATP-bound	$S = 1/2$	Axial	2.03	1.91	
		ADP-bound	$S = 1/2$	Axial	2.02	1.92	
	$[Fe_4S_4]^{0}$	-	$S = 4$			15.9	

The $S = 1/2$ signals of the DT-reduced $[Fe_4S_4]^{1+}$ clusters of *Av*NifH and *Av*VnfH undergo a spectral change upon binding of nucleotides.[3,62] The EPR signal changes from a rhombic

(Figure 1.7, black) to an axial symmetry upon binding of MgATP (Figure 1.7A, blue) or MgADP (Figure 1.7B, red). Similar effects are also observed for *Av*VnfH (not shown).[62] This nucleotide-induced change in the EPR spectrum is consistent with the protein conformational changes that are observed for *Av*NifH in solution and will be described in more detail in Section 1.3.2.4. To date, detailed EPR analysis of *Av*AnfH with nucleotide binding has not been reported; however, due to the similarity of *Av*NifH and *Av*VnfH, it is predicted that *Av*AnfH would likely behave similarly.

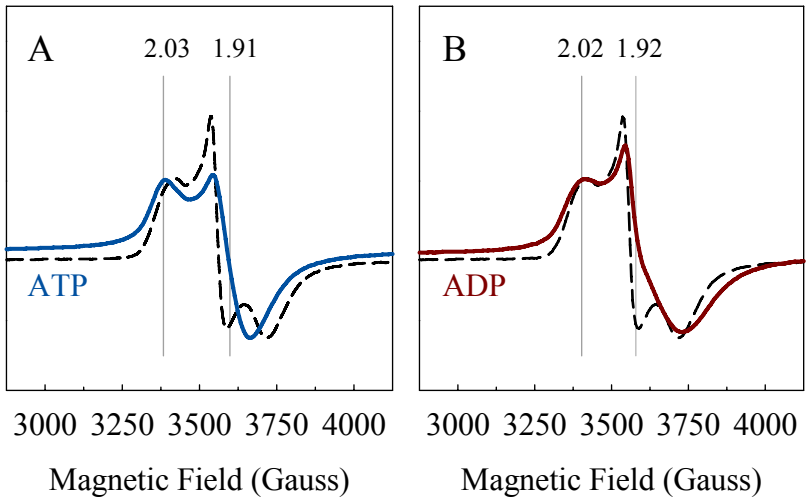

Figure 1.7 EPR spectra of *Av*NifH bound with nucleotides in the DT-reduced ($[Fe_4S_4]^{1+}$) State. (**A**) EPR spectra of *Av*NifH in the presence (solid blue) and absence (dotted black) of MgATP. (**B**) EPR spectra of *Av*NifH in the presence (solid blue) and absence (dotted black) of MgADP. The g-values of the nucleotide-bound spectra are indicated on the spectra. Conditions: four scans were run at 10 K with a microwave power of 50 mW and a microwave frequency of 9.62 GHz.

1.3.2.3 Reduction Potential of Fe Proteins

The $[Fe_4S_4]^{1+/2+}$ transition is proposed as the physiologically relevant transition involved in electron transfer by the Fe protein.[3,53,71] The $[Fe_4S_4]^{1+}$ state can be accessed *in vitro* using excess DT whereas flavodoxins and ferrodoxins drive the reduction *in vivo*.[72–76] To better understand the electron transfer reactions facilitated by *Av*NifH, the midpoint reduction potential (E_m) was determined under a series of conditions using microcoulometry.[77] This is a technique

where fully oxidized *Av*NifH ($[Fe_4S_4]^{2+}$) was introduced into a glass electrochemical cell containing a buffered solution under a controlled potential, and the change in current was measured over time. The E_m for the $[Fe_4S_4]^{1+/2+}$ transition of *Av*NifH was determined to be ≈-290 mV versus the standard hydrogen electrode (SHE) (Figure 1.8).[78] The addition of either MgATP or MgADP to *Av*NifH shifted the E_m to ≈-430 and ≈-440 mV, respectively).[78] Hu and co-workers later used a redox titration method to measure the E_m of both *Av*NifH and *Av*VnfH. They observed reduction potentials of -300 and -346 mV versus SHE for *Av*NifH and *Av*VnfH without nucleotide present, and -405 and -430 mV in the presence of MgATP, respectively.[62] The decrease in the reduction potential caused by nucleotide binding may only have a limited effect on catalysis as the reduction potential of Fe proteins from other organisms (such as *Klebsiella pneumoniae* or *Clostridium pasteurianum*) can vary by as much as 100 mV.[3] To date, the E_m of *Av*AnfH has yet to be reported.

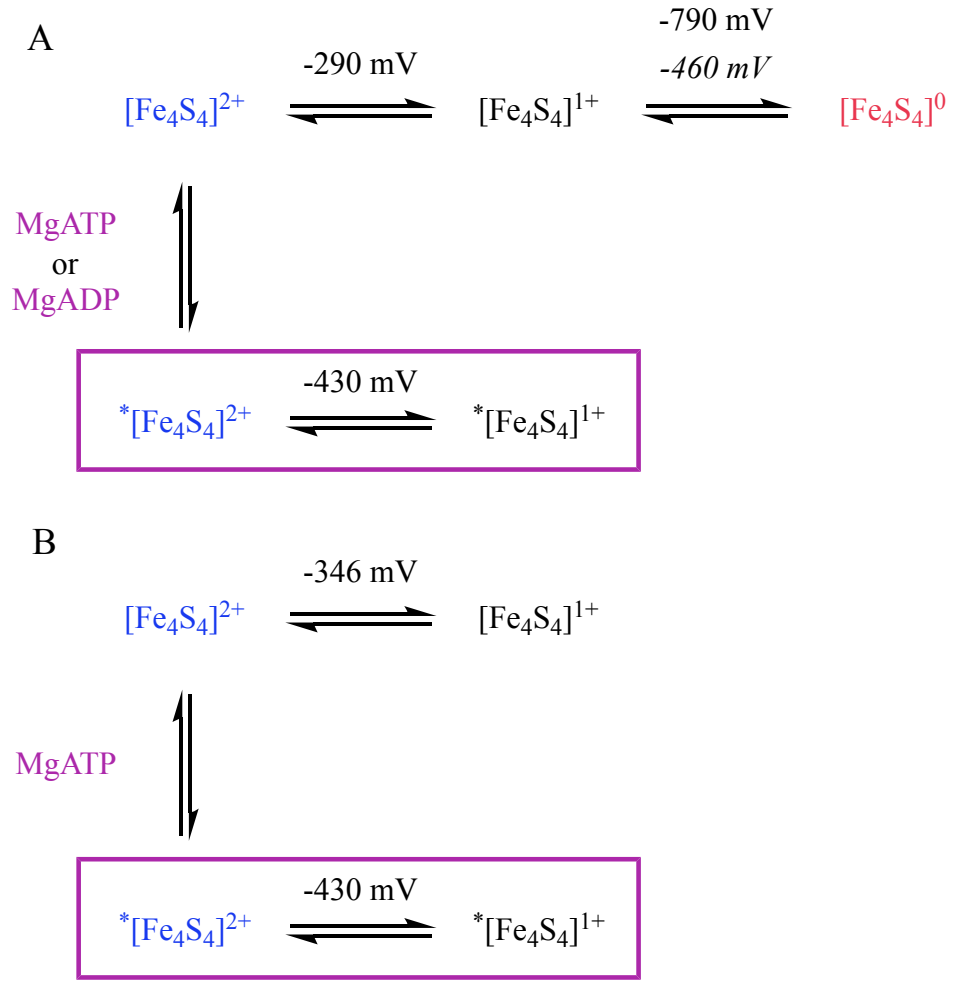

Figure 1.8 Summary of the midpoint reduction potentials (E_m) for the Fe proteins from *A. vinelandii*. (**A**) The E_m for *Av*NifH with the oxidized, reduced, and all-ferrous states are shown in blue, black and pink, respectively. The E_m value for the $[Fe_4S_4]^{1+/0}$ transition reported for the $S = 4$ state is shown in plain text and the $S = 0$ state is shown in italics. The addition of nucleotide is depicted in the purple box. (**B**) The E_m for *Av*VnfH with the oxidized and reduced states shown in blue and black, respectively. Addition of MgATP is depicted in the purple box.

The E_m of the $[Fe_4S_4]^{1+/0}$ transition was also measured using microcoulometry, and was observed to have an E_m of -460 mV versus the normal hydrogen electrode (NHE).[79] This species was generated using either methyl viologen or flavodoxin hydroquinone as redox reagent and was proposed to have an $S = 0$ spin state.[79,80] Using titanium (III) citrate as a strong reductant, Burgess and co-workers followed up on the previously mentioned work and generated an all-ferrous *Av*NifH $[Fe_4S_4]$ cluster with a definitively assigned $S = 4$ spin state.[53]

Spectroelectrochemical methods were used to measure the E_m of the all-ferrous $S = 4$ *Av*NifH species, and it resulted in an E_m of 790 mV versus NHE (Figure 1.8).[81] Subsequent work found that the $S = 4$ *Av*NifH species could also be generated more rapidly using europium (II) chelate complexes instead of the titanium (III) citrate.[82]

1.3.2.4 Nucleotide-induced Conformational Changes of *Av*NifH

Prior to the report of the first crystal structure, calorimetric chelation studies were performed on *Av*NifH in the presence of nucleotides to asses the extent of structural change associated with nucleotide binding.[83–85] These studies revealed that the [Fe_4S_4] cluster was accessible, and the Fe atoms were more easily extracted from the Fe protein in the presence of chelating agents like 2,2'-bipyridine and bathophenanthrolinedisulfonate when MgATP was present than when MgADP or no nucleotide was present.[83–85] This led to the conclusion that the [Fe_4S_4] cluster in *Av*NifH was more solvent exposed when MgATP was bound to the protein. Small-angle X-ray scattering (SAXS) studies, which are able to assess protein conformational changes without the need for crystalline material, also indicated that there was a more significant protein rearrangement in *Av*NifH in the presence of MgATP compared to either MgADP or nucleotide-free samples, both of which were indistinguishable from each other.[86] Additional insights about nucleotide binding have come to light after crystal structures of *Av*NifH and *Av*NifH/*Av*NifDK were solved containing different nucleotides bound in the non-complexed and complexed states, respectively.

When the non-complexed *Av*NifH (protein, pale green; cluster, forest green) with and without MgADP (protein, light blue; cluster, sky blue) are overlaid (Figure 1.9A), there appears to be little difference in the overall structure of the proteins, consistent with the SAXS and chelation data.[83–86] However, overlaying the MgADP- (protein, light blue; cluster, sky blue) and

MgATP-bound (pale yellow; cluster, bright orange) *Av*NifH structures (Figure 1.9B) from the *Av*NifH/*Av*NifDK complexed structures reveals that the [Fe_4S_4] cluster is ~3 Å closer to the protein surface in the MgATP structure than the MgADP structure.[33,53,59] It has been proposed that the MgATP-bound *Av*NifH with a more surface-exposed cluster primes the protein to readily transfer electrons to *Av*NifDK, whereas the recession of the [Fe_4S_4] cluster upon MgATP cleavage helps to prevent a backflow of electrons.[3,87]

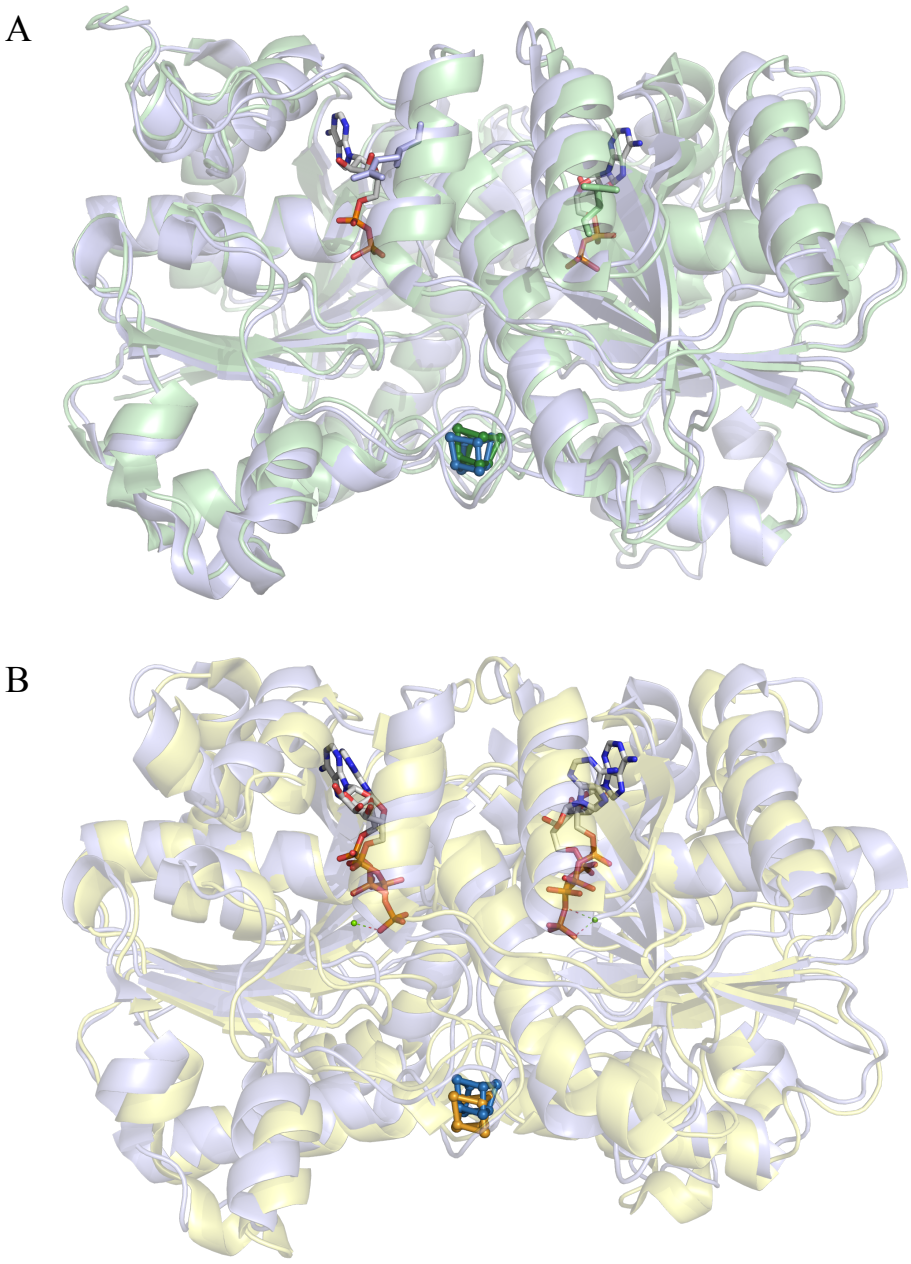

Figure 1.9 Structural comparison of nucleotide-free and nucleotide-bound *Av*NifH, both as free proteins and in complex with *Av*NifDK. (**A**) The structures of the nucleotide-free (PDB code: 1G5P; protein, pale green; cluster, forest green) and the MgADP-bound (PDB code: 1FP6; protein, light blue; cluster, sky blue) free *Av*NifH are overlaid. (**B**) The crystal structures of the MgADP-bound (PDB code: 2AFI; protein, light blue; cluster, sky blue) and MgATP-bound (PDB code: 1G21; protein, pale yellow; cluster, bright orange) *Av*NifH in complex with *Av*NifDK are overlaid (*Av*NifDK portion is not shown). Atoms are colored as follows: C, white; N, blue; O, red; Mg, green; Al, gray; F, pale cyan. PyMOL was used to generate this figure.[38]

1.3.3 Structural Description of the *Av*NifH/*Av*NifDK Complex

While N_2 reduction is facilitated by *Av*NifDK at the M-cluster site, the reductase partner *Av*NifH is crucial for nitrogenase activity.[3,7,34] This raised the question of how these two proteins bind to each other, as well as how they interact during catalysis. Chemical cross-linking was one experimental approach that was used to understand which amino acids residues on *Av*NifH and *Av*NifDK came in contact with one another during the formation of a putative *Av*NifH/*Av*NifDK complex.[88] It was found that an isopeptide bond formed between the Glu^{112} of *Av*NifH and the Lys^{399} of the β subunit of *Av*NifDK roughly indicating how these proteins would interact.[88,89] Site-directed mutagenesis and post-translational modifications were also used to modify residues of both proteins to explore other potential points of interaction. Additional studies expanded the strategies that were available to probe this protein-protein interaction. As previously mentioned, *Av*NifH binds nucleotides and subsequently undergoes conformational changes that affect the solvent access to the $[Fe_4S_4]$ cluster depending on which nucleotide was bound to the protein.[3,53] With the FeS cluster 'exposed' in the presence of nucleotides, chelating agents are readily able to bind the Fe atoms and degrade the cluster.[83–85] Taking advantage of this fact, *Av*NifH and *Av*NifDK were mixed together in solution in the presence of MgATP, presumably forming a complex. Chelation agents were then added which resulted in a greatly reduced rate of Fe chelation from *Av*NifH when *Av*NifDK was present, compared to *Av*NifH alone.[83,90] This supported the notion that the cluster was protected in the presence of the catalytic component, implying the cluster-containing face of *Av*NifH docks to the surface of *Av*NifDK.

Similar experiments employing the use of *Av*NifH variants were also used to explore additional aspects of the *Av*NifH/*Av*NifDK complex. A set of experiments showed that K15Q and A157S *Av*NifH variants, proteins that could still bind MgATP but did not result in the

associated MgATP-induced conformational change, were unable to compete with wildtype *Av*NifH in an activity assay despite being able to form normal cross-linking complexes with *Av*NifDK.[91] Conversely, *Av*NifH variants that form a MgATP-like or partial MgATP-like conformation in the absence of MgATP (e.g. D129E, ΔL127) bound to *Av*NifDK more tightly than nucleotide-free *Av*NifH.[78,92] It was concluded from these experiments that a MgATP-induced conformational change was required to form an active *Av*NifH/*Av*NifDK complex.[3] Burgess and co-workers further proposed that the structural change in nitrogenase evolved because the conformation of the proteins was a prerequisite to form a *Av*NifH/*Av*NifDK complex that optimally positioned the enzyme for MgATP hydrolysis and electron transfer between metallocofactors. [3]

The first *Av*NifH/*Av*NifDK complex structure was published by Rees and coworkers in 1997 (Figure 1.10, left).[34] The structure shows the $\alpha_2\beta_2$ heterotetramer of *Av*NifDK, with one *Av*NifH docked to each αβ dimer (Figure 1.10). This complex was "locked" in the ATP-bound conformation through the use of MgADP·AlF_4^-, a non-hydrolyzable ATP analog. In the complexed form, the [Fe_4S_4] cluster of *Av*NifH is positioned ~15 Å away from the P-cluster of *Av*NifDK, and the P-cluster is ~14 Å away from the M-cluster.[35–37] This protein complex places all of the FeS clusters in close proximity likely to better facilitate the interprotein electron transfer (ET) that is required for subsequent substrate reduction. Electrons are transferred from the [Fe_4S_4] cluster of *Av*NifH to the P-cluster, and the P-cluster transfers electrons to the M-cluster; and this process occurs concomitantly with the hydrolysis of two molecules of MgATP by *Av*NifH for every electron transferred (Figure 1.10, right).[52,93–98] Additional insights into how the ET process occurs in nitrogenase will be described in further detail in Section 1.5.2.

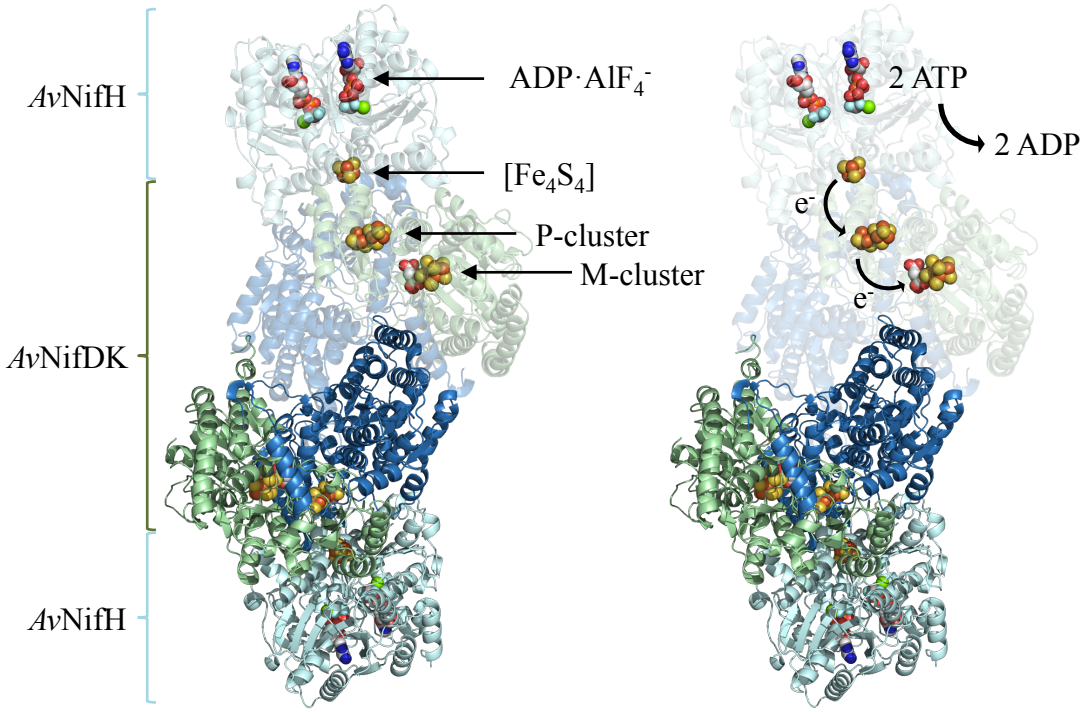

Figure 1.10 The crystal structure of the ADP·AlF_4^- stabilized *Av*NifH/*Av*NifDK complex at 3 Å resolution (PDB code: 1N2C). The crystal structure cartoon on the left highlights the nucleotides and metalloclusters, while the structure on the right highlights the components involved in electron transfer. The NifH, NifD, and NifK subunits are represented in pale cyan, pale green, and sky blue, respectively. Atoms are colored as follows: Fe, rust; S, yellow; Mo, cyan; C, white; N, blue; O, red; Mg, green; Al, gray; F, pale cyan. PyMOL was used to generate this figure.[38]

1.4 The Biosynthesis of the Metalloclusters of *Av*NifDK

The metalloclusters of nitrogenase are vital to the function of the enzyme, and unsurprisingly, the construction of these cofactors requires the involvement of and regulation by many other proteins in the *nif* operon.[7] The cluster biosynthesis can be generally split into two parts: and "ex situ" portion that describes the synthesis of the M-cluster, as it occurs on proteins other than *Av*NifDK, and an "in situ" portion that describes the P-cluster synthesis, as this takes place almost entirely on *Av*NifDK.

1.4.1 The Ex Situ Biosynthesis of the M-cluster

The M-cluster of the nitrogenase active site (Figure 1.1C) is one of the most complex metalloclusters found in any known biological system. Efforts to synthetically replicate the cluster are challenging because of features such as the asymmetric Mo atom on one end of the cluster, the interstitial carbon atom, as well as the organic *R*-homocitrate ligand. Despite these complications, a synthetic asymmetric mimic of the M-cluster was recently described, but was not functional for N_2 reduction.[99] In parallel to synthetic approaches to M-cluster synthesis, the biosynthesis of the M-cluster has been a key focus of nitrogenase research that comes with its own set of challenges. The biosynthesis involves a cascade of proteins working in concert to produce the active cluster (Figure 1.11).[100–105] There are multiple steps involved in M-cluster assembly; including the formation of $[Fe_4S_4]$ clusters, the formation of an M-cluster precursor known as the L-cluster ($[Fe_8S_9C]$), Mo and homocitrate insertion into the L-cluster, and the transfer of fully-mature M-cluster to the active site on *Av*NifDK.[7,101–106]

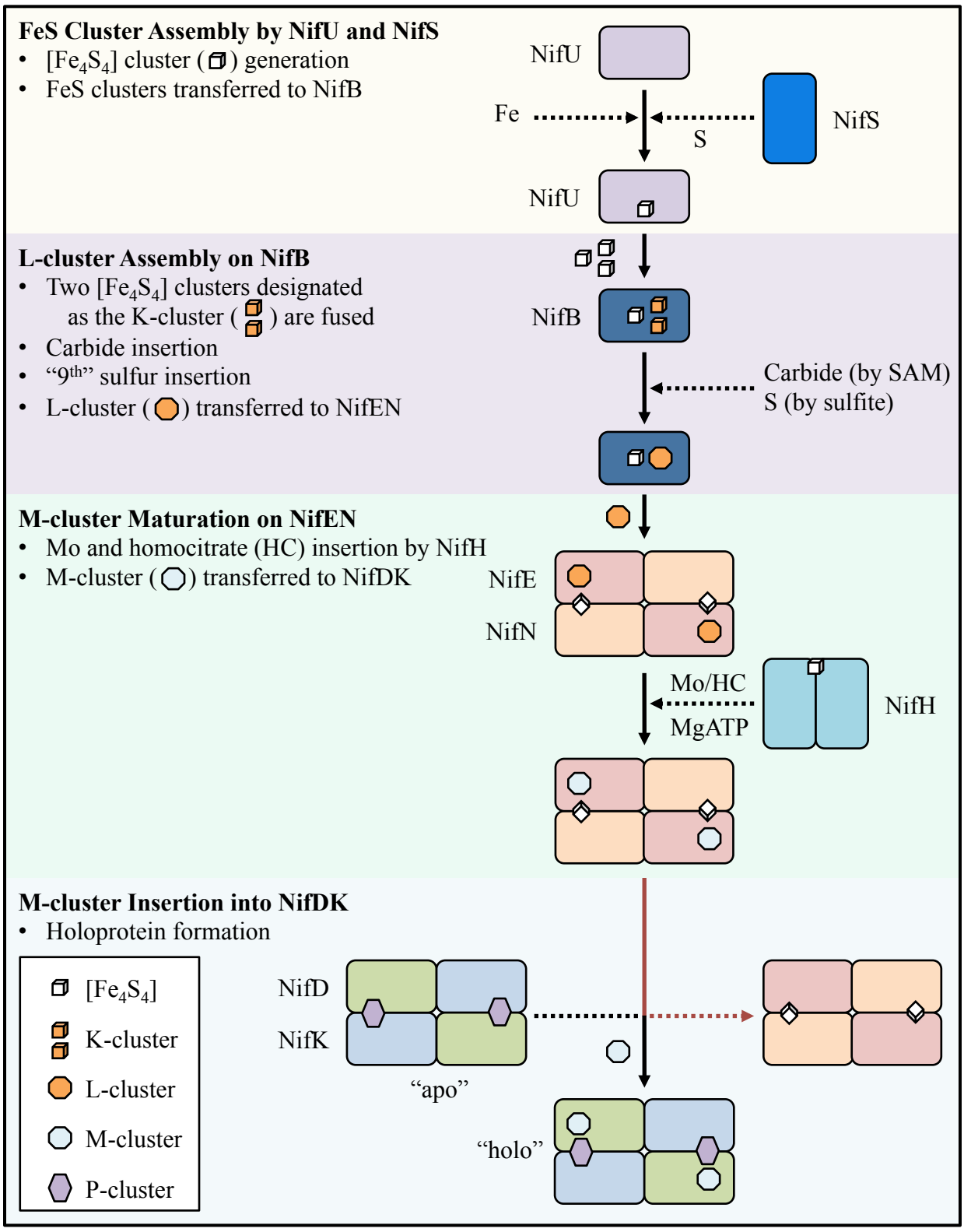

Figure 1.11 A schematic representation of the M-cluster biosynthetic pathway. In *A. vinelandii*, *Av*NifS delivers sulfur to *Av*NifU for the assembly of small FeS clusters. Three $[Fe_4S_4]$ clusters synthesized on *Av*NifU are transferred to *Av*NifB, two of which are thereafter

referred to as K-cluster. *Av*NifB facilitates the radical S-adenosyl methionine (SAM) cleavage reaction that converts the K cluster into the L-cluster via carbide insertion and 9th sulfur insertion.[107,108] The L cluster is subsequently transferred from *Av*NifB to *Av*NifEN for further processing. *Av*NifH acts as a Mo- and homocitrate insertase and interacts with the scaffold protein *Av*NifEN to convert L-cluster into M-cluster. The M-cluster is then transferred to apo-*Av*NifDK. NifS is represented in royal blue; NifU in light purple; NifB in dark blue; NifE in pink; NifN in orange; NifH in cyan; NifD in green; NifK in light blue; and the [Fe_4S_4], K-, L-, P-, and M-clusters are indicated on the legend.

1.4.1.1 Formation of 2Fe and 4Fe Clusters

Like other FeS cluster-containing nitrogenase proteins, M-cluster synthesis in *A. vinelandii* begins with the generation of small FeS clusters ([Fe_2S_2] and [Fe_4S_4]) by *Av*NifU and *Av*NifS (Figure 1.11).[8–13,109] *Av*NifS is a pyridoxal-dependent cysteine desulfurase that catabolizes cysteine and functions to deliver a sulfur source to a scaffold protein, *Av*NifU. The sulfur is then combined with Fe atoms on *Av*NifU, and these components are processed into FeS clusters.[8–13]

1.4.1.2 Formation of L-cluster

*Av*NifB is a S-adenosyl-L-methionine (SAM)-dependent enzyme that plays a vital role as a scaffold for the assembly of the M-cluster. The importance of *Av*NifB was M-cluster was recognized in *Av*NifDK variants expressed in a *nifB*-deletion background (designated Δ*nifB* *Av*NifDK, or apo- *Av*NifDK), as these proteins lacked an M-cluster.[110–114] Subsequently, *Av*NifB was characterized as a ~55 kDa protein that houses three [Fe_4S_4] clusters, and contains a canonical CXXXCXXC motif on the N-terminal end, characteristic of radical SAM-dependent enzymes.[105] One of the [Fe_4S_4] clusters on *Av*NifB reacts with SAM, while the other two clusters are the precursor to the M-cluster, designated as the K-cluster. Initial expression of *Av*NifB was not entirely fruitful; however, when *Av*NifB was fused to another scaffold protein *Av*NifEN, *Av*NifB was stabilized and biochemical characterization became feasible. This new protein was

generated by fusing the 3' end of the *nifEN* gene to the 5'end of the *nifB* gene, and this protein was expressed in a *nifHDK*-deletion strain of *A. vinelandii*.[115]

Recent work by Hu and co-workers has shed light on the specific role that the three [Fe_4S_4] clusters play in L-cluster biosynthesis.[116] It was found that a NifB protein from the organism *Methanosarcina acetivorans*, *Ma*NifB, could be heterologously expressed in *Escherichia coli* and was competent for M-cluster assembly with the other *A. vinelandii* proteins, without requiring fusion to another protein.[25,116] One SAM molecule transfers a methyl to one of the [Fe_4S_4] clusters of the K-cluster (Figure 1.11). Subsequently, a second SAM molecule interacts with the SAM-cleaving [Fe_4S_4] cluster to form a 5'-deoxyadenosine radical (5'-dA·), which is used to abstract a hydrogen atom from the methyl group bound to the K-cluster. This reaction results in a methylene radical bound to the K-cluster. Two additional hydrogen atoms are then lost, and a structural rearrangement that presumably allows for the coupling of the two [Fe_4S_4] clusters of the K-cluster with the generated carbide follows.[14,116] The carbide-inserted cluster then receives a 9th sulfur, which forms a stable [Fe_8S_9C] cluster called the L-cluster.[108] A structure of the L-cluster has been proposed, and is based on spectroscopic characterization and comparison to the M-cluster; however, there are currently no crystal structures of the L-cluster.[17,117,118] Analogous to the M-cluster, the L-cluster is proposed to be two [Fe_4S_3] partial cubanes that are bridged by three μ_2-sulfides with a μ_6-insterstitial carbide coordinated in the central cavity (Figure 1.12).[17,115,117] After L-cluster has been synthesized on *Av*NifB, it is transferred to *Av*NifEN (Figure 1.11).

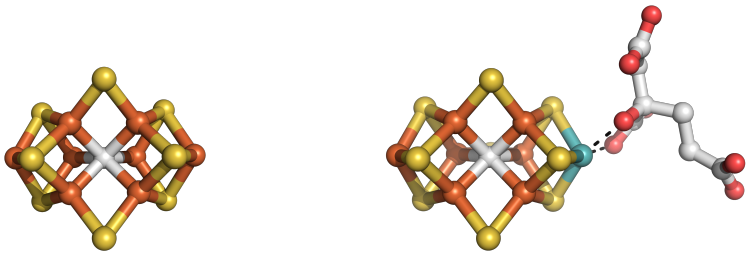

[Fe_8S_9C] **L-cluster**

[$MoFe_7S_9C$-(R)-homocitrate] **M-cluster**

Figure 1.12 Structural comparison of the proposed L-cluster structure to the M-cluster. The clusters are shown as ball-and-stick models. The M-cluster coordinates were used from a crystal structure of *Av*NifDK (PDB code: 3U7Q). Atoms are colored as follows: Fe, rust; S, yellow; Mo, cyan; C, light gray; O, red.

1.4.1.3 Mo and Homocitrate Insertion into the L-cluster

As previously mentioned, *Av*NifEN is a scaffold protein that is ~414 kDa in size and has a high degree of sequence homology to *Av*NifDK.[119] Like *Av*NifDK, *Av*NifEN also forms a $\alpha_2\beta_2$ heterotetramer (Figure 1.13) and houses two types of metalloclusters.[17,120] The P-cluster analogous site on *Av*NifEN contains four Cys residues ($Cys^{\alpha37}$, $Cys^{\alpha62}$, $Cys^{\alpha124}$, $Cys^{\beta44}$), compared to the six found in *Av*NifDK, and houses a [Fe_4S_4] cluster called the O-cluster at the interface of the αβ subunits. The specific L/M-cluster binding site on *Av*NifEN is still somewhat ambiguous, as the electron density for the cluster in the crystal structure was not well defined.[17] However, spectroscopic and biochemical characterization supports the notion that *Av*NifEN receives the L-cluster after it has been assembled by *Av*NifB.

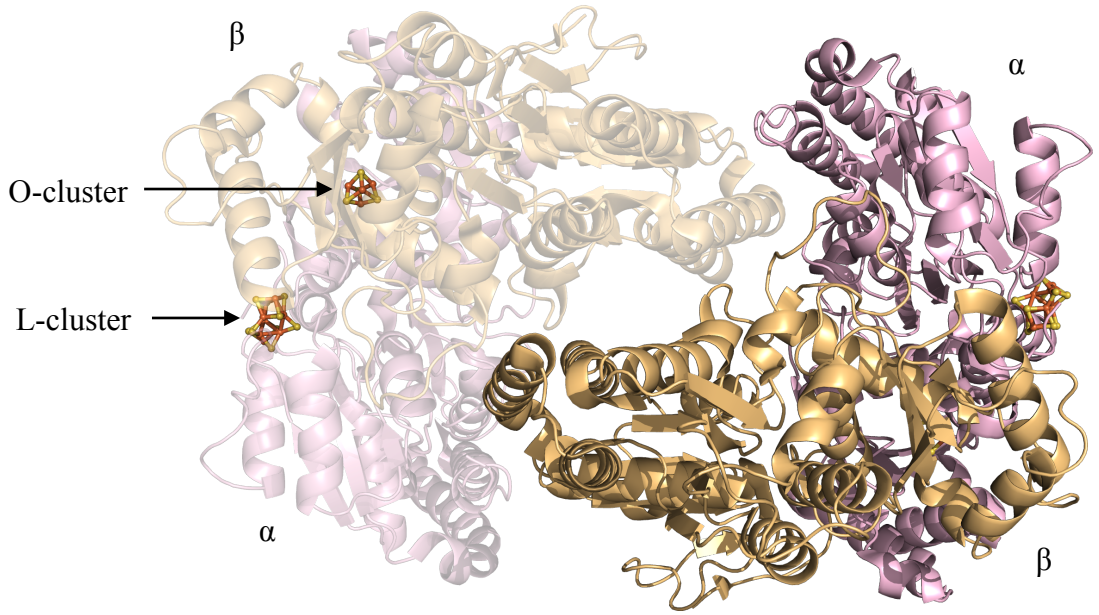

Figure 1.13 The crystal structure cartoon of *Av*NifEN at 2.4 Å resolution (PDB code: 3PDI). The NifE and NifN subunits are represented in light pink and light orange, respectively. Atoms are colored as follows: Fe, rust; S, yellow; Mo, cyan; O red. PyMOL was used to generate this figure.[38]

L-cluster conversion to M-cluster requires *Av*NifH and *Av*NifEN, emphasizing that *Av*NifH plays multiple roles in the nitrogenase system (Figure 1.11).[16,18,60] This conversion takes place when *Av*NifEN loaded with L-cluster is incubated with *Av*NifH, MgATP, molybdate (MoO_4^{2-}), and *R*-homocitrate; a process that will be described more in Section 1.5.1. The precise mechanism by which Mo and homocitrate insertion occurs is still unknown and requires additional study to fully characterize the reaction. Once the M-cluster is synthesized, the cluster can then be transferred to the active site on *Av*NifDK.[16,18,121]

1.4.1.4 Transfer of M-cluster to the Active Site on *Av*NifDK

Biochemical analysis suggests that a conformational change in *Av*NifEN accompanies M-cluster maturation, and this change allows for the formation of a *Av*NifEN/*Av*NifDK complex and subsequent transfer of the M-cluster from *Av*NifEN to apo-*Av*NifDK (Figure 1.11).[121] While there is currently no crystal structure of an *Av*NifEN/*Av*NifDK complex, comparison of the

individual crystal structures paired with biochemical analysis helps to shed light on the process. The putative cluster insertion channel in apo-*Av*NifDK is rich in positively charged residues and may facilitate the transfer of the negatively charged M-cluster into *Av*NifDK.[101–106,114] Sequence alignment between *Av*NifEN and *Av*NifDK reveals that *Av*NifDK has unique residues around the M-cluster site that may allow the cluster to bind to the protein more tightly to *Av*NifDK than to *Av*NifEN.[106] It has therefore been postulated that M-cluster can be transferred from a lower affinity binding site on *Av*NifEN to a higher affinity site on *Av*NifDK.

Once the cluster has been transferred to *Av*NifDK, there is an associated conformational change in *Av*NifDK that buries the cluster ~10 Å below the protein surface (Figure 1.1 and Figure 1.11). The overall conformation of the protein becomes more compact as observed by small-angle X-ray scattering (SAXS), which provides information about the protein conformation without requiring a crystalline structure.[122]

1.4.2 The In Situ Biosynthesis of the P-cluster

The P-cluster in *Av*NifDK (Figure 1.1B) is the metallocluster that supports nitrogen reduction catalysis through the transfer of electrons from the reductase partner *Av*NifH to the M-cluster.[26,35,36] Unlike the M-cluster, the P-cluster has yet to be extracted from the protein intact, likely due to rapid decomposition of the cluster once the bridging μ_2-cysteine ligands from the protein are removed.[4,7] Synthetic efforts to synthesize the P-cluster have resulted in structural analogs that have been generated by the fusion of two cubane clusters, suggesting a possible mechanism in the biosynthetic pathway.[123–125] However, similar to M-cluster assembly, the biosynthesis of the P-cluster is a multi-step process involving several proteins, including an important role played by *Av*NifH.

1.4.2.1 Synthesis of the P-cluster Precursor (P^P-cluster)

P-cluster assembly is initiated by the synthesis of FeS clusters on *Av*NifU and *Av*NifS (Figure 1.14), the same as in M-cluster biosynthesis.[8–13] Two [Fe_4S_4] clusters are transferred from NifU to the P-cluster site of *Av*NifDK, and these clusters are referred to as the P-cluster pre-cursor, P^P-cluster. The P^P-cluster is observed in *Av*NifDK variants expressed in a *nifH*-deletion background (Δ*nifH Av*NifDK) (Figure 1.14).[21,22,126] Fe K-edge XAS analysis of Δ*nifH Av*NifDK reveals that the P^P-cluster consists of a normal [Fe_4S_4] cluster and an atypical [Fe_4S_4] cluster that is either distorted by a bridging Cys ligand in place of a sulfide, or a coordinated light atom such as a N or O from Asp, Ser, His, or adventitious water.[22,126] This assignment is further supported by magnetic circular dichroism (MCD) spectroscopy, which determined that one of the clusters exists as a $[Fe_4S_4]^{1+}$ cluster and the other as a diamagnetic [Fe_4S_4]-like cluster in the DT-reduced state.[127,128]

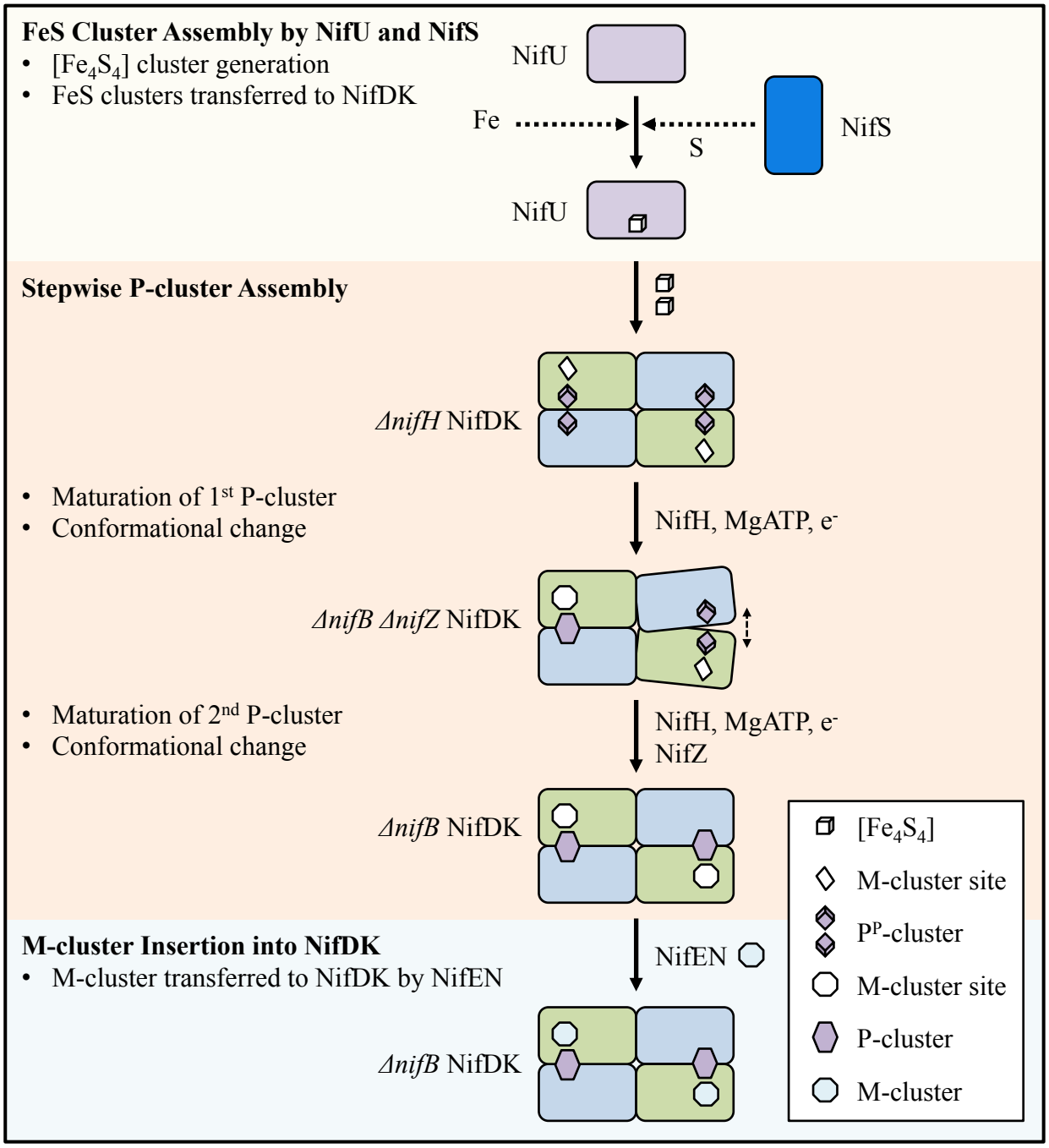

Figure 1.14 A schematic representation of the P-cluster biosynthetic pathway. *Av*NifH is solely required to synthesize the first equivalent of P-cluster on *Av*NifDK, while the second P-cluster requires both NifH and NifZ. The P-cluster assembly results in a structural change to the cluster that stabilizes the protein and opens active site to receive the M-cluster. NifD is represented in green; NifK in blue; and the $[Fe_4S_4]$, P-, and M-clusters are indicated on the legend.

1.4.2.2 Conversion of the P^P-cluster to the P-cluster

P^P-cluster can be converted into P-cluster *in vitro* by incubating Δ*nifH* *Av*NifDK with *Av*NifH, MgATP, and DT.[22] Cluster formation can be observed over time with EPR spectroscopy. As the reaction proceeds, the $S = 1/2$ signal associated with the P^P-cluster (*g*-values of 2.05, 1.93, and 1.90) decreases and the P^{Ox}-cluster signal (g = 11.8) increases along with the reconstituted activity of the protein. There is an apparent "lag" phase in the maturation process that appears to be associated with the completion of P-cluster assembly in one of the αβ-dimers, and this occurs at approximately 50% of the respective maximum values. The EPR signal during this lag phase corresponds well with the signal seen from the gene product of a *nifB*- and *NifZ*-deleted *Av*NifDK strain (Δ*nifB* Δ*nifZ* *Av*NifDK) (Figure 1.14) and is consistent with approximately a 50% signal intensity of the P^P-cluster signal and the P^{Ox}-cluster signal.[24,129]

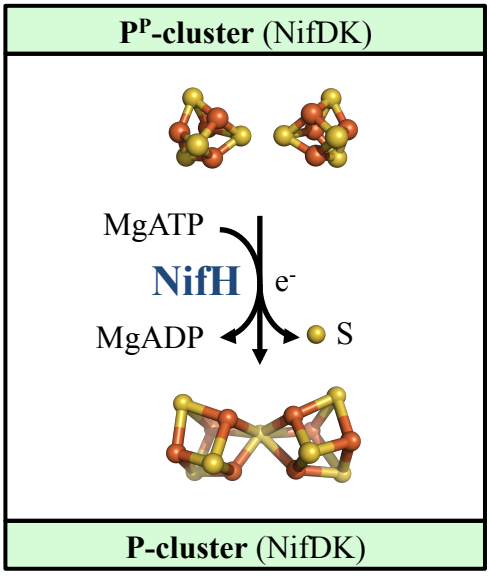

Figure 1.15 *In vitro* maturation of the first P-cluster requires Δ*nifH* *Av*NifDK, *Av*NifH, MgATP, and DT. *Av*NifZ has also been shown to play a role in the maturation of the second P-cluster on *Av*NifDK. Atoms of the metalloclusters are shown as ball-and-stick models and are colored as follows: Fe, rust; S, yellow.

P-cluster formation in the second αβ-dimer of Δ*nifH* *Av*NifDK can be achieved with longer incubation times (post-lag maturation), which is supported by the doubling of activities

and P^{Ox}-cluster EPR signal.[22,23] The EPR signal of the post-lag maturation Δ*nifH Av*NifDK variant coincides with that observed in the Δ*nifB Av*NifDK variant (Figure 1.14), which is known to contain two fully-formed P-clusters. Interestingly, the P^{P}-cluster in the Δ*nifB* Δ*nifZ Av*NifDK variant can also be matured under similar conditions as the post-lag maturation of Δ*nifH Av*NifDK (Figure 1.14), but the addition of NifZ is required, suggesting that NifZ plays a role in P-cluster maturation.[22,23] The activities and EPR signal of the matured Δ*nifB* Δ*nifZ Av*NifDK variant are consistent with those observed by the post-lag maturation of Δ*nifH Av*NifDK, likely indicating that the maturation process proceeds analogously. It is still uncertain the exact role that NifZ plays in P-cluster maturation, but the Δ*nifH Av*NifDK variant (which was expressed in a *nifZ*-intact system) did not require additional NifZ to mature the second P-cluster whereas the Δ*nifB* Δ*nifZ Av*NifDK variant did. It has been proposed that NifZ may function in a chaperone-like role and possibly modifies certain residues in the second αβ-dimer to prepare it for cluster maturation.[23,24]

P-cluster biosynthesis prepares *Av*NifDK for M-cluster insertion. Prior to P-cluster biosynthesis, the M-cluster site occupies a closed conformation that does not allow for the insertion of M-cluster (Figure 1.14, Δ*nifH Av*NifDK). After conversion of the P^{P}-cluster to the P-cluster, *Av*NifDK undergoes a conformational change that opens the M-cluster site and allows for M-cluster insertion (Figure 1.14, Δ*nifB Av*NifDK).[114] Once the M-cluster has been received, there is a subsequent conformational change that covers the P-cluster and protects it from solvent exposure (Figure 1.14, Δ*nifB Av*NifDK) producing a functional nitrogenase.[122]

1.5 The Multiple Functions *Av*NifH

The reductase component from *A. vinelandii* plays a surprising number of important roles in the nitrogenase system. Most obviously, *Av*NifH facilitates electron transfer from

physiological sources to ultimately the M-cluster in the catalytic component of *Av*NifDK. Along with this function, *Av*NifH also binds and cleaves the MgATP equivalents that are required for substrate reduction, and as described in previous sections, the nucleotide binding and cleavage induces conformational changes that help to regulate the electron transfer process. A role of *Av*NifH that is less obvious is in the involvement in the biosynthesis of the two important metallocofactors in *Av*NifDK, the P- and M-cluster. Further still is that the Fe protein has been found to facilitate seemingly adventitious reactivity, interconverting CO_2 and CO.[62] This section will cover the specific roles that *Av*NifH plays in nitrogenase with slightly more detail.

1.5.1 Nitrogenase Cofactor Maturation

As outlined in Section 1.4, nitrogenase cofactor biosynthesis is a multi-step process that takes Fe and S and converts these components into multinuclear metalloclusters. These processes involve contributions from multiple proteins and co-substrates such as SAM and MgATP. One factor that is not usually emphasized is that without *Av*NifH, not only would nitrogenase be unable to reduce N_2 to NH_3, functional P- and M-clusters could not be assembled.

The P-cluster maturation process has been explained in great detail in Section 1.4.2.1; however, there is benefit to concisely summarizing the specific role *Av*NifH plays here. When *Av*NifDK is expressed in a Δ*nifH* background, the P-cluster observed is incompletely formed an composed of to separate $[Fe_4S_4]$ clusters (called P^P-cluster).[21,22,126] Each αβ-dimer of Δ*nifH* *Av*NifDK has one P^P-cluster and when *Av*NifH is incubated with the *Av*NifDK variant, reductant, and MgATP *in vitro*, the P-cluster of one αβ-dimer is formed quickly, followed by the much slower formation of the P-cluster in the second αβ-dimer.[22,23] However, *Av*NifH is not solely responsible for the fusion of the P-cluster precursor, as *Av*NifDK expressed in a Δ*nifH* Δ*nifZ* background will not have functional P-cluster in the second αβ-dimer without incubation of both

*Av*NifH and a *Av*NifZ.[23,24] Not only does *Av*NifH transfer electrons, it functions to help synthesize other electron transfer cofactors.

M-cluster assembly (Section 1.4.1) is an arguably more complex multi-step process than P-cluster assembly, which includes the formation of an iron-only precursor ($[Fe_8S_9C]$) called the L-cluster that is synthesized first on *Av*NifB and then is transferred to *Av*NifEN. With L-cluster loaded on *Av*NifEN, *Av*NifH is able to facilitate the insertion of molybdenum and homocitrate, converting the L-cluster to the M-cluster (Figure 1.11). The gene products of an *A. vinelandii nifHDK*-deletion *nifEN* (Δ*nifHDK Av*NifEN) or *nifHDK*-deletion *nifEN-B* fusion (Δ*nifHDK Av*NifEN-B) expression strains are isolated with L-cluster loaded in the proteins.[15,115,118] The L-cluster on these species is readily identified by a characteristic EPR resonance at $g = 1.94$ in the IDS-oxidized state. *In vitro*, L-cluster maturation to M-cluster can occur directly on *Av*NifEN by, at minimum, incubating Δ*nifHDK Av*NifEN or Δ*nifHDK Av*NifEN-B with NifH, MgATP, DT, molybdate (MoO_4^{2-}), and *R*-homocitrate to form active M-cluster (Figure 1.16).[15,16,18,60] To monitor the conversion of L- to M-cluster, the L-cluster specific signal at $g = 1.94$ was observed over the time course of the reaction. The decrease in intensity of the $g = 1.94$ resonance implied that the L-cluster was disappearing; however, a new signal with resonances at $g = 4.45$, 3.96, and 3.60 indicated that M-cluster was being generated.[16,18] Fe and Mo K-edge XAS analyses also demonstrated that the M-cluster species on *Av*NifEN that resulted from incubation with *Av*NifH was nearly identical to that on wild-type *Av*NifDK, except for a slight perturbation of the Mo coordination environment.[16,18] Importantly, it was observed that step-wise addition of Mo and homocitrate was insufficient for the conversion of the L- to the M-cluster, implying that their insertion may occur in one concerted step.[121]

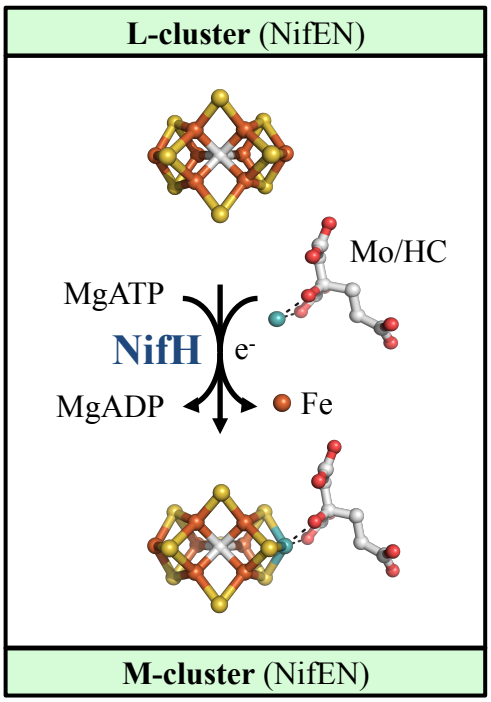

Figure 1.16 Summary of the *in vitro* maturation of the L-cluster to the M-cluster. The maturation of L-cluster requires, at minimum, *Av*NifEN, *Av*NifH, MgATP, DT, molybdate (MoO_4^{2-}), and *R*-homocitrate. *Av*NifH facilitates the insertion of Mo and *R*-homocitrate into the L-cluster to mature functional M-cluster. Atoms are colored as follows: Fe, rust; S, yellow; Mo, cyan; C, light gray; O, red.

After M-cluster maturation on *Av*NifEN, *Av*NifH can be re-isolated from the solution mixture to characterize any changes that may have occurred. Analysis of the repurified *Av*NifH showed that the protein had become loaded with Mo and homocitrate, and this loaded *Av*NifH could be used to insert Mo and homocitrate into NifEN-bound L-cluster.[60] Additionally, Mo- K-edge XAS analysis was used to compare the loaded *Av*NifH with the supplied MoO_4^{2-} starting material, and the results suggested that the Mo-bound to *Av*NifH was in a different form than the starting material, likely a product of molybdate reduction.[60] The EPR spectrum of the Mo-bound *Av*NifH species features a characteristic $S = 1/2$ resonance, but also has the addition of a small signal with *g*-values at 4.44, 4.05, and 3.96 that appears to coincide with Mo-binding. One possibility for the Mo-binding location is in the position that is generally occupied by the γ-phosphate of ATP, as a partial molybdate occupancy was observed in this location in the first

reported structure of *Av*NifH.[52,60] Further studies are required to fully elucidate the mechanism of Mo and *R*-homocitrate insertion into the L-cluster, as well as the specific role that the Fe protein plays in these processes.

1.5.2 Electron Transfer in Nitrogenase

The electron transfer (ET) process and subsequent substrate reduction of N_2 and substrate analogs by the catalytic component has been studied extensively over the past several decades.[93,94] As eight electrons are required for the reduction of every equivalent of N_2, ET is a rather fundamental aspect of nitrogenase catalysis and the Fe protein is specifically responsible for this process. To understand the ET reaction in nitrogenase, methods such as stopped-flow and rapid freeze-quench techniques allow for the observation of spectroscopic changes on very fast time scales that would otherwise not be accessible.

The first step in what is referred to as the "Fe protein cycle" is the reduction of *Av*NifH to the $[Fe_4S_4]^{1+}$ state, followed by two equivalents of MgATP binding to the protein (Figure 1.17).[3,71] The reduction of the Fe protein can be facilitated *in vitro* by DT or likely *in vivo* by flavodoxins or ferrodoxins.[73–76] The binding of MgATP induces a conformational change that allows *Av*NifH to bind to *Av*NifDK to make an *Av*NifH/*Av*NifDK complex (see Section 1.3.2.4). It is important to note that there are two equivalents of *Av*NifH that bind to *Av*NifDK in this complex, on *Av*NifH per αβ-dimer. Seefeldt and co-workers have proposed that MgATP-loaded *Av*NifH binding to *Av*NifDK results in a "conformation gated" change in *Av*NifDK, which allows for an initial transfer of an electron from the all-ferrous P^N-cluster to the M-cluster.[130] Once the P^N-cluster transfers an electron and converts to the P^{1+} state, the $[Fe_4S_4]^{1+}$ cluster of *Av*NifH rapidly transfers an electron to the P-cluster, generating the $[Fe_4S_4]^{2+}$ and P^N states on *Av*NifH and *Av*NifDK, respectively. This overall electron transfer scheme is referred to as a

"deficit-spending" model, as the P-cluster pushes an electron to the M-cluster before receiving exogenous electrons from *Av*NifH.[71,130] It was initially unclear what relationship existed between ET and MgATP hydrolysis in nitrogenase; whether these two events were separate or concerted.[3] Seefeldt and co-workers reported that ET precedes MgATP hydrolysis in nitrogenase, supporting the notion that these two events are not concerted.[131]

After ET to *Av*NifDK, the two MgATP molecules on *Av*NifH are hydrolyzed to form two MgADP and two P_i molecules, in a seemingly rapid reaction, but it is still unclear what specifically induces this hydrolysis.[71] The next step, determined to be the rate-limiting step in the nitrogenase catalytic cycle, is the release of the two P_i from the complex, followed by the rapid release of the MgADP-bound *Av*NifH from *Av*NifDK.[131,132] It has been suggested that phosphate release form the *Av*NifH/*Av*NifDK complex serves to induce the conformational change observed in the MgADP-bound state of *Av*NifH, as described in the previous sections, which lowers the binding affinity of the protein form *Av*NifDK.[71,130] Once freed, the $[Fe_4S_4]^{2+}$ cluster of the MgADP-bound *Av*NifH is then reduced, lowering the binding affinity of MgADP to *Av*NifH, and allowing for the release of MgADP and subsequent replacement by two MgATP molecules, completing the Fe protein cycle (Figure 1.17).[3,71]

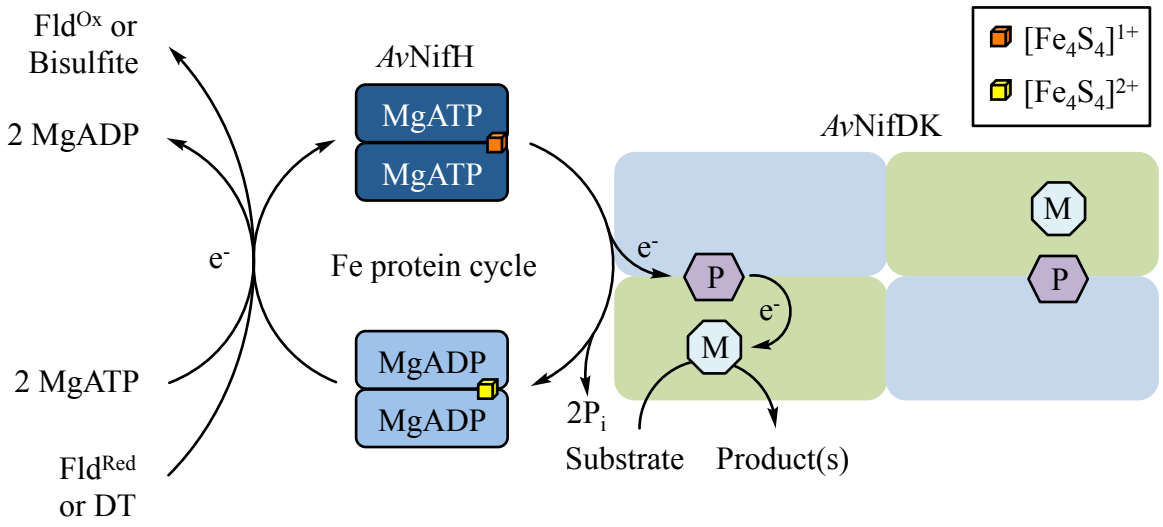

Figure 1.17 A depiction of the MgATP-dependent electron transfer (ET) from *Av*NifH to *Av*NifDK. For ET to occur, the Fe protein must be loaded with 2 equivalents of MgATP and reduced by either DT (*in vitro*) or flavodoxin (*in vivo*). A conformational change accompanies MgATP binding that allows for the Fe protein to interact with *Av*NifDK and form an *Av*NifH/*Av*NifDK complex. After binding, an electron is proposed to transfer from the P-cluster to the M-cluster, followed by ET from the [Fe_4S_4] cluster of *Av*NifH to the P-cluster. The MgATP are then hydrolyzed and the phosphate dissociates from the Fe protein. Finally, the Fe protein dissociates from the catalytic component, MgADP is released, and the Fe protein is prepared for additional redox cycles. This process must be repeated until enough electrons have been transferred to completely reduce the substrate. Fld^{Ox} = oxidized flavodoxin, Fld^{Red} = reduced flavodoxin, and the P- and M-clusters are represented by hexagons and octagons, respectively.

1.5.3 Interconversion of CO_2 and CO

It was recently discovered that the *A. vinelandii* V-nitrogenase could perform an adventitious function similar to the reaction catalyzed in the Fischer-Tropsch process, that is to reduce CO and form short-chain hydrocarbons.[133] Later, Hu and co-workers discovered that both *Av*NifH and *Av*VnfH could interconvert CO_2 and CO under certain conditions *in vitro*, independent of the presence of the catalytic component, functioning as a carbon monoxide dehydrogenase (CODH)-like system.[62] In their work, they also demonstrated that the Fe proteins could reduce CO_2 to CO *in vivo* by expressing *nifDK*- and *vnfDGK*-deletion strains of *A. vinelandii*.[62] Nitrogenase genes can be expressed in the absence of NH_3 and repressed when it is

present. It was observed that CO_2 reduction did not occur in either the *nifDK*- or *vnfDGK*-deletion strains in the presence of NH_3, but that CO_2 reduction did occur in the absence of NH_3.[62] It is still unclear what physiological implications this reaction has on the nitrogenase system, but the ability of Fe proteins to interconvert CO_2 and CO provides an additional direction of study for these proteins.

1.6 Conclusion and Aims of the Dissertation

The Fe protein is essential for nitrogenase to catalyze the reduction of N_2 to NH_3. Not only is the Fe protein responsible for transferring electron to the catalytic component, but it also plays important roles in the assembly of the two metalloclusters found within the catalytic component. The work presented herein will discuss the expression and characterization of various Fe protein homologs in *E. coli*, a non-native nitrogenase host. This work takes a step towards the long-standing nitrogenase research goal to transform nitrogenase genes into plants so that they have the necessary machinery to produce bioavailable ammonia as a viable nitrogen source. Because transforming complete gene cassettes into heterologous hosts has thus far proven to be unsuccessful, the approach that has been taken is to individually express each of the essential nitrogenase genes separately in *E. coli*. Our lab has previously expressed and characterized *Ma*NifB in *E. coli* and showed that the protein was functional and could produce the catalytic cofactor pre-cursor, the L-cluster, after re-constitution of the protein with $[Fe_4S_4]$ clusters.[25,116] Despite having worked on the individual expression of *nifB*, *nifEN*, *nifH*, and *nifDK* gene products in *E. coli*, the primary emphasis of my work has dealt with the Fe proteins and will be the focus of this dissertation.

This dissertation will be divided into two main sections. Section 1 will focus on the physiological roles of the Fe protein and Section 2 will focus on the adventitious function of Fe

proteins to reduce CO_2 and CO. Each section will contain multiple chapters relating to the main theme of that particular section.

1.7 Acknowledgments

A special thanks to Andrew Jasniewski and Megan Newcomb who read multiple versions of this chapter and provided helpful insights in making it become what it is.

Section 1 Characterization of Fe Protein Homologs – The Physiological Functions

The Fe protein is one of two protein components required for N_2 reduction by nitrogenase. The fundamental role of the Fe protein is to transfer electrons to the catalytic component so substrate reduction can occur, and without this component, catalysis cannot occur. Because of this role, there is the possibility of tuning the electron flux through nitrogenase without perturbing the catalytic cofactor by creating hybrid nitrogenase systems. These hybrid systems can be generated by either mismatching the Fe protein and catalytic component from two different nitrogenase systems from the same organism (e.g. pairing *Av*NifH with *Av*VnfDGK) or by using an Fe protein from one organism and a catalytic component from another (e.g. pairing *Ma*NifH with *Av*NifDK). To this end, Fe proteins from the Mo- and V-nitrogenase systems were expressed from *M. acetivorans* (*Ma*NifH and *Ma*VnfH, respectively) and from *A. vinelandii* (*Av*NifH and *Av*VnfH, respectively) and paired with the Mo- and V-nitrogenase catalytic components from *A. vinelandii* (*Av*NifDK and *Av*VnfDGK, respectively); thereby generating six total hybrid systems to compare to the two wildtype systems. The work presented in this section is built around the premise that electron flux can be tuned in nitrogenase by creating hybrid nitrogenase systems.

Working towards the goal of expressing individual nitrogenase genes in a non-diazotrophic organism, Chapter 2 outlines the expression and characterization of the Mo- and V-nitrogenase Fe proteins from *M. acetivorans*, *Ma*NifH and *Ma*VnfH, in *E. coli*.[134] Pairing *Ma*NifH and *Ma*VnfH with the Mo- and V- nitrogenase catalytic components from *A. vinelandii*, *Av*NifDK and *Av*VnfDGK, generated four hybrid nitrogenase systems. Two additional hybrid systems were generated by mismatching the two components from the Mo- and V- nitrogenase systems of *A. vinelandii*, i.e. pairing *Av*NifH with *Av*VnfDGK and *Av*VnfH with *Av*NifDK. Catalytic activity of the six hybrid systems was compared to the wildtype *A. vinelandii* Mo- and

V- nitrogenase systems using four standard activity assays, including the N_2-, C_2H_2-, CO-, and H^+-reduction assays. It was observed that the electron flux of the *Ma*VnfH/*Av*VnfDGK hybrid system was reduced enough such that the alternative V-nitrogenase substrate, CO, was trapped on the V-cluster. In addition to the biochemical assays performed, a homology modeling/*in silico* docking system was generated to screen potential Fe protein sequences to predict their ability to dock with and transfer electrons to the catalytic component. This system was created with the hope that either a hybrid system that could more efficiently turnover N_2 or a hybrid system that could decrease electron flux enough that N_2 can be trapped on the cofactor can be identified.

Chapter 3 builds off the finding from Chapter 2 that CO can be trapped on the catalytic cofactor of *Av*VnfDGK by creating a hybrid nitrogenase system utilizing *Ma*VnfH and *Av*VnfDGK.[135] In this chapter, the catalytic relevance of singly- and multi-bound CO states (i.e. the lo-CO and hi-CO states) of V-nitrogenase to C−C coupling and N_2 reduction are analyzed. Changing the pressure of CO generates the lo-CO and hi-CO states, and comparison using EPR spectroscopy indicates a change in signal between these two states. EPR spectroscopy of the *Ma*VnfH/*Av*VnfDGK hybrid reveals a hi-CO-like state, indicating that an additional CO was indeed trapped on the cluster. Further analysis reveals that the multiple CO moieties in the hi-CO state cannot be coupled as they are, which suggests that C-C couple requires further activation and/or reduction of the bound CO entity.

The MgADP bound crystal structure of *Ma*VnfH is reported in Chapter 4. The MgADP-bound state is one of multiple Fe protein states that are involved in the transfer of electrons from the Fe protein to the catalytic component. This is planned to be the second physiological *Ma*VnfH structure reported, and third overall *Ma*VnfH structure. The other two structures are the

nucleotide-free structures of *Ma*VnfH with the cluster in the $[Fe_4S_4]^{1+}$ and $[Fe_4S_4]^{0}$ states, and these will be discussed in Chapter 7.

Chapter 5 discusses more recent work in characterizing additional Fe protein homologs in *E. coli*. Five additional Mo-nitrogenase Fe proteins were characterized in a similar fashion as described in Chapter 2.[134] Excitingly, two of the hybrid systems transferred electron to the catalytic component at a rate nearly half that of the wild-type. As it cannot be predicted which organisms will generate functional gene products in *E. coli*, there is a desire to build an arsenal of each individual essential nitrogenase gene product so that they can be matched with the other functioning components to generate the most active nitrogenase system.

Chapter 2 Tuning Electron Flux through Nitrogenase with Methanogen Iron Protein Homologs

2.1 Introduction

Nitrogenase is a key enzyme in the global nitrogen cycle, catalyzing the ambient conversion of atmospheric N_2 to bioavailable NH_3.[3] In addition, nitrogenase can reduce CO to hydrocarbons, further illustrating its importance in energy- and environment-related areas.[133,136] The Mo- and V-nitrogenases from the soil bacterium, *Azotobacter vinelandii*, share a good degree of homology with each other, both comprising a reductase component and a catalytic component.[3,137] Categorically termed the Fe proteins, the reductase components of the Mo- and V-nitrogenases are homodimers of ≈ 60 kDa that house a subunit-bridging $[Fe_4S_4]$ cluster and an MgATP-binding site within each subunit. During substrate turnover, the Fe protein of Mo- or V-nitrogenase (designated *Av*NifH or *Av*VnfH) forms a functional complex with its catalytic partner (designated *Av*NifDK or *Av*VnfDGK), in which electrons are transferred concomitantly with ATP hydrolysis from the $[Fe_4S_4]$ cluster of the former, via a so-called P-cluster species (designated P- or P*-cluster), to the cofactor site (designated M- or V-cluster) of the latter, where substrate reduction eventually occurs (Figure 2.4A in Supplemental Tables and Figures). Other than playing a key role in catalysis, the Fe protein is also essential for the maturation of P- and M-clusters in *Av*NifDK, functioning as an ATP-dependent reductase in these biosynthetic events in an analogous manner to its role in catalysis (Supplemental Figure 2.4B, C).[7]

The effectiveness of the Fe protein as a reductase is underlined by the redox versatility of its $[Fe_4S_4]$ cluster. Both *Av*NifH and *Av*VnfH can assume three oxidation states (i.e., 0, +1, and +2), although the $[Fe_4S_4]^{2+/1+}$ couple is believed to be used under physiological conditions.[3,138] Binding of nucleotides induces conformational changes of *Av*NifH and *Av*VnfH while lowering the midpoint potentials of their $[Fe_4S_4]$ clusters, which further impacts their ability to interact

with and deliver electrons to their catalytic partners for substrate turnover.[3,5] The essential role of the Fe protein in nitrogenase catalysis makes it an excellent target for modulating protein–protein interactions and electron fluxes through the nitrogenase complex; in particular, identification of new Fe protein species that can be mixed and matched with the catalytic components from homologous nitrogenase systems will not only contribute to understanding the impact of binding energetics and electron-transfer efficiencies on nitrogenase catalysis, but also enable generation of nitrogenase hybrids with reduced electron fluxes that could be used to capture substrates/intermediates for mechanistic investigations without directly perturbing the immediate surroundings of the active site of nitrogenase.

2.2 Results and Discussion

2.2.1 Expression and Characterization of *Ma*NifH and *Ma*VnfH

One interesting pool of candidates for this line of investigation is the Fe proteins of methanogenic organisms. These archaeal microorganisms are distinct from *A. vinelandii*, a member of the bacteria domain; yet, many methanogens carry genes encoding the homologs of the Mo- and V-nitrogenases, thereby providing a good array of previously uncharacterized Fe proteins for investigation of their cross-reactivity with the catalytic components of the homologous, yet distinct *A. vinelandii* nitrogenases.[139] Based on the characteristic assembly patterns of *nif* and *vnf* gene clusters on the chromosomal DNA (see Supplemental Figure 2.5), the Fe proteins of the Mo- and V-nitrogenases (designated *Ma*NifH and *Ma*VnfH) were identified from the genome of *M. acetivorans*, a mesophilic methanogenic organism. His-tagged forms of *Ma*NifH and *Ma*VnfH were subsequently co-expressed with the FeS assembly machinery, IscSUA, in *Escherichia coli* and purified as homodimers of 59.9 and 61.1 kDa, respectively (Supplemental Figure 2.6). *Ma*NifH and *Ma*VnfH contained 3.5 ± 0.1 and 3.4 ± 0.2

mol Fe/mol protein, consistent with an occupancy of 88% and 85% of the single $[Fe_4S_4]$ cluster-binding site in each protein. The observation of such a high cluster occupancy in the as-isolated *Ma*NifH and *Ma*VnfH is exciting, as it suggests the feasibility to express fully complemented Fe proteins in a non-nitrogen-fixing host that does not have effective means to protect the oxygen-labile nitrogenase proteins.

2.2.2 EPR Spectroscopy of Fe Protein Homologs

Like their counterparts in *Av*NifH and *Av*VnfH, the $[Fe_4S_4]$ clusters in *Ma*NifH and *Ma*VnfH could adopt three oxidation states upon redox treatments: the EPR-silent, $[Fe_4S_4]^{2+}$ state (Figure 2.1A); the reduced, $[Fe_4S_4]^{1+}$ state (Figure 2.1B); and the "super reduced", $[Fe_4S_4]^{0}$ state (Figure 2.1E).[62,82,140] Additionally, *Ma*NifH and *Ma*VnfH underwent the same line-shape changes as *Av*NifH and *Av*VnfH upon binding of nucleotides, showing a transition of the S=1/2 signals of their $[Fe_4S_4]^{1+}$ clusters from a rhombic line-shape in the nucleotide-free state (Figure 2.1B) to either an axial (Figure 2.1C) or an intermediary line-shape between rhombic and axial (Figure 2.1D) upon binding of ATP and ADP, respectively. Despite their overall homology, *Ma*NifH and *Ma*VnfH displayed somewhat different electronic properties than *Av*NifH and *Av*VnfH, such as a stronger S = 3/2 contribution to the spectra of their $[Fe_4S_4]^{1+}$ clusters (Figure 2.1B), a decreased magnitude of the parallel-mode, g = 16.4 signals of their $[Fe_4S_4]^{0}$ clusters (Figure 2.1E), and a moderate line-shape change of the S = 1/2 signals of their $[Fe_4S_4]^{1+}$ clusters upon nucleotide binding (Figure 2.1C, D). *Ma*VnfH seemed to deviate most from the other Fe proteins, showing the strongest S = 3/2 feature in the $[Fe_4S_4]^{1+}$ state and the weakest g = 16.4 signal in the $[Fe_4S_4]^{0}$ state (Figure 2.1B, E, blue).

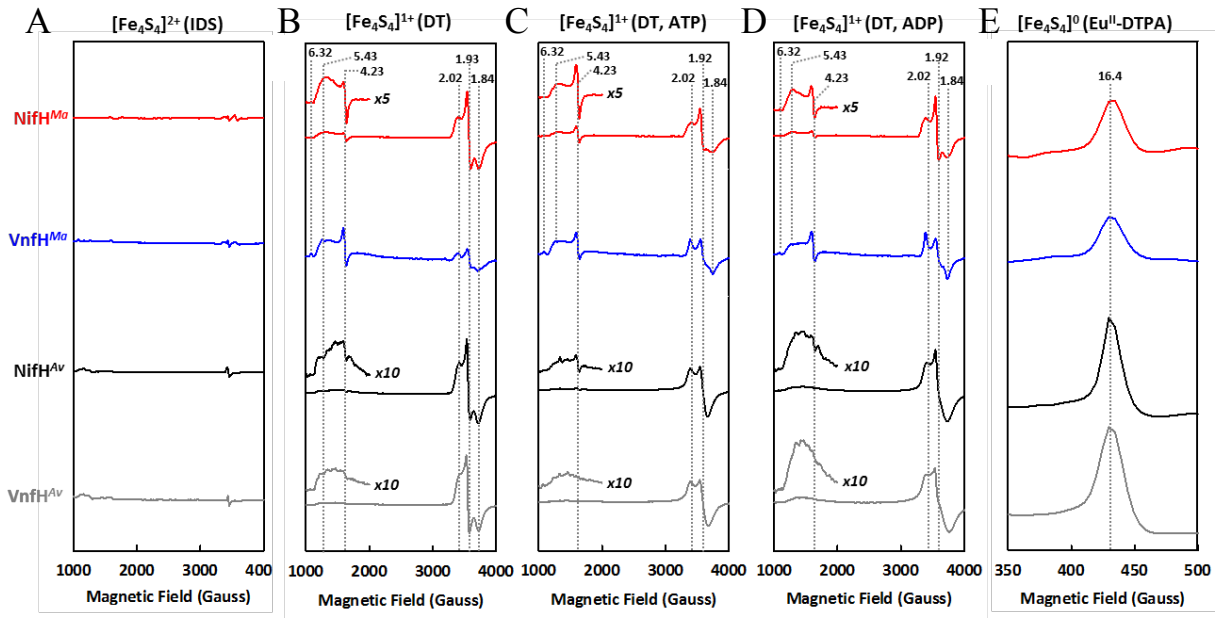

Figure 2.1 EPR features of the Fe proteins. Shown are EPR spectra of IDS-oxidized (**A**), DT-reduced (**B–D**), and Eu^{II}-DTPA reduced (**E**) *Ma*NifH (red), *Ma*VnfH (blue), *Av*NifH (black) and *Av*VnfH (gray). The oxidation states of the [Fe_4S_4] clusters in these Fe proteins are 2+ (**A**), 1+ (**B–D**), and 0 (**E**), respectively. The S = 3/2 regions of the DT-reduced spectra of *Ma*NifH (red), *Av*NifH (black), and *Av*VnfH (gray) in the nucleotide-free (**B**) and ATP- (**C**) and ADP- (**D**) bound states are enlarged above the corresponding spectra. The g-values are indicated. IDS = indigo disulfonate; DT = dithionite; Eu^{II}-DTPA = europium (II) diethylenetriaminepentaacetic acid.

2.2.3 Cross-reactivities of the Catalytic and Reductase Components

When combined with the catalytic component of *A. vinelandii* (*Av*NifDK or *Av*VnfDGK), the Fe protein of *M. acetivorans* (*Ma*NifH or *Ma*VnfH) was capable of supporting reduction of the full spectrum of nitrogenase substrates (Supplemental Table 2.1). Moreover, the hybrid nitrogenase systems between *M. acetivorans* and *A. vinelandii* displayed the characteristic catalytic features as the native V- and Mo-nitrogenases of *A. vinelandii*, with the *Av*VnfDGK-based hybrids showing a stronger bias than the *Av*NifDK-based hybrids toward formation of hydrocarbons and H_2, respectively, in the presence of substrates CO and N_2 (Supplemental Table 2.1). However, the total electron fluxes through the nitrogenase hybrids between *M. acetivorans* and *A. vinelandii*—calculated based on the amount of electrons that appeared in the

products—were considerably reduced compared to those through the native Mo- and V-nitrogenases of *A. vinelandii* (Figure 2.2A, B, left); most notably, the CO-reducing activity was substantially reduced (by 98 %) when *Av*VnfDGK was combined with *Ma*VnfH.

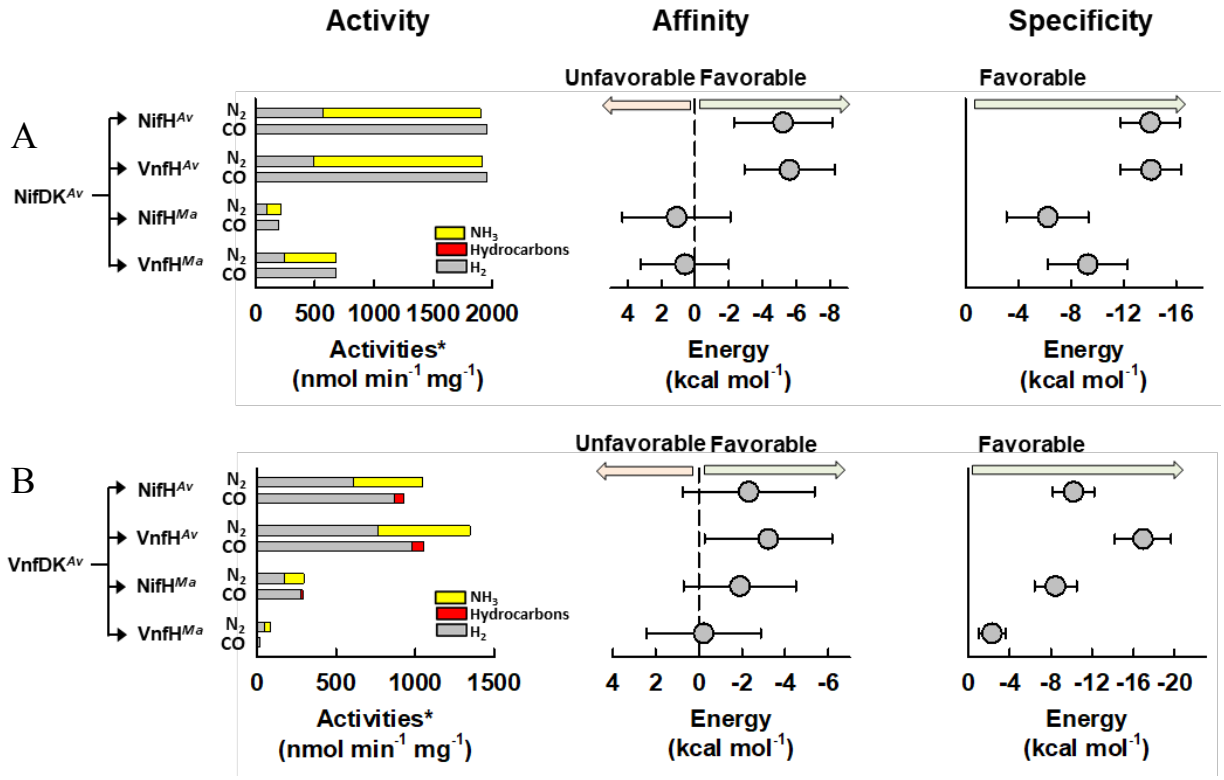

Figure 2.2 Interactions between the Fe Protein and its catalytic partner. Shown are the substrate-reducing activity, binding affinity, and docking specificity when *Av*NifH, *Av*VnfH, *Ma*NifH, or *Ma*VnfH is combined with *Av*NifDK (**A**) or *Av*VnfDGK (**B**). Error bars represent root-mean-square deviations. *Activities are expressed as nmoles of electrons in products per minute per mg of Fe protein. The experimentally determined activity data (left) aligned well with the calculation-derived affinity (middle) and specificity (right) markers (also see Supplemental Figure 2.4), as well as the qualitatively evaluated affinities between the component proteins within these complexes (see Supplemental **Figure 2.5**).

2.2.4 Homology Modeling and In Silico Docking

The interaction between the component proteins of the nitrogenase complexes was further examined by combined homology modeling/in silico docking, which gave rise to an "affinity marker" based on the mean binding energy of the ensemble of conformations generated for each complex (see Supplemental Figure 2.4A, D).[141–143] This marker could be correlated with the

catalytic activity of the complex, with a lower mean binding energy corresponding to a higher substrate-reducing activity (Figure 2.2A, B, middle). Subsequent alignment of the exothermic binding energies with distances between the [Fe_4S_4] cluster of Fe protein and the contact surface of its catalytic partner (see Supplemental Figure 2.4B, E) led to the identification of a proximal (designated P) and a distal (designated D) group of conformations for each complex, with the complex adopting favorable binding energies at either short (P group) or long (D group) cluster-interface distances. Consistent with an exponential decrease of the electron tunneling probability with increasing distances, the average binding energy of the conformations in the P group could be used as a "specificity marker" for correlation with the electron-transfer efficiency and, consequently, the catalytic activity of this complex (Figure 2.2A, B, right). A comparison of the affinity and specificity values provided good explanations for the observed "switch" in catalytic capacity between *Ma*NifH and *Ma*VnfH when they were paired with different catalytic partners, *Av*NifDK and *Av*VnfDGK (Figure 2.2A, B, left), showing promise for these markers in assisting analysis of the efficiency of nitrogenase complex formation. The effectiveness of this two-marker system was further illustrated by the success of aligning the binding affinity and specificity of a P-cluster assembly complex with the activity of P-cluster maturation (see Figure 2.9 and Figure 2.10 in the Supplemental Section).

2.2.5 Substrate Trapping Using *Ma*VnfH/*Av*VnfDGK Complex

Compared to other Fe proteins, *Ma*VnfH displayed the lowest affinity (Figure 2.2B, middle) and specificity (Figure 2.2B, right) when it was paired with *Av*VnfDGK. Most interestingly, the *Ma*VnfH/*Av*VnfDGK complex adopted an energetically least favorable P group of conformations of all *Av*VnfDGK-based complexes; moreover, the P group conformations of the *Ma*VnfH/*Av*VnfDGK complex were even slightly less favored than its D group of

conformations in the overall binding energy (Supplemental Figure 2.4E, right), suggesting docking between the two component proteins at long cluster–interface distances with reduced electron-transfer efficiencies. A closer examination of the docking models of the *Ma*VnfH/*Av*VnfDGK complex in the D group confirmed "improper" docking between these two proteins at cluster–interface distances as far as 8–9 Å with a significant deviation from the conformation of the native *Av*VnfH/*Av*VnfDGK complex (Figure 2.3A), which could account for an altered product profile of the *Ma*VnfH/*Av*VnfDGK hybrid and, most notably, a substantial decrease in the ratio between hydrocarbon- and H_2-formation when CO was supplied as a substrate (Supplemental Table 2.1).[40] Spectroscopic and biochemical analyses further demonstrated capture of the substrate CO and/or intermediate(s) on *Av*VnfDGK with the assistance of the "imperfect" electron donor *Ma*VnfH, suggesting a "re-purposing" of electrons from CO-reduction to CO-binding concomitant with a substantially decreased electron flux (Figure 2.3B; Supplemental Figure 2.11). Such a feat could not be readily achieved under normal turnover conditions by the native *Av*VnfH/*Av*VnfDGK complex, as the product profiles remained practically unchanged even when the electron flux was lowered through a reduction of the molar ratio between *Av*VnfH and *Av*VnfDGK (Supplemental Figure 2.11). Remarkably, consistent with a 3.4-fold increase in the amount of captured CO, the intensity of the ′lo-CO′ features — previously assigned to a conformation with one CO bridged between two Fe atoms across the "belt" of the V-cluster (Figure 2.3C, upper) —increased dramatically in the spectrum of the *Ma*VnfH/*Av*VnfDGK hybrid (Figure 2.3B, black) relative to that of the ′lo-CO′ state of *Av*VnfDGK (Figure 2.3B, blue).[144–146] Moreover, the difference spectrum between the *Ma*VnfH/*Av*VnfDGK complex and ′lo-CO′ state of *Av*VnfDGK (Figure 2.3B, dashed) revealed new features that resembled the ′hi-CO′ signal, previously documented only in the case of the M-

cluster, where the signal was assigned to a conformation with two CO bound to a pair of neighboring "belt" Fe atoms.[144] A model of multi-CO-bound conformation of *Av*VnfDGK can be proposed based on the homology between V- and Mo-nitrogenases (Figure 2.3C, lower) and, given that CO is a substrate of the V-nitrogenase, this conformation could be further explored for its mechanistic relevance to C−C coupling, something that cannot be achieved with the hi-CO state of Mo-nitrogenase, where CO is "stuck" on the M-cluster as an inhibitor.

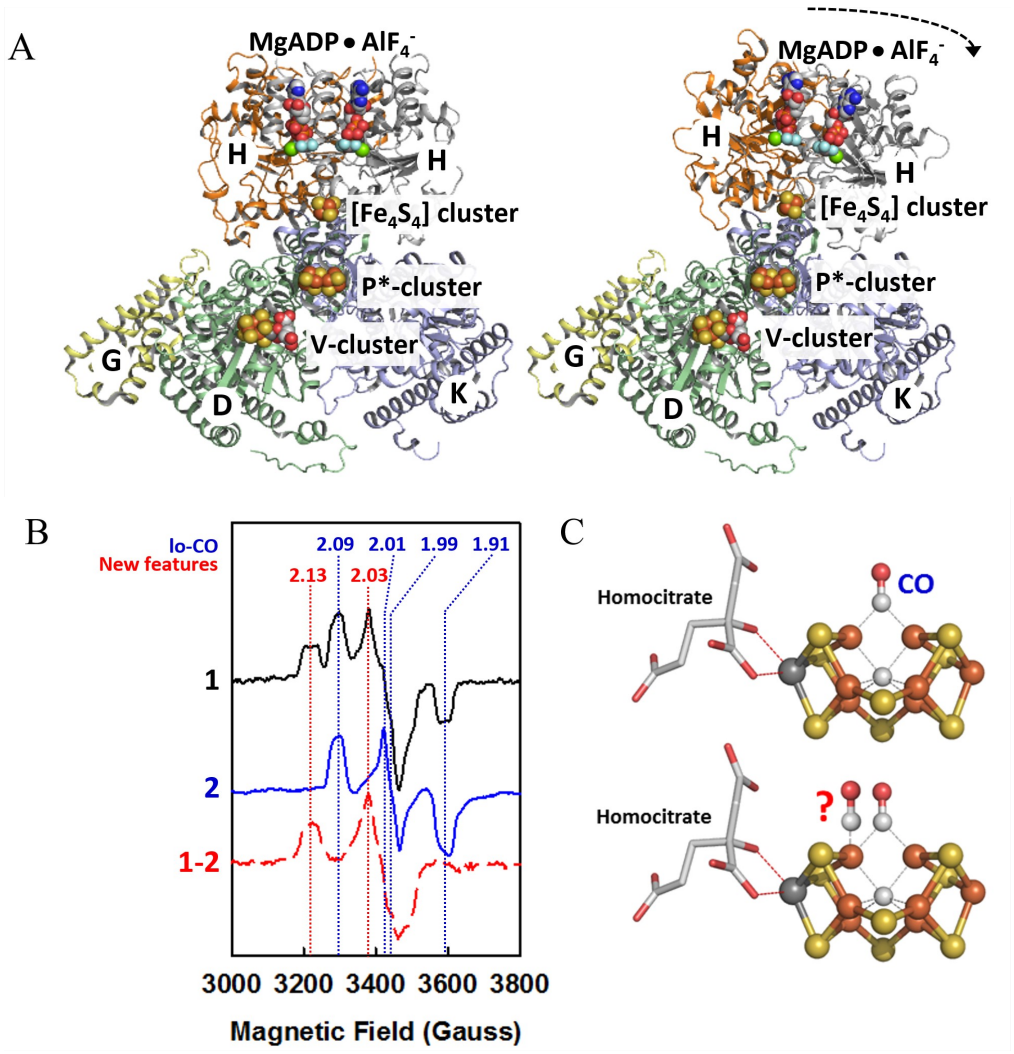

Figure 2.3 Capture of CO on the *Ma*VnfH/*Av*VnfDGK hybrid. (**A**) Comparison of the energy-optimized models of ½ ADP·AlF_4^--stabilized *Av*VnfH/*Av*VnfDGK complex (left) and *Ma*VnfH/*Av*VnfDGK hybrid (right). Colors of atoms: Fe=orange; S=yellow; V=gray; O=red; C=dark gray; N=dark blue; Mg=green; Al=beige; F=light blue. (**B**) EPR spectra of the *Ma*VnfH/*Av*VnfDGK complex upon turnover at 1 atm CO (black), the one-CO-bound, 'lo-CO'

state of *Av*VnfDGK (blue), and the difference spectrum between the two samples (dashed). When quenched by acid, the amount of CO released from the *Ma*VnfH/*Av*VnfDGK sample was 3.4-fold higher than that from the lo-CO state of *Av*VnfDGK. (**C**) Proposed models of the ′lo-CO′ (upper) and ′hi-CO′ (lower) states of the V-cluster.[144] The ′hi-CO′ model of the V-cluster was adapted from that derived from an ENDOR study of the multi-CO-bound M-cluster and the crystal structure of the one-CO-bound M-cluster.[145,146]

2.3 Summary and Conclusion

These observations are exciting, as they suggest the utility of the homolog-based approach in tuning the electron flux through nitrogenase. By further validating our homology modeling/docking approach through testing a much larger pool of NifH homologs and developing automated screening and data processing software, suitable NifH candidates may be identified and combined with various catalytic components for trapping N_2/intermediates through reduced/modified electron fluxes without introducing modifications at the cofactor site of nitrogenase.[139,147] This approach could be further complemented by protein design calculations and in silico mutant screening, with the aim to tailor nitrogenase systems toward enhanced substrate-reducing activities or desired alterations of product profiles. Efforts along this line could potentially facilitate the ongoing attempts of transgenic expression of nitrogenase through synthetic biology approaches and enable future biotechnological adaptations of nitrogenase-based applications for the generation of useful chemical products.

2.4 Materials and Methods

2.4.1 Experimental Section

Unless noted otherwise, all chemicals and reagents were obtained from Fisher Scientific or Sigma-Aldrich. All protein work was performed under Ar gas at an O concentration of less than 5 ppm.

2.4.2 Cell Growth and Protein Purification

E. coli strains expressing His-tagged *Ma*NifH (strain YM135EE) and *Ma*VnfH (strain YM136EE) were constructed by co-transforming a plasmid carrying IscSUA and a pET-14b vector carrying the *nifH* or *vnfH* gene of *M. acetivorans* (see Supplemental Figure 2.5) into *E. coli* strain BL21(DE3). These strains were grown in 10-L batches in Difco LB medium containing 100 mg/L ampicillin (BD Biosciences) in a BIOFLO 415 fermenter (New Brunswick Scientific) at 37 °C, with 200 rpm agitation and 10 L/min airflow. Growth rates were monitored by measuring cell density at 600 nm using a Spectronic 20 Genesys spectrometer (Spectronic Instruments). When OD_{600} reached 0.5, the temperature was lowered to 25°C before expression of the NifH homologs was induced by addition of 25 μM IPTG. Expression of protein was allowed to continue for 16 h before cells were harvested by centrifugation using a Thermo Fisher Scientific Legend XTR centrifuge. Subsequently, His-tagged *Ma*NifH and *Ma*VnfH were purified by immobilized metal affinity chromatography (IMAC) using methods adapted from the purification of His-tagged nitrogenase proteins.[21,148] *A. vinelandii* strains expressing *Av*NifDK, *Av*NifH, *Av*VnfDGK, and *Av*VnfH proteins were grown at 30°C in 180-L batches in a 200-L fermenter (New Brunswick Scientific) in Burke's minimal medium supplemented with 2 mM ammonium acetate. Growth rates were monitored by measuring cell density at 436 nm. Cells were harvested once OD_{436} reached 1.0 by a flow-through centrifugal harvester (Cepa). Published methods were used to purify these proteins.[21,148]

2.4.3 SDS-PAGE Analysis and Molecular Mass Determination

SDS-PAGE analysis was performed using a 4-20% Mini-PROTEAN TGX precast gel (BioRad), which was run at 100 V in a TGX running buffer for 1 hr, followed by staining with Coomassie Brilliant Blue. The native molecular masses of *Ma*NifH and *Ma*VnfH were

determined by gel filtration on a column packed with Ultrogel ACA 34 (Pall Life Science; ID: 1.5 cm, length: 1.4 m) at a flow rate of 0.5 mL/min. Protein standards (GE Healthcare) used for molecular mass determination were carbonic anhydrase (29 kDa), ovalbumin (43 kDa), albumin (66 kDa), catalase (232 kDa) and ferritin (440 kDa) (see Supplemental Figure 2.6).

2.4.4 Iron Determination.

The iron (Fe) contents of *Ma*NifH and *Ma*VnfH were determined by inductively coupled plasma optical emission spectroscopy (ICP-OES) using a Thermo Scientific iCAP7000. Stock solutions of elemental Fe (1 mg/mL, Thermo-Fisher Scientific) were diluted to make standard solutions for calibration. Each protein sample was mixed with 100 μL concentrated sulfuric acid (H_2SO_4) and 100 μL concentrated nitric acid (HNO_3) and heated at 250°C for 30 min. This procedure was repeated until the solutions became colorless. Subsequently, the solutions were cooled to room temperature, diluted to a total volume of 10.0 mL with 2% HNO_3 (vol/vol), and subjected to sample analysis.

2.4.5 EPR Analysis

The electron paramagnetic resonance (EPR) samples were prepared in a Vacuum Atmospheres glove box with less than 5 ppm O_2 and flash frozen in liquid nitrogen prior to analysis. The dithionite (DT)-reduced samples contained 10 mg/mL of *Ma*NifH, *Ma*VnfH, *Av*NifH or *Av*VnfH, 25 mM Tris·HCl (pH 8.0), 10% (vol/vol) glycerol, 250 mM imidazole, 2 mM DT ($Na_2S_2O_4$) and, in some cases, 5.4 mM ATP or ADP. The indigo disulfonate (IDS)-oxidized samples were prepared by incubating the DT-reduced samples with excess IDS for 5 min, followed by removal of excess IDS using a G25 desalting column. The super-reduced, all-ferrous samples were prepared by incubating the DT-reduced sample with 20 mM europium (II) diethylenetriaminepentaacetic acid (Eu^{II}-DTPA) for 5 min, followed by removal of excess Eu^{II}-

DTPA using a G25 desalting column. The turnover samples were prepared as described elsewhere, which contained 15 mg/mL *Av*VnfDGK, 1 mg/mL *Av*VnfH, *Ma*NifH or *Ma*VnfH, 6 mM ATP, 8 mM $MgCl_2$, 50 mM phosphocreatine, 0.2 mg/mL creatine phosphokinase, 10% glycerol, 0.4 mM $Na_2S_2O_4$, and 25 mM Tris-HCl (pH 8.0) in the presence of 1 atm CO.[149] All components except the Fe protein were added in a sealed vial and stirred for 20 min before turnover was initiated by addition of the Fe protein. This reaction mixture was incubated for 3 min prior to its transfer into an EPR tube, or it was run through a G25 desalting column to remove the solution-dissolved CO prior to the release of protein-bound CO by acid quench and the subsequent quantification of CO by a GC-FID coupled with a methanizer (Thermo Scientific). EPR spectra were recorded by an ESP 300 Ez spectrophotometer (Bruker) interfaced with an ESR-9002 liquid-helium continuous-flow cryostat (Oxford Instruments) using a microwave power of 50 mW, a gain of 5×10^4, a modulation frequency of 100 kHz, and a modulation amplitude of 5 G. Five scans were recorded for each EPR sample at a temperature of 10 K and a microwave frequency of 9.62 GHz.

2.4.6 P-Cluster Maturation Assays

This assay contained, in a total volume of 1 mL, 25 mM Tris·HCl (pH 8.0), 20 mM $Na_2S_2O_4$, 0.45 mg *ΔnifH Av*NifDK, 0.21 mg *Ma*NifH, *Ma*VnfH or *Av*NifH, 0.8 mM ATP, 1.6 mM $MgCl_2$, 10 mM creatine phosphate, 8 units creatine kinase, and 8 nmol isolated M-cluster (cofactor) from the Mo-nitrogenase. This mixture was then incubated at 30°C for 60 min, followed by determination of enzymatic activities.

2.4.7 Enzymatic Assays

Enzymatic assays were conducted as previously described.[24,148] The assay contained, in a total of 1 mL, 0.27 mg *Av*NifDK or *Av*VnfDGK, 0.15 mg *Ma*NifH, *Ma*VnfH, *Av*NifH or

*Av*VnfH, 20 mM $Na_2S_2O_4$, 0.8 mM ATP, 1.6 mM $MgCl_2$, 10 mM creatine phosphate, and 8 units creatine kinase. For CO-, C_2H_2-, H^+-, and N_2-reduction assays, 1 atm CO, 0.1 atm C_2H_2, 1 atm Ar, and 1 atm N_2, respectively, were added to the headspaces of samples. Determination of H_2, C_2H_4 and NH_3 were performed as described previously.[91,150] Hydrocarbon products were quantified by a gas chromatograph-flame ionization detector (GC-FID), where 250 μL headspace of each sample was injected onto a Grace 5664PC column (3.2 mm diameter, 1.5 m length), held at 55 °C for 1 min, heated to 180 °C at 12.5 °C/min, and held at 180 °C for 2.6 min prior to the determination of hydrocarbon products by GC-FID. The catalytic activities of the *Av*NifDK- and *Av*VnfDGK-based nitrogenase complexes are summarized in Supplemental Table 2.1.

2.4.8 Docking Analyses

Docking calculations were performed to define the affinity and specificity markers of the nitrogenase complexes that could be used for correlation with the experimentally determined activities of the catalytic and assembly complexes of nitrogenase.

2.4.9 Catalytic Complexes

To this end, homology models of the Fe proteins (*Av*VnfH, *Ma*NifH and *Ma*VnfH) were generated with SWISS-MODEL using the crystal structure of the ADP·AlF4$^-$- stabilized, transition-state Mo-nitrogenase complex (*Av*NifH/*Av*NifDK) [PDB entry: 1M34] as a template.[141,142,151–153] The ADP·AlF_4^--stabilized, transition-state V-nitrogenase complex (*Av*VnfH/*Av*VnfDGK) was generated using the same template and the crystal structure of *Av*VnfDGK [PDB entry: 5M6Y].[40]

Based on the homology models, ensembles of possible protein-protein complexes between the various Fe proteins (*Av*NifH, *Av*VnfH, *Ma*NifH and *Ma*VnfH) and the catalytic components of Mo- and V-nitrogenases (*Av*NifDK and *Av*VnfDGK) were created with the

ClusPro server, and binding energies of all of these complexes were calculated with FoldX in a process automatized by Bash and Perl scripting.[143,154–159] As no parameters for FeS clusters were provided in the FoldX force field, the reported binding energies did not include contributions from these clusters. Given the mediation of protein-protein interactions by surface residues, and an overall high degree of structural conservation of the proteins considered (especially with regard to the locations of the cluster sites), the comparative docking approach used in this study should not be negatively impacted by this omission, as it focuses on the relative differences in binding affinity and, therefore, will not be affected by the distinct, yet mostly constant, systematic deviation due to the high spatial conservation of cluster sites. A more refined approach, however, would include force-field descriptions for all clusters present in the proteins in order to offset the constant, systematic deviation generated by the omission of the clusters. For further analysis (see below), all in silico low-energy docking models determined by ClusPro were considered for all coefficients of the scoring energy term. However, different numbers of docking solutions were used for further analysis of individual nitrogenase complexes/hybrids due to a variation of the number of docking models fulfilling the final energy screening of ClusPro (see Supplemental Table 2.2).

To evaluate the affinity between the two components in each complex, an energy landscape was first generated by arranging the binding energies of all docking models, from the left to the right, in the order of energetically most favorable (exothermic) to the energetically most unfavorable (endothermic) conformations (Supplemental Figure 2.7A, D). The percentages of exothermic and endothermic dockings, as well as the mean binding energy, were then calculated for each complex (Supplemental Figure 2.7A, D). Since the mean binding energy is derived from ensembles of low-energy docking structures rather than the optimal solution alone,

it provides a better measure of the binding affinity, a prerequisite for creating functional protein complexes. This energy metric was then used as the 'affinity marker' for correlation with the substrate-reducing activities of various catalytic complexes of nitrogenase (Figure 2.2A, B, middle).

To evaluate the specificity between the two components in each complex, the distance between the $[Fe_4S_4]$ cluster of the Fe protein and the interface between the Fe protein and its catalytic partner was considered. Given the exponential decrease of electron tunneling/transfer probability with increasing distances, the catalytically most productive docking models should feature the smallest distances between the $[Fe_4S_4]$ cluster of the Fe protein and the Fe protein/*Av*NifDK or Fe protein/*Av*VnfDGK interface. Such a distance was calculated based on the average position of the Cβ atoms of the $[Fe_4S_4]$ cluster-coordinating Cys residues of the Fe protein (Cys^{H97*}, Cys^{H132*}, Cys^{H97**} and Cys^{H132**}, where * and ** denote residues from each of the two identical subunits of the Fe protein) and the average position of the Cβ atoms of residues in a conserved hydrophobic patch, formed by Leu^{D158}, Ile^{D159}, Val^{K157} and Ile^{K158} on the surface of *Av*NifDK, or Leu^{D142}, Ile^{D143}, Val^{K119} and Ile^{K120} on the surface of *Av*VnfDGK (Supplemental Table 2.2). This hydrophobic batch contains the only residues of *Av*NifDK or *Av*VnfDGK that are located within 5 Å of the $[Fe_4S_4]$ cluster in the crystal structure of the ADP·AlF_4^--stabilized *Av*NifH/*Av*NifDK complex (PDB entry: 1M34) or the energy-optimized homology model of the ADP·AlF_4^--stabilized *Av*VnfH/*Av*VnfDGK complex.[141] Distance computation for all solutions provided by ClusPro was automatized with a Python script that calculated the distance between groups of atoms provided by the user, and the calculated distances in the exothermic conformations were then aligned with the binding energies to reveal the relationship between the complex geometry and the binding affinity (Supplemental Figure 2.7B, E). Two energetically

favorable, exothermic groups of conformations were identified based on this alignment: (i) a proximal group (P group) that centers at a cluster-interface distance of ~5-6 Å; and (ii) a distal group (D group) that centers at a distance at a cluster-interface distance of ~8-9 Å (Supplemental Figure 2.7B, E). Since the exothermic conformations in the P group are those with higher electron transfer efficiency, the average binding energy of these conformations represents an energy metric for the docking specificity of proteins within a complex. This energy metric was then used as the 'specificity marker' for correlation with the substrate-reducing activities of various catalytic complexes of nitrogenase (Figure 2.2A, B, right). Note that, compared to other Fe proteins, *Ma*VnfH displayed the lowest affinity (Figure 2.2B, middle) and specificity (Figure 2.2B, right) when it was paired with *Av*VnfDGK.

2.4.10 Assembly Complexes

Docking calculations of the nitrogenase complexes involved in P-cluster maturation were carried out as described above except that (i) a SAXS-derived model of the P-cluster precursor (designated P^P-cluster)-containing *ΔnifH Av*NifDK protein was used as one of the complex components for the calculations; and (ii) the electron transfer efficiency was evaluated based on the distance calculated between the average position of the Cβ atoms of the $[Fe_4S_4]$ cluster-coordinating Cys residues of the Fe protein (Cys^{H97*}, Cys^{H132*}, Cys^{H97**} and Cys^{H132**}, where * and ** denote residues from each of the two identical subunits of the Fe protein) and the average position of the Cβ atoms of the P^P-cluster-coordinating Cys residues (Cys^{D62}, Cys^{D88}, Cys^{D154}, Cys^{K70}, Cys^{K95} and Cys^{K153}) (Supplemental Table 2.2).[122] The mean binding energy of each complex was derived from the energy landscape comprising all calculated docking models (Supplemental Figure 2.8A), and alignment of the cluster-cluster distances of the exothermic conformations with the corresponding binding energies revealed the presence of one or both of

the P and D groups of conformations in these assembly complexes (Supplemental Figure 2.8B). The mean binding energy of all docking models and the average binding energy of the exothermic conformations in the P peak were then used as the markers of binding affinity and specificity, respectively, for correlation with the P-cluster maturations of the assembly complexes of nitrogenase (Supplemental Figure 2.9).

2.4.11 Evaluation of Complexation Affinities

In a total volume of 1.5 mL, 0.9 mg of *Av*NifDK or *Av*VnfDGK was mixed with 6-fold molar excess of *Av*NifH, *Av*VnfH, *Ma*NifH or *Ma*VnfH in the presence of 7.5 mM NaF, 0.3125 mM $AlCl_3$, 0.5 mM $MgCl_2$, 0.25 mM ATP, 20 mM dithionite, and 100 mM Tris (pH 8.0). The reaction mixture was incubated at 30°C for 20 min to allow complex formation and, subsequently, the complex in each mixture was isolated by size exclusion chromatography (Sephacryl S300, 1.5 cm x 75 cm, GE Healthcare). An equal amount (2.5 μg) of each isolated complex was loaded on a 4-20 % precast gel for SDS-PAGE analysis (Supplemental Figure 2.8).

2.5 Supplemental Tables and Figures

Table 2.1 Substrate-reducing activities of various nitrogenase complexes. The table in the published paper contains additional columns to include percent activity of hybrid complexes compared to the *A. vinelandii* complex; however, this table had to be modified to fit the formatting requirements for this dissertation.

Protein Complex		Activities[a] (nmol electron min^{-1} mg^{-1})						
		Substrate N_2		Substrate CO		Substrate C_2H_2		Substrate H^+
		Product		Product		Product		Product
		NH_3	H_2	HC[b]	H_2	C_2H_4	H_2	H_2
*Av*NifDK	*Av*NifH	1326 ± 90	575 ± 23	0.2 ± 0.04	1959 ± 97	1703 ± 65	152 ± 19	1900 ± 43
	*Av*VnfH	1431 ± 78	489 ± 17	0.2 ± 0.03	1952 ± 87	1834 ± 57	145 ± 17	1955 ± 31
	*Ma*NifH	123 ± 10	95 ± 8	<0.1 ± 0.2	193 ± 15	198 ± 19	64 ± 9	234 ± 17
	*Ma*VnfH	438 ± 19	244 ± 14	0.1 ± 0.002	682 ± 46	438 ± 25	244 ± 15	656 ± 31
*Av*VnfDGK	*Av*NifH	432 ± 10	615 ± 33	66 ± 8	855 ± 45	374 ± 43	808 ± 23	1335 ± 27
	*Av*VnfH	579 ± 12	768 ± 56	78 ± 12	979 ± 72	392 ± 33	845 ± 15	1358 ± 34
	*Ma*NifH	123 ± 8	174 ± 19	13 ± 2	276 ± 11	84 ± 15	198 ± 22	335 ± 15
	*Ma*VnfH	39 ± 4	47 ± 3	0.3 ± 0.1	22 ± 5	13 ± 2	81 ± 5	89 ± 7

[a]Activities were calculated based on nmoles of electrons that appeared in products per min per mg of Fe protein
[b]HC = hydrocarbons

Table 2.2 Summary of docking calculations.

Protein complex		Total number of docking models #	Basis of distance calculation A and B: [Fe4S4] cluster-interface distance C: [Fe4S4] cluster-P^P cluster distance Structural model of amino acids used for distance calculation	Average distance of P group
*Av*NifDK	*Av*NifH	73	A 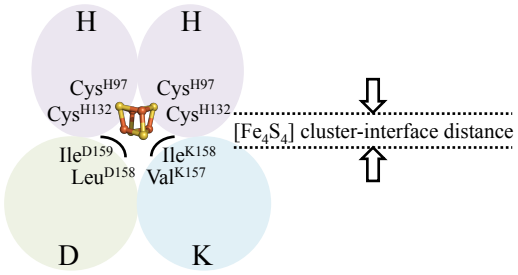	5.39 ± 0.73
	*Av*VnfH	59		5.69 ± 0.95
	*Ma*NifH	98		5.58 ± 0.71
	*Ma*VnfH	106		5.34 ± 0.52
*Av*VnfDGK	*Av*NifH	91	B 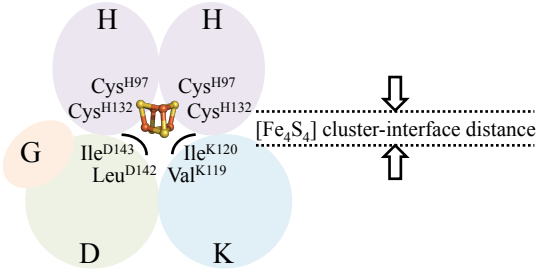	5.87 ± 0.80
	*Av*VnfH	85		5.15 ± 0.15
	*Ma*NifH	103		6.83 ± 0.91
	*Ma*VnfH	93		6.82 ± 0.73
Δ*nifH* *Av*NifDK	*Av*NifH	79	C 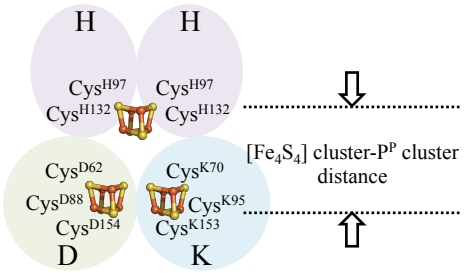	18.5 ± 0.5
	*Ma*NifH	102		19.6 ± 0.5
	*Ma*VnfH	85		20.0 ± 0.7

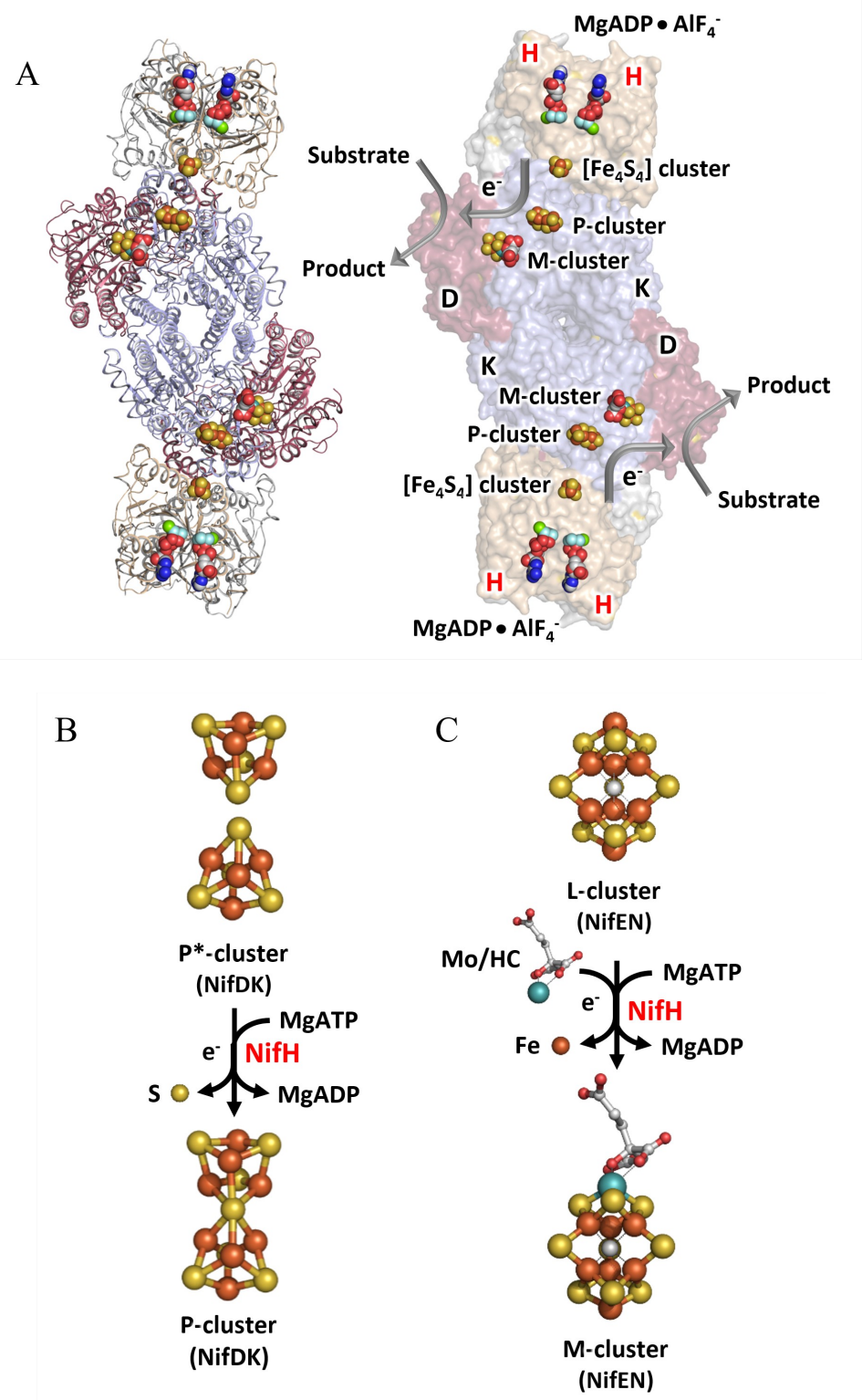

Figure 2.4 Functions of the nitrogenase Fe protein. The *nifH*-encoded Fe protein (designated NifH) functions in the electron transfer process during substrate turnover (**A**), P-cluster maturation (**B**) and M-cluster assembly (**C**). (**A**) During catalysis, NifH serves as an ATP-dependent reductase, transferring electrons from its [Fe_4S_4] cluster, via the P-cluster, to the M-

cluster (or cofactor) of NifDK, where substrate reduction occurs. (**B**) During the maturation of P-cluster, NifH facilitates the reductive coupling and rearrangement of the two [Fe_4S_4] modules of the P-cluster precursor (designated P^P-cluster) into a mature P-cluster ([Fe_8S_7]) on NifDK in an ATP-dependent process. (**C**) During the maturation of M-cluster, NifH acts as an ATP-dependent homocitrate/molybdenum insertase, converting an all-iron precursor ([Fe_8S_9]) into a mature M-cluster ([$MoFe_7S_9C$-homocitrate]) on the assembly scaffold NifEN. Shown are the cartoon (**A**, left) and surface (**A**, right) presentations of the ADP·AlF_4^--stabilized *Av*NifDK-*Av*NifH complex. The subunits are colored as described in **Figure 2.1**. All clusters and ADP·AlF_4^- are shown as ball-and-stick models, with the atoms colored as described in **Figure 2.1**.

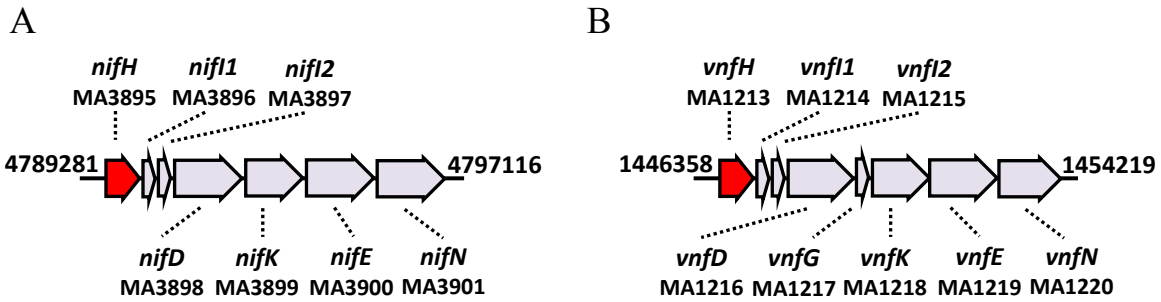

C

```
NifH^Av     1   MRQCAIYGKGGIGKSTTTQNLVAALAEMG-KKVMIVGCDPKADSTRLILHSKAQNTIME  58
NifH^Ma     1   MRQIAIYGKGGIGKSTTTQNLTAALSTMG-NNILLVGCDPKADSTRMLLGGLNQKTVLD  58
VnfH^Ma     1  MTRKIAFYGKGGIGKSTTQQNTAAAMAYYHGKNVFIHGCDPKADCTRLALGGVPQTTIMD  60
                 *  * ********** **  **           ******* **  *    * *

NifH^Av    59  MAAEAGTVEDLELEDVLKAGYGGVKCVESGGPEPGVGCAGRGVITAINFLEEEGAYEDDL 118
NifH^Ma    59  TLRSEG-DEGIDLDTVLQPGFGGIKCVESGGPEPGVGCAGRGIITSIGLLENLGAYTDDL 117
VnfH^Ma    61  TLRELG-EEAVTVDNVVNTGFKGIRCVESGGPEPGVGCAGRGVITAINLMEELGAYSDDL 119
                     *  *      *   *  *  **************** ** *   *  *** ***

NifH^Av   119  DFVFYDVLGDVVCGGFAMPIRENKAQEIYIVCSGEMMAMYAANNISKGIVKYANSGSVRL 178
NifH^Ma   118  DYVFYDVLGDVVCGGFAMPIREGKAKEIYIVASGELMAIYAANNICKGLAKFAKGG-ARL 176
VnfH^Ma   120  DFVHFDVLGDVVCGGFAMPIREGKAQEVYIVASGEMMATYAANNICKGLLKYAEQSGVRL 179
               * *  ****************** ** * *** *** ** ****** **  * *     **

NifH^Av   179  GGLICNSRNTDREDELIIALANKLGTQMIHFVPRDNVVQRAEIRRMTVIEYDPKAKQADE 238
NifH^Ma   177  GGIICNSRKVDGERELLEAFAKKLGSHLIHFVPRDNIVQRAEINRKTVIDFDRESDQAKE 236
VnfH^Ma   180  GGIICNSRKVDNELEMMEEFVSALGTQLIHFVPRDNIVQKAEFNKKTVVEFDPECNQAKE 239
               ** *****  * * *        **   ******** ** **    **   *    ** *

NifH^Av   239  YRALARKVVDNKLLVIPNPITMDELEELLMEFGIMEVEDESIVGKTAEEV 288
NifH^Ma   237  YLTLADNVQNNNKLVVPTPLPMEELEAMMVEFGIVEL 273
VnfH^Ma   240  YGKLAKKILENDMFVIPKPLSMDQLEKMVARYGLMD 275
                  **     *   * * *  *  **      *
```

Figure 2.5 Nitrogenase-encoding operons of *M. acetivorans* and sequence alignment of Fe proteins. Operons of (**A**) Mo-nitrogenase (*nif*-encoded) and (**B**) V-nitrogenase (*vnf*-encoded) were obtained from the open Joint Genome Institute (JGI) database (https://img.jgi.doe.gov/cgibin/m/main.cgi). The *vnf* gene cluster has the characteristic 'G' gene between the 'D' and 'K' genes, which is absent from the *nif* gene cluster. Moreover, the *vnf* gene cluster does not contain the 'O' gene, which is characteristic of the *anf* gene cluster that encodes

for the Fe-only nitrogenase. Locus tags (composed of MA and a four digit number) and DNA coordinates (base-pair starting- and ending-points of the operon) refer to the genome of *M. acetivorans* C2A. (**C**) The sequences of *Av*NifH, *Ma*NifH and *Ma*VnfH were aligned using CLUSTALW (http://www.genome.jp/tools/clustalw/). The identical amino acids are indicated by *. The conserved Cys ligands of the [Fe_4S_4] cluster are highlighted in green.

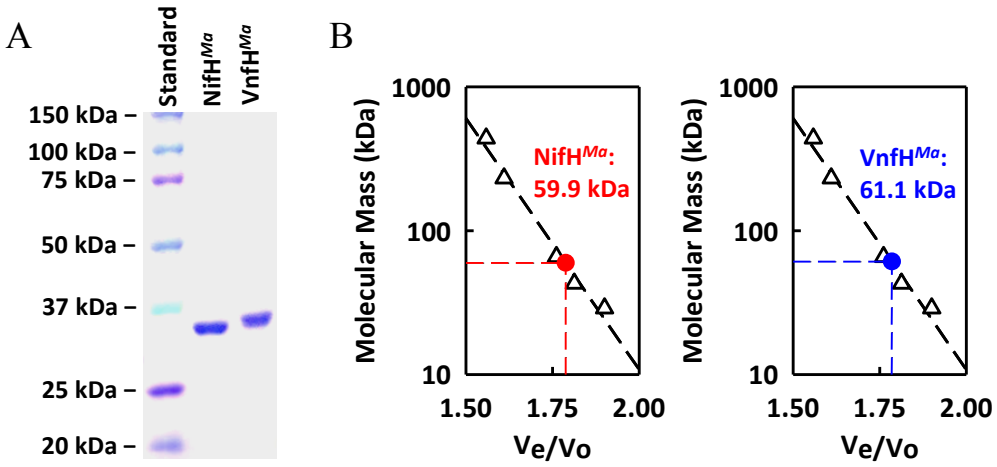

Figure 2.6 Purification of M. acetivorans Fe Proteins. (**A**) Coomassie Blue-stained 4-20% SDS-PAGE of purified proteins. From left, lane 1, 15 µg protein standard; lane 2, 1.5 µg purified *Ma*NifH; lane 3, 1.5 µg purified *Ma*VnfH. (**B**) Determination of the native molecular masses of *Ma*NifH and *Ma*VnfH by gel filtration. V_0, void volume; V_e, elution volume. Protein standards (open triangles) are: carbonic anhydrase (29 kDa), ovalbumin (43 kDa), albumin (66 kDa), catalase (232 kDa) and ferritin (440 kDa).

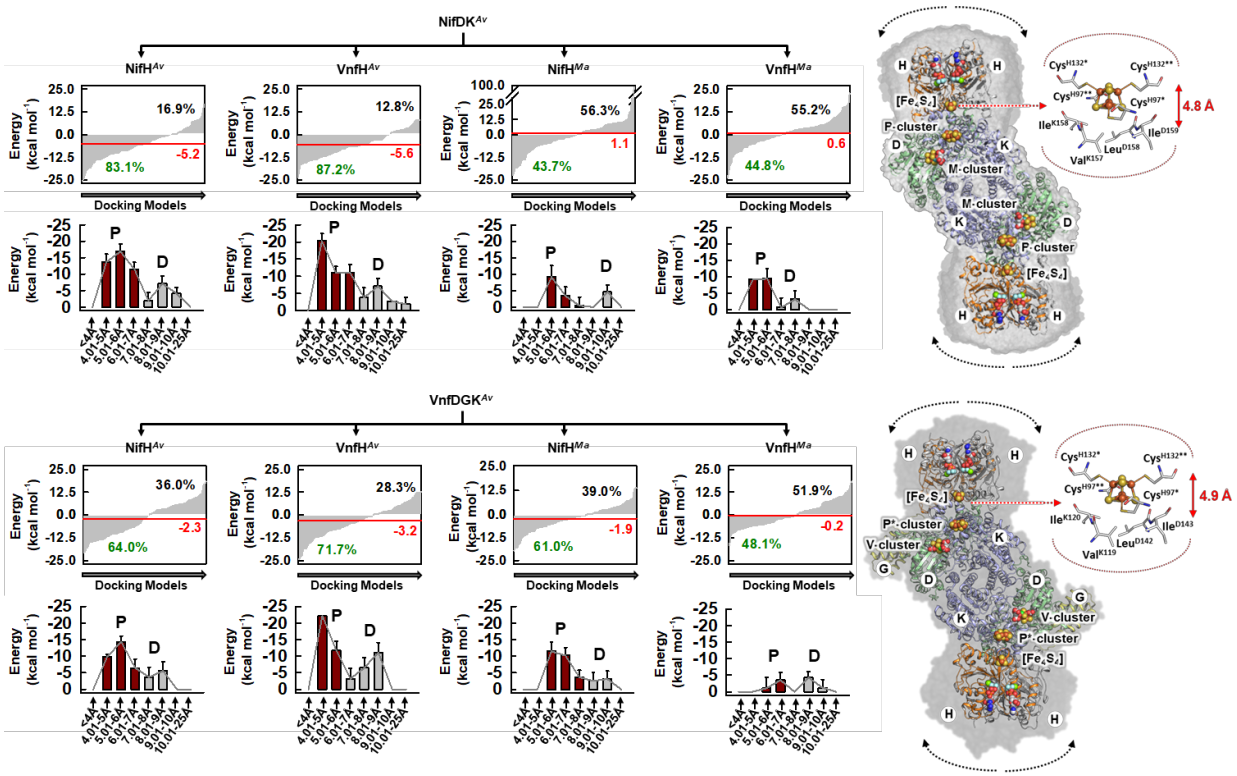

Figure 2.7 Docking between component proteins in catalytic complexes. Shown are energy landscapes of *in silico* docking models (**A**, **D**), alignments of exothermic docking energies with distances of inter-protein electron transfer paths (**B**, **E**), and overlays of native catalytic complexes with the docking models of hybrids (**C**, **F**). The percentages of exothermic and endothermic dockings are shown in green and black font, respectively; whereas the mean binding energy is shown in red font (**A**, **D**). The exothermic proximal (abbreviated as 'P') and distal (abbreviated as 'D') distance groups of conformations are derived by plotting the average energy value of all exothermic docking models at 1 Å increment of the inter-protein electron transfer path (**B**, **E**). The mean binding energy of all docking conformations (from **A**, **D**) and the average binding energy of the exothermic conformations in the P group (from **B**, **E**, red bars) are used as the affinity and specificity marker, respectively, for correlation with the catalytic activities (see **Figure 2.2**). Error bars represent root-mean-square deviations (**B**, **E**). The ADP·AlF_4^--stabilized *Av*NifH/*Av*NifDK complex (**C**, crystal structure) and *Av*VnfH/*Av*VnfDGK complex (**F**, homology model) are shown in cartoon presentation in the foreground, and all docking models of the corresponding hybrids are shown in surface presentation in the background (**C**, **F**). The dashed black arrows indicate variations in the positions of the Fe proteins in the calculated models relative to those in the native, ADP·AlF_4^--stabilized complexes (**C**, **F**). Enlarged views of the [Fe_4S_4] clusters, as well as residues used for calculation of inter-protein electron transfer distances, are shown along with the 'ideal' distances of electron transfer in the native complexes (**C**, **F**). All clusters and ADP·AlF_4^- are shown as space-filling models. Atoms are colored as follows: Fe, orange; S, yellow; Mo, cyan; V, gray; O, red; C, dark gray; N, dark blue; Mg, green; Al, beige; F, light blue. PyMOL was used to create this figure.

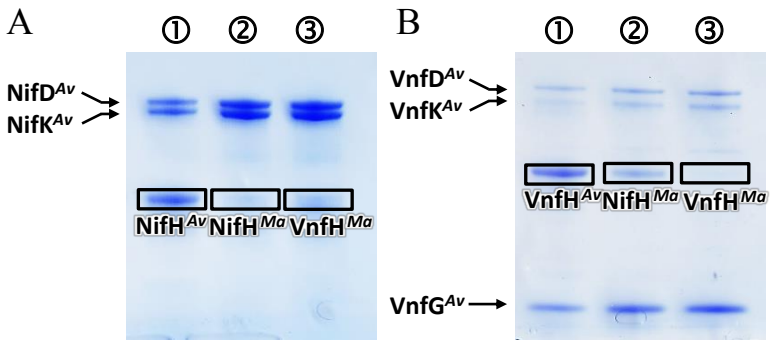

Figure 2.8 Comparison of the affinities between the component proteins in various catalytic complexes. Shown are SDS-PAGE analyses of the complexes between (**A**) *Av*NifDK and *Av*NifH (①), *Ma*NifH (②) and *Ma*VnfH (③); and between (**B**) *Av*VnfDGK and *Av*VnfH (①), *Ma*NifH (②) and *Ma*VnfH (③). These complexes were generated with the assistance of a non-hydrolysable ATP analog, ADP•AlF_4^-, and subsequently subjected to size exclusion chromatography prior to SDS-PAGE analysis. This procedure can be used for qualitative determination of the strengths of nitrogenase complexation, as complexes with weaker affinities between the component proteins have stronger tendencies to dissociate after size exclusion chromatography. For the purpose of comparison, the same amount (2.5 μg) of each complex was used for SDS-PAGE analysis upon recovery from the size exclusion chromatography procedure. Based on a qualitative assessment of the decreasing intensities of the Fe protein bands on SDS-PAGE (**A**, **B**, boxes), the affinities between the component proteins in these complexes are ranked in a decreasing order of (**A**) *Av*NifH/*Av*NifDK (①) > *Ma*VnfH/*Av*NifDK (③) > *Ma*NifH/*Av*NifDK (②) and (**B**) *Av*VnfH/*Av*VnfDGK (①) > *Ma*NifH/*Av*VnfDGK (②) > *Ma*VnfH/*Av*VnfDGK (③). These results are consistent with the calculation-derived orders of affinities between the component proteins within these complexes (see **Figure 2.2**).

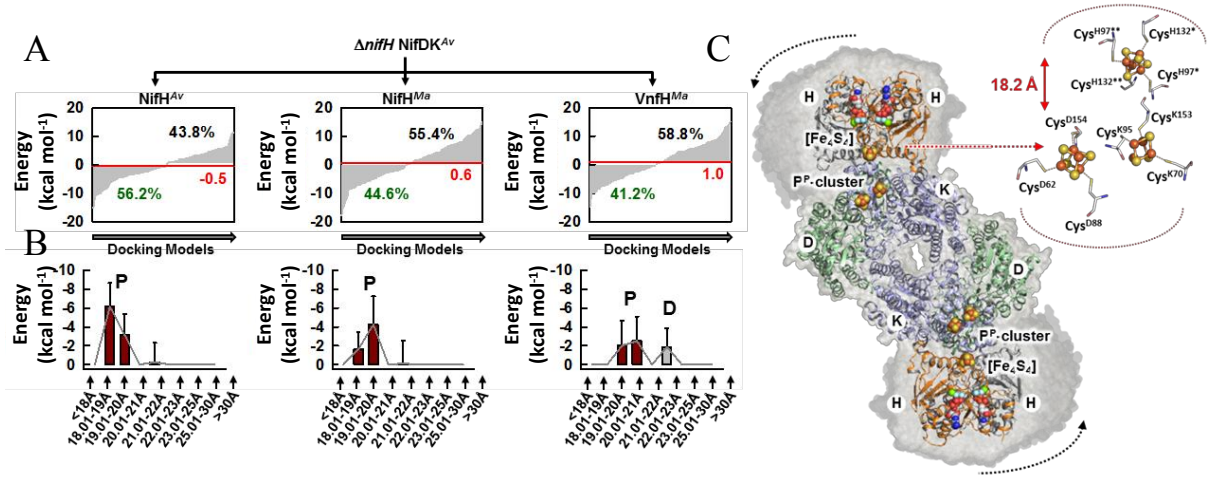

Figure 2.9 Docking between component proteins in an assembly complex. Shown are energy landscapes of *in silico* docking models (**A**), alignments of exothermic docking energies with distances of inter-protein electron transfer paths (**B**), and overlay of the native assembly complex with docking models of hybrids (**C**). The percentages of exothermic and endothermic dockings

are shown in green and black font, respectively; whereas the mean binding energy is shown in red font (**A**). The exothermic proximal (abbreviated as 'P') and distal (abbreviated as 'D') distance groups of conformations are derived by plotting the average energy value of all exothermic docking models at 1 Å increment of the inter-protein electron transfer path (**B**). The mean binding energy of all docking conformations (from **A**) and the average binding energy of the exothermic conformations in the P peak (from **B**, red bars) are used as the affinity and specificity marker, respectively, for correlation with the P-cluster maturation activities (see Supplemental **Figure 2.7**). Error bars represent root-mean-square deviations (**B**). The $ADP{\cdot}AlF_4^-$-stabilized *Av*NifH/*ΔnifH Av*NifDK (homology model) is shown in cartoon presentation in the foreground, and all docking models of the hybrids are shown in surface presentation in the background (**C**). The dashed black arrows indicate variations in the positions of the Fe proteins in the calculated models relative to those in the native, $ADP{\cdot}AlF_4^-$-stabilized complexes (**C**). Enlarged views of the $[Fe_4S_4]$ clusters, as well as residues used for calculation of inter-protein electron transfer distances, are shown along with the 'ideal' distances of electron transfer in the native complexes (**C**). All clusters and $ADP{\cdot}AlF_4^-$ are shown as space-filling models. Atoms are colored as follows: Fe, orange; S, yellow; O, red; C, dark gray; N, dark blue; Mg, green; Al, beige; F, light blue. PyMOL was used to create this figure.

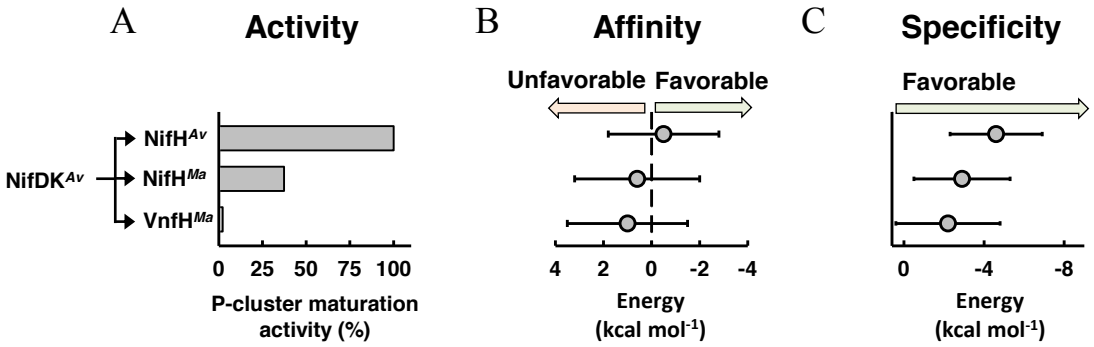

Figure 2.10 Interactions between the Fe protein and its assembly partner. Shown are the P-cluster maturation activity (**A**), binding affinity (**B**) and docking specificity (**C**) when *Av*NifH, *Ma*NifH or *Ma*VnfH is combined with *ΔnifH Av*NifDK. Error bars represent root-mean-square deviations (**B, C**).

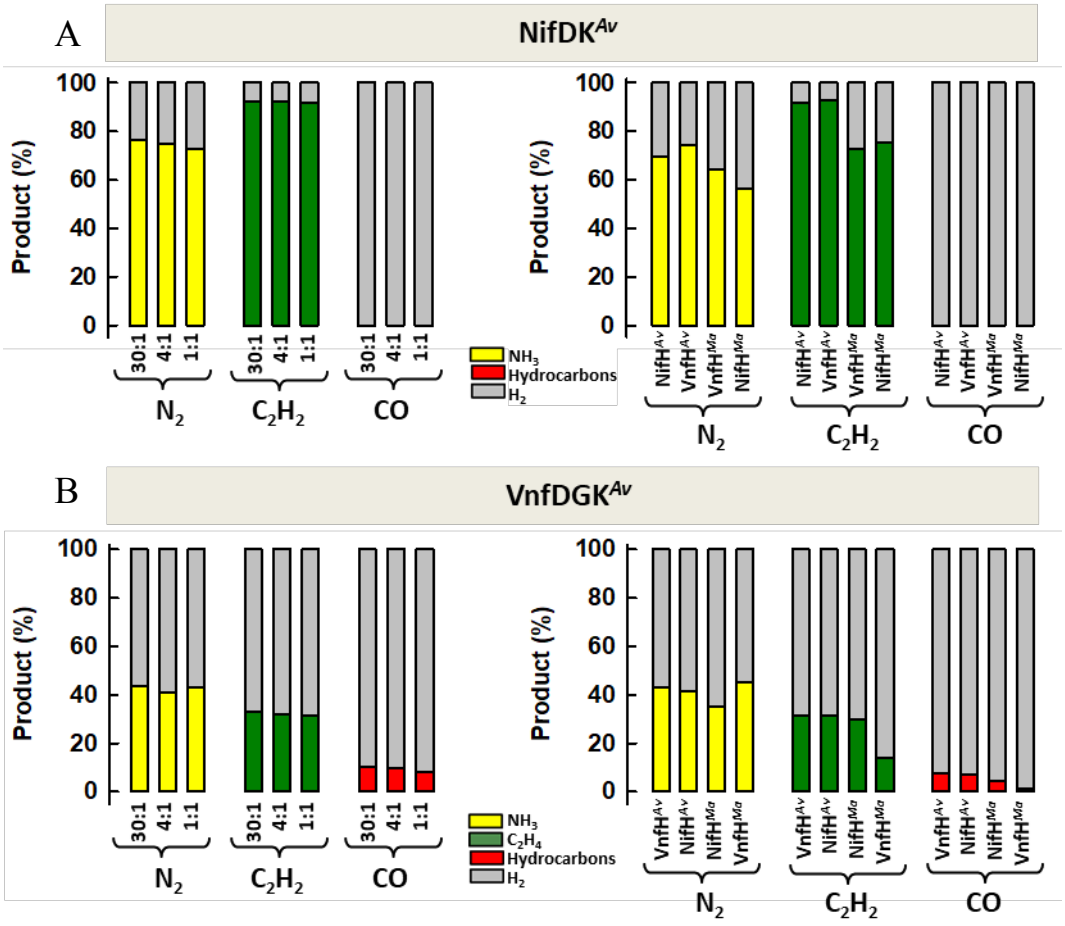

C

	Fe protein ratio	Average Activity[a] (nmol min^{-1} mg^{-1})		F e protein type	Average Activity[a] (nmol min^{-1} mg^{-1})
NifDK^{Av}	30:1	4017 ± 167	NifDK^{Av}	NifH^{Av}	1904 ± 37
	4:1	3200 ± 102		VnfH^{Av}	1951 ± 21
	1:1	1904 ± 37		VnfH^{Ma}	673 ± 11
				NifH^{Ma}	227 ± 25
VnfDGK^{Av}	30:1	2191± 233	VnfDGK^{Av}	VnfH^{Av}	1250 ± 121
	4:1	1674 ± 136		NifH^{Av}	1124 ± 150
	1:1	1250 ± 121		NifH^{Ma}	294 ± 25
				VnfH^{Ma}	73 ± 29

[a]Activities in nmoles of electrons that appeared in products per min per mg of protein

Figure 2.11 Comparison of product profiles of a given or altered nitrogenase complex upon variation of electron fluxes. Product profiles generated at (**A**) varying molar ratios of 30:1, 4:1 and 1:1 between *Av*NifH and *Av*NifDK (left), or a fixed molar ratio of 1:1 between *Av*NifH, *Av*VnfH, *Ma*VnfH or *Ma*NifH and *Av*NifDK (right); and (**B**) varying molar ratios of 30:1, 4:1 and 1:1 between *Av*VnfH and *Av*VnfDGK (left), or a fixed molar ratio of 1:1 between *Av*VnfH, *Av*NifH, *Ma*NifH or *Ma*VnfH and *Av*VnfDGK (right). (**C**) Activities of a given complex upon variation of molar ratios between component proteins (numbers used to calculate product distributions in **A**, **B**, left), or upon alteration of the Fe protein component at a fixed molar ratio of 1:1 to its catalytic partner (numbers used to calculate product distributions in a, b, right).

While a reduction of electron flux could be achieved in both cases (see numbers in **C**), the product profile remained unchanged in a given complex upon variation of the ratio between component proteins (**A**, **B**, left), but underwent apparent changes in an altered complex upon substitution of the Fe protein component (**A**, **B**, right).

2.6 Acknowledgments

I would like to thank John Wiley and Sons for permission to include Chapter 2 in my dissertation, which was originally published in *Chemistry – A European Journal*.[134] This work was supported by a Hellman Fellowship (to Y.H.), NSF Career grant CHE-1651398 (to Y.H.) and NSF grant CHE-1608926 (to M.W.R. and Y.H.).

2.7 Contributions

Caleb Hiller, CC Lee, and Jasper Liedtke performed the biochemical work. Martin Stiebritz performed the theoretical calculations.

Chapter 3 Evaluation of the Catalytic Relevance of the CO-Bound States of V-Nitrogenase

3.1 Introduction

Nitrogenase is a versatile metalloenzyme that is capable of ambient reduction of a wide range of small molecules.[3] Utilizing a reductase component to deliver electrons to its catalytic component, nitrogenase is best known for its function in reducing N_2 to NH_4^+ in a process called biological nitrogen fixation, which predates and parallels the industrial Haber–Bosch process.[2] Recently, this enzyme was also shown to reduce CO to hydrocarbons in a reaction that mirrors the industrial Fischer–Tropsch process, further highlighting its importance in energy- and environment-related areas.[133,160–162] Binding and activation of CO by nitrogenase has been a topic of vigorous research because CO is isoelectronic to N_2. Interestingly, despite their overall similarities (Supplemental Figure 3.5), the homologous, wildtype Mo- and V-nitrogenases display differential reactivities toward CO, with the former capable of binding CO but nearly inactive in CO reduction and the latter showing an activity of 16.5 nmol reduced C nmol^{-1} protein min^{-1} in reducing CO to hydrocarbons.[24,26,35,40,136,144,160,163] The disparate CO reactivities of these homologous nitrogenases suggest the possibility to investigate the activity of V-nitrogenase in CO reduction by drawing comparisons between V-nitrogenase and its Mo-counterpart in their interactions with CO. Previously, we generated a one CO-bound form of the resting-state VFe protein (the catalytic component of V-nitrogenase) in the presence of Eu^{II}-DTPA, which displayed an EPR signal resembling that of the one-CO-bound (that is, the lo-CO state) MoFe protein (the catalytic component of Mo-nitrogenase), although the latter could only be generated under turnover conditions.[144] This conformation of VFe protein was subsequently assigned as one with CO bridged between a pair of Fe atoms across the belt of the cofactor based on its homology to the one-CO-bound MoFe protein (Supplemental Figure 3.6A, left).[144,145] However, contrary to the lo-CO conformation of the MoFe protein, the lo-CO

conformation of the VFe protein was capable of turning over the bound CO molecule, generating C1 and C2 hydrocarbon products, respectively, in the absence and presence of extra CO.[144] Success in generating such a catalytically competent, one CO-bound state of the VFe protein has prompted us to seek conditions to trap more than one CO molecule on this protein (that is, the hi-CO state) for investigations of C−C coupling by V-nitrogenase.

3.2 Results and Discussion

3.2.1 Generating a Singly-bound and Multi-bound CO State on *Av*VnfDGK

To generate a multi-CO-bound state, the resting-state VFe protein of *A. vinelandii* (designated *Av*VnfDGK) was first incubated with CO at an overpressure of 2.6 atm in the presence of a strong reductant, europium (II) diethylenetriaminepentaacetic acid (Eu^{II}-DTPA; $E^{0'} = -1.14$ V at pH 8.0), and then re-isolated into a reductant-free buffer under 1 atm Ar.[82,164] Compared to the one-CO-bound conformation of *Av*VnfDGK that was generated by the same procedure under 1 atm CO (Figure 3.1A, *1*), *Av*VnfDGK generated under over-pressurized CO not only displayed EPR features (g = 2.09, 1.99, and 1.91) of the one-CO-bound (lo-CO) conformation, but also showed additional EPR features (g = 2.13, 2.01, and 1.97) that originated from the capture of extra CO molecules on the protein (Figure 3.1B, *1*). Interestingly, the major features of the lo-CO spectrum and the extra-CO spectrum (that is, the difference spectrum between the multi-CO- and one-CO-bound spectra) could be approximated by simulating a single species for each spectrum (Figure 3.1A, *2*; Figure 3.1C, *2*); whereas the features of the unsubtracted, multi-CO-bound (hi-CO) spectrum could be approximated by summation of the lo-CO and extra-CO components (Figure 3.1B, *2*). However, there were additional fine structures that could not be resolved based on these CW EPR data.

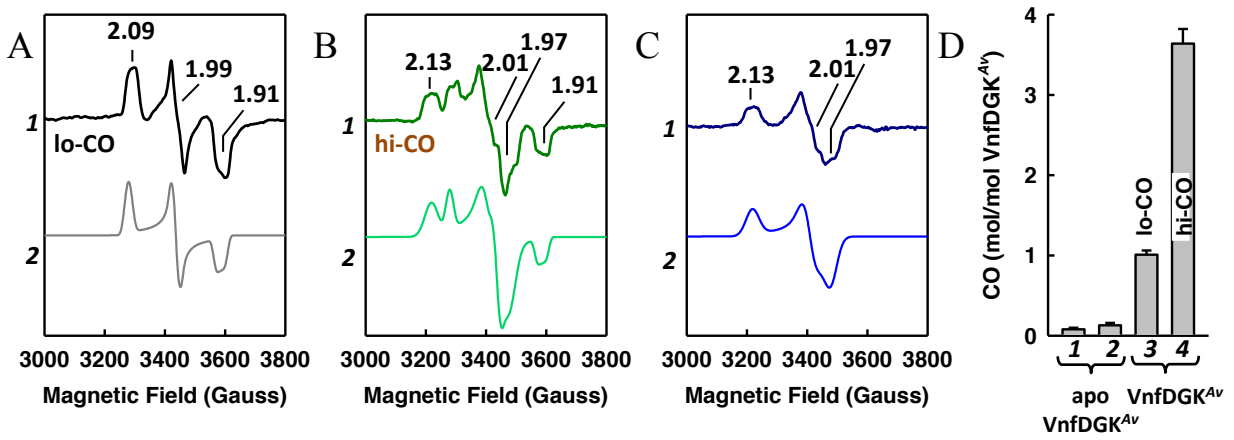

Figure 3.1 EPR spectra of CO-bound *Av*VnfDGK. EPR spectra of (**A**) the one-CO-bound (lo-CO) state generated in the presence of 1 atm CO (*1*, black trace) and (**B**) the multi-CO-bound (hi-CO) state generated in the presence of 2.6 atm CO (*1*, dark green trace). Both states were generated with the resting-state *Av*VnfDGK (that is, without the Fe protein, the reductase partner of *Av*VnfDGK) using Eu^{II}-DTPA as a reductant. (**C**) The difference spectrum between the hi-CO (**B**, *1*) and lo-CO state (**A**, *1*) reflects features generated upon binding of "extra" CO molecules (*1*, gray trace). The *g* values are indicated. Spectra (**A**, *1*), (**B**, *1*) and (**C**, *1*) were simulated as described in the Materials and Methods (see Section 3.4) and are shown as traces (**A**, *2*), (**B**, *2*), and (**C**, *2*) below the corresponding spectra. (**D**) Quantification of the amounts of *Av*VnfDGK-bound CO in the lo-CO (*3*) and hi-CO (*4*) states. The amount of bound CO was quantified upon acid quench of the hi- or lo-CO states of *Av*VnfDGK. The same experiment was conducted on the V-cluster-deficient, apo-*Av*VnfDGK, which was incapable of capturing CO under the conditions described for the formation of the lo-CO (*1*) and hi-CO (*2*) states.

3.2.2 Quantification of CO on *Av*VnfDGK

Quantification of CO that was bound to *Av*VnfDGK was performed by acid quench and revealed the presence of 1.0 ± 0.1 and 3.7 ± 0.2 mol bound CO mol^{-1} protein, respectively, in the lo-CO and hi-CO states (Figure 3.1D, *3, 4*). The inability of the cofactor-deficient, apo-VnfDGK to capture any CO under the same experimental conditions used to generate the lo- and hi-CO states (Figure 3.1D, *1*, *2*; Supplemental Figure 3.7) pointed strongly to the cofactor (V-cluster) as the site of CO binding. Notably, an earlier stopped-flow FTIR study of the *A. vinelandii* MoFe protein (designated *Av*NifDK) reported observation of a single absorption at low CO concentrations and 3–4 absorptions at high CO concentrations, which were in line with our

results of *Av*VnfDGK - the counterpart of *Av*NifDK in the V-nitrogenase system.[165] Moreover, the extra-CO EPR spectrum of *Av*VnfDGK (Figure 3.1C, *1*) loosely resembled the previously reported spectrum of *Av*NifDK that was bound with neighboring CO molecules, suggesting the presence of adjacently bound CO molecules in the multi-CO-bound *Av*VnfDGK, as was described in the case of the multi-CO-bound *Av*NifDK.[166,167] Given the spectral analogy between *Av*VnfDGK and *Av*NifDK in CO binding, the multi-CO-bound, hi-CO state of *Av*VnfDGK could assume a conformation analogous to the one that was suggested for its *Av*NifDK counterpart, with at least two CO molecules bound side by side to a pair of Fe atoms across the S belt of the cofactor (Supplemental Figure 3.6A, right).[146,168,169]

3.2.3 *Ma*VnfH/*Av*VnfDGK Hybrid Produces Hi-CO conformation

Interestingly, upon reduction of the electron flux, the same hi-CO conformation of *Av*VnfDGK could be observed under turnover conditions, when *Av*VnfDGK was combined with the Fe protein (the reductase component of V-nitrogenase), ATP and dithionite.[169] Reduction of the electron flux was enabled by replacing the *vnfH*-encoded Fe protein of *A. vinelandii* (designated *Av*VnfH) with the *vnfH*-encoded Fe protein homolog of *Methanosarcina acetivorans* (designated *Ma*VnfH), which resulted in a V-nitrogenase hybrid with decreased substrate-reducing activities (Figure 3.2A, *1* vs. *2*).[134] Calculations of the total amount of electrons that appeared in the products revealed an average reduction of electron flux by about 94 % through the *Ma*VnfH/*Av*VnfDGK hybrid (Figure 3.2B, *2*, left) relative to that through the native *Av*VnfH/*Av*VnfDGK complex, although the most drastic decrease of electron flux was observed when CO was supplied as the substrate (Figure 3.2B, *2*, right). Strikingly, the EPR signal of the CO-bound *Av*VnfDGK that was generated under turnover conditions (that is, in the presence of *Ma*VnfH) at 1 atm CO (Figure 3.2C, *1*) assumed a line-shape that was nearly

indistinguishable from the EPR spectrum of the hi-CO state of *Av*VnfDGK generated with the resting state protein (that is, in the absence of *Ma*VnfH) at 2.6 atm CO (Figure 3.1B, *1*). Thus, a dramatically reduced electron flux seemed to have enabled binding of CO to the cofactor of *Av*VnfDGK at site(s) with low affinity to CO, a feat that could only be accomplished otherwise under over-pressurized CO. This observation firmly established the relevance of the hi-CO state of *Av*VnfDGK generated in the resting state (designated hi-CO^{A}; Figure 3.1B, *1*) to that generated under limited turnover conditions (designated hi-CO^{B}; Figure 3.2C, *1*), thereby providing two useful probes into the mechanistically-relevant questions of (i) whether the hi-CO conformation is catalytically competent in C−C coupling and (ii) which CO-bound state specifically impacts the reaction of N_2 reduction.

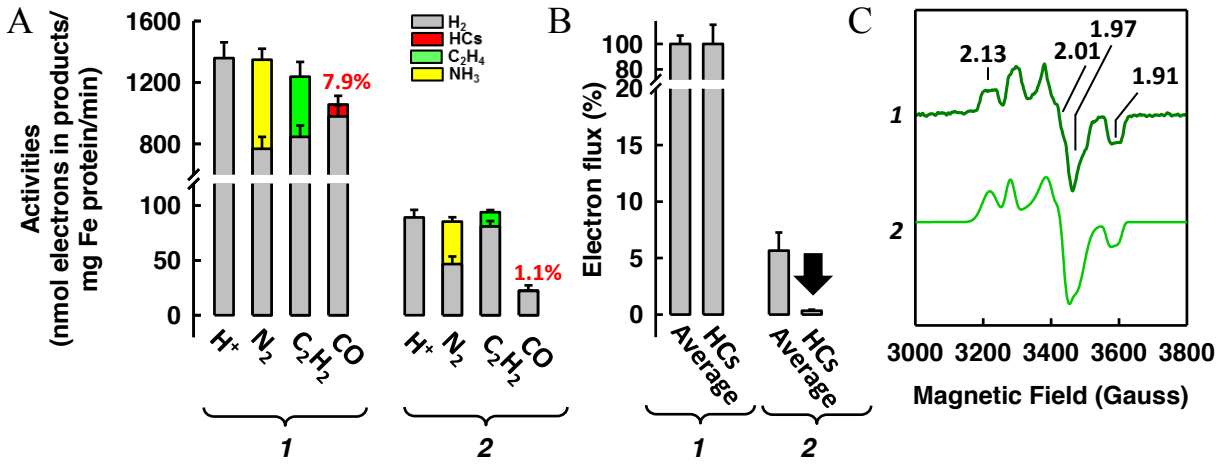

Figure 3.2 *Av*VnfDGK/*Av*VnfH activities. (**A**) Substrate-reducing activities of *Av*VnfDGK with *Av*VnfH (*1*) and *Ma*VnfH (*2*) as the respective electron donors. The activities were calculated based on the amounts of electrons required for the formation of the products. Substrates and products are indicated in the Figure. Percentage activities of hydrocarbon formation in the presence of CO are shown in red fonts. HCs=hydrocarbons. (**B**) Average electron fluxes of all substrate-reducing reactions (left) and the electron fluxes of the reactions of hydrocarbon formation from CO reduction (right) by *Av*VnfDGK, with *Av*VnfH (*1*) and *Ma*VnfH (*2*) as the respective electron donors. (**C**) EPR spectra of the turnover samples of *Av*VnfDGK with *Ma*VnfH (*1*) as the electron donor in the presence of 1 atm CO. The *g* values

are indicated. Spectrum *2* was simulated as described in the Materials and Methods (see Section 3.4) and is shown below the corresponding spectrum *1*.

3.2.4 Catalytic Relevance of the Hi-CO State Using *Ma*VnfH/*Av*VnfDGK Complex

To address the catalytic relevance of the hi-CO conformation to C−C coupling, hi-CO^A was subjected to turnover conditions upon incubation with *Av*VnfH, ATP, and dithionite in the absence or presence of extra CO, and examined for C−C coupling (that is, formation of C2 products) during this process. Interestingly, C−C coupling was not detectable upon turnover of hi-CO^A without additional CO, as no C2 product was formed under this condition (Figure 3.3A, *1*; Supplemental Figure 3.6C); however, it could be detected in the form of C_2H_4 and C_2H_6 in small quantities when hi-CO^A was subjected to turnover under 0.02 atm CO (Figure 3.3A, *2*), a CO concentration supplied at a 1:1 molar ratio to the concentration of cofactor that was bound to the hi-CO^A state of *Av*VnfDGK. Remarkably, the amount of C2 products generated by hi-CO^A did not exceed that by the lo-CO state of *Av*VnfDGK upon turnover in the presence of an equimolar amount of externally supplied CO (Figure 3.3A, *2* vs. *3*), suggesting that the extra CO in hi-CO^A, which could have contributed to an increased yield of C2 products upon turnover, was not involved in C−C coupling; instead, only the CO moiety in the lo-CO conformation was catalytically competent, and it was this CO moiety that participated in C−C coupling with the CO molecule supplied in addition in the headspace. Isotope labeling experiments further demonstrated that when hi-CO^A was generated with ^{13}CO and subsequently turned over under 0.02 atm ^{12}CO, the C2 products generated in this process contained mixed $^{12}C/^{13}C$ labels (that is, $^{13}CH_2{=}^{12}CH_2$ and $^{13}CH_3{-}^{12}CH_3$) instead of a single ^{13}C label (that is, $^{13}CH_2{=}^{13}CH_2$ and $^{13}CH_3{-}^{13}CH_3$) (Figure 3.3B, C; Supplemental Figure 3.6D), providing additional support for the coupling between a bound carbon (that is, a labeled ^{13}C atom) and an externally supplied carbon (that is, an unlabeled ^{12}C atom) instead of between two bound ^{13}C

atoms. Together, these observations strongly suggested that C−C coupling did not occur between the CO moieties trapped on the V-cluster in the hi-CO state, where some CO molecules were likely bound in a side-by-side manner (Supplemental Figure 3.6A, right); instead, it took place between the carbon in the lo-CO conformation and a second carbon that was supplied externally in the headspace under turnover conditions (Supplemental Figure 3.6D).

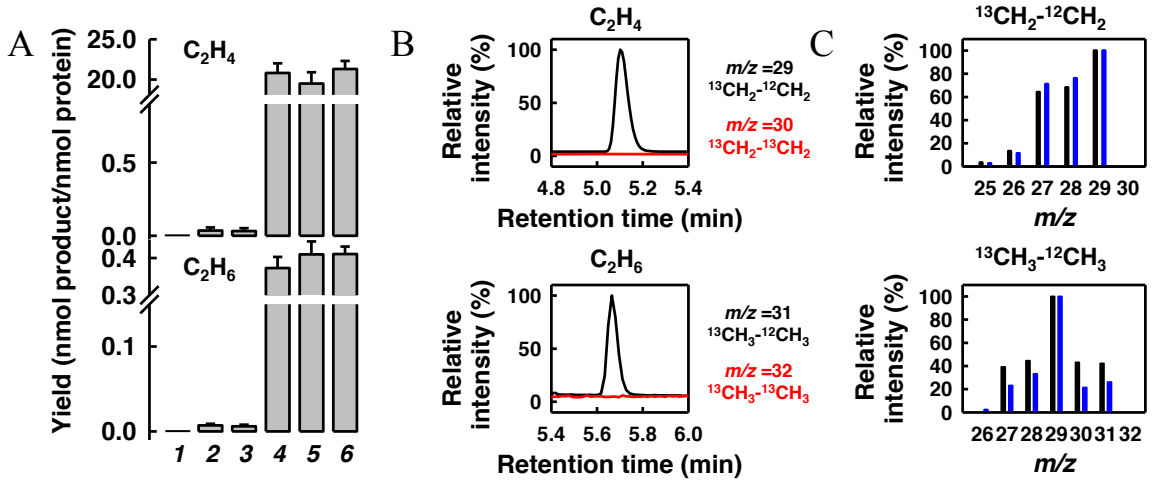

Figure 3.3 Relevance of the CO-bound states of *Av*VnfDGK to C−C coupling. (**A**) Formation of C_2H_4 (upper) and C_2H_6 (lower) by placing (*1*) hi-CO^A of *Av*VnfDGK under turnover with no additional CO, (*2*) hi-CO^A of *Av*VnfDGK under turnover with 0.02 atm CO, (*3*) lo-CO of *Av*VnfDGK under turnover with 0.02 atm CO, (*4*) hi-CO^A of *Av*VnfDGK under turnover with 1 atm CO, (*5*) lo-CO of *Av*VnfDGK under turnover with 1 atm CO, and (*6*) *Av*VnfDGK under turnover with 1 atm CO. All activities were measured upon incubation with *Av*VnfH, ATP and dithionite. The observation that hi-CO^A (*4*) and lo-CO (*5*) generated approximately the same yields of the C2 products as *Av*VnfDGK upon direct turnover of CO (*6*) in the presence of 1 atm CO demonstrated that the hi-CO^A and lo-CO species were as turnover-capable as the CO-free *Av*VnfDGK. (**B**) GC-MS analysis of C_2H_4 (upper) and C_2H_6 (lower) that were generated by placing the ^{13}CO-labeled hi-CO^A under 0.02 atm ^{12}CO (that is, the same turnover experiment as that in a, *2*, except for the ^{13}C labeling of hi-CO^A in this case). Both C2 products were traced at masses that would either contain mixed ^{12}C/^{13}C labels (black traces) or single ^{13}C isotope label (red traces). (**C**) GC-MS fragmentation patterns of the mixed ^{12}C/^{13}C labeled C_2H_4 (upper, black) and C_2H_6 (lower, black). The corresponding fragmentation patterns of the respective standards (blue) are presented based on the information from the NIST MS database (http://webbook.nist.gov). The intensities of the base peaks are set at 100 % in all panels.

3.2.5 Effects of CO Binding to *Av*VnfDGK by Addition of N_2

To address the impact of CO binding on N_2 reduction, *Av*VnfDGK was subjected to turnover conditions in the presence of a fixed concentration of N_2 (0.1 atm) and increasing concentrations of CO (0.1, 0.5 and 0.9 atm), and monitored for changes in its activity to reduce N_2 to NH_3 concomitant with the appearance of the one-CO and extra-CO EPR features in thus-generated hi-CO^B state. Consistent with the well-established competition between N_2 and CO, the activity of NH_3 formation decreased in the presence of increasing concentrations of CO (Figure 3.4A), and this decrease was accompanied by an increase in the intensities of the CO-related EPR features (Figure 3.4B); in particular, the g = 2.09 and g = 2.13 features, which did not overlap with other CO-originated signals, were used as markers to monitor the change of one- and extra-CO features, respectively, in this process (Figure 3.4B).[3] Interestingly, while the decrease of N_2 reduction correlated well with the intensity gain of the one-CO feature at g = 2.09 (Figure 3.4C), the extra-CO feature at g = 2.13 did not appear until the N_2-reducing activity was mostly abolished (Figure 3.4D). The fact that there is no inflection in the N_2-reducing activity curve as the intensity of the extra-CO feature increases suggests that binding and reduction of N_2 occurs independently from binding of additional CO molecules. The sharp decay of the N_2-reducing activity concomitant with a significant increase of the intensity of the one-CO feature, on the other hand, implies that N_2 and CO may compete for the same pair of reactive Fe sites across the S belt of the cofactor, although an indirect impact of CO binding on N_2 reduction (such as a change in the redox or structural properties of the cofactor upon CO binding) cannot be excluded.

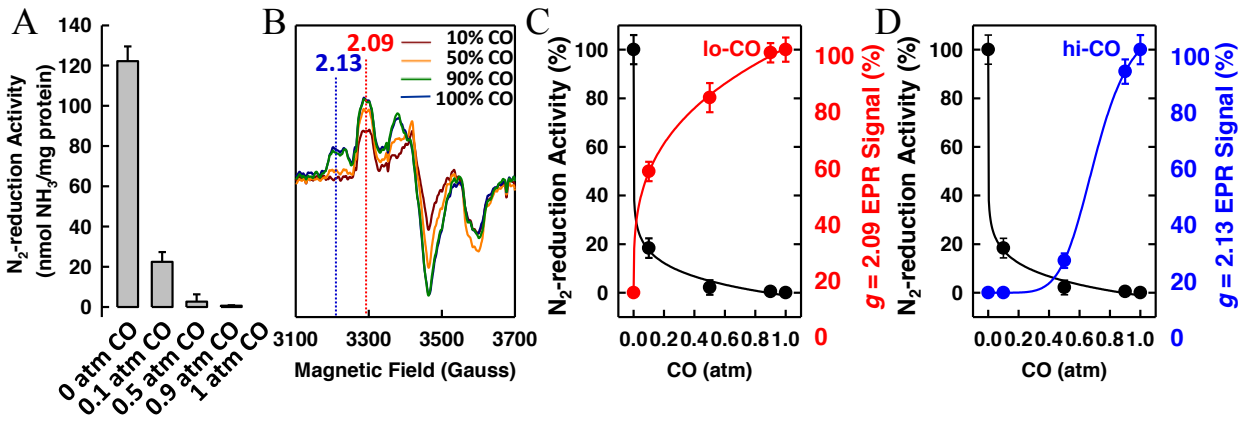

Figure 3.4 Relevance of the CO-bound states of *Av*VnfDGK to N_2 reduction. (**A**) Activities of N_2-reduction and (**B**) corresponding EPR spectra of the turnover samples in the presence of 0.1 atm N_2 and increasing CO concentrations of 0.1, 0.5 and 0.9 atm. The *g* values are indicated. Correlation of the activity of N_2 reduction with the intensity of (**C**) lo-CO or (**D**) hi-CO^B EPR signal in the presence of increasing CO concentrations. The EPR features at $g = 2.09$ and $g = 2.13$ were integrated and used as markers for the lo-CO and hi-CO^B signals, respectively, as they had nearly no overlap with all other CO-associated EPR features. The activity of N_2 reduction in the absence of CO, as well as the EPR signal intensities at $g = 2.09$ and $g = 2.13$ in the presence of 1 atm CO, are set as 100 % (**C**, **D**).

3.3 Summary and Conclusion

Binding of CO to the wildtype Mo-nitrogenase, as well as reduction of CO by certain Mo-nitrogenase variants, has been reported previously; however, the catalytic mechanism of CO reduction has remained elusive.[145,146,165–173] Consistent with the DFT calculation-predicted pathway of CO reduction, the current study reveals that the multiple CO moieties in the hi-CO conformation cannot be coupled as they are.[174] Further, it provides the initial biochemical evidence for the potential relevance of the belt Fe atoms to N_2 reduction, which aligns well with results of the previous spectroscopic and structural analyses of the belt region of the cofactor.[145,175,176] Further exploration of the utility of the catalytically competent, CO-bound conformation of V-nitrogenase, along with H/D exchange experiments and a more extensive EPR study aiming to unveil the fine structure of the CO-bound state, is currently underway in hopes of gaining relevant insights into the catalytic mechanism of CO reduction by nitrogenase.

3.4 Materials and Methods

3.4.1 Experimental Section

Unless noted otherwise, all protein work was performed under Ar gas at an O_2 concentration of less than 5 ppm.

3.4.2 Cell Growth and Protein Purification.

The *E. coli* strain expressing a His-tagged form of *Ma*VnfH was grown in 10-L batches in Difco LB medium containing 100 mg/L ampicillin (BD Biosciences) in a BIOFLO 415 fermenter (New Brunswick Scientific) at 37 °C, with an agitation of 200 rpm and an airflow of 10 L/min.[134] Growth rates were monitored by measuring the cell density at a wavelength of 600 nm using a Spectronic 20 Genesys spectrometer (Spectronic Instruments). When OD_{600} reached 0.5, the temperature was lowered to 25 °C before expression of *Ma*VnfH was induced by addition of 25 μM IPTG. Expression of protein was allowed to continue for 16 hr before cells were harvested by centrifugation using a Thermo Fisher Scientific Legend XTR centrifuge. Subsequently, the His-tagged *Ma*VnfH was purified by immobilized metal affinity chromatography (IMAC) using methods adapted from the purification protocol of His-tagged nitrogenase proteins.[21,148] *A. vinelandii* strains expressing *Av*VnfDGK and *Av*VnfH were grown at 30 °C in 180-L batches in a 200-L fermenter (New Brunswick Scientific) in Burke's minimal medium supplemented with 2 mM ammonium acetate. Growth rates were monitored by measuring the cell density at a wavelength of 436 nm. When OD_{436} reached 1.0, cells were harvested by a flow-through centrifugal harvester (Cepa). Published methods were used to purify these proteins.[21,43,148]

3.4.3 Activity Assays of V-nitrogenase

Activity assays were conducted as described previously.[24,43,148] Each assay contained, in a total volume of 1 mL, 0.27 mg *Av*VnfDGK, 0.15 mg *Av*VnfH or *Ma*VnfH, 20 mM sodium dithionite ($Na_2S_2O_4$), 0.8 mM Na_2ATP, 1.6 mM $MgCl_2$, 10 mM creatine phosphate, and 8 units of creatine kinase. For CO-, C_2H_2-, H^+-, and N_2-reduction assays, 1 atm CO, 0.1 atm C_2H_2, 1 atm Ar and 1 atm N_2, respectively, were added to the headspaces. Products H_2, C_2H_4 and NH_3 were determined as described elsewhere.[91,150] Hydrocarbon products were quantified by a gas chromatography-flame ionization detector (GC–FID). Specifically, 250 μL of the headspace of each sample was injected onto a Grace 5664PC column (3.2 mm diameter, 1.5 m length; Grace), and the column was then held at 55 °C for 1 min, heated to 180 °C at 12.5 °C/min, and held at 180 °C for 2.6 min prior to product analysis.

3.4.4 Generation of the CO-bound V-nitrogenase

Preparation of the lo-CO state of *Av*VnfDGK in the resting state was carried out under 1 atm CO, in the presence of Eu^{II}-DTPA, as described previously.[144] Preparation of the hi-CO state of *Av*VnfDGK in the resting state (designated hi-CO^A) was carried out under 2.6 atm CO by placing the Eu^{II}-DTPA-reduced *Av*VnfDGK protein under CO for 15 min with gentle stirring at 30 °C. The *Av*VnfDGK sample was then quickly passed through a G-25 column to remove dissolved CO and excess reductant prior to EPR, decay and turnover experiments.

Preparation of the hi-CO state of *Av*VnfDGK under turnover conditions (designated hi-CO^B) was carried out using a protocol adapted from that used to generate the hi-CO state of *Av*NifDK.[166,167] Specifically, a 1-mL reaction mixture containing 15 mg *Av*VnfDGK, 1 mg *Ma*VnfH, 6 mM Na_2ATP, 8 mM $MgCl_2$, 50 mM phosphocreatine, 0.20 mg/mL creatine phosphokinase, 10% (v/v) glycerol, 0.4 mM $Na_2S_2O_4$ and 25 mM Tris-HCl (pH 8.0) was placed

under 1 atm CO with gentle stirring at room temperature for 5 min prior to EPR analysis. For studies of the impact of CO binding on N_2 reduction, the same procedure was used to prepare *Av*VnfDGK samples with *Ma*VnfH, except that these samples were placed under a fixed concentration of 0.1 atm N_2 and increasing concentrations of CO of 0.1, 0.5 and 0.9 atm, respectively, with the remainder of the headspace supplemented by Ar, prior to activity and EPR analyses. Additionally, two controls prepared in the presence of 1 atm N_2 and 1 atm CO, respectively, were included and examined by activity and EPR analyses.

3.4.5 Quantification of the Cofactor-bound CO in V-nitrogenase

The cofactor-bound CO molecules in the hi-CO^A and lo-CO states of V-nitrogenase were released by acid quenching. Quantification of released CO was performed as described previously, which was initiated with injection of 0.25 mL of the headspace of each sample into a Thermo Scientific Trace 1300 Gas Chromatograph–Flame Ionization Detector (GC–FID) that was interfaced with a methanizer (Thermo Electron North America LLC).[144] Subsequently, CO was resolved on a TG-BOND Msieve 5A column (30 m × 0.32 mm ID × 30 μm film; Thermo Electron North America LLC), which was held at 45 °C for 1 min and heated to 245 °C at a rate of 25 °C/min before CO was hydrogenated at 350 °C in the methanizer. The resulting CH_4 was measured by FID, which is coupled directly behind the methanizer. The overall detection limit of CO is ~2 ppm.

3.4.6 Turnover Experiments of the CO-bound V-nitrogenase

The lo-CO or hi-CO sample of *Av*VnfDGK generated in the resting state was subjected to turnover conditions upon incubation with 10-fold molar excess of *Av*VnfH in a 2.5-mL reaction mixture containing 20.4 mM Na_2ATP, 43.2 mM $MgCl_2$, 245 mM creatine phosphate, 420 U/mL creatine phosphokinase, and 25 mM Tris-HCl (pH 8.0). The incubation mixture was placed

under 1 atm Ar, 0.02 atm CO/0.98 atm Ar ('controlled' turnover with CO added to the gas atmosphere at a molar ratio of 1:1 to the amount of CO that is bound to the hi-CO^A state of *Av*VnfDGK) or 1 atm CO ('normal' turnover with CO added to the gas atmosphere in excess to the amount of CO that is bound to the hi-CO^A state of *Av*VnfDGK) with gentle stirring at 30 °C for 1 hr before hydrocarbons products were analyzed by GC-FID as described above. As a positive control, formation of hydrocarbon products was also examined by directly mixing *Av*VnfDGK with *Av*VnfH, CO, ATP and dithionite in an activity assay.

3.4.7 GC-MS Experiments of the CO-bound V-nitrogenase

The hi-CO state of *Av*VnfDGK was generated in the resting state as described above, except for the use of ^{13}CO instead of the natural abundance ^{12}CO. Subsequently, the hi-^{13}CO sample was subjected to turnover conditions as described above in the presence of 0.02 atm ^{12}CO/0.98 atm Ar. GC-MS analysis of the hydrocarbon products formed in this reaction was carried out as described previously.[177]

3.4.8 EPR Analysis of the CO-bound V-nitrogenase

For electron paramagnetic resonance (EPR) analysis, samples were prepared in a Vacuum Atmospheres glove box with less than 5 ppm O_2 and flash frozen in liquid nitrogen (LN2) before analysis. The lo- and hi-CO samples of *Av*VnfDGK were prepared either in the resting state or under turnover conditions as described above. Subsequently, 0.3 mL of the sample was transferred to quartz EPR tubes and quickly frozen in LN2. EPR spectra were recorded by an ESP 300 Ez spectrophotometer (Bruker) interfaced with an ESR-9002 liquid-helium continuous-flow cryostat (Oxford Instruments) using a microwave power of 5 mW, a gain of 5×10^4, a modulation frequency of 100 kHz, and a modulation amplitude of 5 G. Five scans of all EPR samples were recorded at 20 K using a microwave frequency of 9.62 GHz. Spectral simulations

were performed using the EasySpin 4.0 toolbox in Matlab.[178] The following parameters were used for these simulations: lo-CO state (Figure 3.1A, gray trace), g = [2.095 1.999 1.916] with σ (g-strain) = [0.01 0.006 0.006]; 'extra-CO' state (Figure 3.1C, light blue trace), g = [2.135 2.016 1.975] with σ =[0.03 0.025 0.025]; hi-CO state (Figure 3.1B and Figure 3.2C, light green traces, sum of lo-CO plus 'extra-CO' state simulations).

3.5 Supplemental Tables and Figures

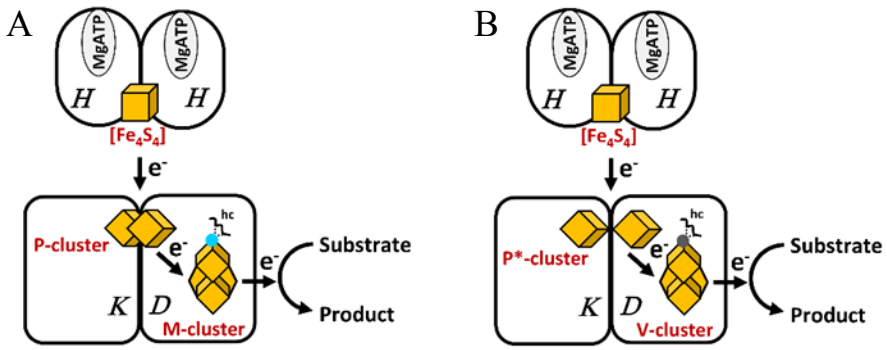

Figure 3.5 Schematic presentations of (A) molybdenum (*nif*-encoded) and (B) vanadium (*vnf*-encoded) nitrogenases. The two nitrogenases share a good degree of homology, each comprising a reductase component (*nifH*- or *vnfH*-encoded Fe protein) and a catalytic component (*nifDK*-encoded MoFe protein or *vnfDGK*-encoded VFe protein). Substrate turnover by both nitrogenases involves ATP-dependent transfer of electrons from the $[Fe_4S_4]$ cluster of the reductase component (NifH or VnfH), via the P-cluster (P- or P^*-cluster), to the cofactor (M- or V-cluster) of the catalytic component (NifDK or VnfDGK), where substrate reduction occurs. For the purpose of simplicity, only one half of the catalytic component is shown, and the small subunit of V-nitrogenase (VnfG) is omitted. The metal clusters are depicted in orange. Mo and V are colored cyan and dark gray, respectively. hc, homocitrate

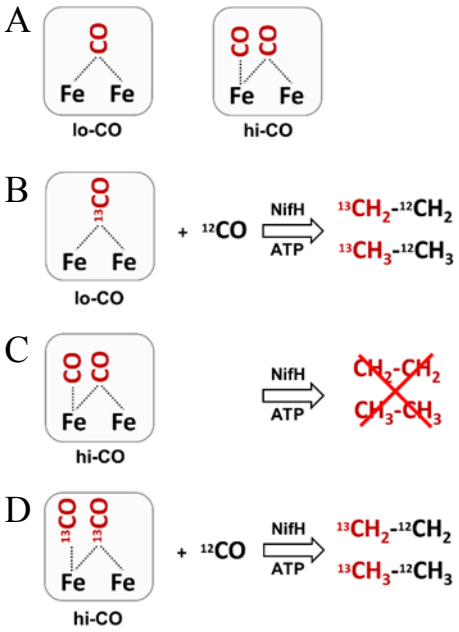

Figure 3.6 Proposed CO binding modes to the V-cluster. (**A**) Proposed CO binding modes to the cofactor (V-cluster) in the lo-CO (left) and hi-CO (right) states of *Av*VnfDGK. Based on its homology to the one-CO-bound, lo-CO state of *Av*NifDK,[144,145] the lo-CO state of *Av*VnfDGK may have one CO moiety bridged between a pair of Fe atoms across the 'belt' of the cofactor. Given the spectral analogy between *Av*VnfDGK and *Av*NifDK in CO binding, the hi-CO state of *Av*VnfDGK could assume a conformation analogous to the one suggested for its *Av*NifDK counterpart,[146,168,169] with at least two CO molecules bound side by side to a pair of Fe atoms across the S belt of the cofactor. Only the cofactor Fe atoms involved in CO binding are shown in the figure. (**B-D**) Schematic presentations of experiments performed to evaluate the relevance of the CO-bound states of *Av*VnfDGK to C-C coupling (see **Figure 3.3**). (**B**) When the lo-CO state of VnfDGK was generated with ^{13}CO in the resting state and subsequently turned over (upon addition of NifH and ATP) in the presence of a limited amount of externally supplied ^{12}CO in the headspace, mixed ^{12}C/^{13}C-labeled C2 products were generated between a bound ^{13}C atom and an external ^{12}C atom,[144] which firmly established the competence of the lo-CO state in C-C coupling. (**C**) When the hi-CO state was generated with CO in the resting state and subsequently turned over in the absence of externally supplied CO, no C2 product was generated (see **Figure 3.3**A, 1), suggesting no C-C coupling between the bound CO molecules. (**D**) When the hi-CO state was generated with ^{13}CO in the resting state and subsequently turned over in the presence of a limited amount of externally supplied ^{12}CO, only mixed ^{12}C/^{13}C-labeled C2 products were detected (see **Figure 3.3**B, C), suggesting no coupling between the bound CO molecules but, rather, coupling between a bound 13C atom and an external ^{12}C atom. The observation that the lo-CO and hi-CO states of *Av*VnfDGK showed comparable yields of C2 products upon turnover in the presence of a limited amount of externally supplied CO (see **Figure 3.3**A, 2 vs. 3, 4 vs. 5) suggested that the 'extra' CO did not participate in C-C coupling, as it would have increased the C2 product yield of the hi-CO state. Taken together, these results strongly pointed to the lo-CO conformation as the catalytically competent state in C-C coupling.

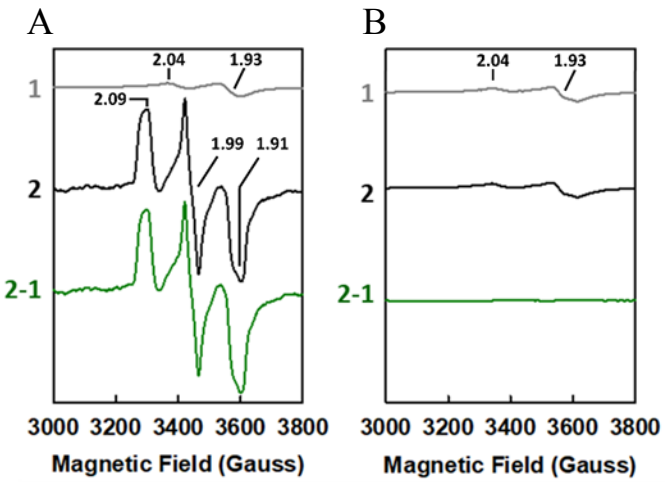

Figure 3.7 EPR spectra of (A) *Av*VnfDGK and (B) V-cluster-deficient *Av*VnfDGK protein incubated with and without 2.6 atm CO in the presence of Eu^{II}-DTPA. Shown are the spectra of protein incubated without (**A**, **B**, 1, gray traces) and with (**A**, **B**, 2, black traces) CO, and the difference spectra between the two (**A**, **B**, 2-1, green traces). The minor features of the samples prepared in the absence of CO (**A**, **B**, 1, gray traces) originate from the P-cluster of *Av*VnfDGK; whereas the absence of CO-related signals from the spectrum of the V-cluster-deficient, apo-*Av*VnfDGK demonstrates that this protein is unable to capture CO due to the absence of the cofactor.

3.6 Supplemental Discussion

Binding of CO to the wildtype Mo-nitrogenase has been investigated by a number of spectroscopic and structural techniques,[134,145,146,165–168,170,171] which contributed greatly to our understanding of the interaction between the inhibitor CO and the cofactor of Mo-nitrogenase. However, the catalytic mechanism of CO reduction has remained elusive due to the inability of the wildtype Mo-nitrogenase to turn over CO. The current study provides the initial insight into the catalytic relevance of the hi-CO conformation of nitrogenase and the competition between CO-binding and N_2-reduction, taking advantage of our approach to generate distinctive lo-CO and hi-CO conformations of the V-nitrogenase while exploiting the unique ability of the V-nitrogenase (contrary to the Mo-nitrogenase) to turn over CO as a substrate. The fact that the multiple CO moieties associated with the hi-CO conformation cannot be coupled as they are suggests that C-C coupling requires further activation and/or reduction of the bound CO entity,

which is consistent with the DFT calculation-predicted reaction pathway of CO reduction; whereas the observation that the activity of N_2 reduction only correlates with the population of the lo-CO conformation provides the first piece of biochemical evidence for the potential relevance of the belt Fe atoms to N_2 reduction, which aligns well with the outcome of previous spectroscopic and structural analyses. These results address the long-standing question in the field as to the relevance of the hi-CO conformation to catalysis, thereby pointing future investigation to the direction of using the turnover-capable, lo-CO state of V-nitrogenase to generate 'hi-C1' conformations comprising neighboring, reactive C1 species that are capable of C-C coupling. Efforts along this line can be combined with the approach of tuning the electron flux via the use of mismatched pairs of reductase/catalytic component of nitrogenase (like the *Ma*VnfH/*Av*VnfDGK pair used in this study) in order to capture the intermediate-trapped states of CO reduction. In a broader context, such a strategy could be employed in many other metalloprotein systems to elucidate the substrate or intermediate-trapped states. In the case of nitrogenase, it could shed light on the mechanism of enzymatic CO reduction, as well as facilitate future development of biomimetic catalysts for ambient carbon fuel production, which has a far-reaching impact on energy- and environment-related areas. Further exploration of the utility of the catalytically competent, CO-bound conformation of V-nitrogenase, along with a more extensive EPR study aiming to unveil the fine structure of the CO-bound state that could not be understood by CW EPR alone, is currently underway in hopes of gaining relevant insights into the elusive mechanism of CO reduction by nitrogenase.

3.7 Acknowledgments

I would like to thank John Wiley and Sons for permission to include Chapter 3 in my dissertation, which was originally published in *Angewandte Chemie International Edition*.[135]

This work was supported by NSF Career grant CHE-1651398 (to Y.H.), NSF grant CHE-1608926 (to M.W.R. and Y.H.), and NIH grant GM-104543 (to R.D.B.).

3.8 Contributions

CC Lee performed the bulk of the biochemical work. Jarett Wilcoxen performed the theoretical calculations. Caleb Hiller supplied *Ma*VnfH protein and ran activity assays relating to that protein.

Chapter 4 The MgADP-Bound Crystal Structure of the Vanadium Nitrogenase Iron Protein from *Methanosarcina acetivorans*

4.1 Introduction

Diazotrophic organisms contain enzyme systems known as nitrogenases that are able to fix dinitrogen (N_2) to form bioavailable ammonia (NH_3).[3,4] The most studied nitrogenase system is the molybdenum (Mo-) system from *Azotobacter vinelandii*, encoded by the *nif*-genes.[3,4,7] Catalysis requires two components: a reductase component and a catalytic component. The reductase component, also known as the Fe protein or *Av*NifH, is responsible for shuttling electrons to the catalytic component, the MoFe protein or *Av*NifDK, so that reduction of substrate can occur.

The electron transfer (ET) process of the *A. vinelandii* Mo-nitrogenase system begins with the reduction of the [Fe_4S_4] cluster of the Fe protein, *Av*NifH, from the 2+ to the 1+ oxidation state, followed by two equivalents of MgATP binding to the protein.[3,71] *In vivo* this process is likely carried out by flavodoxins or ferrodoxins, whereas this is typically carried out by dithionite *in vitro*.[72,74–76] A conformational change is induced in the Fe protein when MgATP binds, which then allows the protein to dock with the catalytic component, *Av*NifDK.[3] Upon complex formation, one of the clusters in *Av*NifDK, the P-cluster, is thought to initially transfer an electron to the catalytic cluster of *Av*NifDK, the M-cluster, whereupon the Fe protein rapidly transfers an electron to the P-cluster.[130] Because the P-cluster pushes an electron to the M-cluster prior to receiving an exogenous electron from *Av*NifH, this process is referred to as a "deficit-spending" model.[71,179] In conjunction with ET by the Fe protein, it also hydrolyzes the two MgATP molecules; however, it is no longer thought that these events are occur in a concerted step despite hydrolysis being a requisite for ET.[3,131] The next step involves the release of the inorganic phosphate, P_i, which results from MgATP hydrolysis, followed by the rapid release of the Mg-ADP-bound *Av*NifH from the complex.[71,130,132] Once freed, the [Fe_4S_4] cluster of the Fe

protein is again reduced, lowering the binding affinity of MgADP, and allowing for its release and subsequent replacement by two MgATP molecules.[3,71] This cycle must be repeated eight times for the reduction of N_2 by *Av*NifDK as shown by the balanced reaction: $N_2 + 8H^+ + 16MgATP + 8e^- \rightarrow 2NH_3 + H_2 + 16MgADP + 16P_i$.

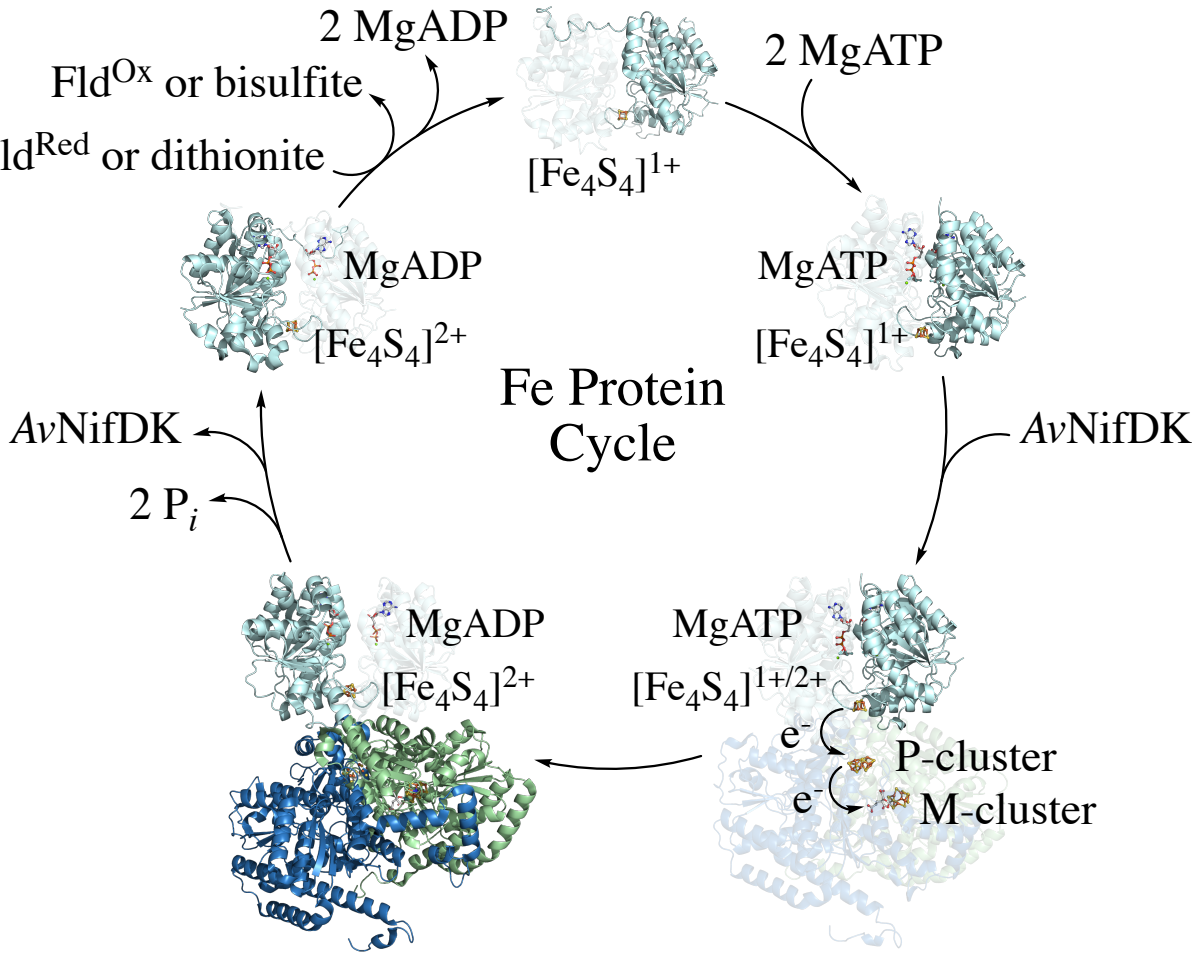

Figure 4.1 A depiction of the MgATP-dependent electron transfer (ET) from *Av*NifH to *Av*NifDK. For ET to occur, the Fe protein must be reduced by either DT (*in vitro*) or flavodoxin (*in vivo*) and loaded with 2 equivalents of MgATP. A conformational change accompanies MgATP binding that allows for the Fe protein to interact with *Av*NifDK and form an *Av*NifH/*Av*NifDK complex (only one αβ-dimer is shown). After binding, an electron is proposed to transfer from the P-cluster to the M-cluster, followed by ET from the [Fe_4S_4] cluster of *Av*NifH to the P-cluster. The MgATP are then hydrolyzed and the phosphate dissociates from the Fe protein. Finally, the Fe protein dissociates from the catalytic component, MgADP is released, and the Fe protein is prepared for additional redox cycles. This process must be repeated until enough electrons have been transferred to completely reduce the substrate. Fld^{Ox} = oxidized flavodoxin, Fld^{Red} = reduced flavodoxin. The NifH, NifD, and NifK subunits are represented in

pale cyan, pale green, and sky blue, respectively. PDB Codes 1G5P, 1N2C, 2AFI, and 1FP6 were used to generate this figure. The MgATP-bound *Av*NifH structure was generated by excluding *Av*NifDK from the original structure (PDB Code 1N2C). The MgATP represented in the figure is actually a MgATP analog, $ADP{\cdot}AlF_4^-$. Atoms are colored as follows: Fe, rust; S, yellow; Mo, cyan; C, white; N, blue; O, red; Mg, green; Al, gray; F, pale cyan. PyMOL was used to generate this figure.[38]

Despite reports of alternative nitrogenase systems in *A. vinelandii*, the vanadium (V-) and iron only (Fe-only) nitrogenases, beginning in the 1980's, these systems are not characterized as well as the Mo-system.[5,39] V-nitrogenase, encoded by the *vnf*-genes, only recently had the first crystal structure of the *A. vinelandii* V-nitrogenase catalytic component, *Av*VnfDGK, published in 2017; and a year later the first crystal structure of the V-nitrogenase reductase component, *Av*VnfH, was published.[40,56] Herein we report the MgADP-bound structure of the V-nitrogenase reductase component from *Methanosarcina acetivorans*. We have previously shown that the Mo- and V-nitrogenase Fe proteins from *M. acetivorans*, *Ma*NifH and *Ma*VnfH, respectively, can be heterologously expressed in *Escherichia coli* and that they can form hybrid nitrogenase systems when paired with either *Av*NifDK or *Av*VnfDGK.[134] The electron flux in the *Ma*VnfH/*Av*VnfDGK hybrid is reduced enough that the alternative *Av*VnfDGK substrate, CO, is trapped on the catalytic cofactor.[133–135,180] While these findings are fascinating and are providing insights into the mechanism of nitrogenase, they are also helping work toward accomplishing another goal of nitrogenase research, that of expressing a functional nitrogenase system in plants, by providing a well-studied, non-diazotrophic organism in which to work. The crystal structure of *Ma*VnfH further characterizes this Fe protein may continue to provide additional insights into the interactions between the catalytic and reductase components of nitrogenase.

4.2 Results and Discussion

Brown-colored monoclinic crystals of *Ma*VnfH soaked with MgADP diffracted and the structure was solved to 1.70 Å (Figure 4.2A and B). Similar to the previously described

nucleotide-free structure, the crystal contained one *Ma*VnfH dimer in the unit and belonged to the P 1 21 1 space group. The unit cell dimensions of the protein were a = 45.519 Å, b = 78.5098 Å, and c = 87.2982 Å, and other pertinent crystallographic statistics are summarized in Table 4.1.

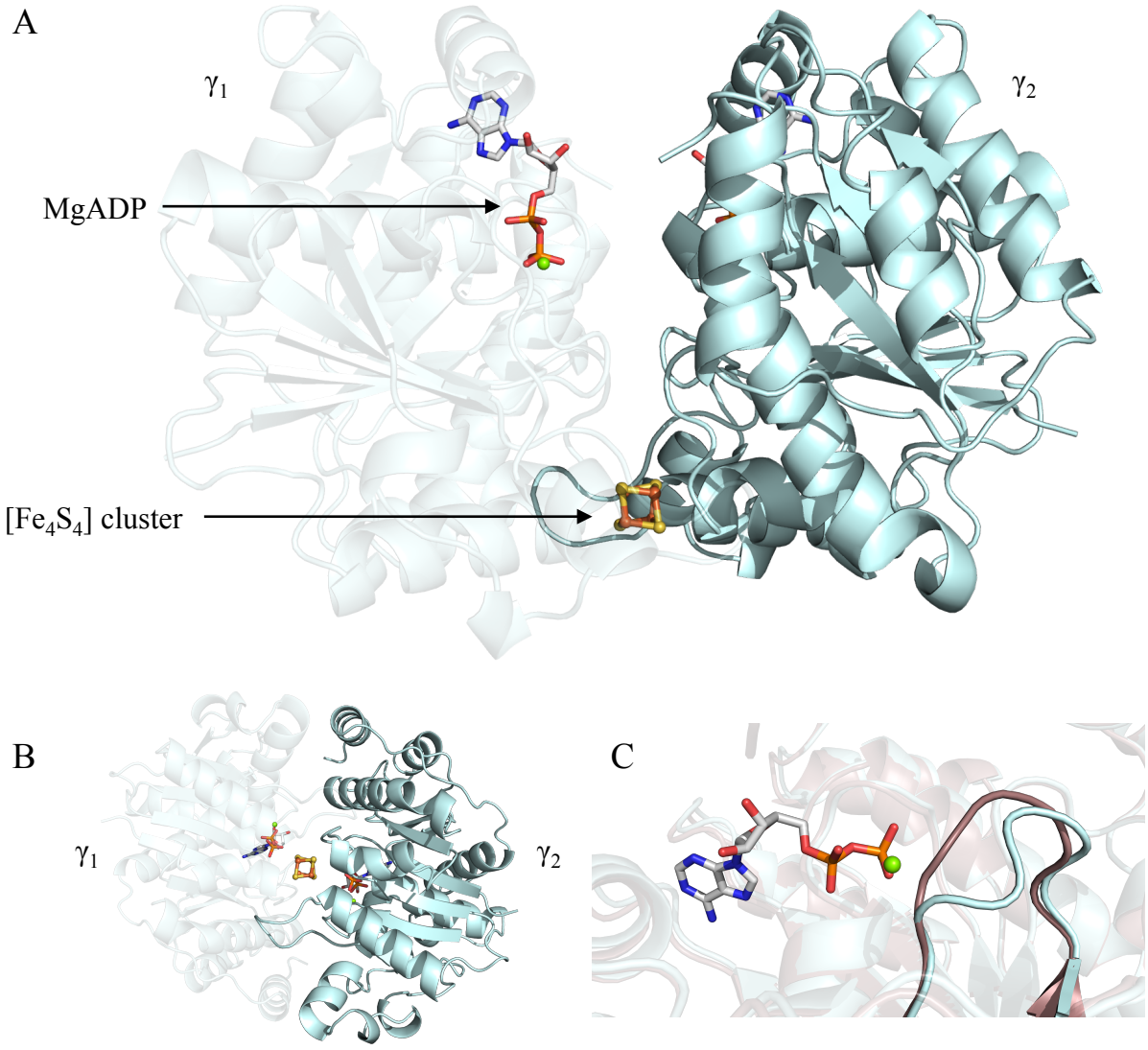

Figure 4.2 The crystal structure of *Ma*VnfH with MgADP bound at 1.70 Å resolution. (**A**) Crystal structure cartoon of *Ma*VnfH with the metallocluster and nucleotides highlighted. (**B**) A 90° rotation of the *Ma*VnfH crystal structure, with a view down the two-fold rotation axis. (**C**) The conformational change of Loop 41-44 (highlighted) to accommodate the binding of MgADP as compared between the MgADP-bound, blue, and nucleotide-free, purple, structures. Atoms are colored as follows: Fe, rust; S, yellow; C, white; N, blue; O, red; Mg, green. PyMOL was used to generate this figure.[38]

Table 4.1 Data Collection and Refinement Statistics for the MgADP-bound *Ma*VnfH Structure.

	MgADP-bound *Ma*VnfH
Wavelength	1.0 Å
Resolution range	58.14 - 1.7 (1.761 - 1.7)
Space group	P 1 21 1
Unit cell a, b, c (Å)	45.519 78.5098 87.2982
Unit cell α, β, γ (°)	90 97.59 90
Total reflections	122538 (10766)
Unique reflections	66387 (6349)
Multiplicity	1.8 (1.7)
Completeness (%)	99.02 (95.00)
Mean I/sigma(I)	5.89 (1.20)
Wilson B-factor	21.53
R-merge	0.07278 (0.467)
R-meas	0.1029 (0.6604)
R-pim	0.07278 (0.467)
CC1/2	0.983 (0.729)
CC*	0.996 (0.918)
Reflections used in refinement	66355 (6349)
Reflections used for R-free	3335 (295)
R-work	0.1806 (0.2900)
R-free	0.2150 (0.3240)
CC(work)	0.964 (0.832)
CC(free)	0.947 (0.745)
Number of non-hydrogen atoms	4671
macromolecules	4184
ligands	74
solvent	413
Protein residues	555
RMS(bonds)	0.011
RMS(angles)	1.13
Ramachandran favored (%)	98.16
Ramachandran allowed (%)	1.84
Ramachandran outliers (%)	0.00
Rotamer outliers (%)	0.90
Clashscore	2.83
Average B-factor	29.04
macromolecules	28.07
ligands	36.82
solvent	37.48

Statistics for the highest-resolution shell are shown in parentheses.

Like other Fe proteins, the 275 amino acid *Ma*VnfH polypeptide chains form an ~60 kDa homodimer that contains a nucleotide binding site in each subunit and a $[Fe_4S_4]$ cluster that is

located at the interface of the two subunits, near the surface of the protein.[52,56,134] The cluster is coordinated to the protein through two cysteine residues from each subunit and it is presumed that the physiologically relevant oxidation states of the reductase during ET are the $[Fe_4S_4]^{1+}$ and $[Fe_4S_4]^{2+}$ states, despite having also been shown to be able to adopt an all-ferrous $[Fe_4S_4]^0$ state by addition of a strong reductant, like titanium (III) citrate or europium (II) diethylenetriaminepentaacetic acid (Eu^{II}-DTPA).[134] This structure confirms that MgADP binds to this Fe protein as it was presumed based on the 1) sequence, which contains a canonical GXXXXGKS Walker A motif, also known as a P-loop, located at residues 9-16, indicative of a nucleotide binding site, 2) the tertiary structure of the other two *Ma*VnfH structures, which shows a Rossman-type βαβ-fold, typical of NTP-ases, and 3) a similar electron paramagnetic resonance (EPR) spectral change in the presence of nucleotide as observed in *Av*NifH.[52,54,56,134]

As observed with the *Av*NifH structures, the nucleotide-free and MgADP-bound structures are highly similar.[53] The most notable difference is the re-location of the loop containing residues 41-44, so as to accommodate the nucleotide in the binding pocket (Figure 4.2C).

*Ma*VnfH is only the second V-nitrogenase Fe protein to be crystallized, and now the second most structurally well-characterized Fe protein, behind *Av*NifH, as it has been crystallized in three states, including the MgADP-bound, and nucleotide free with the cluster in both the $[Fe_4S_4]^{1+}$ and $[Fe_4S_4]^0$ states (see Chapter 7). This is the first V-nitrogenase Fe protein that has been heterologously expressed in a non-diazotrophic organism and is therefore working towards one of the longstanding goals of nitrogenase research, that of expressing a functional nitrogenase in plants to enable them with the machinery to fix their own nitrogen.[134] Two approaches have been pursued to accomplish this goal; that of expressing complete nitrogenase

systems in *E. coli* and that of expressing individual gene products. To date, the expression of complete systems with reasonable turnover has not been accomplished; however, the Fe protein is now the second individual gene product that has been expressed in *E. coli*.[25,116,134] As it is uncertain whether the other gene components from *M. acetivorans* can be functionally expressed in *E. coli*, it may be necessary to cross these proteins with those from other organisms to obtain the goal of functional nitrogenase expression in a heterologous host. It would be of benefit to further structurally characterize *Ma*VnfH, in obtaining the other crystal conformations shown in Figure 4.1 so that additional comparisons can be made relating to the interprotein interactions between the Fe protein and the catalytic component.

4.3 Materials and Methods

4.3.1 Cell Growth and Purification

E. coli strains of His-tagged *Ma*VnfH were grown in 40-L batches in a similar fashion as reported earlier.[134] Likewise, the protein was purified under anaerobic conditions and purity was confirmed using SDS-PAGE following established protocols.[15,22,134]

4.3.2 Crystallization and Data Collection

*Ma*VnfH was crystallized using a microbatch method in a glove box containing < 2 ppm O_2. Equal volumes, 1 μL, of a protein solution (containing ~10 mg/mL *Ma*VnfH) and buffer solution (containing 0.04 M citric acid, 0.06 M BIS-TRIS propane pH 6.4, and 20% w/v polyethylene glycol 3,350) were combined until crystals were grown. MgADP was allowed to soak into the crystals for 20 minutes by adding 2 μL of a buffered solution (containing 12.5 mM ADP, 25 mM $MgCl_2$, 0.15 M ammonium sulfate, 0.075 M MES monohydrate pH 6.5, and 30% w/v polyethylene glycol monomethyl ether 5,000) to the crystals, followed by rinsing in paraben

oil and flash freezing in liquid nitrogen. Diffraction data was collected at the ALS beamline 5.0.1 equipped with a Pilatus detector at a wavelength of 1.0 Å.

4.3.3 Structure Solution and Refinement

The data was indexed and integrated with iMosflm and scaled with AIMLESS from the CCP4 suite. The structure was solved by molecular replacement using Phaser-MR and the *Ma*VnfH in the $[Fe_4S_4]^{1+}$ state as a model structure, yielding a P 1 21 1 unit cell. The protein was further refined in Phenix and the data collection and refinement statistics are summarized in Table 4.1. All figures were generated with PyMOL.[38]

4.4 Acknowledgments

This work was supported by NSF Career grant CHE-1651398 (to Y.H.), NSF grant CHE-1608926 (to M.W.R. and Y.H.), and NIH grant GM-104543 (to R.D.B.).

4.5 Contributions

Caleb Hiller performed all biochemical work and solved the crystal structure of the MaVnfH protein. Wonchull Kang is providing feedback regarding the structure.

Chapter 5 Continued Work toward Characterizing the Physiological Roles of Fe Protein Homologs of Nitrogenase

5.1 Introduction

In Chapter 2, the expression and characterization of the Mo- and V- nitrogenase iron (Fe) proteins from *M. acetivorans* and their ability to perform the three known physiological roles of Fe proteins were compared to those from *A. vinelandii*.[134] One of the purposes of this work is to follow-up on what was done previously with additional Fe proteins. The expression of additional Fe protein homologs in a non-diazotrophic system also provides the benefit of generating an arsenal of Fe proteins that could be combined with the other nitrogenase components to accomplish one of the goals of nitrogenase research: the expression of a functioning nitrogenase system in a heterologous host. As it is impossible to predict whether a nitrogenase gene component from one organism can be expressed in a heterologous and non-diazotrophic system, it may be necessary to mix-and-match genes from a variety of diazotrophic organisms. The theoretical docking model discussed in Chapter 2 was used to predict how well Fe protein homologs would interact with *Av*NifDK and *Av*VnfDGK. Using this model, additional Mo-nitrogenase Fe protein homologs (Table 5.1) were selected for heterologous expression and characterization according to their predicted ability to interact with *Av*NifDK and *Av*VnfDGK (see Section 5.2). The experimental activities will be compared to those predicted by the model to determine the effectiveness of the model.

Table 5.1 The Fe protein homologs, protein designations, and affinity and specificity markers. With the exception of the *A. vinelandii* proteins, all the proteins herein were expressed heterologously in *E. coli* (see 5.4.2).

Organism	Abbrev.	Affinity Marker	Specificity Marker
Azotobacter vinelandii (*A. vinelandii*)	*Av*NifH	-5.2	-14
Methanosarcina acetivorans (*M. acetivorans*)	*Ma*NifH	1.1	-6
Methanococcus maripaludis (*M. maripaludis*)	*Mmp*NifH	0.8	-7.8
Chlorobium phaeobacteroides (*C. phaeobacteroides*)	*Cp*NifH	2.4	-6.3
Geobacter uraniireducens (*G. uraniireducens*)	*Gu*NifH	-4.6	-19.7
Methanosphaerula palustris (*M. palustris*)	*Mp*NifH	-1.9	-8.6
Desulfovibrio vulgaris (*D. vulgaris*)	*Dv*NifH	-2.9	-7.7

5.2 Theoretical Docking Model

Homology modeling and *in silico* docking calculations can provide a screen and aid in determining how certain proteins may interact without the arduous task of expressing and purifying protein. To this end, we developed a technique that would allow us to screen for potential Mo-nitrogenase Fe proteins to predict how well they would bind with *Av*NifDK and thereby affect electron flux for the nitrogenase hybrid system. We have a three-fold goal in trying to 1) identify an Fe protein that more efficiently transfers electrons to the catalytic component to increase nitrogenase activity, 2) identify an Fe protein that can trap substrate on the catalytic cofactor to determine the reaction mechanism of N_2 reduction, and 3) build an arsenal of Fe protein homologs that can be used in association with catalytic component homologs. Two *in silico* docking calculations were used to select the Fe proteins that would be expressed: the "affinity marker" and the "specificity marker". The methodology for calculating these markers was previously presented, but are again mentioned for clarity of the discussion.[134] Theoretical docking conformations of each Fe protein homolog and catalytic component hybrid was calculated and an energy landscape of the binding energies was plotted from most exothermic to most endothermic, a representative energy landscape of the *Av*NifH/*Av*NifDK is

shown in Figure 5.1A. The mean binding energy of all docking conformations was calculated (Figure 5.1A, blue) and was designated as the "affinity marker". The "specificity marker" was generated by plotting the distance (in 1 Å intervals) between the $[Fe_4S_4]$ cluster of the Fe protein and four residues on the catalytic component (Ile^{D143}, Leu^{D142}, Ile^{K120}, Val^{K119}) against the average binding energy of the exothermic conformations, as represented in Figure 5.1B. In most cases two peaks appear, the most probable is the one where the cluster can get closest to the residues of the catalytic component to interact, and is labeled as the "P" peak, represented in Figure 5.1B, blue. As mentioned, these calculations were performed to screen various Fe protein homologs. Five new Mo-nitrogenase Fe protein homologs with an assortment of affinity and specificity markers were selected to examine the effectiveness of this tool and are presented in Table 5.1 along with the organism name and protein designation, and will be compared to *Av*NifH and *Ma*NifH.

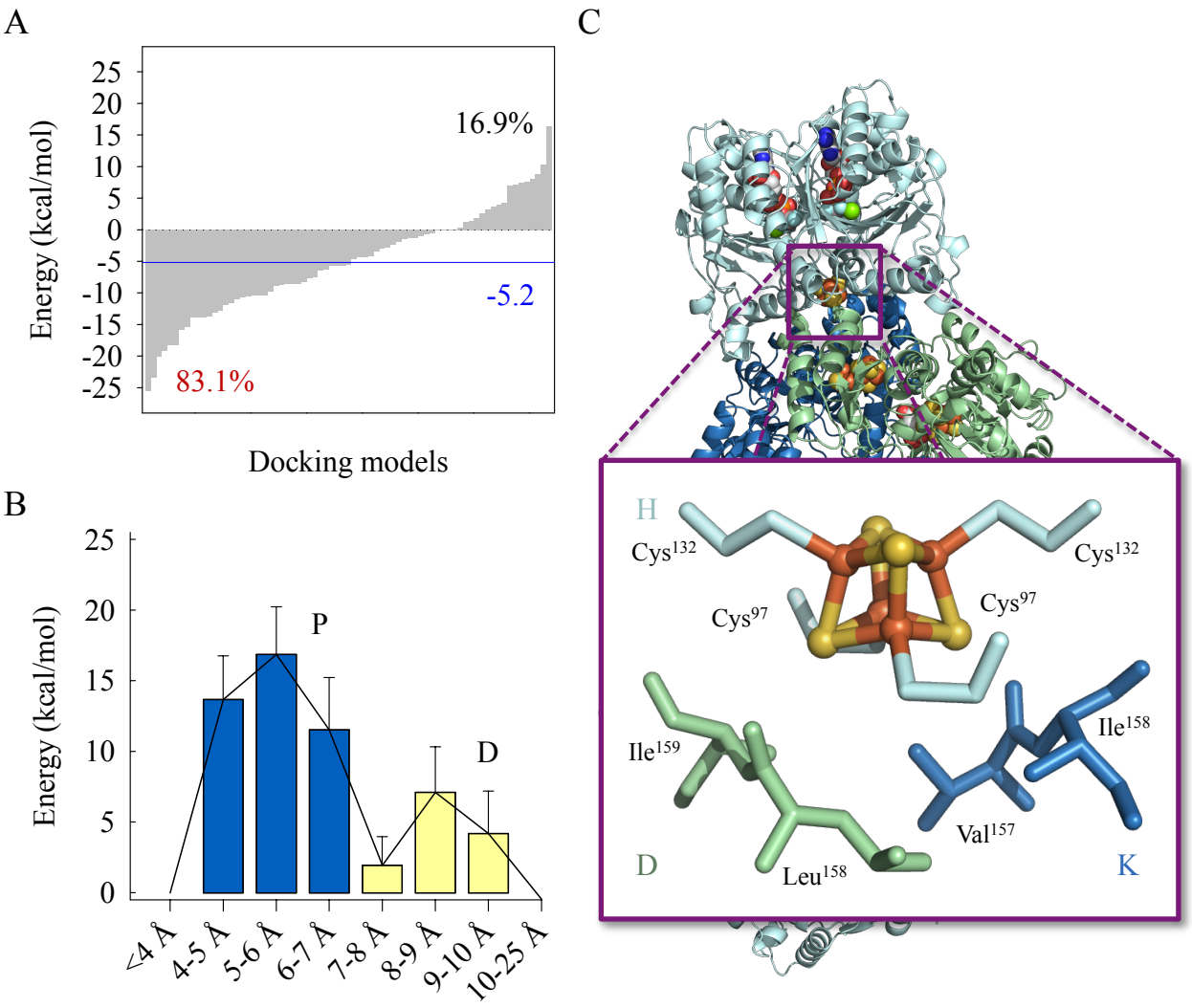

Figure 5.1 Energy landscape and binding efficiency plots used to determine the affinity and specificity markers. (**A**) An energy landscape plot of the docking energies of the *Av*NifH/*Av*NifDK complex from most exothermic to most endothermic. The mean binding energy or "affinity marker" is represented in blue. (**B**) The average energies of all exothermic docking models are plotted in 1 Å intervals. These are grouped into categories based on their proximity to the docking residues as either a proximal or distal groups, designated as 'P' or 'D', respectively. The average value of the P values represents what is termed as the "specificity marker".

5.3 Expression and Characterization of Fe Protein Homologs

*Av*NifH was purified as previously reported, and all the Fe protein homologs were co-expressed in *Escherichia coli* (*E. coli*) with the FeS assembly machinery, IscSUA and purified on a Ni-sepharose column. Protein purity was examined using SDS-PAGE and the subunits size

(≈30 kDa) was consistent with *Av*NifH (Figure 5.2). Metals analysis indicated decent [Fe_4S_4] cluster occupancy in most of the homologs, see Table 5.2. *Gu*NifH could be further purified to remove "junk" iron (Fe that binds adventitiously to the protein), but the junk iron didn't affect the [Fe_4S_4] cluster's ability to transfer electrons to the catalytic component.

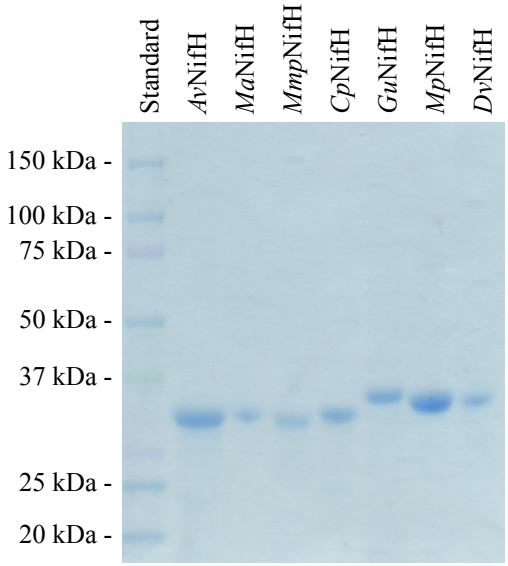

Figure 5.2 SDS-PAGE of select Fe protein homologs.

Table 5.2 Metals analysis of the Fe protein homologs.

Protein	# Fe / homodimer	% Occupancy
*Av*NifH	3.51 ± 0.10	88
*Ma*NifH	4.09 ± 0.11	102
*Mmp*NifH	3.37 ± 0.20	84
*Cp*NifH	3.98 ± 0.04	100
*Gu*NifH	6.75 ±0.15	169
*Mp*NifH	2.65 ± 0.06	66
*Dv*NifH	2.52 ± 0.02	63

5.3.1 Characterization of the [Fe_4S_4] Cluster Using EPR Spectroscopy

EPR spectroscopy was used to characterize the [Fe_4S_4] cluster of these five Fe protein homologs and to compare them to the Fe proteins from *A. vinelandii*. Figure 5.3A, B, and C

shows the EPR signals of the [Fe_4S_4] cluster in the 2+, +1 and 0 oxidation states, respectively. Addition of the chemical oxidant indigo disulfonate (IDS), oxidizes the cluster to the $[Fe_4S_4]^{2+}$ state, where it exists in an $S = 0$ spin state and does not show an EPR signal (Figure 5.3A). As purified in dithionite, ($Na_2S_2O_4$, DT), the $[Fe_4S_4]^{1+}$ cluster exists as a mixture of an $S = 1/2$ and $S = 3/2$ spin state (Figure 5.3B), with the $S = 1/2$ rhombic signal being predominantly featured, comparable to that found with *Av*NifH. These five homologs also exhibit the all-ferrous $S = 4$ EPR signal at $g = 15.9$ that is consistent with the *A. vinelandii* Fe proteins (Figure 5.3B).

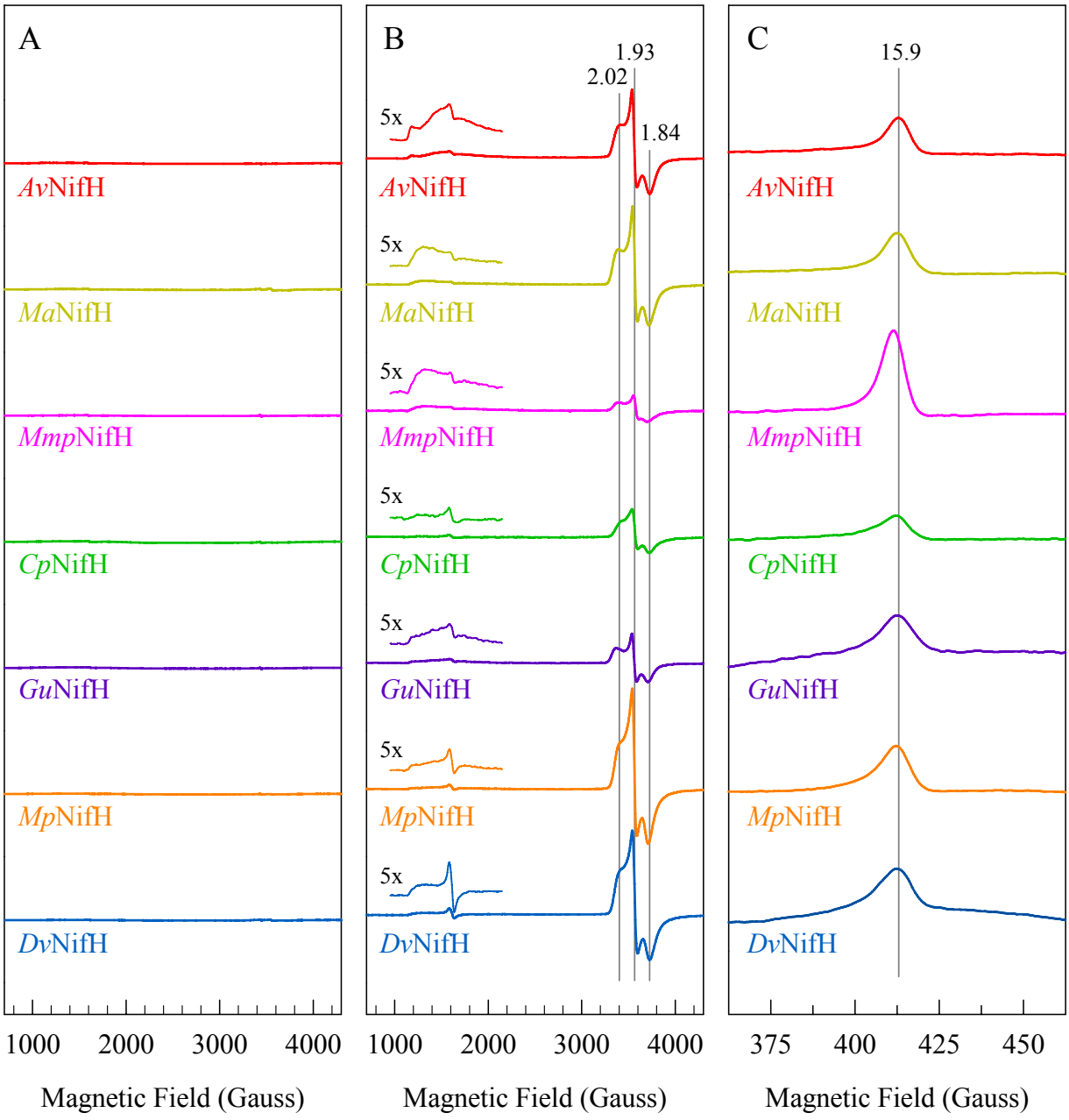

Figure 5.3 EPR spectra of Fe protein homologs in the IDS-oxidized ($[Fe_4S_4]^{2+}$, A), DT-reduced ($[Fe_4S_4]^{1+}$, B), Eu^{II}-reduced all-ferrous states ($[Fe_4S_4]^{0}$, C), and the observed all-ferrous signal observed in the DT-reduced state ($[Fe_4S_4]^{1+}$, D). The *g*-values are indicated by vertical lines. IDS = indigo disulfonate, DT = dithionite, Eu^{II}-DTPA = europium (II) diethylenetriaminepentaacetic acid. Conditions: four (**A** and **B**) or ten scans (**C** and **D**) were run at 10 K with a microwave power of 50 mW and a microwave frequency of 9.62 GHz.

Additional samples have been prepared to complete the EPR characterization of the $[Fe_4S_4]$ cluster. This includes samples with nucleotides present (both MgATP- and MgADP-

bound). It is expected that the rhombic $S = 1/2$ line-shape signals from the DT-reduced samples will change to the axial signals, as has been observed for the other characterized Fe proteins.[134] There is also a plan to analyze whether the DT-reduced sample has partial occupancy in the all-ferrous state, the $S = 4$ signal at $g = 15.9$, similar to what was observed for *Ma*VnfH (Figure 7.10D), by analyzing these samples in the parallel mode.

5.3.2 Cross-reactivities of the Fe Protein Homologs with *Av*NifDK

Four standard assays were used to monitor substrate reduction: N_2-, CO-, C_2H_2-, and H^+-reduction. The *Cp*NifH/*Av*NifDK, *Gu*NifH/*Av*NifDK, and *Mp*NifH/*Av*NifDK showed minimal activity (≈ 2% that of *Av*NifH/*Av*NifDK). Excitingly two of the hybrid nitrogenase systems, *Mmp*NifH/*Av*NifDK and *Dv*NifH/*Av*NifDK, measured an electron flux nearly half of those measured with *Mmp*NifH/*Av*NifDK, results shown in Figure 5.4 and Table 5.3. This is the highest reported activity for a nitrogenase hybrid system.

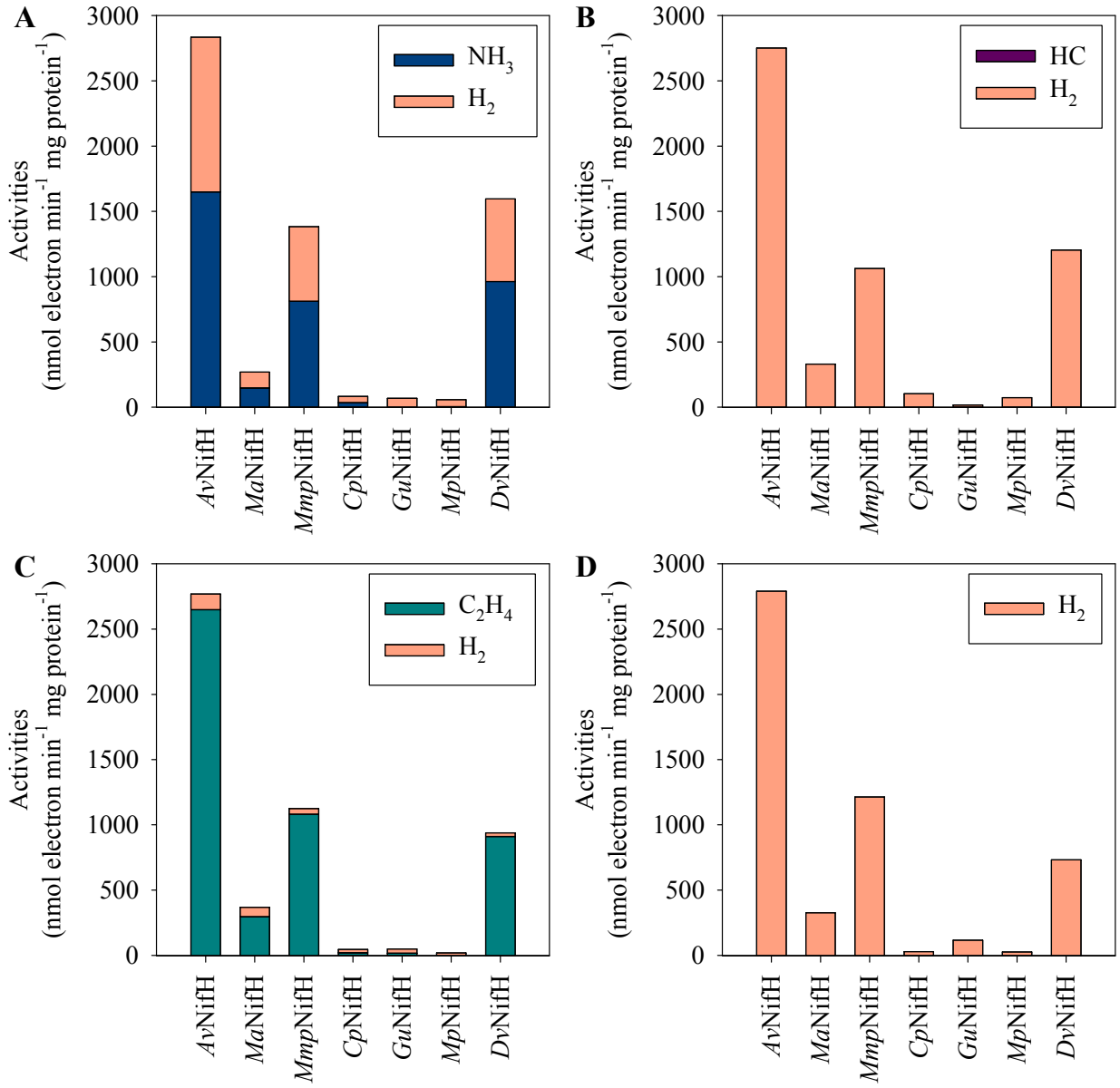

Figure 5.4 Interactions of the Fe proteins with *Av*NifDK. Cross-reactivities of the Fe protein homologs with *Av*NifDK were monitored using four standard substrates: N_2 (**A**), CO (**B**), C_2H_2 (**C**), and H^+ (**D**). Activities were calculated based on the nmoles of electrons that appeared in the products per min per mg Fe protein. HC = hydrocarbons.

Table 5.3 Interactions of the Fe proteins with *Av*NifDK. Cross-reactivities of the Fe protein homologs with *Av*NifDK were monitored using four standard substrates: N_2, CO, C_2H_2, and H^+. Activities were calculated based on the nmoles of electrons that appeared in the products per min per mg Fe protein. HC = hydrocarbons.

	Activities (nmol electron min^{-1} mg^{-1})						
Substrate:	N_2		CO		C_2H_2		H^+
Product:	NH_3	H_2	HC	H_2	C_2H_4	H_2	H_2
*Av*NifH	1650 ± 54	1185 ± 39	0.2 ± 0.7	2752 ± 4	2651 ± 54	120 ± 48	2793 ± 67
*Ma*NifH	149 ± 19	121 ± 8	0.0 ± 0.5	332 ± 254	300 ± 1	72 ± 6	330 ± 37
*Mmp*NifH	813 ± 6	571 ± 30	0.3 ± 0.2	1064 ± 109	1084 ± 66	44 ± 12	1216 ± 23
*Cp*NifH	36 ± 13	49 ± 16	0.5 ± 0.3	104 ± 5	24 ± 0	25 ± 8	32 ± 3
*Gu*NifH	0 ± 15	70 ± 11	0.3 ± 0.0	18 ± 1	20 ± 16	32 ± 20	120 ± 49
*Mp*NifH	6 ± 3	53 ± 3	0.0 ± 0.1	75 ± 1	2 ± 1	20 ± 6	29 ± 10
*Dv*NifH	964 ± 20	633 ± 17	0.0 ± 0.0	1205 ± 26	914 ± 25	28 ± 4	735 ± 117

There is a plan to repeat the cross-reactivity assays using *Av*VnfDGK as the catalytic component. The values obtained, like those for *Av*NifDK, will be compared to predictive screen to determine the efficacy and potential modify the screen to improve the predictive power.

5.3.3 M-cluster Maturation

Besides shuttling electrons to the catalytic component, the Fe protein is known to play a role in both P-cluster biosynthesis (see Section 1.4.2) and M-cluster assembly (see Section 1.4.1). M-cluster maturation assays were performed to compare the ability of the Fe protein homologs to mature L-cluster to M-cluster and determine their effectiveness in assisting in cofactor assembly (Table 5.4). A correlation between the N_2-reduction and M-cluster maturation assays is not apparent. However, this can easily be explained by the fact that the Fe protein interacts with *Av*NifDK during N_2-reduction and with *Av*NifEN for M-cluster maturation.

Table 5.4 The comparative effectiveness of the Fe protein homologs to synthesize the M-cluster, represented as a percent to *Av*NifH.

	Relative M-cluster Formation (%)
*Av*NifH	100
*Ma*NifH	21.6
*Mmp*NifH	1.9
*Cp*NifH	7.8
*Gu*NifH	0
*Mp*NifH	0
*Dv*NifH	11.9

5.4 Materials and Methods

5.4.1 Experimental Section

Unless noted otherwise, all chemicals and reagents were obtained from Fisher Scientific or Sigma-Aldrich. All protein work was performed under Ar gas at an O_2 concentration of less than 5 ppm.

5.4.2 Cell Growth and Protein Purification

Non-tagged Mo-nitrogenase *nifH*-encoded Fe protein from *Azotobacter vinelandii* (designated as *Av*NifH) was grown as described elsewhere.[15,22] A His-tagged Mo-nitrogenase *nifH*-encoded Fe protein from *M. acetivorans* (designated as *Ma*NifH) was grown as reported earlier.[134] Published methods were used for the purification of *Av*NifH and *Ma*NifH from their respective expression strains.[15,22,134] His-tagged Mo-nitrogenase *nifH*-encoded Fe proteins from *Methanococcus maripaludis* (designated as *Mmp*NifH, strain YM 218EE), *Chlorobium phaeobacteroides* (designated as *Cp*NifH, strain YM 221EE), *Geobacter uraniireducens* (designated as *Gu*NifH, strain YM 222EE), *Methanosphaerula palustris* (designated as *Mp*NifH, strain YM 220EE), *Desulfovibrio vulgaris* (designated as *Dv*NifH, strain YM 224EE) were constructed, grown, and purified using the same methods as published for *Ma*NifH.[134]

5.4.3 SDS-PAGE Analysis

SDS-PAGE analysis was performed using a 4-15% Mini-PROTEAN TGX precast gel (BioRad), run at 200 V and 50 mA, for 40 min, followed by staining with Coomassie Brilliant Blue.

5.4.4 Iron Determination

Metals analysis of the Fe protein homologs was determined using inductively coupled plasma optical emission spectroscopy (ICP-OES) using a Thermo Scientific iCAP7000 instrument. Sample preparation was performed using the same methods as published for *Ma*NifH.[134]

5.4.5 EPR Analysis

Electron paramagnetic resonance (EPR) samples were prepared in a Vacuum Atmosphere glove box with less than 2 ppm O_2 and flash frozen in liquid nitrogen prior to analysis using the same methods as published for *Ma*NifH.[134] The Fe protein concentration of all the samples prepared was 10 mg/mL.

5.4.6 Enzymatic Assays

The enzymatic assays were conducted as previously described.[24,134,148] The assays contained 0.27 mg *Av*NifDK, 0.15 mg Fe protein, 20 mM $Na_2S_2O_4$, 0.8 mM ATP, 1.6 mM $MgCl_2$, 10 mM creatine phosphate, and 8 units of creatine kinase in a total volume of 1 mL. 1 atm N_2, 1 atm CO, 0.1 atm C_2H_2, and 1 atm Ar was added to the headspace of the N_2-, CO-, C_2H_2-, and H^+- reduction assays, respectively. Determination of H_2, C_2H_4, and NH_3 were performed as previously described.[91,134,150]

5.4.7 M-cluster Maturation Assay

This assay contained 25 mM Tris·HCl (pH 8.0), 20 mM $Na_2S_2O_4$, 1.3 mg *ΔnifHDK Av*NifEN, 0.3 mg *ΔnifB Av*NifDK, 1.0 mg Fe protein, 0.4 mM molybdate (MoO_4^-), 0.4 mM (*R*)-homocitrate, 0.8 mM MgATP, 1.6 mM $MgCl_2$, 10 mM creatine phosphate, 8 units creatine kinase, in a total volume of 1 mL. This mixture was then incubated at 30°C for 60 min, followed by determination of enzymatic activities, as previously described.[15,16,18,60]

5.4.8 Docking Calculations

Homology modeling and docking experiments were carried out using the same methods as previously described.[134]

5.5 Acknowledgments

This work was supported by NSF Career grant CHE-1651398 (to Y.H.), NSF grant CHE-1608926 (to M.W.R. and Y.H.), and NIH grant GM-104543 (to R.D.B.).

Caleb Hiller, Matty Rasekh, and Joe Solomon performed the biochemical work. Martin Stiebritz performed the theoretical calculations.

5.6 Contributions

Caleb Hiller, Matty Rasekh, and Joe Solomon performed the biochemical work. Martin Stiebritz performed the theoretical calculations.

Section 2 Characterization of Fe Protein Homologs – The Adventitious Function of the Fe Protein to Reduce CO_2 and CO

It was recently discovered that the *A. vinelandii* V-nitrogenase could perform an adventitious function similar to the reaction catalyzed in the Fischer-Tropsch process, that is to reduce CO and form short-chain hydrocarbons.[133] Later, Hu and co-workers discovered that both *Av*NifH and *Av*VnfH could function as a carbon monoxide dehydrogenase (CODH)-like system and interconvert CO_2 and CO under certain conditions *in vitro*, independent of the presence of the catalytic component.[62] In their work, they also demonstrated that the Fe proteins could reduce CO_2 to CO *in vivo* by expressing *nifDK*- and *vnfDGK*-deletion strains of *A. vinelandii*.[62] Nitrogenase genes can be expressed in the absence of NH_3 and repressed when it is present. It was observed that CO_2 reduction did not occur in either the *nifDK*- or *vnfDGK*-deletion strains in the presence of NH_3, but that CO_2 reduction did occur in the absence of NH_3.[62] It is still unclear what physiological implications this reaction has on the nitrogenase system, but the ability of Fe proteins to interconvert CO_2 and CO provides an additional direction of study for these proteins. Building off the premise that Fe proteins can interconvert CO_2 and CO, this section focuses on comparing the reactivity of other Fe protein homologs to carry out this reaction and determining how structural differences may result in the different activities observed.

Chapter 6 compares the effectiveness of *Ma*NifH to reduce CO_2 to that of *Av*NifH and *Av*VnfH. Herein is reported the ability of *Ma*NifH to reduce both CO_2 and CO to hydrocarbons under ambient conditions, a reaction not observed in the *A. vinelandii* Fe protein homologs. It is also observed that this reductive ability is inherent to $[Fe_4S_4]$ clusters by showing that a synthetic $[Fe_4S_4]$ compound can catalyze the same reaction in ambient conditions. Theoretical calculations suggest a potential reaction mechanism for this reduction that may provide a framework into generating FeS catalysts capable of converting CO_2 and CO into fuel.

Crystal structures of *Dv*NifH with the cluster in the $[Fe_4S_4]^{1+}$ state and *Ma*VnfH with the cluster in the $[Fe_4S_4]^{1+}$ and $[Fe_4S_4]^{0}$ states are reported in Chapter 7. Comparisons are made to the crystal structures and the observed ability of the various Fe protein homologs to reduce CO_2 and CO. It is observed that *Dv*NifH generates a product profile similar to that observed by *Ma*NifH, but at lower yields while *Ma*VnfH generates a product profile previously unobserved. A comparison between the Fe protein homolog structures provides insights into why these proteins may have different reactivities toward the same substrates, with cluster location and accessibility appearing to play a major role in the ability of Fe proteins to reduce substrates to form their products. It also appears that the redox potential of the cluster may also contributes to the ability to reduce substrate.

Chapter 6 Ambient Conversion of CO_2 to Hydrocarbons by Biogenic and Synthetic $[Fe_4S_4]$ clusters

6.1 Introduction

Iron sulfur (FeS) proteins are crucial for a wide variety of biological functions, such as electron transfer, enzyme catalysis, iron homeostasis, DNA synthesis and gene regulation.[3,181–184]. Designated the iron (Fe) protein, the reductase component of nitrogenase is a homodimeric protein containing a subunit-bridging [Fe_4S_4] cluster, and it serves as an obligate electron donor for its catalytic partner during catalysis.[52,185,186] Recently, the Fe protein of Azotobacter vinelandii, a soil bacterium, was shown to act as a reductase on its own and catalyze the ambient reduction of CO_2 to CO under in vitro or in vivo conditions via the redox change of its [Fe_4S_4] center; however, further reduction past CO was not detected in this case.[62] This observation has piqued our interest in further exploring the reactivity of the nitrogenase Fe protein toward CO_2 and addressing the question of whether the Fe protein can reduce CO_2 beyond CO into hydrocarbon products. The Fe protein homologs from methanogenic organisms are interesting subjects of study along this line of pursuit, given the high concentration of CO_2 in the habitat of these organisms and their metabolic adaptation to CO_2 reduction. Moreover, the relatively surface-exposed location of the [Fe_4S_4] cluster in the Fe protein points to the possibility that [Fe_4S_4] clusters that exist freely in solutions may have the same CO_2-reducing activity as their protein-bound counterpart.[52,185,186] Understanding the reactivity of the [Fe_4S_4] cluster toward CO_2 is important, as it enables identification of simple FeS clusters as catalysts that mimic the function of the industrial Fischer–Tropsch process in carbon fuel production under ambient conditions.[161]

Here we show that the Fe protein of Methanosarcina acetivorans is capable of ambient reduction of CO_2 and CO to hydrocarbons. We further demonstrate that this reactivity is inherent to [Fe_4S_4] clusters, as a synthetic [Fe_4S_4] compound can catalyze the same reaction in solutions.

Our theoretical calculations suggest a reaction mechanism involving an aldehyde-like intermediate, thereby providing a useful framework for mechanistic investigations of FeS-based CO_2 reduction and future development of strategies to recycle CO_2 into valuable chemical commodities.

6.2 Results and Discussion

6.2.1 Reduction of CO_2 and CO by Protein-bound $[Fe_4S_4]$ Clusters

To examine the reactivity of methanogen Fe proteins toward CO_2, we expressed the Fe protein of *M. acetivorans* in *Escherichia coli* and conducted comparative CO_2 reduction assays of this Fe protein with the Fe protein of *A. vinelandii*.[134] Like its *A. vinelandii* counterpart (designated *Av*NifH), the Fe protein of *M. acetivorans* (designated *Ma*NifH) was capable of reducing CO_2 to CO in the presence of a strong reductant, europium (II) diethylenetriaminepentaacetic acid (Eu^{II}–DTPA; $E^{0'} = -1.14$ V at pH 8.0).[82] In the case of *Av*NifH, the yield of CO increased when the concentration of Eu^{II}–DTPA was increased from 10 to 100 mM (Figure 6.1A). In the case of *Ma*NifH, however, while the formation of CO increased slightly upon an increase of the concentration of Eu^{II}–DTPA from 10 to 20 mM, it decreased concomitantly with an increase in the formation of C_1–C_3 hydrocarbons when Eu^{II}–DTPA concentration was increased beyond 20 mM, reaching a maximum hydrocarbon yield of 3.9 nmol reduced C per nmol cluster at 100 mM Eu^{II}–DTPA (Figure 6.1A). Gas chromatography–mass spectrometry (GC–MS) analysis further confirmed that these hydrocarbon products originated from CO_2, showing the characteristic fragmentation patterns and expected mass shifts of C_1 (CH_4), C_2 (C_2H_4, C_2H_6) and C_3 (C_3H_6, C_3H_8) products by + 1, + 2 and + 3, respectively, upon substitution of $^{13}CO_2$ for $^{12}CO_2$ (Figure 6.1B). Interestingly, despite an increase in the hydrocarbon/CO ratio with increasing concentrations of Eu^{II}–DTPA, the total carbon yield

calculated on the basis of both CO and hydrocarbons remained approximately the same (~5 nmol reduced C per nmol cluster) when ≥ 20 mM Eu^{II}–DTPA was supplied to the *Ma*NifH-catalyzed reaction (Figure 6.1A), suggesting a reductant-concentration-dependent re-distribution of electrons between CO and hydrocarbon formation in the *Ma*NifH-catalyzed reaction (Supplemental Figure 6.6). By contrast, hydrocarbon products could not be detected in the *Av*NifH-catalyzed reaction (Figure 6.1A), highlighting the difference between *Ma*NifH and *Av*NifH in their reactivities toward CO_2.

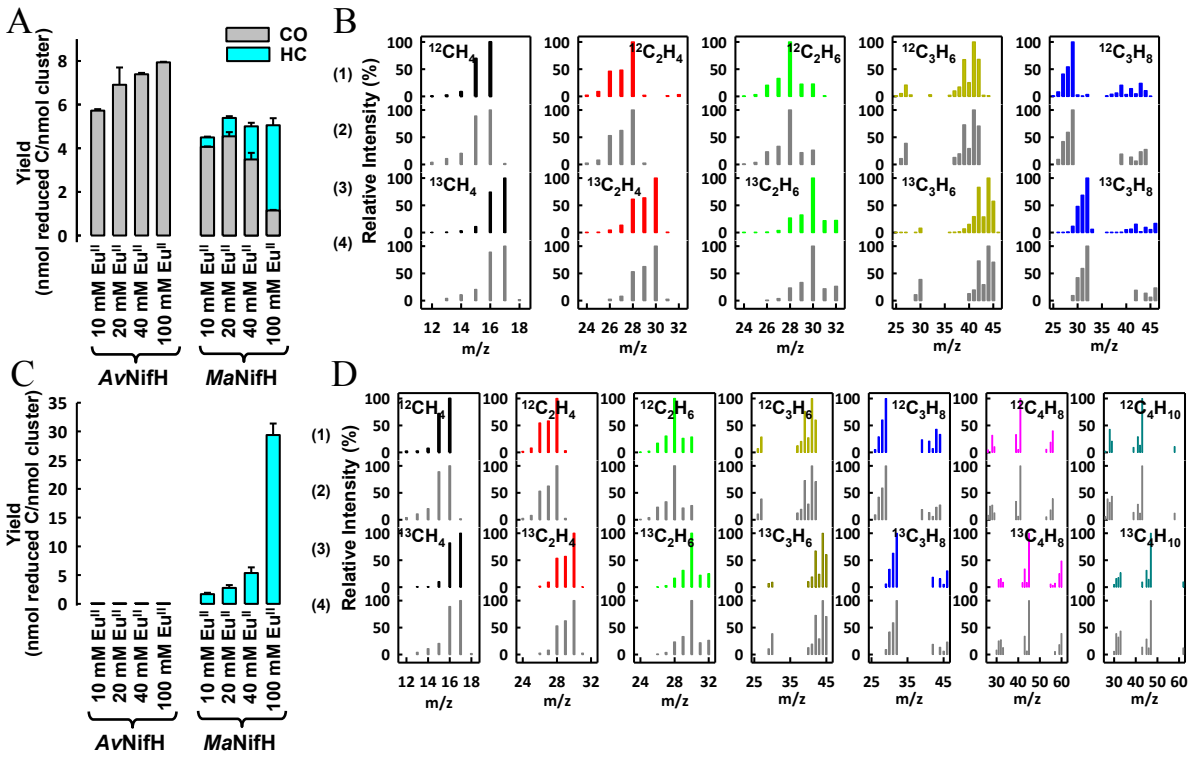

Figure 6.1 Reduction of CO_2 and CO by protein-bound [Fe_4S_4] clusters. (**A**, **C**) Yields of CO (gray) or hydrocarbons (cyan) generated from the reduction of CO_2 (**A**) or CO (**C**) by *Av*NifH or *Ma*NifH at increasing Eu^{II}-DTPA concentrations. Yields were calculated based on nmol reduced C in CO or hydrocarbons per nmol cluster. HC, hydrocarbons; Eu^{II}, Eu^{II}-DTPA (**B**, **D**) GC-MS analysis of the hydrocarbon products generated from the reduction of $^{12}CO_2$ (**B**, 1), $^{13}CO_2$ (**B**, 3), ^{12}CO (**D**, 1) or ^{13}CO (**D**, 3) by *Ma*NifH, shown in comparison with the fragmentation patterns of the corresponding ^{12}C (**B**, **D**, 2) or ^{13}C (**B**, **D**, 4) labeled hydrocarbon standards. Color code for GC-MS experimental data (1, 3): CH_4, black; C_2H_4, red; C_2H_6, green; C_3H_6, yellow; C_3H_8, blue; C_4H_8, pink; C_4H_{10}, dark green. The corresponding hydrocarbon standards (2, 4) are shown in gray.

The same discrepancy between *Ma*NifH and *Av*NifH was observed when CO was supplied as a substrate, as C_1–C_4 hydrocarbons were only detected in the reaction catalyzed by *Ma*NifH (Figure 6.1C). The reduction of CO to hydrocarbons by *Ma*NifH, like that of CO_2 to hydrocarbons, increased dramatically with increasing Eu^{II}–DTPA concentrations, reaching a maximum turnover number (TON) of 29.5 at 100 mM Eu^{II}–DTPA (Figure 6.1C). GC–MS analysis provided evidence that these hydrocarbons were derived from the substrate CO, showing the expected fragmentation patterns and mass shifts of the C_1 (CH_4), C_2 (C_2H_4, C_2H_6), C_3 (C_3H_6, C_3H_8) and C_4 (C_4H_8, C_4H_{10}) products when ^{12}CO was replaced by ^{13}CO (Figure 6.1D). Notably, the TONs of the reactions of CO-reduction were consistently higher than those of the reactions of CO_2-reduction at varying concentrations of Eu^{II}–DTPA, with the biggest difference between the two (by 7.5-fold) observed at 100 mM Eu^{II}–DTPA (Figure 6.2A, B). Moreover, there was a shift toward formation of longer hydrocarbon chains when CO-reduction was compared with CO_2-reduction, although both reactions showed a tendency toward formation of longer hydrocarbon products with increasing concentrations of Eu^{II}–DTPA (Figure 6.2A, B). Despite these differences, the reduction of CO and CO_2 by *Ma*NifH displayed similar hydrocarbon product distributions (Figure 6.2A, B), suggesting routing of the reduction of CO_2 via CO or CO-derived intermediates. It is plausible, therefore, that the differential reactivities of *Ma*NifH and *Av*NifH toward CO_2 originate from differential binding affinities of these proteins to the intermediate CO, with *Ma*NifH having a much stronger affinity for CO than *Av*NifH, which facilitates the reduction of CO and formation of C–C bonds by *Ma*NifH while permitting the release of CO as an end product by *Av*NifH. The observation that the product yield of *Ma*NifH saturated quickly (at ~0.5% CO) with increasing CO concentrations provided support for a high affinity of *Ma*NifH for CO (Supplemental Figure 6.7). Additionally, the ability of the

oxidized *Av*NifH to catalyze the conversion of CO to CO_2—a feature resembling the CO/CO_2 interconverting enzyme, carbon monoxide dehydrogenase—was not duplicated in the case of the oxidized *Ma*NifH (Supplemental Figure 6.8A), which could further contribute to the differential reactivities of these two Fe proteins toward CO and CO_2.[62,187–189] Such a difference likely reflected a difference in the redox potentials of *Ma*NifH and *Av*NifH, with the $[Fe_4S_4]^{1+/2+}$ couple of the former protein (E^0 = –395 mV) showing a significantly lower redox potential than that of the latter protein (E_0 = –301 mV) (Supplemental Figure 6.8B, C). Indeed, when driven by 200 mM dithionite ($E^{0'} \approx$ –430 mV at pH 7), *Ma*NifH was capable of reducing CO to hydrocarbons at low yields, with a product profile resembling that generated in the presence of Eu^{II}– DTPA; whereas no hydrocarbon could be detected in the reaction catalyzed by *Av*NifH under the same conditions (Supplemental Figure 6.9A, B).[190] Importantly, the fact that CO can be reduced by *Ma*NifH at a redox potential mimicking that in the cell suggests a potential physiological relevance of this reaction.

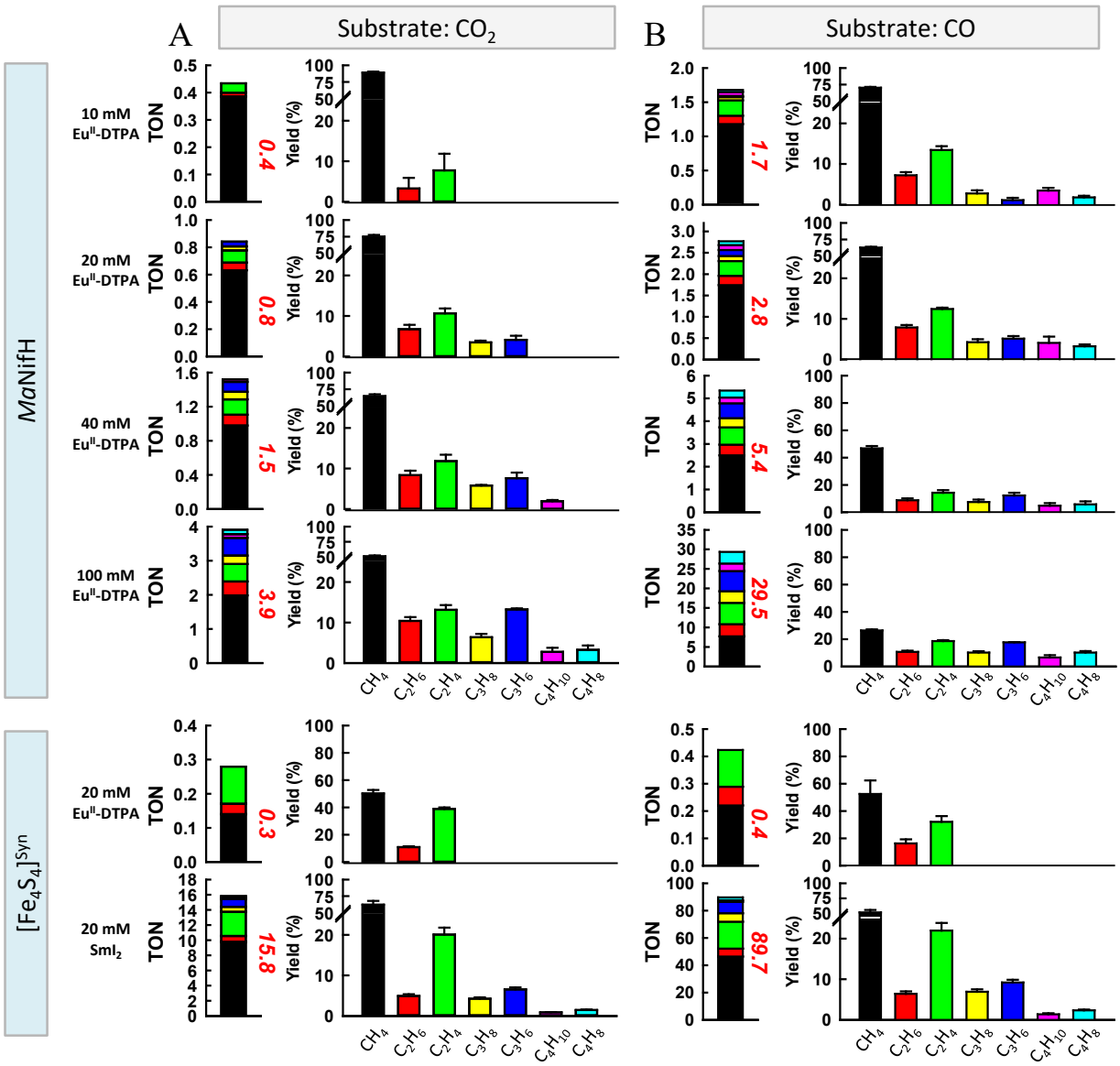

Figure 6.2 Formation of hydrocarbons in reactions of CO_2- and CO-reduction by protein-bound and synthetic $[Fe_4S_4]$ clusters. Turnover numbers (TONs) calculated based on all hydrocarbons (left charts) and percentage yields of individual hydrocarbon products (right charts) generated from the reduction of CO_2 (**A**) or CO (**B**) by *Ma*NifH at increasing Eu^{II}-DTPA concentrations, or by $[Fe_4S_4]^{Syn}$ in the presence of Eu^{II}-DTPA or SmI_2. TONs, or total nmol reduced C in all hydrocarbons per nmol cluster, are shown in red fonts next to the stacked bars (**A**, **B**, left charts).

6.2.2 Reduction of CO_2 and CO by Synthetic $[Fe_4S_4]$ Clusters

The observation of ambient conversion of CO_2 and CO to hydrocarbons by a protein-bound $[Fe_4S_4]$ cluster (Supplemental Figure 6.10A) has led to the question of whether the

reactivity toward these substrates is an inherent catalytic feature of the $[Fe_4S_4]$ clusters. To address this question, a synthetic $[PPh_4]_2[Fe_4S_4(SCH_2CH_2OH)_4]$ compound (designated $[Fe_4S_4]^{Syn}$) with a $[Fe_4S_4]$ core and four cysteine-like β-mercaptoethanol (BME) thiolate ligands (Supplemental Figure 6.10B) was tested for its ability to reduce CO_2 and CO.[191,192] Driven by 20 mM Eu^{II}–DTPA in an aqueous buffer, $[Fe_4S_4]^{Syn}$ was capable of generating up to C_2 hydrocarbon products (CH_4, C_2H_4, C_2H_6) hydrocarbons at TONs of 0.3 and 0.4, respectively, in the reactions of CO_2 and CO reduction (Figure 6.2A, B). Substitution of 20 mM samarium (II) iodide (SmI_2; $E^{0'} \approx -1.5$ V in DMF) along with a proton source, triethyl-ammonium tetrafluoroborate $[Et_3NH(BF_4)]$, in the organic solvent dimethylformamide (DMF) for Eu^{II}–DTPA in an aqueous buffer resulted in substantial increases of hydrocarbon formation to TONs of 15.8 and 89.7, respectively, in the $[Fe_4S_4]^{Syn}$-catalyzed reactions of CO_2 and CO reduction while pushing both reactions toward the formation of up to C_4 hydrocarbon products (CH_4, C_2H_4, C_2H_6, C_3H_6, C_3H_8, C_4H_8, C_4H_{10}) (Figure 6.2A, B).[193] Remarkably, the maximum TONs of $[Fe_4S_4]^{Syn}$ in the reactions of CO_2 and CO reduction were fourfold and threefold, respectively, of those of the biogenic $[Fe_4S_4]$ cluster in *Ma*NifH (Figure 6.2A, B), likely due to the improved accessibility of the reaction site in solutions of $[Fe_4S_4]^{Syn}$ clusters that increased the overall yields of hydrocarbons in the reactions of CO2 and CO reduction. Compared to the activity of hydrocarbon formation by $[Fe_4S_4]^{Syn}$, the CO_2- and CO-reducing activities of iron (III) chloride ($FeCl_3$) solutions containing equimolar Fe to that of the $[Fe_4S_4]^{Syn}$ cluster were only 7% and 4%, respectively, in the presence of sodium sulfide (Na_2S); and 2% and 2%, respectively, in the absence of Na_2S (Supplemental Figure 6.11A, B), providing strong, albeit indirect proof that the activity of $[Fe_4S_4]^{Syn}$ did not originate from small Fe/S fragments/constituents.

6.2.3 Proposed Reaction Pathway of CO_2 Reduction Catalyzed by the $[Fe_4S_4]$ Cluster

Based on our observations, density functional theory (DFT) calculations, which provided mechanistic insights into the reaction of CO reduction by vanadium nitrogenase, were performed on the $[Fe_4S_4]$ cluster, leading to the proposal of plausible mechanisms of $[Fe_4S_4]$-cluster-catalyzed CO_2/CO reduction (see 6.4.11; also see Supplemental Figure 6.12).[174] One mechanism involves protonation and dissociation of a thiolate ligand, which permits C–C coupling at the same Fe center of the cluster (Figure 6.3; also see Figure 6.13A and Figure 6.14A in the Supplemental Section). Binding of CO_2 to the cluster is only slightly exothermic (Figure 6.3A, step 1), which might contribute to the moderate turnover efficiency of this catalyst. Favorable coordination of CO_2 to one Fe atom of the free cluster, like that observed in the case of the protein-bound cluster, occurs when the cluster is present in the all-ferrous oxidation state with an $S = 0$ spin state (see 6.5.1.3).[62] Protonation of the coordinated CO_2 species, followed by proton-coupled electron transfer, then initiates cleavage of a water molecule and leaves the cluster in a CO-bound, $[Fe_4S_4]^+$ state (Figure 6.3A, steps 2 and 3). The reaction pathway becomes branched at this point. In one branch, the reaction continues with dissociation of CO (Figure 6.3A, step 4) and re-reduction of the cluster (Figure 6.3A, step 5). Dissociation of CO is energetically disfavored, as is the re-reduction of the cluster, which is consistent with the low CO_2-reducing activity of the cluster. In the other branch, the reaction proceeds with protonation-induced dissociation of the thiolate ligand at the Fe atom coordinated by CO (Figure 6.3B, step 6), followed by proton-coupled electron transfer to the Fe-coordinated CO moiety, forming an aldehyde-like, iron-formyl species (Figure 6.3B, step 7). Subsequently, this moiety could undergo an overall exothermic series of proton-coupled electron transfer steps (see Supplementary Fig. 9A), which, coupled with dissociation of a water molecule, eventually lead

to a reactive cluster-bound CH_3 group (Figure 6.3B, steps 8–11). Subsequent electron- and proton-transfer from a free thiol molecule readily yield CH_4 and restore the cluster to its fully thioethanolate-coordinated form (Figure 6.3B, step 12).

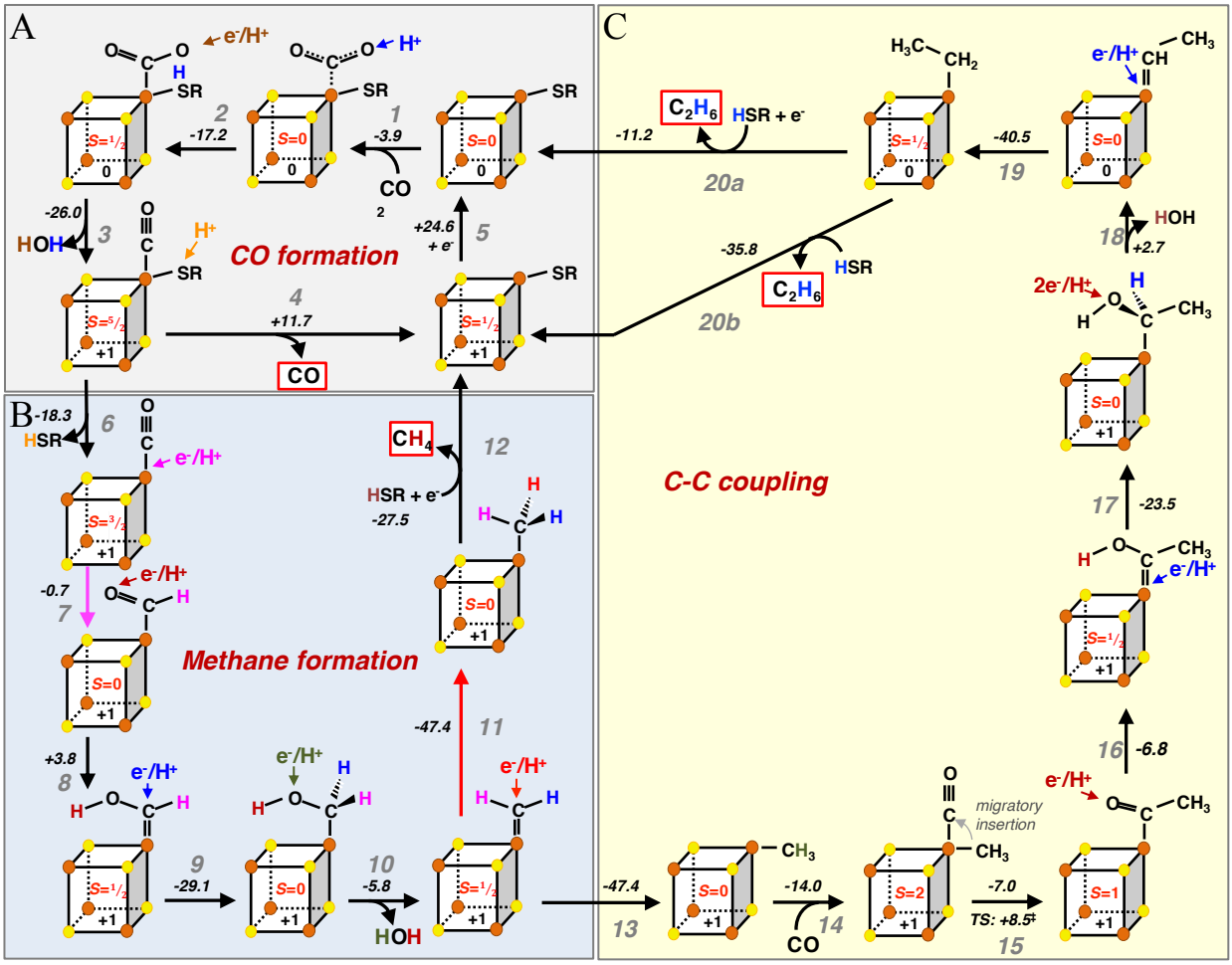

Figure 6.3 Proposed reaction pathway of CO_2 reduction catalyzed by the $[Fe_4S_4]$ cluster. Shown is the energetically plausible pathway derived from DFT calculations. Cluster ligand (-SR, $SC_2H_4OH^-$ or HSR, HSC_2H_4OH) is indicated as needed for the purpose of simplicity. The calculated reaction energy (kcal/mol) is indicated for each step (above or next to the arrow). (**A**) Coordination of CO_2 to a $[Fe_4S_4]^0$ cluster and release of CO upon reduction of CO_2. (**B**) Reduction of a $[Fe_4S_4]^+$-cluster-bound CO moiety to CH_4 via the formation of an aldehyde-like intermediate. (**C**) Formation of a C-C bond via migratory insertion that involves a $[Fe_4S_4]^+$-cluster-bound -CH_3 species and a second CO molecule coordinated to the same Fe atom. See Supplemental **Figure 6.13**A for the transition state and Supplemental **Figure 6.14**A for the energy landscape of the proposed mechanism.

Several mechanistic branching points are possible that involve coordination of a second CO molecule when a primary C_1 species is still bound to the cluster. One likely pathway for C–C bond formation involves coordination of CO at the CH_3-bound Fe site, which is exothermic by approx. –14 kcal mol^{-1} and allows for an exothermic migratory insertion, yielding an iron-acetyl intermediate (Figure 6.3C, steps 14, 15). A subsequent series of reduction and proton-transfer steps, which is overall highly exothermic (Supplemental Figure 6.14A), results in dissociation of a water molecule and formation of an Fe-bound ethyl moiety (Figure 6.3C, steps 16–19). Note that, for the dissociation of water to occur, the cluster has to be formally present in the all-ferrous $[Fe_4S_4]^0$ state (Figure 6.3C, step 18, transfer of two electrons). Subsequent exothermic proton-coupled electron transfer readily yields a cluster-bound ethyl species. Analogous to the formation of the C_1 species, 'recombination' of the cluster with a thiol molecule results in the formation of C_2H_6 (Figure 6.3C, step 19) and restores the cluster to the $[Fe_4S_4]^0$ or $[Fe_4S_4]^+$ state, depending on whether an additional electron is simultaneously transferred (Figure 6.3C, steps 20a, 20b). It seems energetically plausible for the cluster to employ a similar mechanism for the formation of longer carbon chains: CO could coordinate to an ethyl-bound Fe atom with a reaction energy of approx. –12 kcal mol^{-1}, followed by another round of migratory insertion, which would be exothermic by approx. –9 kcal mol^{-1}. Due to multiple competing reaction branches, however, the probability for this chain elongation event to occur would be substantially lower than that for the C_2 mechanism (for example, dissociation of the carbon species), which is in line with the experimentally observed bias toward short-chain product formation (see Figure 6.2).

Other than the mechanism proposed above, which involves removal of the thiolate ligand (Figure 6.3A, step 6) for the subsequent C–C coupling via migratory insertion at a single Fe site (Figure 6.3C, step 14), an alternative mechanism is conceivable for the fully ligated cluster,

which allows the pathway to proceed through coordination events at two neighboring Fe centers (Figure 6.4; also see Figure 6.13B and Figure 6.14B in the Supplemental Section). The two mechanisms share the same pathway for CO reduction (Figure 6.3A and Figure 6.4A, steps 1–5) and analogous pathways for CH_4 formation except for variations of energetics in the presence of the thiolate ligand (Figure 6.3B, steps 6–12; Figure 6.4B, steps 6–11). In the latter mechanism, however, the second CO molecule can be reduced to a CH_2 species by a sequence of proton/electron transfer steps (Figure 6.4C, steps 14–17), strongly resembling the reduction of the first CO molecule. The resulting, highly reactive CH_2 moiety can then be combined with the CH_3 moiety at the proximal Fe atom to form an Fe-bound ethyl species with an energy barrier of only approx. 7 kcal mol^{-1} (Figure 6.4C, step 18). Exothermic proton or coupled proton/electron transfer and ethane formation close the cycle (Figure 6.4C, steps 19a,b). Coordination of a second CO molecule to the ethyl-bound cluster is energetically feasible and could explain the formation of longer carbon chains following the same sequence of events that lead to the formation of the C2 species (Figure 6.4C, steps 13–18), although the chain extension process would occur at a significantly reduced efficiency due to the multitude of competing reactions.

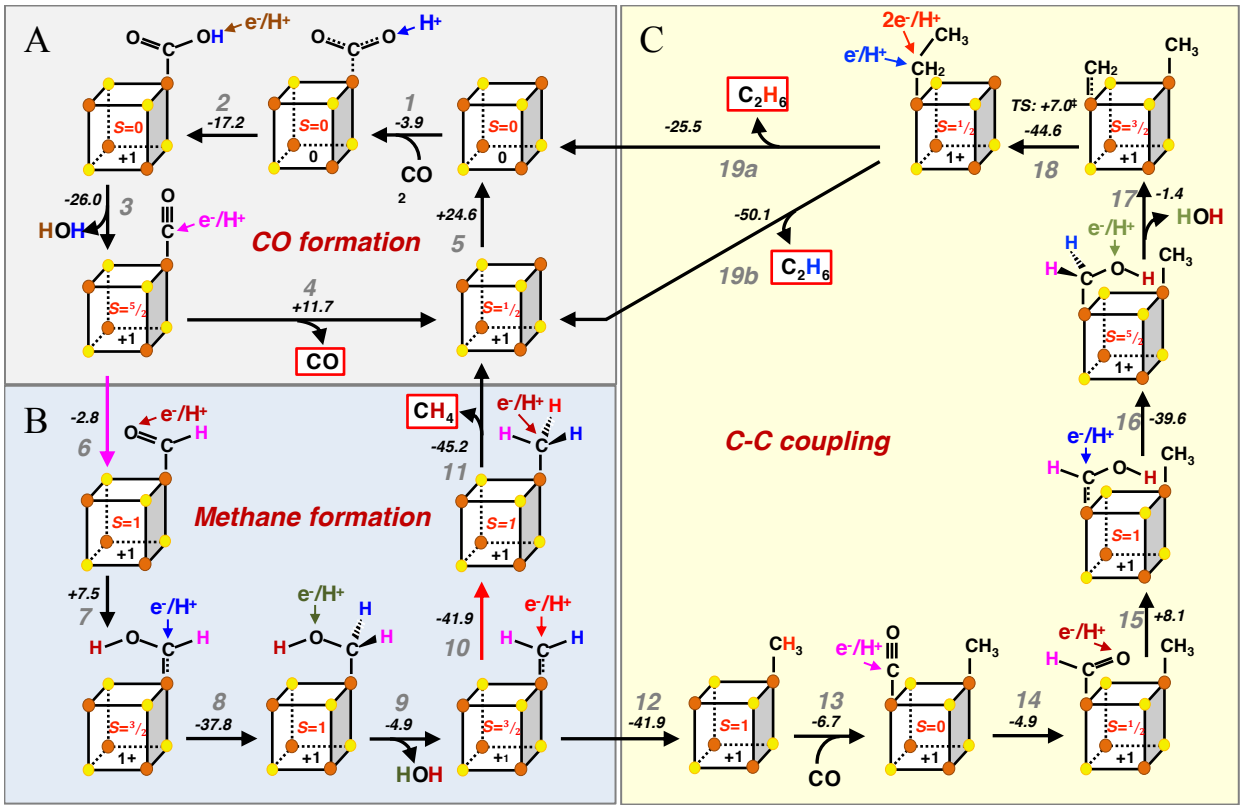

Figure 6.4 Alternative reaction pathway of CO_2 reduction catalyzed by the $[Fe_4S_4]$ cluster. Shown is the energetically plausible pathway derived from DFT calculations. The calculated reaction energy (kcal/mol) is indicated for each step (above or next to the arrow). Unlike the mechanism proposed in **Figure 6.3**, this pathway doesn't involve dissociation of a thiolate ligand and proceeds by coordination events at two neighboring Fe centers. Note that the thiolate groups are not depicted in the figure for the purpose of simplicity. (**A**) Coordination of CO_2 to a $[Fe_4S_4]^0$ cluster and release of CO upon reduction of CO_2. (**B**) Reduction of a $[Fe_4S_4]^+$-cluster-bound CO moiety to CH_4 via the formation of an aldehyde-like intermediate. (**C**) Formation of a C-C bond via coupling between a $[Fe_4S_4]^+$-cluster-bound $-CH_3$ species with a reactive, bridged Fe-CH_2 intermediate that is derived from the second bound CO. See Supplementary Information for the transition state (Supplemental **Figure 6.13**B) and energy landscape (Supplemental **Figure 6.14**B) of the proposed mechanism.

Based on these calculations, a constantly high supply of electrons would steer the reactivity of the cluster from CO dissociation (Figure 6.3A, and Figure 6.4A, steps 4,5) towards CO reduction (Figure 6.3B, steps 6–12; Figure 6.4B, steps 6–11), which is corroborated by the experimentally observed increase of the hydrocarbon/CO ratio in response to increasing amounts of the reductant (Figure 6.1A). Moreover, consistent with the calculation-based proposal of an aldehyde-like intermediate, $[Fe_4S_4]^{Syn}$ was shown to reduce formaldehyde (CH_2O) at a yield of

16 nmol CH_4 per nmol cluster (Figure 6.5A), and GC–MS analysis further demonstrated the expected mass shift and fragmentation pattern of the product CH_4 upon substitution of $^{13}CH_2O$ for $^{12}CH_2O$, thereby confirming that the carbon in CH_4 originated from CH_2O (Figure 6.5B–E). Of the CO reduction events, however, C–C coupling has to compete with protonation of the CH_3 moiety, which can occur for every intermediate and which would consequently generate intermediates for CH_4 formation (Figure 6.3B, Figure 6.4B), thereby further increasing the yield of CH_4.

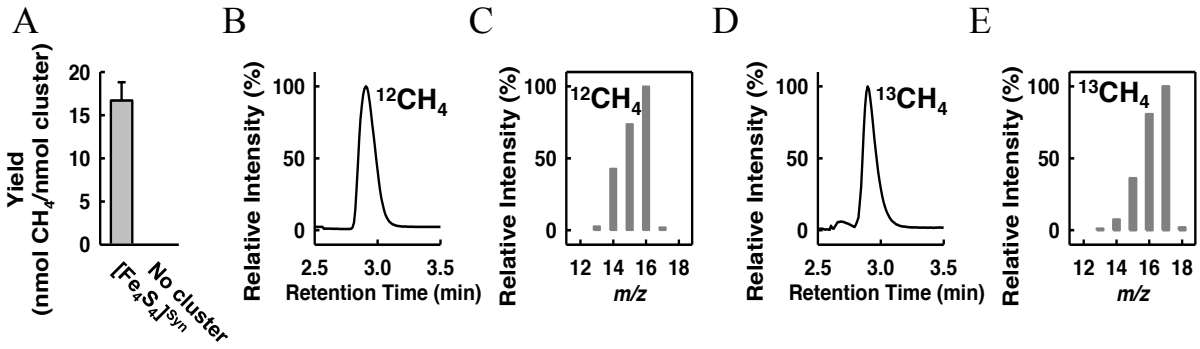

Figure 6.5 Reduction of CH_2O to CH_4 by synthetic $[Fe_4S_4]$ cluster. Turnover number (TON) calculated based on CH_4 generated from the reduction of CH_2O (**A**), and GC-MS traces (**B**, **D**) and fragmentation patterns (**C**, **E**) of $^{12}CH_4$ and $^{13}CH_4$, respectively, generated from the reduction of $^{12}CH_2O$ (**B**, **C**) and $^{13}CH_2O$ (**D**, **E**).

6.3 Summary and Conclusion

The ability of $[Fe_4S_4]$ clusters to catalyze the ambient reduction of CO_2 and CO to hydrocarbons could have implications for the prebiotic evolution of organic molecules, as previous studies have suggested a role of Fe- or FeS-containing minerals around undersea hypothermal vents in forming hydrocarbons and other organic molecules in the presence of CO_2.[194–197] It has been demonstrated that CO can react with CH_3SH on coprecipitated FeS and NiS to form carboxylic acids, carbohydrates and amino acids, suggesting a prebiotic CO fixation pathway that could be correlated to the emergence of primordial lipids, sugars and

peptides/proteins on Earth (see Section 6.7 for further discussion).[198–201] By analogy, the reduction of CO by FeS clusters in a speculated, highly reducing early atmosphere might represent another prebiotic route of CO activation, which generates small alkenes and alkanes as carbon and/or electron sources for certain methane- and ethene-assimilating organisms.[202,203] It is plausible, therefore, that the activity of *Ma*NifH in reducing CO_2 to hydrocarbons may represent an evolutionary relic of the function of FeS proteins in methanogens. Given the CO_2-rich habitats of many methanogenic organisms, the differential abilities of the methanogenic and non-methanogenic organisms to handle CO_2 may account for the differential reactivities of the [Fe4S4] clusters in *Av*NifH and *Ma*NifH toward CO_2. Although the impact of protein environments on the reactivities of these biogenic [Fe_4S_4] clusters awaits further investigation, the reaction pathway proposed for the [Fe_4S_4] cluster serves as a good starting point for further exploration of the mechanism of FeS-based ambient reduction of CO_2, which will in turn facilitate future development of FeS catalysts that convert the greenhouse gas CO_2 into useful fuel products.

6.4 Materials and Methods

6.4.1 Experimental Section

Unless otherwise specified, all chemicals were purchased from Thermo-Fisher Scientific and Sigma-Aldrich. Natural abundance ^{12}CO (99.9% purity) and $^{12}CO_2$ (99.98% purity) were purchased from Praxair. Isotopologs ^{13}CO (99% isotopic purity) and $^{13}CO_2$ (99% isotopic purity) were purchased from Cambridge Isotope Laboratories. An Fe/S/Mo/V standard solution for metal content determination was purchased from Inorganic Ventures. Air-free manipulations were performed in a Vacuum Atmospheres Omni-lab glovebox with an argon atmosphere operating at < 2 ppm O_2. Water was purified using a Barnstead E-Pure water purification system

(Thermo Scientific). Organic solvents were dried over columns containing Q-5 and molecular sieves and sparged with Ar; the solvents were stored over molecular sieves in the glovebox. Triethylammonium tetrafluoroborate ($[Et_3NH(BF_4)]$), samarium (II) diiodide tetrahydrofuran adduct ($[SmI_2(THF)_2]$), and the $[Fe_4S_4]^{Syn}$ cluster ($[Ph_4P]_2[Fe_4S_4(SCH_2CH_2OH)_4]$) were prepared as described earlier.[192,204,205]

6.4.2 Cell Growth and Protein Purification

An *Azotobacter vinelandii* strain expressing a non-tagged, *nifH*-encoded Fe protein of the Mo-nitrogenase (designated *Av*NifH) was grown as described elsewhere.[15,22] An *E. coli* strain expressing a His-tagged, *nifH*-encoded Fe protein of the Mo-nitrogenase of *Methanosarcina acetivorans* (designated *Ma*NifH) was grown as reported earlier.[134] Published methods were used for the purification of *Av*NifH and *Ma*NifH from their respective expression strains.[15,22,134]

6.4.3 Redox Potential Determination

Redox titration was performed at ambient temperature in a glove box under anaerobic conditions. A series of *Ma*NifH samples were prepared in a 20 mM Tris-HCl buffer (pH 8.0) at a protein concentration of 2.5 mg mL^{-1}. Redox mediator dyes, including methyl viologen, benzyl viologen, safranin O and phenosafranin, were added at a final concentration of 10 μM to the series of *Ma*NifH protein samples. Subsequently, these samples were first reduced by excess sodium dithionite (DT; $Na_2S_2O_4$) and then subjected to oxidative titration with 1 mM potassium ferricyanide. Reduction potentials were monitored with a combination electrode comprising a platinum working electrode and a saturated Ag/AgCl reference electrode (Microelectrodes), which were used to report potentials relative to the standard hydrogen potential (SHE). After achieving the desired potential, a 200 μL aliquot of each mixture was transferred to a capped

quartz cuvette, and the transition between the $[Fe_4S_4]^{1+/2+}$ couple was monitored at 420 nm by UV/vis spectroscopy.

6.4.4 Assays of CO- and CO_2-reduction with Fe Proteins

The *in vitro* CO and CO_2 reduction assays were carried out in 9.4 mL assay vials with crimped butyl rubber serum stoppers. Each assay contained, in a total volume of 1.0 mL, 500 mM Tris-HCl (pH 10.0, for CO_2 reduction assays) or 250 mM Tris-HCl (pH 8.0, for CO reduction assays), 0.5 mg Fe protein (*Av*NifH or *Ma*NifH), and either 200 mM dithionite or increasing concentrations (10, 20, 40 or 100 mM) of europium (II) diethylenetriaminepentaacetate (Eu^{II}-DTPA). The optimum concentration of CO (0.53%) or CO_2 (100%) that yielded the maximum amount of product was determined via titration against increasing concentrations of CO or CO_2 added to the headspace of the respective assay for activity analysis. For reactions of CO reduction, assays were assembled by repeatedly flushing and exchanging the buffer solution (without Eu^{II}-DTPA and protein) with 100% Ar, followed by the addition of 0.53% CO; whereas for reactions of CO_2 reduction, assays were assembled by repeatedly flushing and exchanging the buffer solution (without Eu^{II}-DTPA and protein) with 100% CO_2, and equilibrating for 30 min until pH stabilized at approximately 8.1. The reaction was initiated by the addition of Fe protein, followed immediately by the addition of Eu^{II}-DTPA and incubation with continuous shaking at 30 °C until the reaction was complete (300 min) before it was quenched by the addition of 100 μL of 30% trichloroacetic acid. Subsequently, headspace samples were taken to examine the production of CO and hydrocarbons (see 6.4.8 and 6.4.9 below).

6.4.5 Assays of CO Oxidation with Fe Proteins

The *in vitro* CO oxidation assays were carried out under 100% CO in 9.4 mL assay vials with crimped butyl rubber serum stoppers. Each assay contained, in a total volume of 1.0 mL, 250 mM Tris-HCl (pH 8.0), 10 mg *Av*NifH or *Ma*NifH, and 20 mM IDS. All assays were assembled by repeatedly flushing and exchanging the buffer solution (without IDS and protein) first with 100% Ar and then with 100% CO, followed by equilibration for 30 min. The reaction was initiated by the addition of Fe protein, followed immediately by the addition of IDS and incubation with continuous shaking at 30 °C until the reaction was complete (300 min). Subsequently, 100 μL concentrated hydrochloric acid (HCl) was added to each assay to release the dissolved CO_2 before the headspace sample was examined for the production of CO_2 (see 6.4.8 below).

6.4.6 Assays of CO- and CO_2-reduction with $[Fe_4S_4]^{Syn}$ Clusters and SmI_2

The $SmI_2(THF)_2$ stock solution was prepared by dissolving solid $SmI_2(THF)_2$ in dry THF. The reaction buffer was prepared by dissolving $Et_3NH(BF_4)$ in dry dimethylformamide (DMF), followed by addition of 1.5% (v/v) triethylamine (Et_3N). A stock solution of the $[Fe_4S_4]^{Syn}$ cluster ($[Ph_4P]_2[Fe_4S_4(SCH_2CH_2OH)_4]$) was prepared by dissolving crystals of the cluster in dry DMF. Assays were performed in 9.4 mL assay vials with crimped butyl rubber serum stoppers. Each assay contained, in a total volume of 1 mL, 100 mM $Et_3NH(BF_4)$, 2 μM $[Fe_4S_4]^{Syn}$, and 20 mM $SmI_2(THF_2)$. In addition, the headspace of each assay contained 100% CO or CO_2, which was determined as the optimum concentration that yielded the maximum amount of products via titration against increasing concentrations of CO or CO_2. The negative controls had the same composition as the assays, except for the omission of either the cluster or the substrate. The reaction was initiated with the addition of $[Fe_4S_4]^{Syn}$, followed immediately by

injection of SmI_2 via a syringe. All assays and controls were incubated in a 30 °C water bath shaker until the reaction was complete (10 min) before the headspace samples were taken and examined for hydrocarbon formation (see Section 6.4.9 below). The CO-reduction controls with $FeCl_3$ and $FeCl_3/Na_2S$ lacked $[Fe_4S_4]^{Syn}$ but, instead, contained $FeCl_3$ with equimolar Fe to that of $[Fe_4S_4]^{Syn}$, either in the absence or presence of Na_2S at a 1:1 molar ratio to $FeCl_3$. The reaction was initiated with the addition of $FeCl_3$ or $FeCl_3/Na_2S$, followed immediately by injection of SmI_2 via a syringe and incubation in a 30 °C water bath shaker until the reaction was complete (10 min), when the headspace samples were taken and examined for hydrocarbon formation (see Section 6.4.9 below).

6.4.7 Assays of CO- and CO_2-reduction with $[Fe_4S_4]^{Syn}$ and Eu^{II}-DTPA

The Eu^{II}-DTPA stock solution was prepared by dissolving equimolar amounts of europium (II) chloride ($EuCl_2$) and diethylenetriaminepentaacetic acid (H_5DTPA) to a final concentration of 200 mM in 1M Tris-HCl (pH 8.0) buffer. Assays were performed in 9.4 mL assay vials with crimped butyl rubber serum stoppers. Each assay for CO_2 reduction contained, in a total volume of 1 mL, 500 mM Tris-HCl (pH 9.8), 20 mM Eu^{II}-DTPA, and 5 µM $[Fe_4S_4]^{Syn}$, with 100% CO2 in the headspace. This solution was allowed to sparge under CO_2 for 30 min until it reached saturation, when the pH of the solution stabilized at 7.8. Each reaction for CO reduction contained, in a total volume of 1 mL, 50 mM Tris-HCl (pH 7.8), 20 mM Eu^{II}-DTPA, and 5 µM $[Fe_4S_4]^{Syn}$, with 100% CO in the headspace atmosphere. The negative controls had the same composition as the assays, except for the omission of either the cluster or the substrate. The reaction was initiated by the addition of $[Fe_4S_4]^{Syn}$, followed immediately by injection of Eu^{II}-DTPA via a syringe. All assays and controls were incubated in a 30 °C water bath shaker until

the reaction was complete (60 min), when the headspace samples were taken and examined for hydrocarbon formation (see Section 6.4.9 below).

6.4.8 Quantification of CO and CO_2

The amount of CO or CO_2 generated in the in vitro assays was determined through headspace analysis using a Thermo Scientific Trace 1300 Gas Chromatography with flame-ionization detector (GC–FID), in which the detector was interfaced with a methanizer (Thermo Electron). CO or CO_2 in the headspace sample was separated on a TG-BOND Msieve 5A column (30 m × 0.32 mm ID × 30 μm film; Thermo Electron), which was held at 45 °C for 1 min before it was heated to 110 °C at a rate of 25 °C per min. Subsequently, CO or CO_2 was hydrogenated at 350 °C by the methanizer, and the resulting CH_4 was measured by GC–FID. The amount of CO or CO_2 was determined based on a linear standard curve ($R^2 \geq 99.5$) that was derived from the measurement of varying amounts of CO or CO_2 using the same instrument. The detection limit for CO or CO_2 was 2 ppm.

6.4.9 Quantification of Hydrocarbons

The hydrocarbon products CH_4, C_2H_4, C_2H_6, C_3H_6, C_3H_8, 1-C_4H_8, n-C_4H_{10}, 1-C_5H_{10} and n-C_5H_{12} were measured on an activated alumina column (Grace) in an SRI 8610C GC (SRI Instruments) equipped with a flame ionization detector (FID). From each headspace sample, a total of 250 μL gas was injected into the GC. The heating program for separating the gaseous products in the Eu^{II}-DTPA-driven, aqueous assays was as follows: held at 55 °C for 1 min; heated to 180 °C at a rate of 12.5 °C/min; and then held at 180 °C for 0.6 min. The heating program for separating the gaseous products in the SmI_2-driven, DMF-based assays was as follows: held at 55 °C for 1 min; heated to 200 °C at 12.5 °C/min; and then held at 200 °C for 3.6

min. The quantities of all products were determined as described previously using a purchased gas mixture containing ~15 ppm of each hydrocarbon compound (Praxair).[133,160]

6.4.10 Gas Chromatography–mass spectrometry (GC–MS) Analysis

Isotopic CO- and CO_2-reduction assays were prepared in the presence of $^{12}CO/^{13}CO$ and $^{12}CO_2/^{13}CO_2$, respectively, for GC–MS analysis as outlined above (see Section 6.4.4). The reaction products were then analyzed by GC-MS using a Thermo Scientific Trace 1300 GC system coupled to a Thermo ISQ QD (Thermo Electron North America LLC) by comparing its mass and retention time with those of the ^{12}CO or ^{13}CO standard (≥99.9% purity), C_1-C_5 alkane hydrocarbon standard (containing 15 ppm of each gas), or a C_1-C_5 alkene hydrocarbon standard (containing 15 ppm of each gas). For each sample or standard, a total of 250 μL gas was injected into a split/splitless injector operated at 150 °C in split mode with a split ratio of 10. Gas separation was achieved on a HP-PLOT/Q+PT column (30 m × 0.32 mm ID × 20 μm film; Agilent Technologies), which was held at 30 °C for 3 min, heated to 200 °C at a rate of 15 °C/min, and held at 200 °C for 5 min. The rate at which the carrier gas, helium (He) passed through the column was held at 0.7 mL/min for 4 min, increased to 1.4 mL/min at a rate of 0.5 mL/min, and held at 1.4 mL/min for the duration of the run. The mass spectrometer was operated in electron impact (EI) ionization mode. The fragmentation patterns of the products were compared to standards and are consistent with those deposited in the NIST database (http://webbook.nist.gov).

6.4.11 Density Functional Theory Calculations

Density functional theory (DFT) calculations of the mechanism of CO_2 reduction were carried out with the DFT programs in the Turbomole package, version 7.0. Atomistic models of $[Fe_4S_4](SCH_2CH_2OH)_4$ ($[Fe_4S_4]^{Syn}$) (see Lewis model in Supplemental Figure 6.12A) and its

carbon species-bound intermediates were built with Molden and all atoms were allowed to relax fully during structure optimizations.[206] Solvent effects were calculated implicitly by the conductor-like solvent screening model COSMO as implemented in Turbomole, with a dielectric constant of ε = 37 and a solvent radius of 2.65 Å to represent the solvent DMF.[207] The models were treated as open-shell systems in the unrestricted Kohn-Sham framework. Structural optimizations were performed with the TPSS functional and a def2-TZVP basis set assigned to all model atoms.[208–210] Computational time was reduced by utilizing the resolution-of-the-identity approximation.[211,212] Antiferromagnetic coupling in the FeS cluster was accounted for by the broken symmetry approach.[213–215] All intermediates were optimized for at least three different spin states (S = 1/2, 3/2, 5/2 for systems with an odd number of electrons, and S = 0, 1, (2), 4 for those with an even number) in order to obtain low-energy solutions. All protonation energies were obtained by considering the optimized cluster structure (TPSS, def2-TZVP, COSMO ε=37) and explicitly calculating the deprotonation energy of Et_3NH^+—the proton donor used in the DMF-based, cluster-catalyzed reactions—in DMF (see Supplemental Figure 6.12B). The energies of all coordinating and dissociating species, including $HSCH_2CH_2OH$ (Figure 6.3, step 6), were calculated with the same settings. The energy of $HSCH_2CH_2OH$ was also used to calculate the energy for re-ligating the cluster, where $HSCH_2CH_2OH$ simultaneously acted as a proton donor (Figure 6.3, steps 20a, 20b). Reduction energies were first calculated by assuming transfer of a free electron with zero kinetic energy. In order to obtain approximate redox free energies that better describe the energetics of the system, the resulting energies were then corrected with the reported experimental electrode potential of SmI_2, $E^{0'}$ = –1.5 V vs. SHE, following a previously described procedure.[216,217] This value was adapted to the DMF solvent with a previously reported value for the relative electrode potential, ΔE (SHE) = –4.34 V.[218] The

initially obtained reduction energies were transformed into redox free energies by adding the redox free energy of the reductant half reaction: $\Delta G^0 = - n F (E^{0'} - \Delta E (SHE))$ (n, the number of electrons; F, Faraday constant).[216,217] For SmI_2, this value is -65.5 kcal mol^{-1}.

6.5 Supplemental Results

6.5.1 DFT Calculations

6.5.1.1 Transition States for the Steps of C-C Bond Formation

For the rate-determining steps of the mechanisms depicted in Figure 6.3 and Figure 6.4, possible transition states were identified by optimizing distance-constrained structures along the expected reaction coordinates (C-C bond formation), followed by calculating the Hessian using the NumForce script provided with the Turbomole package and visualizing the normal modes with Jmol. Promising guess structures were then optimized with the statpt script provided with Turbomole, employing an eigenvector-following approach. Both transition states reported herein (Supplemental Figure 6.13) show exactly one imaginary frequency, and the associated normal modes are consistent with the expected reaction coordinates. The transition states were further verified by calculating the reaction paths leading to the formation of product and reactant.

6.5.1.2 Other Considered Reaction Pathways Involving Protonation of the Cluster Sulfur Atoms

Protonation of the sulfur atoms of the all-ferrous $[Fe_4S_4]$ cluster is exothermic by -14.3 kcal/mol. However, this protonation event disrupts and opens up the compact cubane structure by weakening the bond between the newly formed SH group and the proximal Fe atom (Supplemental Figure 6.15), which provides an avenue for cluster destruction and contradicts our experimental findings of sustained catalytic turnover. Moreover, the x-ray crystallographic structure of the all-ferrous Fe protein further argues against disruption of its $[Fe_4S_4]$ cluster, as

the cluster remains intact in the all-ferrous state.[55] Nevertheless, we considered possible mechanistic routes starting from this unlikely cluster geometry for the sake of completeness (Supplemental Figure 6.16).

Coordination of CO_2 to the protonated cluster is highly endothermic by +54.9 kcal/mol, (highlighted as a red box in Supplemental Figure 6.16, step 2), and the subsequent reduction of its unlikely reaction product is exothermic by -37.0 kcal/mol (Supplemental Figure 6.16, step 3). Taken together, these two initial steps of this reaction route would still be endothermic. However, we still considered plausible reaction events that occur subsequent to these initial steps. As can be seen from the scheme in Supplemental Figure 6.16, reaction steps analogous to those proposed in Figure 6.3 and Figure 6.4 could in principle occur, which involve protonation of the CO_2 moiety, dissociation of an H_2O molecule, and consecutive e^-/H^+ transfers, yielding an Fe-bound CH_3-species upon dissociation of an additional H_2O molecule (Supplemental Figure 6.16, step 11). In analogy to the mechanisms presented in Figure 6.3 and Figure 6.4, further electron/proton transfer steps result in exothermic methane formation (Supplemental Figure 6.16, step 12). In two alternative scenarios, a second CO molecule can either coordinate to the Fe atom that is already bound with a CH_3 species (exothermic by -18.6 kcal/mol, Supplemental Figure 6.16, step 14), thereby resembling the mechanism proposed in Figure 6.3, or to the neighboring Fe atom (exothermic by -4.3 kcal/mol, Supplemental Figure 6.16, step 15), which corresponds to the scheme presented in Figure 6.4. The first route, however, results in a dead-end; specifically, the migratory insertion step depicted in Figure 6.3 cannot occur in the case of the open cluster, as structural optimization of an activated complex leads to the re-formation of the end product of step 14. The second alternative, on the other hand, proceeds analogously to the mechanism depicted in Figure 6.4, thereby corroborating the originally considered reaction steps.

In addition to the mechanism discussed in Supplemental Figure 6.16, we considered the energetics of proton and coupled electron/proton transfer steps to various intermediates of the main mechanisms presented in Figure 6.3 and Figure 6.4. The results are shown in Supplemental Figure 6.17, which again indicate substantial cluster distortion and unfavorable energetics caused by protonation of the cluster sulfur atoms.

Taken together, given the initial strong endothermic coordination of CO_2 and structural destabilization of the cluster upon sulfur protonation, we strongly favor the mechanisms presented in Figure 6.3 and Figure 6.4 to those involving the protonation of cluster sulfur atoms.

6.5.1.3 Coordination of CO_2 to the Cluster

As reported previously for the coordination of CO_2 to the $[Fe_4S_4]$ cluster of the *A. vinelandii* Fe protein, we only observed exothermic binding when CO_2 was directly coordinated to one of the Fe atoms of the all-ferrous $[Fe_4S_4]^0$ cluster in a singlet spin state (S = 0).[62] Alternative scenarios for different charge and spin states, or alternative binding sites, such as ligand and cluster S atoms, or sites exposed by opening of the cluster, resulted in strongly endothermic reaction energies. Previous EPR spectroscopic data suggest that the cluster can indeed adopt an S = 0 spin state.[80] With the DFT approach described herein, the S = 0 state of the ligand-free cluster is slightly less stable than the S = 4 state (by ≈4-5 kcal/mol). At ambient temperatures, the cluster might be represented best by a mixture of spin states. For all other forms that can be formally considered as existing in the all-ferrous state, the low-spin solution is more stable than the S = 4 state [i.e., -2 to -3 kcal/mol for the CO_2-bound form (see Figure 6.3 and Figure 6.4), -5 to -6 kcal/mol for the CO_2H-bound form (see Figure 6.3 and Figure 6.4), and ~ -10 kcal/mol for the $CHCH_3$-bound cluster (see Figure 6.4, where the most favorable spin state is S=1)].

6.6 Supplemental Tables and Figures

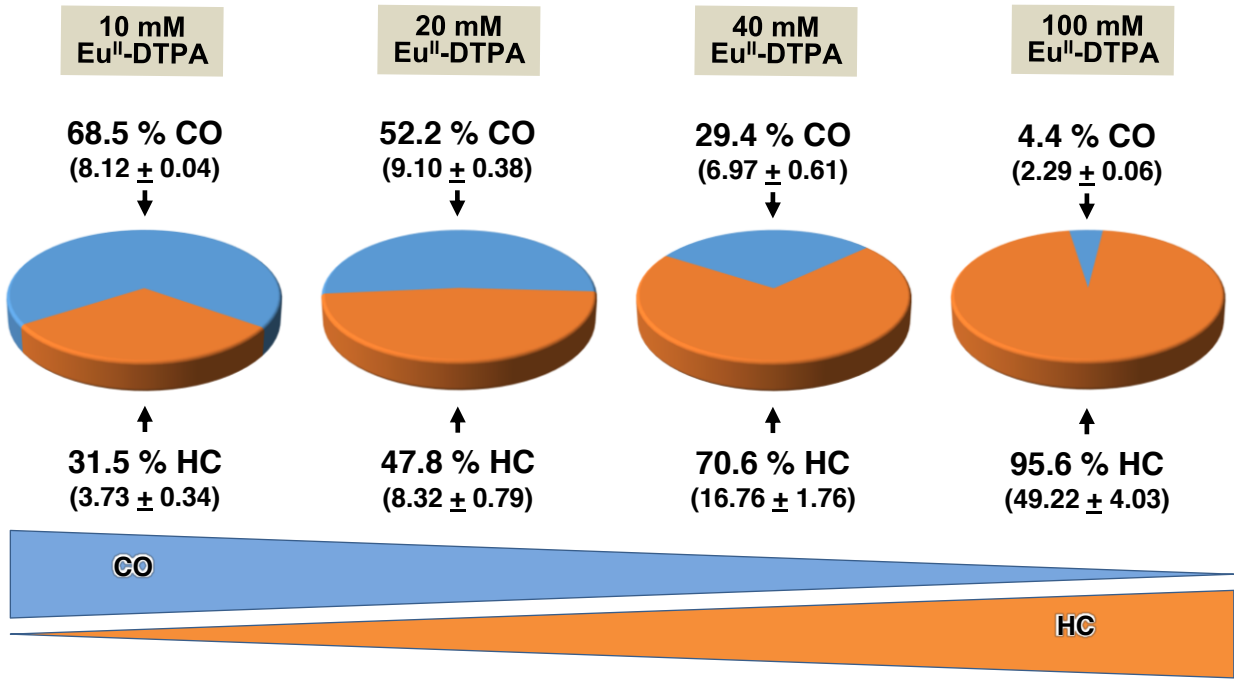

Figure 6.6 Product distribution of CO_2 reduction in the presence of increasing amounts of reductant. Data are taken from **Figure 6.1**A. The activity of CO or hydrocarbon (HC) formation from the reduction of CO_2 by *Ma*NifH is expressed as nmol electrons that appear in CO or HC per nmol cluster and shown in parentheses. The percentage distributions of electrons in CO and HC were calculated based on these numbers. The total amount of electrons that appear in products (both CO and HC) increases concomitantly with a shift toward HC formation when CO_2 is reduced by *Ma*NifH in the presence of increasing Eu^{II}-DTPA concentrations.

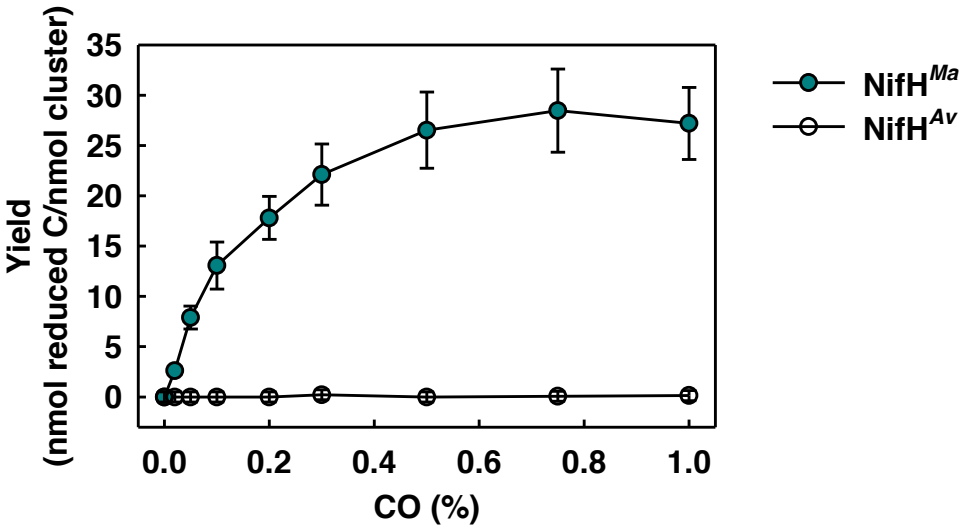

Figure 6.7 Titration of product yield versus CO concentration. Shown are the yields of hydrocarbons generated from increasing amounts of CO by *Av*NifH or *Ma*NifH. Yields were calculated based on nmol reduced C in hydrocarbons per nmol cluster.

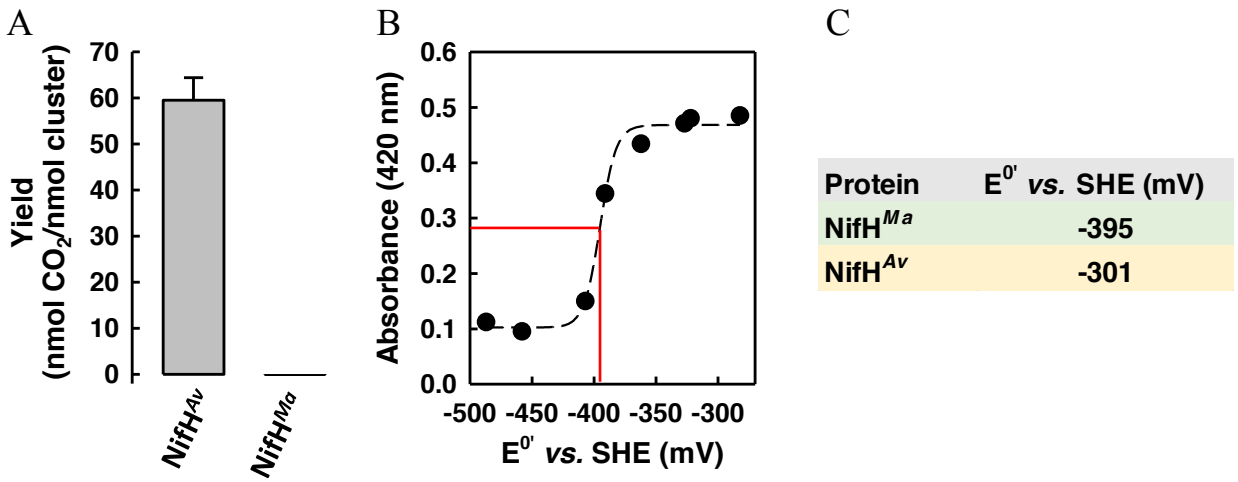

Figure 6.8 Redox properties of protein-bound [Fe_4S_4] clusters. (**A**) Yields of CO_2 generated from the oxidation of CO by *Av*NifH or *Ma*NifH in the presence of 20 mM IDS. (**B**) Titration of the +1/+2 redox couple of the [Fe_4S_4] cluster of *Ma*NifH. The oxidation of the cluster from the +1 to the +2 state was monitored by the absorbance at 420 nm. (**C**) Redox potentials of the +1/+2 couples of the [Fe_4S_4] clusters of *Ma*NifH and *Av*NifH. The potential of *Ma*NifH was determined as described in b, and the potential of *Av*NifH was determined in a previous work.[62] The redox titration experiment was performed 3 times, and the representative result is shown in **B**.

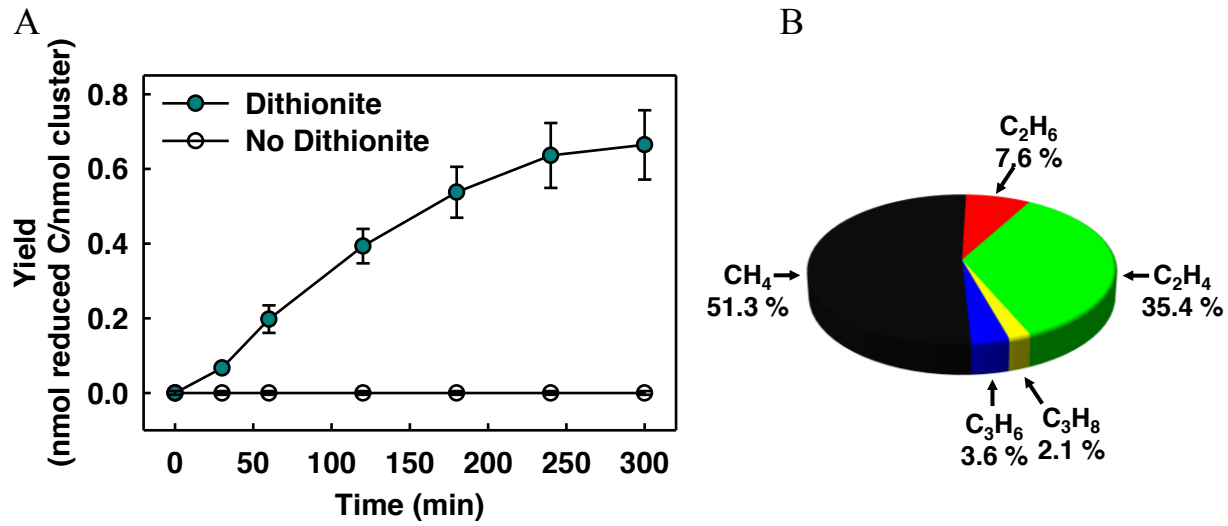

Figure 6.9 Reduction of CO to hydrocarbons by protein-bound [Fe_4S_4] clusters using dithionite as a reductant. (**A**) Time-dependent formation of hydrocarbons from CO reduction by *Ma*NifH. (**B**) Distribution of hydrocarbons generated by *Ma*NifH from the reaction of CO reduction.

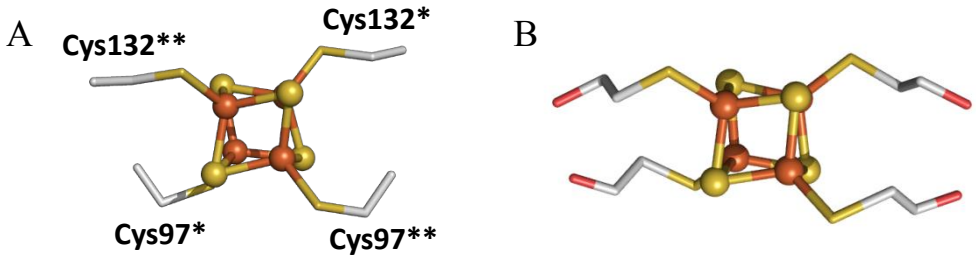

Figure 6.10 Structures of protein-bound and synthetic [Fe_4S_4] clusters. Shown are x-ray crystal structures of (**A**) *Av*NifH-associated [Fe_4S_4] cluster with four protein-bound Cys ligands and (**B**) synthetic [PPh_4][$Fe_4S_4(SCH_2CH_2OH)_4$] compound (designated $[Fe_4S_4]^{Syn}$) with four β-mercaptoethanol thiolate ligands.[52,191,192] Element color code: Fe, orange; S, yellow; C, light gray; O, red.

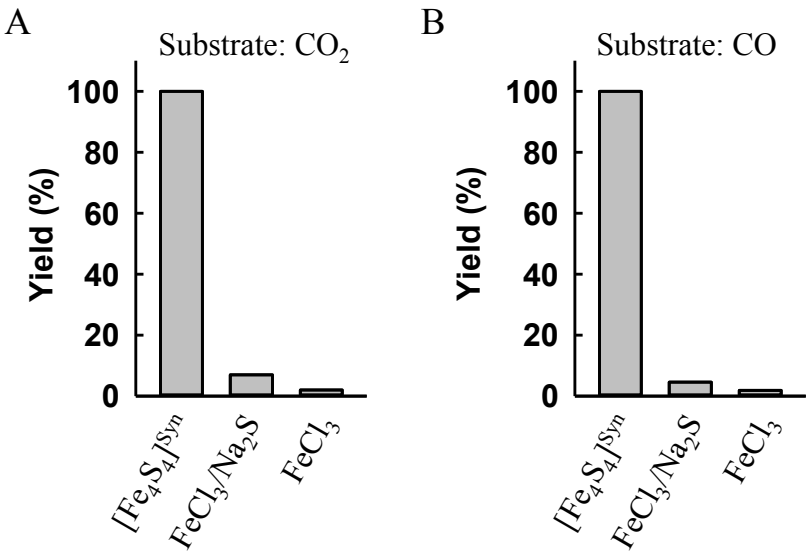

Figure 6.11 Formation of hydrocarbons by $[Fe_4S_4]^{Syn}$ and Fe-containing controls. Shown are the percentage yields of hydrocarbons generated from the reduction of (**A**) CO_2 or (**B**) CO by $[Fe_4S_4]^{Syn}$, or by Fe_3Cl_3 in the presence and absence of Na_2S. The experiments were conducted in 20 mM SmI_2, and the hydrocarbon yield of the $[Fe_4S_4]^{Syn}$-based reaction was set as 100%.

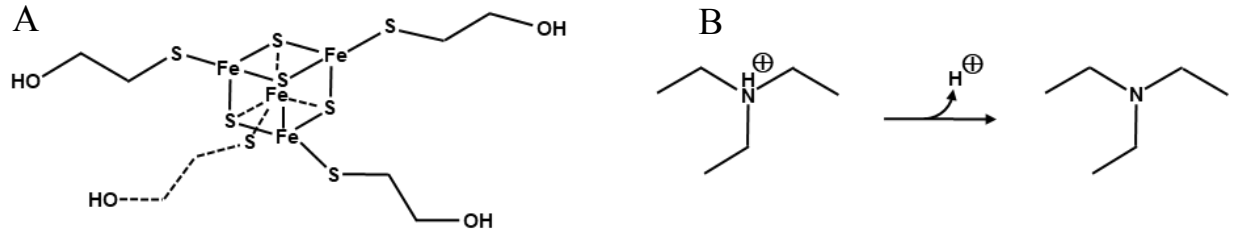

Figure 6.12 Structures of the catalyst and proton source for DFT calculations. (**A**) Lewis Structure of the $[Fe_4S_4]$ cluster considered in the computational investigation. (**B**) Deprotonation reaction of $NHEt^+$ considered for calculations of all protonation energies.

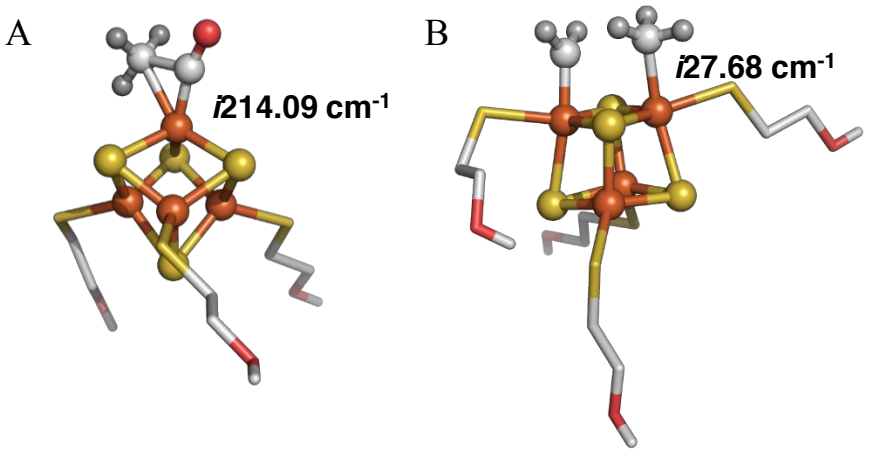

Figure 6.13 Transition states for the proposed mechanisms. Shown are the transition states (TPSS/def2-TZVP) for (**A**) migratory insertion (see **Figure 6.3**, step 15) and (**B**) CH_2-CH_3 bond formation (see **Figure 6.4**, step 18). Element color code: Fe, orange; S, yellow; C, light gray; O, red; H, gray.

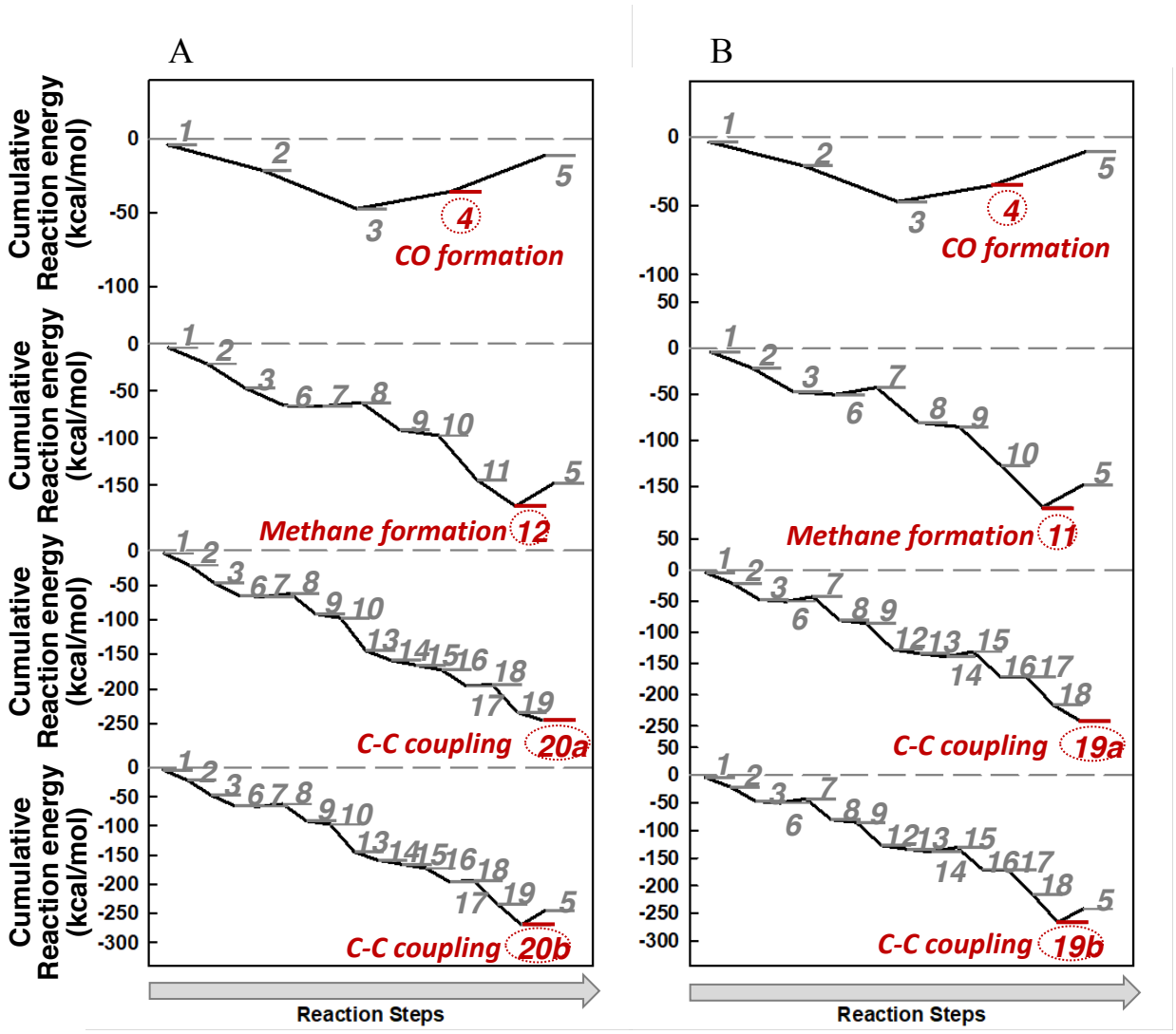

Figure 6.14 Cumulative reaction energies of CO_2 reduction pathways catalyzed by the [Fe_4S_4] cluster. Shown are the energies for the pathways of CO formation, methane formation, and C-C coupling that are depicted in (**A**) **Figure 6.3** and (**B**) in **Figure 6.4**. The steps of CO formation, methane formation, and C-C coupling are indicated by red circles.

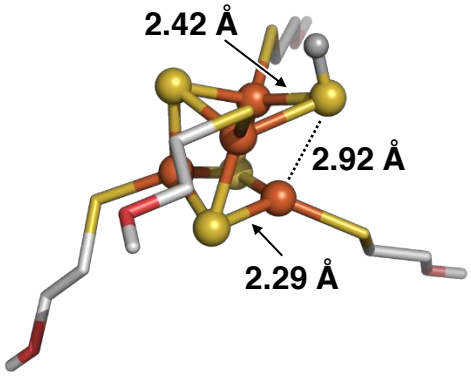

Figure 6.15 Protonation of the [Fe_4S_4] cluster. Shown is the optimized structure (TPSS/def2-TZVP, COSMO ε=37) of the all-ferrous [Fe_4S_4] cluster protonated at one of its S atoms. Protonation leads to significant distortion of the cluster and consequently opens up the cubane. Element color code: Fe, orange; S, yellow; C, light gray; O, red; H, gray.

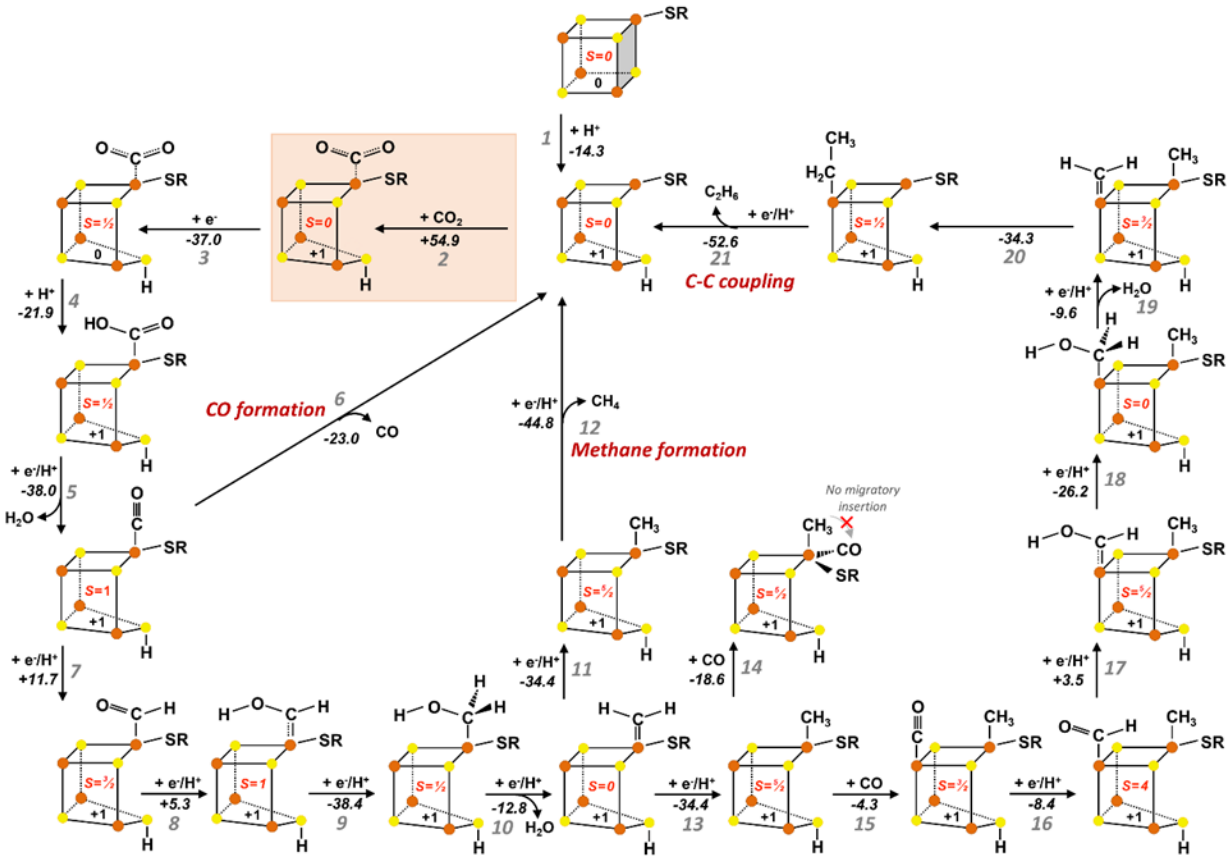

Figure 6.16 Reaction mechanism starting with the protonation of one of the S atoms of the [Fe_4S_4] cluster. Reaction energies were derived from the energies of the structurally optimized compounds (TPSS/def2-TZVP, COSMO ε=37). Cluster models were considered fully coordinated by $SC_2H_4OH^-$. Only the ligand of the open Fe site is depicted. SR, $SC_2H_4OH^-$.

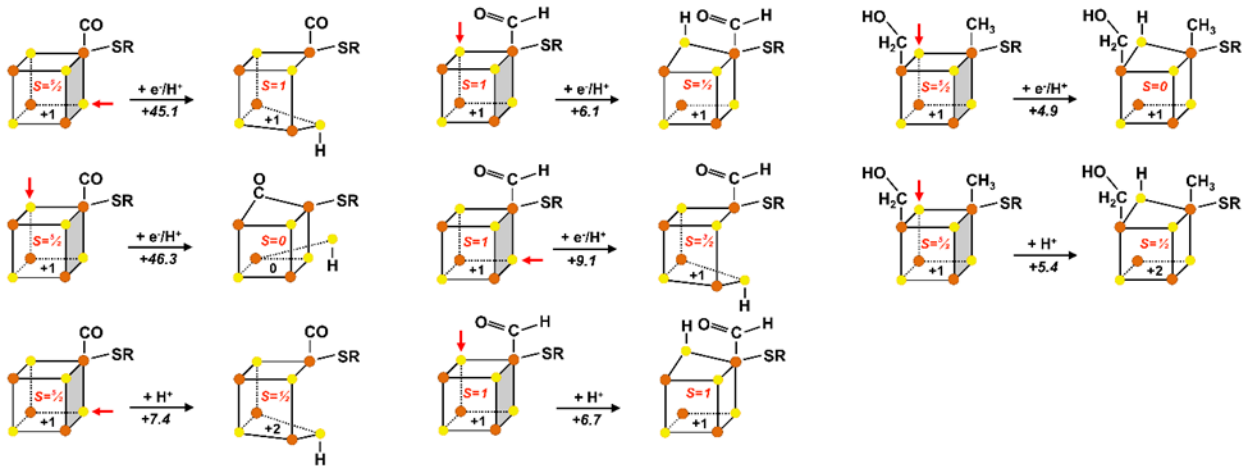

Figure 6.17 Examples of endothermic proton or electron/proton transfer reactions to the sulfur atoms of the [Fe_4S_4] cluster. Reaction energies were derived from the energies of the structurally optimized compounds (TPSS/def2-TZVP, COSMO ε=37). Cluster models were considered fully coordinated by $SC_2H_4OH^-$. Proton or electron/proton transfer is indicated by a red arrow. Only the ligand of the open Fe site is depicted. SR, $SC_2H_4OH^-$.

6.7 Supplemental Discussion

The ambient reduction of CO to hydrocarbons is highly interesting because of its industrial potential and its plausible relevance to prebiotic chemistry. Here, we compare the reactivities of biogenic and synthetic [Fe_4S_4] clusters toward CO with those of several other notable systems, such as (1) the nitrogenase-based catalysts, including the catalytic component of nitrogenases (e.g., MoFe and VFe proteins) and the nitrogenase cofactors (e.g., M- and V-clusters); (2) the Fe/S-based catalysts, including those generated by synthetic approaches (e.g., synthetic FeS clusters) and those associated with prebiotic chemistry (e.g., Fe/S precipitates); and (3) the non-Fe/S catalysts, including homogeneous molecular catalysts (i.e. synthetic compounds) and heterogeneous surface catalysts (e.g., the Fischer-Tropsch catalysts).

6.7.1 Fe Protein (Fe_4S_4) vs. Nitrogenase (Cofactor)

6.7.1.1 Fe Protein vs. Nitrogenase

The V-nitrogenase is the most active enzyme known to convert CO to hydrocarbons under ambient conditions.[133] Using its Fe protein component (*Av*VnfH) to deliver electrons to its

catalytic VFe protein component (*Av*VnfDGK) in the presence of ATP and dithionite, the holo V-nitrogenase of *A. vinelandii* averages approximately 14 turnovers of CO per minute in an *in vitro* assay and produces more than 50 times the yield of hydrocarbons relative to that produced by *Ma*NifH.[133,160] In contrast, the holo Mo-nitrogenase of *A. vinelandii* reduces CO to hydrocarbons at a rate that is approximately 800-fold lower than that the V-nitrogenase when it utilizes its Fe protein component (*Av*NifH) to deliver electrons to its catalytic MoFe protein component (*Av*NifDK) in the presence of ATP and dithionite in an in vitro assay.[160] Under improved conditions, such as upon substitution of D_2O for H_2O in the assay, the yield of hydrocarbon formation by Mo-nitrogenase is comparable to that by *Ma*NifH.[160] In addition, certain variants of M-nitrogenase have been reported to achieve 20-30 turnovers over the course of the reaction, which is comparable to that of *Ma*NifH.[173]

The higher activity of the holo nitrogenase than its Fe protein component in CO reduction is not surprising, given the intricate two-component mechanism employed by nitrogenase that renders it efficient in transferring electrons to the cofactor site, rendering the cofactor in a sufficiently low redox potential for substrate binding and reduction. Moreover, the high-nuclearity metallocofactors likely provide more reaction sites than the smaller [Fe_4S_4] clusters, which could further account for a higher activity of these clusters in catalyzing CO reduction. The disadvantages of this system, however, are the complexity of the reaction mechanism and the ATP-dependent nature of the reaction, making it difficult to use this system for mechanistic investigations of CO reduction, as well as potential applications for industrial use in the future. In comparison, the Fe protein (i.e. *Ma*NifH) is a unique, stand-alone catalyst that can work in an ATP-independent manner, which makes it a simplified template for mechanistic investigations of

FeS-based CO activation, as well as future development of strategies for ambient conversion of CO and CO_2 into useful chemical commodities.

6.7.1.2 Fe_4S_4 Cluster vs. Cofactor

Other than the holo enzyme systems, simplified systems that are ATP-free and consist of only reductants and the cofactors isolated from the Mo- and V-nitrogenases (i.e., the M- and V-clusters) have been shown to reduce CO to hydrocarbons.[136,177,219] Both Eu^{II}-DTPA and SmI_2 are effective in driving the reduction of CO to hydrocarbons by these systems. In the presence of Eu^{II}-DTPA, the hydrocarbon yields of both M- and V-clusters are similar to that of $[Fe_4S_4]^{Syn}$ under the same reaction conditions.[219] In the presence of SmI_2, the hydrocarbon yields of both M- and V-clusters are improved, and a recent study shows a TON of greater than 200 for the M-cluster, which is approximately twice the TON of $[Fe_4S_4]^{Syn}$ reported in this work.[99] The corresponding number for the V-cluster-catalyzed CO reduction under the same reaction conditions has not been reported so far.

The higher activity of the isolated cofactor than the $[Fe_4S_4]$ cluster in this reaction again illustrates the effectiveness of the complex, high-nuclearity metallocofactors in CO reduction, possibly due to the presence of more reaction sites on these larger clusters. However, the disadvantage of this system is the laborious process to isolate sufficient amounts of cofactors from the nitrogenase enzymes. In this light, the current report is unique in demonstrating the surprising ability of a much more accessible, synthetic $[Fe_4S_4]$ cluster to drive difficult reactions of CO_2- and CO-reduction at reasonable yields prior to any optimization, suggesting this system as a potential candidate for future development of strategies of FeS-based conversion of CO and CO_2 to hydrocarbons under ambient conditions.

6.7.2 Fe_4S_4 Cluster vs. Other Fe/S-based Catalysts

6.7.2.1 Fe_4S_4 Cluster vs. Synthetic FeS-based Catalysts

While a large number of synthetic or biomimetic FeS-based clusters have been reported in the literature, only a few of them have been described for their abilities to activate small molecules.[220–223] These handful of examples include the sub-stoichiometric reduction of acetylene to ethylene by a synthetic [Fe_4S_4] cluster, and the catalytic reduction of hydrazine to ammonia by [$MoFe_3S_4$] and [VFe_3S_4] clusters.[223–225] In addition, a report from 1992 describes the $2e^-$-reduction of CO_2 by a $[Mo_2Fe_6S_8(SEt)_9]^{3-}$ catalyst to a product which then reacts with a thioester (CH_3COSEt in this case) to produce a β-ketoacid ($RCOCOO^-$) and SEt^-.[226] The scarcity of early examples for CO_2/CO reduction to hydrocarbons highlights the difficulty of these reactions to occur under ambient conditions. Recently, in light of the discovery of the reactivity of nitrogenase toward CO, two synthetic nitrogenase cofactor mimics—namely, a $[Et_4N]_4[Fe_6S_9(SEt)_2]$ cluster (synthesized by the Holm group) and a $[Cp^*MoFe_5S_9(SH)]^{3-}$ cluster (synthesized by the Tatsumi group), which represent a homometallic and a heterometallic analog of the cofactor, respectively—were examined for their abilities to reduce CO and CO_2 to hydrocarbons.[99,227] Interestingly, these two cofactor mimics demonstrated activities of hydrocarbon production from CO- and CO_2-reduction that were comparable with, but lower than those of the nitrogenase cofactors under the same reaction conditions.[99,228] These results point to the possibility that more reports along this line will surface in the near future, which could help bridge the gap of our current knowledge on the reactivities of synthetic FeS-based catalytic systems toward CO_2 and CO.

6.7.2.2 Fe_4S_4 Cluster vs. Fe/S-containing Precipitates

In their seminal work published in 1997, Huber and Wächtershäuser show that CO can react with CH_3SH on co-precipitated NiS and FeS to form CH_3COOH and H_2S, with CH_3-CO-SCH_3 being the potential intermediate of this reaction.[198] This result suggests a prebiotic CO fixation pathway that might be employed by the earliest organisms living around the hyperthermal vents underneath the deep oceans. Based on this work, a series of follow-up studies using CO as a carbon feedstock and/or an electron donor show that the product profile of this reaction can be substantially extended to include long chain carboxylic acids, carbohydrates (i.e., hydroxyl acids) and amino acids (when CN^- or NH_4^+ is used as a co-reactant), with each of them correlated to the emergence of primordial lipids, sugars and peptides/proteins, respectively, on Earth.[199–201,229] By analogy, the reduction of CO by FeS clusters in a speculated, highly reducing early atmosphere might represent another prebiotic route of CO activation, which generates small alkenes and alkanes as carbon and/or electron sources for certain methane- and ethene-assimilating microorganisms.[202,203] It has been postulated that in the Archean era, there was a methane- and CO-rich atmosphere and anoxic oceans inhabited by iron- and sulfur-metabolizing microbes, such as purple- and green-sulfur bacteria.[230] It is plausible that these microorganisms could produce small hydrocarbons via secondary metabolic pathways that parallel that reported in the case of *A. vinelandii*, which were then assimilated by microorganisms utilizing hydrocarbons for cell growth.[231]

There are some notable differences between these prebiotic synthesis systems and the $[Fe_4S_4]$ cluster-based system reported in this work. One, the reaction described in our work is, in essence, a reductive coupling reaction of CO or CO_2 on the $[Fe_4S_4]$ cluster (see mechanisms depicted in the main text); whereas the general reaction described in the pre-biotic synthesis

models involves the capture of CO on a given carbon backbone through carbonylation, followed by further reaction of the carbonyl moiety to generate carboxylic acids or amino acids. Consequently, hydrocarbons have seldomly been reported as products generated by these models of pre-biotic synthesis. Two, the reaction reported in this work utilizes a homogeneous catalyst (i.e. the $[Fe_4S_4]$ cluster); whereas the primordial model systems are essentially semi-heterogeneous, where substrates are activated on a slurry of material particles. Three, our reaction is driven by low reduction potentials delivered by strong reductants; whereas the prebiotic synthesis reactions are powered by high temperatures (above the boiling point) and often high pressures, and they are allowed to proceed over a much longer reaction time frame.[198–201]

6.7.3 Fe_4S_4 Cluster vs. Non-Fe/S Catalysts

6.7.3.1 Fe_4S_4 Cluster vs. Homogeneous Non-Fe/S Catalysts

Several notable attempts have been made to convert the inactive carbon oxides to useful chemical compounds by combining these molecules with reactive or pre-activated organic compounds, such as the poly- and cyclic carbonate syntheses from CO_2 and the Monsanto acetic acid synthesis from CO.[232–234] In addition, synthetic compounds have been explored for their abilities to directly transform CO and CO_2 into hydrocarbons. One such example was reported by Hou et al. in 2006, where tetranuclear lanthanide polyhydrido clusters were used for selective formation of C_2H_4 from CO.[235] This type of reaction is remarkable in that it achieves selective C-C coupling and cleavage of C-O bond at ambient temperature and pressure; however, the reactions are not catalytic because of the absence of a H^+ source in these systems and, consequently, the need to remove O atoms from CO in the forms of Ln_4O_4 and Si-O-Si species,

resulting in the conversion of the catalysts into dead-end byproducts, i.e., Ln_4O_4 clusters (Ln = Y or Lu).

6.7.3.2 Fe_4S_4 Cluster vs. Heterogeneous Non-Fe/S Catalysts

The best-known example of the heterogeneous catalysis of CO reduction is the Fischer-Tropsch (FT) process, which combines CO with H_2 into hydrocarbons. There are a number of points that distinguish the FT process with the reaction reported in this work.[236–238] One, our reaction occurs at ambient temperature and pressure; whereas the FT process, which is a gas-solid two-phase reaction, typically requires high temperature and pressure. Two, contrary to the reaction described in this report, the reactivity and product selectivity of the FT process vary greatly depending on the reaction conditions and the choice of catalysts. Three, the reaction catalyzed by the $[Fe_4S_4]$ cluster utilizes protons as the hydrogen source; whereas the reducing power of the FT process is provided in the form of molecular hydrogen. Other than the FT process, alternative strategies for the conversion of CO and CO_2 to hydrocarbons, such as the electrochemical reduction of these carbon oxides, have also been explored to circumvent the requirement of high temperature and pressure for the 2-phase catalysis. The products generated by these alternative approaches are mainly methane and ethene, and they typically require a metal surface, such as copper, for catalysis to occur.[239,240] While this electrode-based approach has the shortcomings in needing a relatively large overpotential for preferential hydrocarbon production and having a relatively low selectivity of products comparing to FT synthesis, it bears potential in supplying a continuous flow of electrons that may be combined with the $[Fe_4S_4]$ cluster-based reaction to generate a continuous system for ambient conversion of CO and CO_2 to hydrocarbons.

6.8 Acknowledgments

I would like to thank the Nature Publishing Group for permission to include Chapter 6 in my dissertation, which was originally published in *Nature Catalysis*.[241] This work was supported by NSF Career grant CHE-1651398 (to Y.H.), a grant-in-aid for scientific research (16H04116) from the Japanese Ministry of Education, Culture, Sports, Science and Technology (MEXT), Hori Sciences and Arts Foundation grant, and Takeda Science Foundation grant (to Y.O.).

6.9 Contributions

Caleb Hiller discovered that *Ma*NifH was able to reduce CO_2 to hydrocarbons and performed the biochemistry work related to proteins. Martin Stiebritz performed the theoretical calculations. CC Lee, Nate Sickerman, and Kazuki Tanifuji performed the biochemical work related to the synthetic cluster.

Chapter 7 Structural Implications for the Formation of Hydrocarbons from CO_2 and CO by Nitrogenase Iron Proteins

7.1 Introduction

Nitrogenase iron (Fe) proteins are best known for their ability to transfer electrons to the catalytic component and assist in the assembly of the two metalloclusters of said component so that nitrogen fixation can occur.[3,4,7,71] However, it was recently shown that Fe proteins could function to reduce CO_2 and/or CO, a finding that may result in the generation of new catalysts that can perform Fischer-Tropsch type reactions.[161,241] Through the use of a synthetic ($[Ph_4P]_2[Fe_4S_4(SCH_2CH_2OH)_4]$) compound (Figure 7.1), designated $[Fe_4S_4]^{Syn}$ cluster, that has a $[Fe_4S_4]$ cluster core and four cysteine-like β–mercaptoethanol (BME) thiolate ligands $[Fe_4S_4]$ cluster, it was shown that the $[Fe_4S_4]$ cluster, which resides near the surface of the protein, catalyzes the reduction of CO_2 and CO in the presence of the strong reductant europium (II) diethylenetriaminepentaacetic acid (Eu^{II}-DTPA; $E^{o'} = -1.14$ V at pH 8.0).[241]

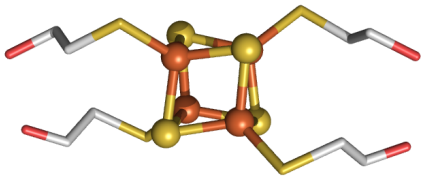

Figure 7.1 Structure of the synthetic $[Fe_4S_4]$ clusters. The synthetic $[PPh_4][Fe_4S_4(SCH_2CH_2OH)_4]$ compound (designated $[Fe_4S_4]^{Syn}$) with four β-mercaptoethanol thiolate ligands.[191,192] Element color code: Fe, orange; S, yellow; C, light gray; O, red.

As discussed in Chapter 6, different Fe protein homologs have exhibited different product profiles.[241] The molybdenum (Mo-) and vanadium (V-) nitrogenase Fe proteins from *Azotobacter vinelandii*, *Av*NifH and *Av*VnfH, respectively, can reduce CO_2 to form CO, but are unable to produce hydrocarbons in the presence of CO_2 or CO.[62,241] The Mo-nitrogenase Fe protein from *Methanosarcina acetivorans*, *Ma*NifH, was shown to be able to reduce CO_2 to both CO and hydrocarbons, and CO to hydrocarbons.[241] The difference in the product profiles of various Fe protein homologs is of interest because the $[Fe_4S_4]^{Syn}$ catalyst was shown to be able to reduce

CO_2 to CO and hydrocarbons, as well as CO to hydrocarbons; and it would therefore be expected that each of the Fe protein homologs would be able to generate the same products because they contain a similar cluster near the surface of the protein.[241] To further investigate the product profiles of Fe protein homologs, an additional Mo-nitrogenase Fe protein from the bacteria *Desulfovibrio vulgaris* was heterologously expressed in *Escherichia coli* and analyzed for its ability to reduce CO_2 and CO.

7.2 Electron Paramagnetic Resonance (EPR) Spectroscopy

EPR spectroscopy has been used as a diagnostic tool to compare the $[Fe_4S_4]$ clusters of Fe proteins, and was used to characterize the cluster of *Dv*NifH for comparison against *Av*NifH to determine whether *Dv*NifH should be expected to behave in a similar fashion to that of *Av*NifH.[134] *Av*NifH has been well characterized and shown to occupy three oxidation states: $[Fe_4S_4]^{2+}$, $[Fe_4S_4]^{1+}$, and $[Fe_4S_4]^{0}$, depending on the conditions. Indigo disulfonate (IDS) is used to oxidize the cluster to the $[Fe_4S_4]^{2+}$ state. In this state, the cluster occupies an $S = 0$ spin state, as determined by Mössbauer spectroscopy, is diamagnetic and does not display an EPR signal.[3] The $[Fe_4S_4]^{1+}$ state is obtained in the presence of dithionite ($Na_2S_2O_4$, DT), and exists as a mixture of an $S = 1/2$ and $S = 3/2$ species, with the predominant feature being the rhombic line-shape at $S = 1/2$, with g-values of 2.01, 1.93, and 1.85.[3,64,65] Eu^{II}-DTPA is used to reduce the cluster to the "all-ferrous" $[Fe_4S_4]^{0}$ state, which exhibits a $g = 15.9$ resonance in the parallel-mode, consistent with an $S = 4$ species.[67–70] Because *Dv*NifH displays the same EPR spectral features as *Av*NifH and *Ma*NifH in IDS (Figure 7.2A), dithionite (Figure 7.2B), and Eu^{II}-DTPA (Figure 7.2C), it is assumed that the cluster can occupy the same oxidation and spin states as *Av*NifH and should therefore also be able to interact with CO_2 and CO.[134]

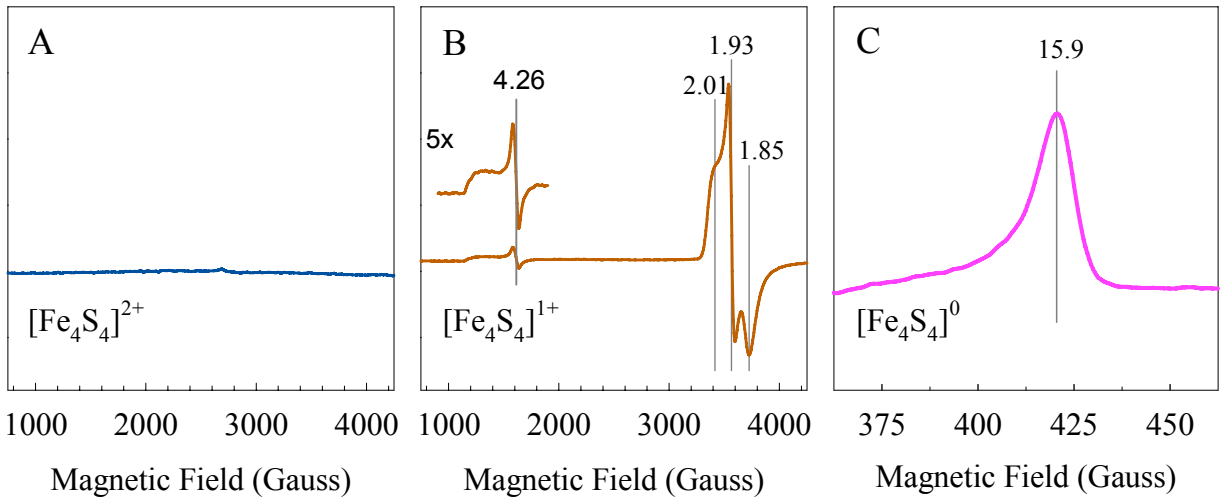

Figure 7.2 EPR spectra of *Dv*NifH in the IDS-oxidized ($[Fe_4S_4]^{2+}$, A), DT-reduced ($[Fe_4S_4]^{1+}$, B), Eu^{II}-reduced all-ferrous states ($[Fe_4S_4]^{0}$, C). The *g*-values are indicated by vertical lines. IDS = indigo disulfonate, DT = dithionite, Eu^{II}-DTPA = europium (II) diethylenetriaminepentaacetic acid. Conditions: four (**A** and **B**) or ten scans (**C**) were run at 10 K with a microwave power of 50 mW and a microwave frequency of 9.62 GHz.

7.3 Comparison of the CO_2 and CO Reduction Capabilities of *Av*NifH, *Ma*NifH, and *Dv*NifH

Comparative CO_2 (Figure 7.3A) and CO (Figure 7.3B) reduction assays indicate that the product profile of *Dv*NifH is more similar to that of the $[Fe_4S_4]^{Syn}$ cluster and *Ma*NifH than *Av*NifH because this homolog can reduce CO_2 to CO and hydrocarbons (Figure 7.3A), and CO to hydrocarbons (Figure 7.3B), albeit at rates on the range of ~9.8% and ~10.2% total carbon turnover per cluster, respectively, compared to *Ma*NifH.

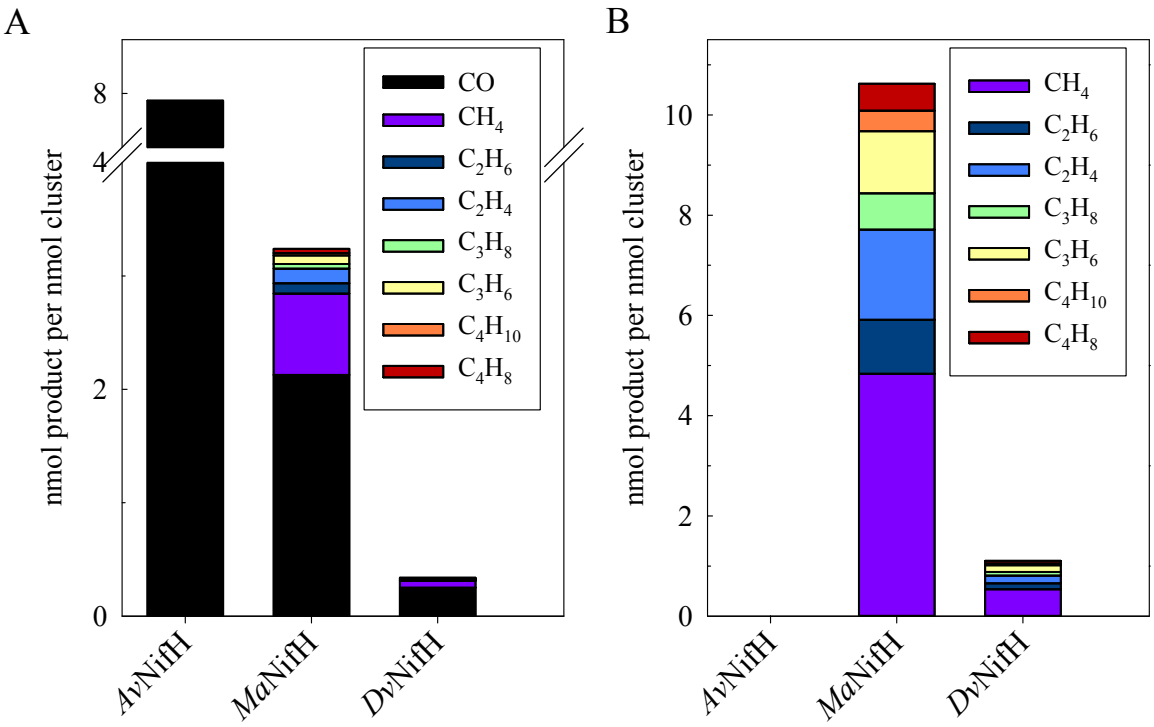

Figure 7.3 Comparative CO_2 (A) and CO (B) Reduction Assays of Fe Protein Homologs. Yield of CO (black) and hydrocarbons (colored) from the reduction of CO_2 or CO using 100 mM Eu^{II}-DTPA as a reductant. Products are identified in the key.

7.4 Crystal Structures of *Dv*NifH

To better understand how the protein and the $[Fe_4S_4]$ cluster particularly play roles in the reduction of these substrates, work was undertaken to obtain crystal structures of these Fe protein homologs. A higher resolution structure of *Av*NifH and also an *Ma*NifH structure have been obtained and will be shortly published. Table 7.1 summarizes the data collection and refinement statistics for these crystal structures. In addition, *Dv*NifH crystals were grown using a microbatch method and X-ray diffraction patterns of these crystals were solved at 2.8 Å (Figure 7.4). *Dv*NifH belonged to the $P6_122$ space group, with cell dimensions of a = 103.33 Å, b = 103.33 Å, and c = 197.02 Å. Table 7.2 summarizes the data collection and refinement statistics for *Dv*NifH.

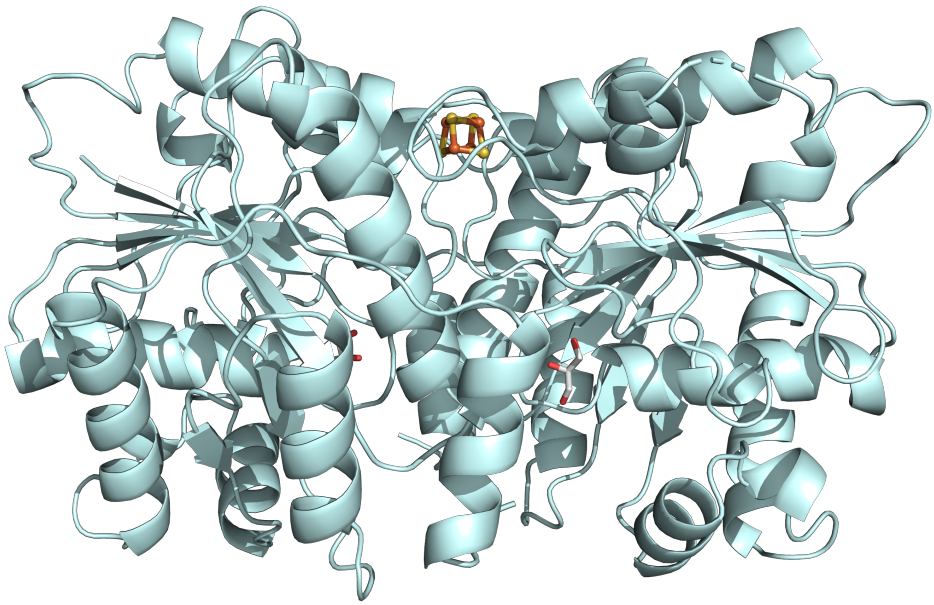

Figure 7.4 The crystal structure of *Dv*NifH at 2.8 Å resolution. Atoms are colored as follows: Fe, rust; S, yellow. PyMOL was used to generate this figure.[38]

7.5 Role of Cluster Location and Accessibility

Because of the role of the cluster to assist in reduction of substrate, the location of and accessibility to the cluster likely contributes to the decreased reaction rates observed with the *Dv*NifH homolog compared to *Ma*NifH. Structural alignment and a cluster location comparison, performed by calculating the average atom displacement for each corresponding vertices of the clusters, of the Fe protein homologs (Figure 7.5A) reveal that the cluster of *Dv*NifH most closely approximates that of *Av*NifH, the most biochemically and structurally characterized Fe protein (Figure 7.5B). The average atom displacement for each vertex of the [Fe_4S_4] clusters between *Av*NifH (Figure 7.5, cyan) and *Dv*NifH (Figure 7.5B, orange) or *Ma*NifH (Figure 7.5C, violet) are 0.2 Å and 1.4 Å, respectively. As the cluster of *Dv*NifH is buried ~1.4 Å further into the protein than the cluster of *Ma*NifH, diffusion of substrate and products to and from the catalytic surface would slow the turnover.

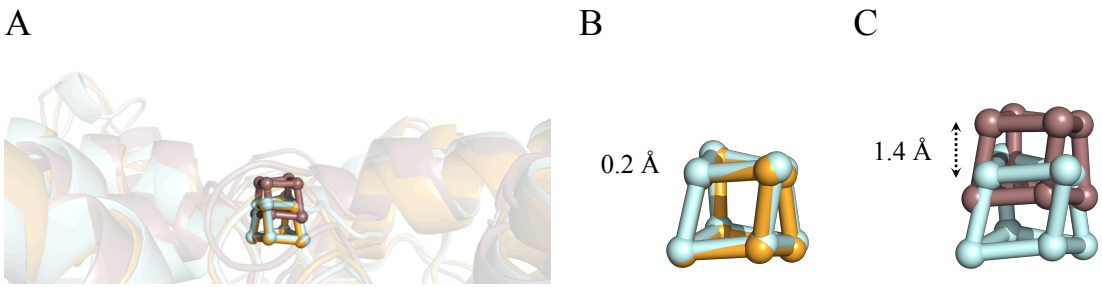

Figure 7.5 Comparison of the location of the [Fe_4S_4] cluster of *Dv*NifH and *Ma*NifH to *Av*NifH. Structural alignment of *Av*NifH, *Dv*NifH, and *Ma*NifH (**A**) reveals that the average atom displacement between the corresponding [Fe_4S_4] atoms of *Dv*NifH to those of *Av*NifH are ~0.2 Å, most of which is a horizontal translation, but does include a slight translation away from the surface of the protein (**B**). The displacement of the [Fe_4S_4] atoms of *Ma*NifH to those of *Av*NifH are ~1.4 Å nearer the surface of the protein (**C**). Proteins and clusters are colored as follows: *Av*NifH, cyan; *Dv*NifH, orange; and *Ma*NifH, violet. PyMOL was used to generate this figure.[38]

Surface analysis also shows that FeS cluster accessibility also differs in these three homologs (Figure 7.6), and that it also correlates to the observed activity of the Fe protein homologs. *Ma*NifH, which exhibits the most prolific substrate reducing ability in that it can reduce CO_2 to CO and hydrocarbons as well as CO to hydrocarbons, has a more exposed [Fe_4S_4] cluster (Figure 7.6B) than *Av*NifH (Figure 7.6A), which can only reduce CO_2 to CO. The cluster of *Dv*NifH is the least accessible, with an additional loop that partially covers the cluster (Figure 7.6C) and it exhibited ~10% activity in reducing both CO_2 and CO as mentioned earlier. It is, however, important to note that *Dv*NifH was able to reduce both substrates, unlike *Av*NifH, and it therefore follows that cluster accessibility is likely not the only contributing factor that affects the ability of the Fe protein to reduce substrate. Further investigation will also be required to determine how the local protein environment may also be contributing to the reactivity of these Fe protein homologs. For instance, there is a conserved arginine residue, Arg^{100} in *Av*NifH, that resides near the FeS cluster that may bind CO_2, allowing the substrate to occupy a conformation more amenable for reduction. This needs to be further investigated through DFT calculations and experimentally though point mutations.

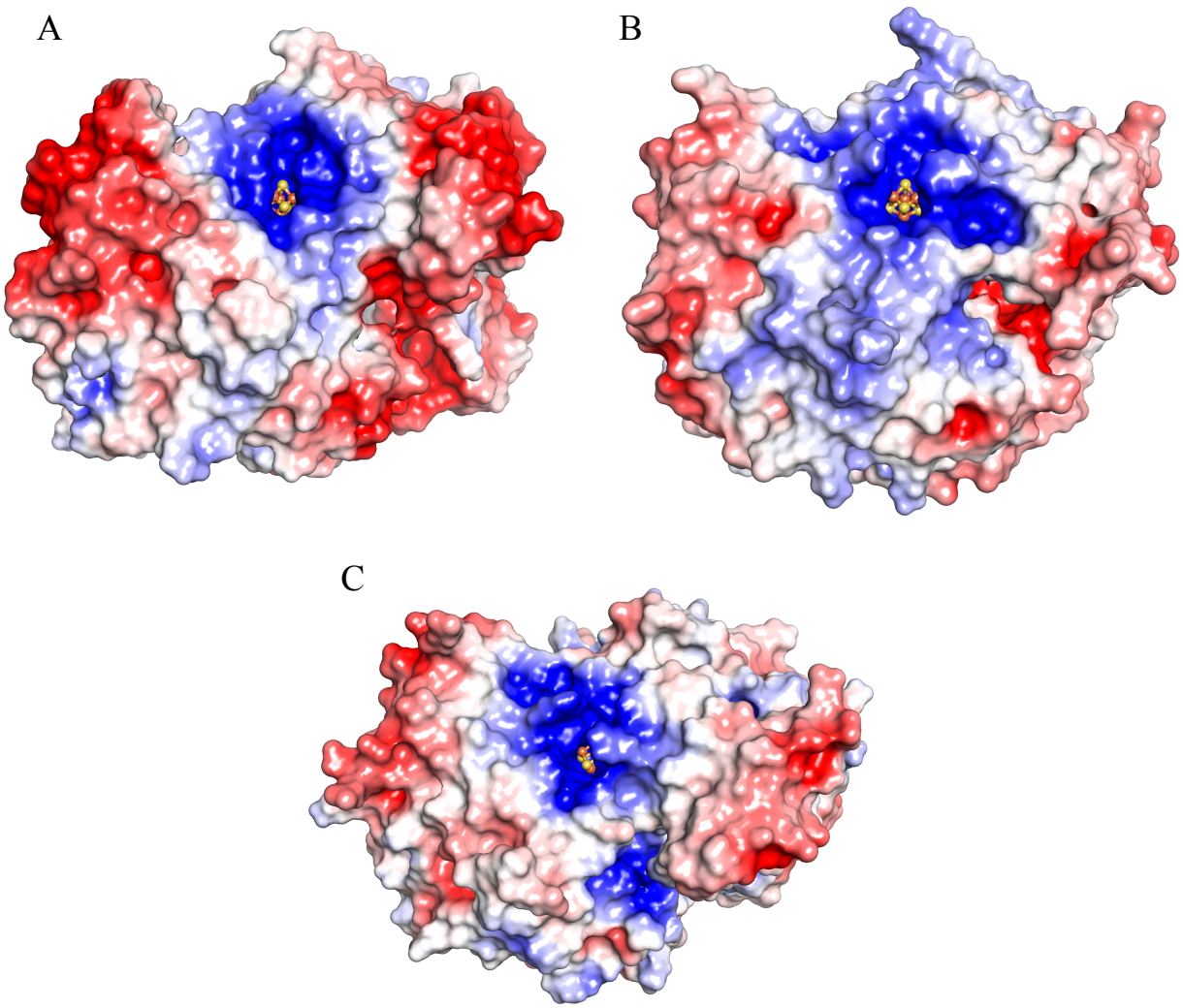

Figure 7.6 Cluster Accessibility comparison of *Av*NifH, *Ma*NifH, and *Dv*NifH. Surface presentations of *Av*NifH (**A**), *Ma*NifH (**B**), and *Dv*NifH (**C**) show that the cluster of *Ma*NifH is more accessible than *Av*NifH or *Dv*NifH. An additional loop over the cluster of *Dv*NifH provides an additional cover over the FeS cluster that is not observed in the other Fe protein homologs. PyMOL was used to generate this figure.[38]

7.6 Characterization of *Ma*VnfH

To further investigate the substrate reducing abilities of Fe protein homologs, the V-nitrogenase Fe protein from *M. acetivorans*, *Ma*VnfH, was also characterized. Comparative CO_2 and CO reduction assays (Figure 7.7A and B, respectively) were run of the four Fe proteins to determine the catalytic effectiveness of *Ma*VnfH to reduce these substrates. Interestingly, *Ma*VnfH generated no detectable amounts of CO or hydrocarbons in the CO_2 reduction assays,

but it was able to generate hydrocarbons when CO was used as a substrate. While hydrocarbon production by *Ma*VnfH in the CO reduction assay is ~11% that of *Ma*NifH.

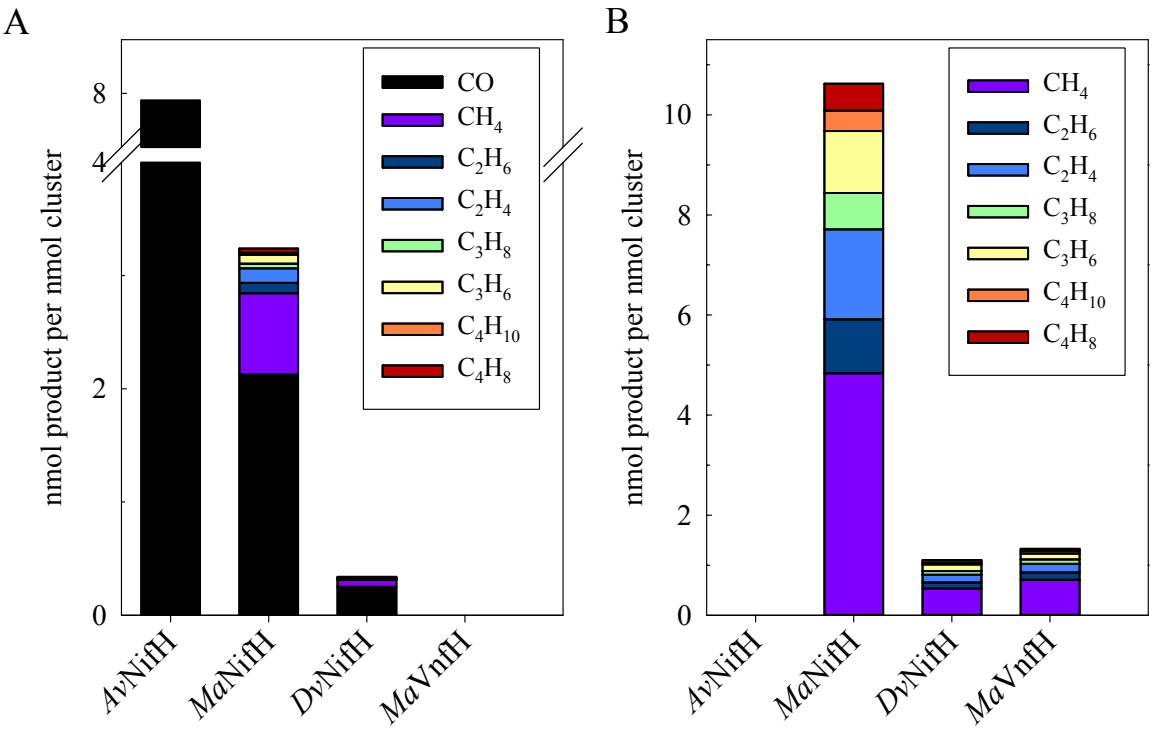

Figure 7.7 Reduction of CO_2 and CO by Fe Protein Homologs. The amount of CO (gray) and hydrocarbons (blue) generated from the reduction of CO_2 (**A**) or CO (**B**) by Fe protein homologs in the presence of 100 mM Eu^{II}-DTPA. Yields are calculated based on the amount of nmol of reduced C per nmol cluster. HC = hydrocarbons.

7.7 Crystal Structures of *Ma*VnfH

Crystal structures of *Ma*VnfH with the FeS cluster in the 1+ and 0 oxidation states were obtained. Brown-colored monoclinic crystals were grown using a microbatch method and X-ray diffraction patterns of these crystals were solved at 1.81 Å. The structure (Figure 7.8A) was determined with auto-build using *Ma*NifH as template for the dithionite-reduced ($Na_2S_2O_4$, DT) $[Fe_4S_4]^{1+}$ structure. The crystal contained one *Ma*VnfH structure in the unit and belonged to the P 1 21 1 space group, with cell dimensions of a = 46.25 Å, b = 79.34 Å, and c = 87.43 Å (Table 7.3). Additionally, an all-ferrous $[Fe_4S_4]^0$ structure was obtained by soaking the DT-reduced

*Ma*VnfH crystals with Eu^{II}-DTPA. Within 30 minutes, the crystals changed from brown to pink and were immediately frozen. The pink crystal color was maintained throughout data collection, similar to what was observed when the all-ferrous *Av*NifH structure was solved.[55] X-ray diffraction patterns for the all-ferrous crystals were solved at 1.75 Å. The structure (Figure 7.8B) was determined with auto-build using the *Ma*VnfH $[Fe_4S_4]^{1+}$ structure as a template, and belonged to the P 1 21 1 space group with cell dimensions of a = 45.0789 Å, b = 75.9596 Å, and c = 87.259 Å (Table 7.3).

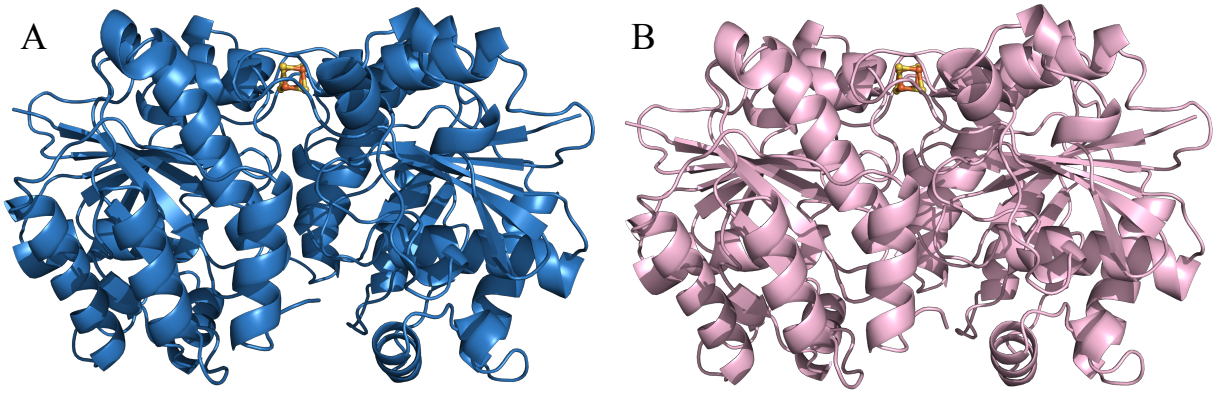

Figure 7.8 The 1.81 Å and 1.75 Å crystal structures of *Ma*VnfH in the DT-reduced ($[Fe_4S_4]^{1+}$, A) and Eu^{II}-DTPA-reduced states ($[Fe_4S_4]^{0}$, B), respectively. Atoms are colored as follows: Fe, rust; S, yellow. PyMOL was used to generate this figure.[38]

7.8 The Cluster Location and Accessibility of *Ma*VnfH

A cluster location comparison was also performed with the additional crystal structure of *Ma*VnfH (Figure 7.9) and compared to *Av*NifH, as in Figure 7.5. This analysis reveals that the average atom displacement of the [Fe4S4] cluster of *Ma*VnfH are shifted ~1.0 Å closer to the surface of the protein than what is observed in *Av*NifH (Figure 7.9B). Likewise, surface analysis comparison of *Ma*VnfH shows that cluster accessibility most closely resembles that of *Ma*NifH when compared to the other Fe protein homologs (see Figure 7.6).

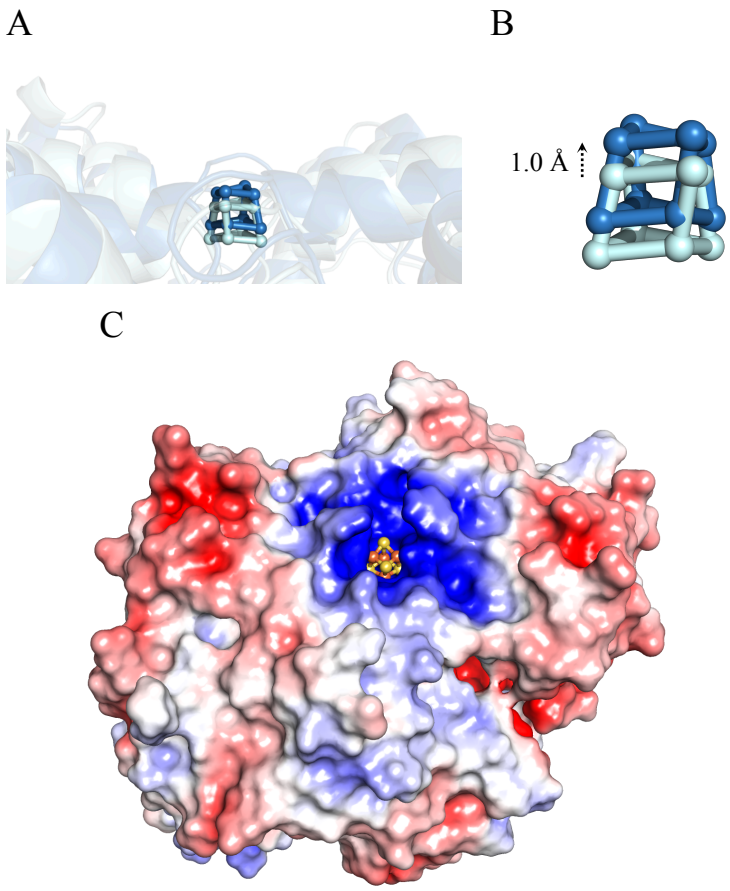

Figure 7.9 Comparison of the location of the [Fe_4S_4] cluster of *Av*NifH and *Ma*VnfH and accessibility to the FeS cluster of *Ma*VnfH. Structural alignment of *Av*NifH and *Ma*VnfH (**A**) reveals that the average atom displacement between the corresponding [Fe_4S_4] atoms of *Ma*VnfH are ~1.0 Å nearer the surface of the protein than those of *Av*NifH (**B**). A surface presentation of *Ma*VnfH (**C**) shows that cluster accessibility is most similar to *Ma*NifH rather than *Av*NifH or *Dv*NifH (see **Figure 7.6**) Proteins and clusters are colored as follows: *Av*NifH, cyan; and *Ma*VnfH, blue. PyMOL was used to generate this figure.[38]

7.9 EPR Spectroscopy of *Ma*VnfH

EPR spectroscopy was used to characterize the FeS cluster of *Ma*VnfH. The IDS-oxidized, DT-reduced, and Eu^{II}-DTPA-reduced samples representing the cluster in the $[Fe_4S_4]^{2+}$, $[Fe_4S_4]^{1+}$, and $[Fe_4S_4]^{0}$ oxidation states are represented in Figure 7.10A-C, respectively.[3,64,65,67–70,134] *Ma*VnfH has a greater $S = 3/2$ spin contribution in the DT-reduced state (Figure 7.10B) than the other homologs, which typically have the rhombic $S = 1/2$ signal as the major component when purified in these conditions.[134] It is uncertain what effect, if any, the altered spin

contribution may have on the ability of this homolog to reduce CO_2 or CO. Interestingly, this study revealed that when the DT-reduced *Ma*VnfH sample is analyzed in parallel mode that it exhibits a small signal at $g = 15.9$ (Figure 7.10D) consistent with that observed in the Eu^{II}-DTPA sample (Figure 7.10C). The appearance of the all-ferrous signal in the DT-reduced sample is unique to this *Ma*VnfH, and may indicate that the reduction potential for the all-ferrous state of *Ma*VnfH is more positive than the other Fe protein homologs. A more positive reduction potential may contribute to the protein's inability to reduce the more stable CO_2, but not CO. Additional work is required to determine the reduction potential of the other Fe protein homologs as only a reduction potential for *Av*NifH, -790 mV versus NHE, has been reported.[81,82]

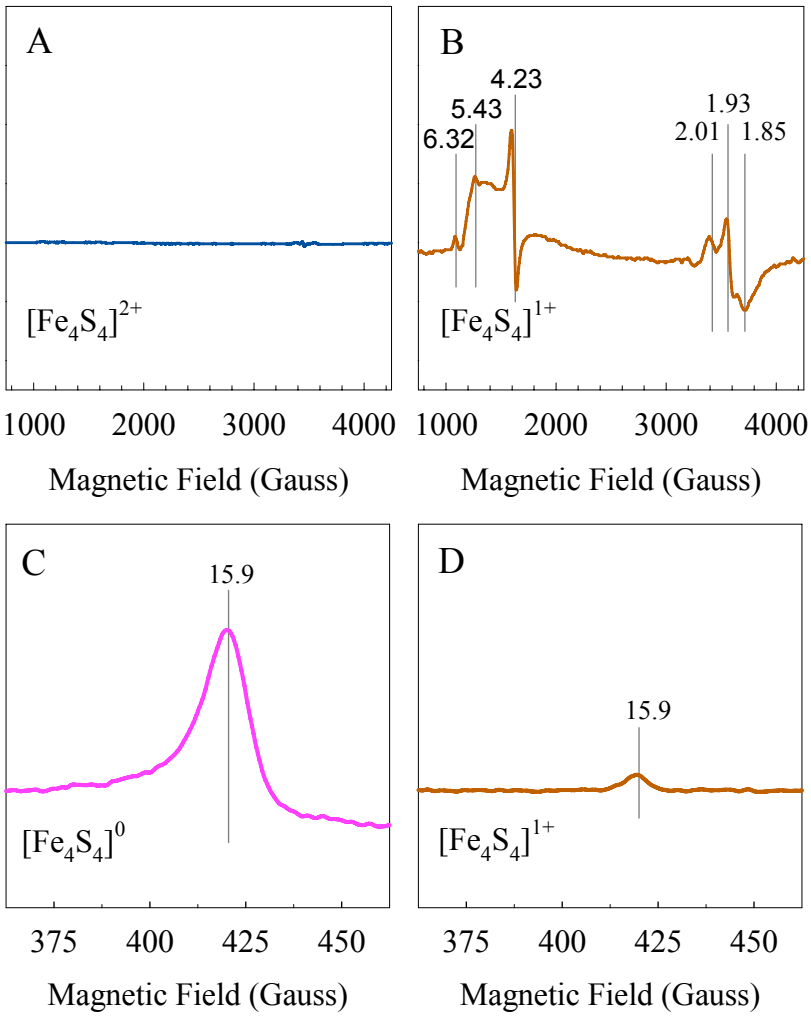

Figure 7.10 EPR spectra of *Ma*VnfH in the IDS-oxidized ($[Fe_4S_4]^{2+}$, A), DT-reduced ($[Fe_4S_4]^{1+}$, B), Eu^{II}-reduced all-ferrous states ($[Fe_4S_4]^{0}$, C), and the observed all-ferrous signal observed in the DT-reduced state ($[Fe_4S_4]^{1+}$, D). The *g*-values are indicated by vertical lines. IDS = indigo disulfonate, DT = dithionite, Eu^{II}-DTPA = europium (II) diethylenetriaminepentaacetic acid. Conditions: four (**A** and **B**) or ten scans (**C** and **D**) were run at 10 K with a microwave power of 50 mW and a microwave frequency of 9.62 GHz.

7.10 Summary and Conclusion

The intrinsic ability of the $[Fe_4S_4]^{Syn}$ cluster to reduce CO_2 and CO implicates the FeS cluster of the various Fe protein homologs to be responsible for the same reaction that has been by these proteins. However, as has been observed, these Fe proteins exhibit unique product profiles. Work was undertaken to investigate the role that the protein scaffold may play on the ability to catalyze this reaction. Cluster location and accessibility appear to be contributing

factors that can be used explain the difference in activity of *Ma*NifH and *Dv*NifH. The inability of *Ma*VnfH to reduce CO_2, despite cluster accessibility similar to that of the most prolific Fe protein to reduce substrate – *Ma*NifH, indicates that other factors also likely contribute to the reactivity of these proteins. It was observed that the cluster of *Ma*VnfH can partially occupy the all-ferrous state in a weaker reductant than other Fe protein homologs, and this may contribute to the reduced activity observed by this Fe protein, also indicating that the reduction potential of this protein may be more positive than other Fe protein homologs. Additional work is required to obtain the reduction potential of the homologs and to determine whether other factors, including the local protein environment, also contribute to the unique product profiles observed. This work may provide structural insights into how synthetic catalysts could be designed to generate fuel from CO_2 or CO.

7.11 Supplemental Tables and Figures

Table 7.1 Data Collection and Refinement Statistics for the *Av*NifH^{0} and *Ma*NifH^{1C} Structures.

	*Av*NifH^{0}	*Ma*NifH^{1C}
Data Collection		
Space group	P 1 21 1	P 65 2 2
Cell dimensions		
a, b, c (Å)	57.071, 93.045, 60.796	96.169, 96.169, 320.273
α, β, γ (º)	90, 98.875, 90	90, 90, 120
Wavelength (Å)	0.98557	0.97741
Number of reflections measured	164723 (15578)*	1251298 (111956)
Number of unique reflections	82895 (5292)	36265 (3530)
Resolution (Å)	35.89 - 1.588 (1.645 - 1.588)	83.28 - 2.38 (2.465 - 2.38)
R_{meas}	0.04522 (0.7816)	0.7685 (1.751)
$CC_{1/2}$	0.997 (0.628)	0.76 (0.641)
Mean I/σ(I)	8.12 (0.92)	20.99 (2.53)
Completeness (%)	99.0 (96.0)	99.94 (99.77)
Multiplicity	2.0 (1.9)	34.5 (31.6)
Refinement		
R_{work} / R_{free} †(%)	19.96/22.38	18.72/22.52
Number of atoms		
Overall	4754	4216
Protein / Ligand / Water	4357/8/0	4092/27/97
Average B factors (Å^2)		
Overall	35.59	49.43
Protein / Ligand / Water	35.04/18.74/42.05	49.62/42.55/43.19
Ramachandran plot statistics		
Favored / Allowed (%)	96/3.5	94.81/4.26
R.M.S. deviations		
Bond lengths (Å)	0.014	0.032
Bond angles (º)	1.54	2.28

* Values in parentheses represent the highest resolution shell.
† R-work is calculated using 95% of the data included in refinement and R-free of the 5% excluded.

Table 7.2 Data Collection and Refinement Statistics for the *Dv*NifH Structure in the DT-reduced state.

Data collection	
Space group	$P6_122$
Cell dimensions	
a, b, c (Å)	103.4, 103.4, 197.1
α, β, γ (º)	90.0, 90.0, 120.0
Wavelength (Å)	0.9999
Number of reflections measured	1,091,807
Number of unique reflections	17,326
Resolution (Å)	89.5 – 2.7
R_{meas} (%)	10.9 (78.9)*
$CC_{1/2}$	0.999 (0.862)
Mean I/σ(I)	6.2 (1.0)
Completeness (%)	97.9 (98.8)
Multiplicity	14.0 (14.3)
Refinement	
R_{work} / R_{free} †(%)	23.37 / 27.74
Number of atoms	
Overall	4,056
Protein / Ligand / Water	3,998 / 20 / 38
Average B factors (Å^2)	
Overall	51.97
Protein / Ligand / Water	52.11 / 39.81 / 43.79
Ramachandran plot statistics	
Favored / Allowed (%)	95.73 / 4.27
R.M.S. deviations	
Bond lengths (Å)	0.002
Bond angles (º)	0.51

* Values in parentheses represent the highest resolution shell.

† R-work is calculated using 95% of the data included in refinement and R-free of the 5% excluded.

Table 7.3 Data Collection and Refinement Statistics for the *Ma*VnfH Structures in the DT-reduced $[Fe_4S_4]^{1+}$ and Eu^{II}-DTPA-reduced $[Fe_4S_4]^0$ states.

	*Ma*VnfH $[Fe_4S_4]^{1+}$	*Ma*VnfH $[Fe_4S_4]^0$
Data Collection		
Space group	*P2₁*	$P2_1$
Cell dimensions		
a, b, c (Å)	46.2, 79.3, 87.4	45.0, 75.9, 87.2
α, β, γ (°)	β =96.6	β=99.29
Wavelength (Å)	0.9794	0.9999
Number of reflections measured	443,697	2,647,524
Number of unique reflections	43,841	45,864
Resolution (Å)	50.0 – 1.95 (2.06– 1.95)	100.0 – 1.90 (2.0 - 1.90)
R_{meas}	8.6 (53.0)	10.8 (46.8)
$CC_{1/2}$	0.992 (0.897)	0.995 (0.893)
Mean I/σ(I)	3.6 (1.4)	4.6 (1.6)
Completeness (%)	93.9 (95.7)	100.0 (100.0)
Multiplicity	2.6 (2.7)	5.8 (5.9)
Refinement		
R_{work} / R_{free} [†](%)	19.65 / 22.34	19.94 / 23.29
Number of atoms		
Overall	4,084	4,191
Protein / Ligand / Water	3,971/8/105	3,994/28/169
Average B factors (Å^2)		
Overall	38.44	25.59
Protein / Ligand / Water	38.41/30.58/39.91	25.37/31.76/29.77
Ramachandran plot statistics		
Favored / Allowed (%)	98.16/1.84	98.52/1.48
R.M.S. deviations		
Bond lengths (Å)	0.010	0.007
Bond angles (°)	1.013	0.788

[*] Values in parentheses represent the highest resolution shell.
[†] R-work is calculated using 95% of the data included in refinement and R-free of the 5% excluded.

7.12 Materials and Methods

7.12.1 Experimental Section

Unless otherwise specified, all chemicals were purchased from Thermo-Fisher Scientific and Sigma-Aldrich. Air-free manipulations were performed in a Vacuum Atmospheres Omni-lab glovebox with an argon atmosphere operating at < 2 ppm O_2. Water was purified using a Barnstead E-Pure water purification system (Thermo Scientific).

7.12.2 Cell Growth and Protein Purification

Non-tagged, Mo-nitrogenase Fe protein from *A. vinelandii*, designated *Av*NifH, was grown as described elsewhere.[15,22] His-tagged Mo- and V-nitrogenase Fe proteins from *M. acetivorans*, designated as *Ma*NifH and *Ma*VnfH, respectively, and His-tagged Mo-nitrogenase Fe protein from *Desulfovibrio vulgaris* were grown in *E. coli* as reported earlier.[134] Published methods were used for the purification of these homologs from their respective expression strains.[15,22,134]

7.12.3 Assays of CO- and CO_2-reduction with Fe Proteins

In vitro CO and CO_2 reduction assays were carried out in the presence of 100 mM europium (II) diethylenetriaminepentaacetate (Eu^{II}-DTPA) following previously published protocols and quantified using the techniques outlined.[62,241]

7.12.4 Crystallization and Data Collection

*Av*NifH was crystallized after Strop *et al.*, with some modifications.[55] The purified protein was buffer exchanged on a Sephadex G-25 fine (GE Healthcare) column equilibrated with 50 mM tris (pH 8.0), 450 mM NaCl, 20% glycerol, and then spin concentrated to 25 mg/mL in an Amicon Ultra 30 kDa MWCO centrifuge filter (Merck Millipore). A solution of 100 mM europium (II)-ethylene glycol-bis(2-aminoethylether)-N,N,N′,N′-tetraacetic acid (Eu^{II}-EGTA) in 1 M tris pH 8.0 was added to the protein to a final concentration of 10 mM Eu^{II}-EGTA. Upon addition of this strong reductant, the protein solution instantly turned from brown to red, indicating the reduction of the protein-bound cluster to the all-ferrous state. *Av*NifH was crystallized by the liquid-liquid diffusion technique in glass capillaries by layering the protein solution beneath a filtered precipitant solution containing 100 mM Tris (pH 8.0), 900 mM NaCl,

and 27% PEG 4,000. Pink crystals appeared within one day and were frozen after a week. Data were collected at -170 °C SSRL beamline 9-2 on a Dectris Pilatus 6M detector.

*Ma*NifH, *Dv*NifH, and *Ma*VnfH were crystallized by the microbatch-under-oil method in microbatch trays (Greiner) under a layer of Al's oil (Hampton Research). *Ma*NifH protein was desalted on a G-25 column equilibrated with 10mM EPPS (pH 8.0), 100 mM NaCl, 10% glycerol, 2 mM dithionite and then spin concentrated to 10 mg/mL. The crystallization drops contained 1 μL protein solution combined with a 3μL of a precipitating solution consisting of 2.3 M ammonium sulfate, 7% PEG 3350, 67 mM sodium malonate, and 2 mM dithionite. Crystals appeared after two weeks and were frozen after four weeks. Data were collected at -170 °C ALS beamline 8.2.1 equipped with an ADSC Q315r CCD array detector.

*Dv*NifH crystals were grown from 1 μL of precipitation solution containing 0.1 M cobalt (II) chloride hexahydrate, 0.1 M MES monohydrate pH 6.5, and 1.8 M ammonium sulfate. Crystals appeared after one week and were frozen. Data were collected at -170 °C ALS beamline 8.2.1 equipped with an ADSC Q315r CCD array detector.

*Ma*VnfH crystals were grown from 1 μL of precipitation solution containing 2% v/v Tacsimate (pH 6.0), 0.1 M Bis-Tris (pH 6.5), and 20% w/v PEG 3,350 and 1 μL of protein solution containing 10 mg/mL of *Ma*VnfH in 50 mM Tris (pH 8.0), 500 mM NaCl, 250 mM imidazole, 10% glycerol, and 2 mM dithionite. *Ma*VnfH crystals appeared after one week. The conditions were appropriate for the cluster to occupy the 1+ oxidation state. Additional crystals were soaked in 5 μL of solution consisting of 10 mM Eu^{II}-DTPA, 0.04 M citric acid, 0.06 M bis-tris propane (pH 6.4), and 20% w/v PEG 3,350. The crystals in this solution changed from brown to pink, indicative of an all-ferrous state, within 15 minutes of adding the Eu^{II}-DTPA solution.[55]

The pink crystals were immediately frozen for later analysis. Data were collected at -170 °C SSRL beamline 9-2 on a Dectris Pilatus 6M detector.

7.13 Contributions

Caleb Hiller performed the biochemistry work related to proteins, crystallized the proteins *Dv*NifH, and collected the data set. Wonchull Kang solved the *Dv*NifH structure. Lee Rettberg and Caleb Hiller worked together to obtain crystals of *Ma*NifH, and Lee solved the structures of *Ma*NifH used in this chapter. Caleb Hiller crystallized both oxidation states of *Ma*VnfH and solved the structures.

References

1. Darwent, B. deB. *Bond dissociation energies in simple molecules*. (U.S. Dept. of Commerce, National Bureau of Standards, 1970).

2. Schlögl, R. Catalytic Synthesis of Ammonia—A "Never-Ending Story"? *Angew. Chem., Int. Ed. Engl.* **42**, 2004–2008 (2003).

3. Burgess, B. K. & Lowe, D. J. Mechanism of molybdenum nitrogenase. *Chem. Rev.* **96**, 2983–3011 (1996).

4. Howard, J. B. & Rees, D. C. Structural basis of biological nitrogen fixation. *Chem. Rev.* **96**, 2965–2982 (1996).

5. Eady, R. R. Structure-function relationships of alternative nitrogenases. *Chem. Rev.* **96**, 3013–3030 (1996).

6. Joerger, R. D. & Bishop, P. E. Bacterial alternative nitrogen fixation systems. *Crit. Rev. Microbiol.* **16**, 1–14 (1988).

7. Ribbe, M. W., Hu, Y., Hodgson, K. O. & Hedman, B. Biosynthesis of nitrogenase metalloclusters. *Chem. Rev.* **114**, 4063–4080 (2014).

8. Dos Santos, P. C., Johnson, D. C., Ragle, B. E., Unciuleac, M.-C. & Dean, D. R. Controlled expression of *nif* and *isc* iron-sulfur protein maturation components reveals target specificity and limited functional replacement between the two systems. *J. Bacteriol.* **189**, 2854–2862 (2007).

9. Smith, A. D. *et al.* NifS-mediated assembly of [4Fe-4S] clusters in the N- and C-terminal domains of the NifU scaffold protein. *Biochemistry* **44**, 12955–12969 (2005).

10. Yuvaniyama, P., Agar, J. N., Cash, V. L., Johnson, M. K. & Dean, D. R. NifS-directed assembly of a transient [2Fe-2S] cluster within the NifU protein. *Proc. Natl. Acad. Sci. U.S.A.* **97**, 599–604 (2000).

11. Zheng, L., White, R. H., Cash, V. L. & Dean, D. R. Mechanism for the desulfurization of L-cysteine catalyzed by the *nifS* gene product. *Biochemistry* **33**, 4714–4720 (1994).

12. Zheng, L., White, R. H., Cash, V. L., Jack, R. F. & Dean, D. R. Cysteine desulfurase activity indicates a role for NifS in metallocluster biosynthesis. *Proc. Natl. Acad. Sci. U.S.A.* **90**, 2754–2758 (1993).

13. Zheng, L. & Dean, D. R. Catalytic formation of a nitrogenase iron-sulfur cluster. *J. Biol. Chem.* **269**, 18723–18726 (1994).

14. Wiig, J. A., Hu, Y., Lee, C. C. & Ribbe, M. W. Radical SAM-dependent carbon insertion into the nitrogenase M-cluster. *Science* **337**, 1672–1675 (2012).

15. Hu, Y., Fay, A. W. & Ribbe, M. W. Identification of a nitrogenase FeMo cofactor precursor on NifEN complex. *Proc. Natl. Acad. Sci. U.S.A.* **102**, 3236–3241 (2005).

16. Hu, Y. *et al.* FeMo cofactor maturation on NifEN. *Proc. Natl. Acad. Sci. U.S.A.* **103**, 17119–17124 (2006).

17. Kaiser, J. T., Hu, Y., Wiig, J. A., Rees, D. C. & Ribbe, M. W. Structure of precursor-bound NifEN: a nitrogenase FeMo cofactor maturase/insertase. *Science* **331**, 91–94 (2011).

18. Yoshizawa, J. M. *et al.* Optimization of FeMoco maturation on NifEN. *J. Am. Chem. Soc.* **131**, 9321–9325 (2009).

19. Filler, W. A. *et al.* The *nifH* gene product is required for the synthesis or stability of the iron-molybdenum cofactor of nitrogenase from *Klebsiella pneumoniae*. *Eur. J. Biochem.* **160**, 371–377 (1986).

20. Hernandez, J. A. *et al.* Metal trafficking for nitrogen fixation: NifQ donates molybdenum to NifEN/NifH for the biosynthesis of the nitrogenase FeMo-cofactor. *Proc. Natl. Acad. Sci. U.S.A.* **105**, 11679–11684 (2008).

21. Ribbe, M. W., Hu, Y., Guo, M., Schmid, B. & Burgess, B. K. The FeMoco-deficient MoFe protein produced by a *nifH* deletion strain of *Azotobacter vinelandii* shows unusual P-cluster features. *J. Biol. Chem.* **277**, 23469–23476 (2002).

22. Lee, C. C. *et al.* Stepwise formation of P-cluster in nitrogenase MoFe protein. *Proc. Natl. Acad. Sci. U.S.A.* **106**, 18474–18478 (2009).

23. Hu, Y., Fay, A. W., Lee, C. C. & Ribbe, M. W. P-cluster maturation on nitrogenase MoFe protein. *Proc. Natl. Acad. Sci. U.S.A.* **104**, 10424–10429 (2007).

24. Hu, Y., Fay, A. W., Dos Santos, P. C., Naderi, F. & Ribbe, M. W. Characterization of *Azotobacter vinelandii nifZ* deletion strains: indication of stepwise MoFe protein assembly. *J. Biol. Chem.* **279**, 54963–54971 (2004).

25. Fay, A. W., Wiig, J. A., Lee, C. C. & Hu, Y. Identification and characterization of functional homologs of nitrogenase cofactor biosynthesis protein NifB from methanogens. *Proc. Natl. Acad. Sci. U.S.A.* **112**, 14829–14833 (2015).

26. Lancaster, K. M. *et al.* X-ray emission spectroscopy evidences a central carbon in the nitrogenase iron-molybdenum cofactor. *Science* **334**, 974–977 (2011).

27. Tufty, R. M. & Kretsinger, R. H. Troponin and parvalbumin calcium binding regions predicted in myosin light chain and T4 lysozyme. *Science* **187**, 167–169 (1975).

28. Hanas, J. S., Hazuda, D. J., Bogenhagen, D. F., Wu, F. Y. & Wu, C. W. Xenopus transcription factor A requires zinc for binding to the 5 S RNA gene. *J. Biol. Chem.* **258**, 14120–14125 (1983).

29. Skou, J. C. The influence of some cations on an adenosine triphosphatase from peripheral nerves. *Biochim. Biophys. Acta.* **23**, 394–401 (1957).

30. Munn, C. A. M. Researches on myohaematin and the histohaematins. *Phil. Trans. R. Soc. Lond.* **177**, 267–298 (1886).

31. Katoh, S. The discovery and function of plastocyanin: a personal account. *Photosyn. Res.* **43**, 177–189 (1995).

32. Stephenson, M. & Stickland, L. H. Hydrogenase: the bacterial formation of methane by the reduction of one-carbon compounds by molecular hydrogen. *Biochem. J.* **27**, 1517–1527 (1933).

33. Tezcan, F. A. *et al.* Nitrogenase complexes: multiple docking sites for a nucleotide switch protein. *Science* **309**, 1377–1380 (2005).

34. Schindelin, H., Kisker, C., Schlessman, J. L., Howard, J. B. & Rees, D. C. Structure of $ADP{\cdot}AlF_4^-$-stabilized nitrogenase complex and its implications for signal transduction. *Nature* **387**, 370–376 (1997).

35. Spatzal, T. *et al.* Evidence for interstitial carbon in nitrogenase FeMo cofactor. *Science* **334**, 940 (2011).

36. Einsle, O. *et al.* Nitrogenase MoFe-protein at 1.16 Å resolution: A central ligand in the FeMo-cofactor. *Science* **297**, 1696–1700 (2002).

37. Kim, J. & Rees, D. C. Crystallographic structure and functional implications of the nitrogenase molybdenum-iron protein from *Azotobacter vinelandii*. *Nature* **360**, 553–560 (1992).

38. *The PyMOL Molecular Graphics System*. (Schrödinger, LLC).

39. Hales, B. J., Case, E. E., Morningstar, J. E., Dzeda, M. F. & Mauterer, L. A. Isolation of a new vanadium-containing nitrogenase from *Azotobacter vinelandii*. *Biochemistry* **25**, 7251–7255 (1986).

40. Sippel, D. & Einsle, O. The structure of vanadium nitrogenase reveals an unusual bridging ligand. *Nat. Chem. Biol.* **13**, 956–960 (2017).

41. Dyer, D. H. *et al.* The three-dimensional structure of the core domain of NafY from *Azotobacter vinelandii* determined at 1.8-Å resolution. *J. Biol. Chem.* **278**, 32150–32156 (2003).

42. Homer, M. J., Paustian, T. D., Shah, V. K. & Roberts, G. P. The *nifY* product of *Klebsiella pneumoniae* is associated with apodinitrogenase and dissociates upon activation with the iron-molybdenum cofactor. *J. Bacteriol.* **175**, 4907–4910 (1993).

43. Lee, C. C., Hu, Y. & Ribbe, M. W. Unique features of the nitrogenase VFe protein from *Azotobacter vinelandii*. *Proc. Natl. Acad. Sci. U.S.A.* **106**, 9209–9214 (2009).

44. Burgess, B. K. The iron-molybdenum cofactor of nitrogenase. *Chem. Rev.* **90**, 1377–1406 (1990).

45. Fay, A. W. *et al.* Characterization of isolated nitrogenase FeVco. *J. Am. Chem. Soc.* **132**, 12612–12618 (2010).

46. Cutsail, G. E., Telser, J. & Hoffman, B. M. Advanced paramagnetic resonance spectroscopies of iron–sulfur proteins: Electron nuclear double resonance (ENDOR) and electron spin echo envelope modulation (ESEEM). *BBA - Mol. Cell Res.* **1853**, 1370–1394 (2015).

47. Pierik, A. J., Wassink, H., Haaker, H. & Hagen, W. R. Redox properties and EPR spectroscopy of the P clusters of *Azotobacter vinelandii* MoFe protein. *Eur. J. Biochem.* **212**, 51–61 (1993).

48. Surerus, K. K. *et al.* Mössbauer and integer-spin EPR of the oxidized P-clusters of nitrogenase: P^{OX} is a non-Kramers system with a nearly degenerate ground doublet. *J. Am. Chem. Soc.* **114**, 8579–8590 (1992).

49. Watt, G. D., Burns, A., Lough, S. & Tennent, D. L. Redox and spectroscopic properties of oxidized MoFe protein from *Azotobacter vinelandii*. *Biochemistry* **19**, 4926–4932 (1980).

50. Chan, M. K., Kim, J. & Rees, D. C. The nitrogenase FeMo-cofactor and P-cluster pair: 2.2 Å resolution structures. *Science* **260**, 792–4 (1993).

51. Peters, J. W. *et al.* Redox-dependent structural changes in the nitrogenase P-cluster. *Biochemistry* **36**, 1181–1187 (1997).

52. Georgiadis, M. M. *et al.* Crystallographic structure of the nitrogenase iron protein from *Azotobacter vinelandii*. *Science* **257**, 1653–1659 (1992).

53. Andrew Jasniewski, Nathaniel Sickerman, Yilin Hu & Markus Ribbe. The Fe protein: An unsung hero of nitrogenase. *Inorganics* **6**, 25 (2018).

54. Walker, J. E., Saraste, M., Runswick, M. J. & Gay, N. J. Distantly related sequences in the alpha- and beta-subunits of ATP synthase, myosin, kinases and other ATP-requiring enzymes and a common nucleotide binding fold. *EMBO J.* **1**, 945–951 (1982).

55. Strop, P. *et al.* Crystal structure of the all-ferrous $[4Fe\text{-}4S]^0$ form of the nitrogenase iron protein from *Azotobacter vinelandii*. *Biochemistry* **40**, 651–656 (2001).

56. Rohde, M., Trncik, C., Sippel, D., Gerhardt, S. & Einsle, O. Crystal structure of VnfH, the iron protein component of vanadium nitrogenase. *J. Biol. Inorg. Chem.* (2018). doi:10.1007/s00775-018-1602-4

57. Jang, S. B., Seefeldt, L. C. & Peters, J. W. Insights into nucleotide signal transduction in nitrogenase: structure of an iron protein with MgADP bound. *Biochemistry* **39**, 14745–14752 (2000).

58. Sen, S. *et al.* Insights into the role of nucleotide-dependent conformational change in nitrogenase catalysis: structural characterization of the nitrogenase Fe protein Leu127 deletion variant with bound MgATP. *J. Inorg. Biochem.* **100**, 1041–1052 (2006).

59. Chiu, H.-J. *et al.* MgATP-bound and nucleotide-free structures of a nitrogenase protein complex between the Leu 127Δ-Fe-Protein and the MoFe-Protein. *Biochemistry* **40**, 641–650 (2001).

60. Hu, Y. *et al.* Nitrogenase Fe protein: a molybdate/homocitrate insertase. *Proc. Natl. Acad. Sci. U.S.A.* **103**, 17125–17130 (2006).

61. Rubio, L. M. & Ludden, P. W. Biosynthesis of the iron-molybdenum cofactor of nitrogenase. *Annu. Rev. Microbiol.* **62**, 93–111 (2008).

62. Rebelein, J. G., Stiebritz, M. T., Lee, C. C. & Hu, Y. Activation and reduction of carbon dioxide by nitrogenase iron proteins. *Nat. Chem. Biol.* **13**, 147–149 (2017).

63. Rees, D. C. Dinitrogen reduction by nitrogenase: if N_2 isn't broken, it can't be fixed. *Curr. Opin. Struc. Biol.* **3**, 921–928 (1993).

64. Onate, Y. A., Finnegan, M. G., Hales, B. J. & Johnson, M. K. Variable temperature magnetic circular dichroism studies of reduced nitrogenase iron proteins and $[4Fe\text{-}4S]^{+}$ synthetic analog clusters. *Biochimica et Biophysica Acta (BBA) - Protein Structure and Molecular Enzymology* **1164**, 113–123 (1993).

65. Blank, M. A. *et al.* Structural models of the $[Fe_4S_4]$ clusters of homologous nitrogenase Fe proteins. *Inorg. Chem.* **50**, 7123–7128 (2011).

66. Lindahl, P. A., Day, E. P., Kent, T. A., Orme-Johnson, W. H. & Münck, E. Mössbauer, EPR, and magnetization studies of the *Azotobacter vinelandii* Fe protein. Evidence for a $[4Fe\text{-}4S]^{1+}$ cluster with spin S = 3/2. *J. Biol. Chem.* **260**, 11160–11173 (1985).

67. Yoo, S. J., Angove, H. C., Burgess, B. K., Hendrich, M. P. & Münck, E. Mössbauer and integer-spin EPR studies and spin-coupling analysis of the $[4Fe\text{-}4S]^{0}$ cluster of the Fe protein from *Azotobacter vinelandii* nitrogenase. *J. Am. Chem. Soc.* **121**, 2534–2545 (1999).

68. Chakrabarti, M., Deng, L., Holm, R. H., Münck, E. & Bominaar, E. L. Mössbauer, electron paramagnetic resonance, and theoretical studies of a carbene-based all-ferrous Fe_4S_4 cluster: electronic origin and structural identification of the unique spectroscopic site. *Inorg. Chem.* **48**, 2735–2747 (2009).

69. Chakrabarti, M., Münck, E. & Bominaar, E. L. Density functional theory study of an all ferrous 4Fe-4S cluster. *Inorg. Chem.* **50**, 4322–4326 (2011).

70. Angove, H. C., Yoo, S. J., Burgess, B. K. & Münck, E. Mössbauer and EPR evidence for an all-ferrous Fe_4S_4 cluster with $S = 4$ in the Fe protein of nitrogenase. *J. Am. Chem. Soc.* **119**, 8730–8731 (1997).

71. Seefeldt, L. C. *et al.* Energy transduction in nitrogenase. *Acc. Chem. Res.* (2018). doi:10.1021/acs.accounts.8b00112

72. Yates, M. G. Electron transport to nitrogenase in *Azotobacter chroococcum* : *Azotobacter* flavodoxin hydroquinone as an electron donor. *FEBS Letters* **27**, 63–67 (1972).

73. Duyvis, M. G., Wassink, H. & Haaker, H. Nitrogenase of *Azotobacter vinelandii*: kinetic analysis of the Fe protein redox cycle. *Biochemistry* **37**, 17345–17354 (1998).

74. Bennett, L. T., Jacobson, M. R. & Dean, D. R. Isolation, sequencing, and mutagenesis of the *nifF* gene encoding flavodoxin from *Azotobacter vinelandii*. *J. Biol. Chem.* **263**, 1364–1369 (1988).

75. Thorneley, R. N. & Deistung, J. Electron-transfer studies involving flavodoxin and a natural redox partner, the iron protein of nitrogenase. Conformational constraints on protein-protein interactions and the kinetics of electron transfer within the protein complex. *Biochem. J.* **253**, 587–595 (1988).

76. Martin, A. E. *et al.* Construction and characterization of an *Azotobacter vinelandii* strain with mutations in the genes encoding flavodoxin and ferredoxin I. *J. Bacteriol.* **171**, 3162–3167 (1989).

77. Watt, G. D. An electrochemical method for measuring redox potentials of low potential proteins by microcoulometry at controlled potentials. *Anal. Biochem.* **99**, 399–407 (1979).

78. Lanzilotta, W. N., Ryle, M. J. & Seefeldt, L. C. Nucleotide hydrolysis and protein conformational changes in *Azotobacter vinelandii* nitrogenase iron protein: defining the function of aspartate 129. *Biochemistry* **34**, 10713–10723 (1995).

79. Watt, G. D. & Reddy, K. R. N. Formation of an all ferrous Fe_4S_4 cluster in the iron protein component of *Azotobacter vinelandii* nitrogenase. *J. Inorg. Biochem.* **53**, 281–294 (1994).

80. Lowery, T. J. *et al.* Flavodoxin hydroquinone reduces *Azotobacter vinelandii* Fe protein to the all-ferrous redox state with a S = 0 spin state. *Proc. Natl. Acad. Sci. U.S.A.* **103**, 17131–17136 (2006).

81. Guo, M., Sulc, F., Ribbe, M. W., Farmer, P. J. & Burgess, B. K. Direct assessment of the reduction potential of the $[4Fe{-}4S]^{1+/0}$ couple of the Fe protein from *Azotobacter vinelandii*. *J. Am. Chem. Soc.* **124**, 12100–12101 (2002).

82. Vincent, K. A. *et al.* Instantaneous, stoichiometric generation of powerfully reducing states of protein active sites using Eu(ii) and polyaminocarboxylate ligands. *Chem. Commun.* 2590–2591 (2003). doi:10.1039/b308188e

83. Walker, G. A. & Mortenson, L. E. Effect of magnesium adenosine 5'-triphosphate on the accessibility of the iron of clostridial azoferredoxin, a component of nitrogenase. *Biochemistry* **13**, 2382–2388 (1974).

84. Ljones, T. & Burris, R. H. Nitrogenase: the reaction between iron protein and bathophenanthrolinedisulfonate as a probe for interactions with MgATP. *Biochemistry* **17**, 1866–1872 (1978).

85. Deits, T. L. & Howard, J. B. Kinetics of MgATP-dependent iron chelation from the Fe-protein of the *Azotobacter vinelandii* nitrogenase complex. Evidence for two states. *J. Biol. Chem.* **264**, 6619–6628 (1989).

86. Chen, L. *et al.* MgATP-induced conformational changes in the iron protein from *Azotobacter vinelandii*, as studied by small-angle x-ray scattering. *J. Biol. Chem.* **269**, 3290–3294 (1994).

87. Tezcan, F. A., Kaiser, J. T., Howard, J. B. & Rees, D. C. Structural evidence for asymmetrical nucleotide interactions in nitrogenase. *J. Am. Chem. Soc.* **137**, 146–149 (2015).

88. Willing, A. H., Georgiadis, M. M., Rees, D. C. & Howard, J. B. Cross-linking of nitrogenase components. Structure and activity of the covalent complex. *J. Biol. Chem.* **264**, 8499–8503 (1989).

89. Willing, A. & Howard, J. B. Cross-linking site in *Azotobacter vinelandii* complex. *J. Biol. Chem.* **265**, 6596–6599 (1990).

90. Seefeldt, L. C. Docking of nitrogenase iron- and molybdenum-iron proteins for electron transfer and MgATP hydrolysis: the role of arginine 140 and lysine 143 of the *Azotobacter vinelandii* iron protein. *Protein Sci.* **3**, 2073–2081 (1994).

91. Gavini, N. & Burgess, B. K. FeMo cofactor synthesis by a *nifH* mutant with altered MgATP reactivity. *J. Biol. Chem.* **267**, 21179–21186 (1992).

92. Ryle, M. J. & Seefeldt, L. C. Elucidation of a MgATP signal transduction pathway in the nitrogenase iron protein: formation of a conformation resembling the MgATP-bound state by protein engineering. *Biochemistry* **35**, 4766–4775 (1996).

93. Seefeldt, L. C., Hoffman, B. M. & Dean, D. R. Electron transfer in nitrogenase catalysis. *Curr. Opin. Chem. Biol.* **16**, 19–25 (2012).

94. Thorneley, R. N., Lowe, D. J., Eday, R. R. & Miller, R. W. The coupling of electron transfer in nitrogenase to the hydrolysis of magnesium adenosine triphosphate. *Biochem. Soc. Trans.* **7**, 633–636 (1979).

95. Hageman, R. V., Orme-Johnson, W. H. & Burris, R. H. Role of magnesium adenosine 5'-triphosphate in the hydrogen evolution reaction catalyzed by nitrogenase from *Azotobacter vinelandii*. *Biochemistry* **19**, 2333–2342 (1980).

96. Yates, M. G. The enzymology of molybdenum dependent nitrogen fixation. in (eds. Stacey, G., Burris, R. H. & Evans, H. J.) 685–735 (Chapman & Hall, 1992).

97. Burgess, B. K. Advances in Nitrogen Fixation Research. in (eds. Veeger, C. & Newton, W. E.) 103 (Nijhoff/Junk Publishers, 1984).

98. Eady, R. R., Lowe, D. J. & Thorneley, R. N. Nitrogenase of *Klebsiella pneumoniae*: a pre-steady state burst of ATP hydrolysis is coupled to electron transfer between the component proteins. *FEBS Lett.* **95**, 211–213 (1978).

99. Tanifuji, K. *et al.* Structure and reactivity of an asymmetric synthetic mimic of nitrogenase cofactor. *Angew. Chem., Int. Ed. Engl.* **55**, 15633–15636 (2016).

100. Dos Santos, P. C., Dean, D. R., Hu, Y. & Ribbe, M. W. Formation and insertion of the nitrogenase iron-molybdenum cofactor. *Chem. Rev.* **104**, 1159–1173 (2004).

101. Hu, Y. & Ribbe, M. W. Biosynthesis of the iron-molybdenum cofactor of nitrogenase. *J. Biol. Chem.* **288**, 13173–13177 (2013).

102. Hu, Y. & Ribbe, M. W. Nitrogenase assembly. *Biochim. Biophys. Acta, Bioenerg.* **1827**, 1112–1122 (2013).

103. Hu, Y. & Ribbe, M. W. Biosynthesis of nitrogenase FeMoco. *Coord. Chem. Rev.* **255**, 1218–1224 (2011).

104. Hu, Y. & Ribbe, M. W. Biosynthesis of the metalloclusters of molybdenum nitrogenase. *Microbiol. Mol. Biol. Rev.* **75**, 664–677 (2011).

105. Schwarz, G., Mendel, R. R. & Ribbe, M. W. Molybdenum cofactors, enzymes and pathways. *Nature* **460**, 839–847 (2009).

106. Hu, Y., Fay, A. W., Lee, C. C., Yoshizawa, J. & Ribbe, M. W. Assembly of nitrogenase MoFe protein. *Biochemistry* **47**, 3973–3981 (2008).

107. Wiig, J. A., Lee, C. C., Hu, Y. & Ribbe, M. W. Tracing the interstitial carbide of the nitrogenase cofactor during substrate turnover. *J. Am. Chem. Soc.* **135**, 4982–4983 (2013).

108. Tanifuji, K. *et al.* Tracing the 'ninth sulfur' of the nitrogenase cofactor via a semi-synthetic approach. *Nat. Chem.* **10**, 568–572 (2018).

109. Kennedy, C. & Dean, D. The *nifU*, *nifS* and *nifV* gene products are required for activity of all three nitrogenases of *Azotobacter vinelandii*. *Mol. Gen. Genet.* **231**, 494–498 (1992).

110. Christiansen, J., Goodwin, P. J., Lanzilotta, W. N., Seefeldt, L. C. & Dean, D. R. Catalytic and biophysical properties of a nitrogenase apo-MoFe protein produced by a *nifB*-Deletion Mutant of *Azotobacter vinelandii*. *Biochemistry* **37**, 12611–12623 (1998).

111. Paustian, T. D., Shah, V. K. & Roberts, G. P. Apodinitrogenase: purification, association with a 20-kilodalton protein, and activation by the iron-molybdenum cofactor in the absence of dinitrogenase reductase. *Biochemistry* **29**, 3515–3522 (1990).

112. Hawkes, T. R. & Smith, B. E. Purification and characterization of the inactive MoFe protein (NifB-Kp1) of the nitrogenase from *nifB* mutants of *Klebsiella pneumoniae*. *Biochem. J.* **209**, 43–50 (1983).

113. Hawkes, T. R. & Smith, B. E. The inactive MoFe protein (NifB-Kp1) of the nitrogenase from *nifB* mutants of *Klebsiella pneumoniae*. Its interaction with FeMo-cofactor and the properties of the active MoFe protein formed. *Biochem. J.* **223**, 783–92 (1984).

114. Schmid, B. *et al.* Structure of a cofactor-deficient nitrogenase MoFe protein. *Science* **296**, 352–356 (2002).

115. Wiig, J. A., Hu, Y. & Ribbe, M. W. NifEN-B complex of *Azotobacter vinelandii* is fully functional in nitrogenase FeMo cofactor assembly. *Proc. Natl. Acad. Sci. U.S.A.* **108**, 8623–8627 (2011).

116. Rettberg, L. A. *et al.* Probing the coordination and function of $Fe_{4S}4$ modules in nitrogenase assembly protein NifB. *Nat. Comm.* **9**, 2824 (2018).

117. Fay, A. W. *et al.* Spectroscopic characterization of the isolated iron-molybdenum cofactor (FeMoco) precursor from the protein NifEN. *Angew. Chem., Int. Ed. Engl.* **50**, 7787–7790, S7787/1-S7787/11 (2011).

118. Corbett, M. C. *et al.* Structural insights into a protein-bound iron-molybdenum cofactor precursor. *Proc. Natl. Acad. Sci. U.S.A.* **103**, 1238–1243 (2006).

119. Brigle, K. E., Weiss, M. C., Newton, W. E. & Dean, D. R. Products of the iron-molybdenum cofactor-specific biosynthetic genes, *nifE* and *nifN*, are structurally homologous to the products of the nitrogenase molybdenum-iron protein genes, *nifD* and *nifK*. *J. Bacteriol.* **169**, 1547–53 (1987).

120. Goodwin, P. J. *et al.* The *Azotobacter vinelandii* NifEN complex contains two identical [4Fe-4S] clusters. *Biochemistry* **37**, 10420–10428 (1998).

121. Fay, A. W. *et al.* Formation of a homocitrate-free iron-molybdenum cluster on NifEN: Implications for the role of homocitrate in nitrogenase assembly. *Dalton Trans.* **39**, 3124–3130 (2010).

122. Corbett, M. C. *et al.* Conformational differences between *Azotobacter vinelandii* nitrogenase MoFe proteins as studied by small-angle X-ray scattering. *Biochemistry* **46**, 8066–8074 (2007).

123. Ohki, Y., Tanifuji, K., Yamada, N., Cramer, R. E. & Tatsumi, K. Formation of a nitrogenase P-cluster [Fe_8S_7] core via reductive fusion of two all-ferric [Fe_4S_4] clusters. *Chem. Asian J.* **7**, 2222–2224 (2012).

124. Zhang, Y. & Holm, R. H. Structural conversions of molybdenum-iron-sulfur edge-bridged double cubanes and P^N-type clusters topologically related to the nitrogenase P-cluster. *Inorg. Chem.* **43**, 674–682 (2004).

125. Zhang, Y., Zuo, J.-L., Zhou, H.-C. & Holm, R. H. Rearrangement of symmetrical dicubane clusters into topological analogues of the P cluster of nitrogenase: nature's choice? *J. Am. Chem. Soc.* **124**, 14292–14293 (2002).

126. Corbett, M. C. *et al.* Comparison of iron-molybdenum cofactor-deficient nitrogenase MoFe proteins by X-ray absorption spectroscopy: implications for P-cluster biosynthesis. *J. Biol. Chem.* **279**, 28276–28282 (2004).

127. Broach, R. B. *et al.* Variable-temperature, variable-field magnetic circular dichroism spectroscopic study of the metal clusters in the *ΔnifB* and *ΔnifH* MoFe proteins of nitrogenase from *Azotobacter vinelandii*. *Biochemistry* **45**, 15039–15048 (2006).

128. Rupnik, K., Lee, C. C., Hu, Y., Ribbe, M. W. & Hales, B. J. $[4Fe4S]^{2+}$ clusters exhibit ground-state paramagnetism. *J. Am. Chem. Soc.* **133**, 6871–6873 (2011).

129. Cotton, M. S. *et al.* VTVH-MCD study of the *ΔnifBΔnifZ* MoFe Protein from *Azotobacter vinelandii*. *J. Am. Chem. Soc.* **131**, 4558–4559 (2009).

130. Danyal, K., Mayweather, D., Dean, D. R., Seefeldt, L. C. & Hoffman, B. M. Conformational gating of electron transfer from the nitrogenase Fe protein to MoFe protein. *J. Am. Chem. Soc.* **132**, 6894–6895 (2010).

131. Duval, S. *et al.* Electron transfer precedes ATP hydrolysis during nitrogenase catalysis. *Proc. Natl. Acad. Sci. U.S.A.* **110**, 16414–16419 (2013).

132. Yang, Z.-Y. *et al.* Evidence that the P_i release event is the rate-limiting step in the nitrogenase catalytic cycle. *Biochemistry* **55**, 3625–3635 (2016).

133. Lee, C. C., Hu, Y. & Ribbe, M. W. Vanadium nitrogenase reduces CO. *Science* **329**, 642 (2010).

134. Hiller, C. J., Stiebritz, M. T., Lee, C. C., Liedtke, J. & Hu, Y. Tuning electron flux through nitrogenase with methanogen iron protein homologues. *Chem. Eur. J.* **23**, 16152–16156 (2017).

135. Lee, C. C., Wilcoxen, J., Hiller, C. J., Britt, R. D. & Hu, Y. Evaluation of the catalytic relevance of the CO-bound states of V-nitrogenase. *Angew. Chem., Int. Ed. Engl.* **57**, 3411–3414 (2018).

136. Hu, Y. & Ribbe, M. W. Nitrogenases-A tale of carbon atom(s). *Angew. Chem., Int. Ed. Engl.* **55**, 8216–8226 (2016).

137. Hu, Y. & Ribbe, M. W. Nitrogenase and homologs. *J. Biol. Inorg. Chem.* **20**, 435–445 (2015).

138. Angove, H. C., Yoo, S. J., Munck, E. & Burgess, B. K. An all-ferrous state of the Fe protein of nitrogenase Interaction with nucleotides and electron transfer to the MoFe protein. *J. Biol. Chem.* **273**, 26330–26337 (1998).

139. Available at the open Joint Genome Institute (JGI) database. Available at: https://img.jgi.doe.gov/cgi-bin/m/main.cgi.

140. Tyree, B. & Webster, D. A. Electron-accepting properties of cytochrome *o* purified from *Vitreoscilla*. *J. Biol. Chem.* **253**, 7635–7637 (1978).

141. Schmid, B. *et al.* Biochemical and structural characterization of the cross-linked complex of nitrogenase: comparison to the ADP-AlF_4^--stabilized structure. *Biochemistry* **41**, 15557–15565 (2002).

142. Arnold, K., Bordoli, L., Kopp, J. & Schwede, T. The SWISS-MODEL workspace: a web-based environment for protein structure homology modelling. *Bioinformatics* **22**, 195–201 (2006).

143. Comeau, S. R., Gatchell, D. W., Vajda, S. & Camacho, C. J. ClusPro: a fully automated algorithm for protein-protein docking. *Nucleic Acids Res.* **32**, W96–W99 (2004).

144. Lee, C. C. *et al.* Uncoupling binding of substrate CO from turnover by vanadium nitrogenase. *Proc. Natl. Acad. Sci. U.S.A.* **112**, 13845–13849 (2015).

145. Spatzal, T., Perez, K. A., Einsle, O., Howard, J. B. & Rees, D. C. Ligand binding to the FeMo-cofactor: structures of CO-bound and reactivated nitrogenase. *Science* **345**, 1620–1623 (2014).

146. Lee, H.-I. *et al.* Electron inventory, kinetic assignment (E_n), structure, and bonding of nitrogenase turnover intermediates with C_2H_2 and CO. *J. Am. Chem. Soc.* **127**, 15880–15890 (2005).

147. Seefeldt, L. C., Hoffman, B. M. & Dean, D. R. Mechanism of Mo-dependent nitrogenase. *Annu. Rev. Biochem.* **78**, 701–722 (2009).

148. Burgess, B. K., Jacobs, D. B. & Stiefel, E. I. Large-scale purification of high activity *Azotobacter vinelandii* nitrogenase. *Biochim. Biophys. Acta* **614**, 196–209 (1980).

149. Maskos, Z., Fisher, K., Sørlie, M., Newton, W. E. & Hales, B. J. Variant MoFe proteins of *Azotobacter vinelandii*: effects of carbon monoxide on electron paramagnetic resonance spectra generated during enzyme turnover. *J. Biol. Inorg. Chem.* **10**, 394–406 (2005).

150. Corbin, J. L. Liquid chromatographic-fluorescence determination of ammonia from nitrogenase reactions: a 2-min assay. *Appl. Environ. Microbiol.* **47**, 1027–1030 (1984).

151. Kiefer, F., Arnold, K., Kunzli, M., Bordoli, L. & Schwede, T. The SWISS-MODEL Repository and associated resources. *Nucleic Acids Res.* **37**, D387–D392 (2009).

152. Guex, N., Peitsch, M. C. & Schwede, T. Automated comparative protein structure modeling with SWISS-MODEL and Swiss-PdbViewer: a historical perspective. *Electrophoresis* **30 Suppl 1**, S162–S173 (2009).

153. Biasini, M. *et al.* SWISS-MODEL: modelling protein tertiary and quaternary structure using evolutionary information. *Nucleic Acids Res.* **42**, W252–W258 (2014).

154. Comeau, S. R., Gatchell, D. W., Vajda, S. & Camacho, C. J. ClusPro: an automated docking and discrimination method for the prediction of protein complexes. *Bioinformatics* **20**, 45–50 (2004).

155. Kozakov, D., Brenke, R., Comeau, S. R. & Vajda, S. PIPER: an FFT-based protein docking program with pairwise potentials. *Proteins* **65**, 392–406 (2006).

156. Kozakov, D. *et al.* How good is automated protein docking?: automated protein docking. *Proteins* **81**, 2159–2166 (2013).

157. Schymkowitz, J. *et al.* The FoldX web server: an online force field. *Nucleic Acids Res.* **33**, W382–W388 (2005).

158. Sánchez, I. E. *et al.* Genome-wide prediction of SH2 domain targets using structural information and the FoldX algorithm. *PLoS Computational Biology* **4**, e1000052 (2008).

159. Van Durme, J. *et al.* A graphical interface for the FoldX forcefield. *Bioinformatics* **27**, 1711–1712 (2011).

160. Hu, Y., Lee, C. C. & Ribbe, M. W. Extending the carbon chain: hydrocarbon formation catalyzed by vanadium/molybdenum nitrogenases. *Science* **333**, 753–755 (2011).

161. Rofer-DePoorter, C. K. A comprehensive mechanism for the Fischer-Tropsch synthesis. *Chem. Rev.* **81**, 447–474 (1981).

162. Gerlach, D. L. & Lehnert, N. Fischer-Tropsch chemistry at room temperature? *Angew. Chem., Int. Ed. Engl.* **50**, 7984–7986 (2011).

163. Hu, Y., Lee, C. C. & Ribbe, M. W. Vanadium nitrogenase: A two-hit wonder? *Dalton Trans.* **41**, 1118–1127 (2012).

164. Danyal, K. *et al.* Uncoupling nitrogenase: catalytic reduction of hydrazine to ammonia by a MoFe protein in the absence of Fe protein-ATP. *J. Am. Chem. Soc.* **132**, 13197–13199 (2010).

165. George, S. J., Ashby, G. A., Wharton, C. W. & Thorneley, R. N. F. Time-resolved binding of carbon monoxide to nitrogenase monitored by stopped-flow infrared spectroscopy. *J. Am. Chem. Soc.* **119**, 6450–6451 (1997).

166. Cameron, L. M. & Hales, B. J. Investigation of CO binding and release from Mo-nitrogenase during catalytic turnover. *Biochemistry* **37**, 9449–9456 (1998).

167. Maskos, Z. & Hales, B. J. Photo-lability of CO bound to Mo-nitrogenase from *Azotobacter vinelandii*. *J. Inorg. Biochem.* **93**, 11–17 (2003).

168. Lee, H.-I., Hales, B. J. & Hoffman, B. M. Metal-ion valencies of the FeMo cofactor in CO-inhibited and resting state nitrogenase by ^{57}Fe Q-band ENDOR. *J. Am. Chem. Soc.* **119**, 11395–11400 (1997).

169. Christie, P. D. *et al.* Identification of the CO-binding cluster in nitrogenase MoFe protein by ENDOR of ^{57} Fe isotopomers. *J. Am. Chem. Soc.* **118**, 8707–8709 (1996).

170. Pollock, R. C. *et al.* Investigation of CO bound to inhibited forms of nitrogenase MoFe protein by ^{13}C ENDOR. *J. Am. Chem. Soc.* **117**, 8686–8687 (1995).

171. Yan, L. *et al.* IR-monitored photolysis of CO-inhibited nitrogenase: a major EPR-silent species with coupled terminal CO ligands. *Chem. Eur. J.* **18**, 16349–16357 (2012).

172. Scott, A. D. *et al.* Structural characterization of CO-inhibited Mo-nitrogenase by combined application of nuclear resonance vibrational spectroscopy, extended X-ray absorption fine structure, and density functional theory: new insights into the effects of CO binding and the role of the interstitial atom. *J. Am. Chem. Soc.* **136**, 15942–15954 (2014).

173. Yang, Z.-Y., Dean, D. R. & Seefeldt, L. C. Molybdenum nitrogenase catalyzes the reduction and coupling of CO to form hydrocarbons. *J. Biol. Chem.* **286**, 19417–19421 (2011).

174. Dance, I. How does vanadium nitrogenase reduce CO to hydrocarbons? *Dalton Trans* **40**, 5516–5527 (2011).

175. Hoffman, B. M., Lukoyanov, D., Yang, Z.-Y., Dean, D. R. & Seefeldt, L. C. Mechanism of nitrogen fixation by nitrogenase: the next stage. *Chem. Rev.* **114**, 4041–4062 (2014).

176. Spatzal, T., Perez, K. A., Howard, J. B. & Rees, D. C. Catalysis-dependent selenium incorporation and migration in the nitrogenase active site iron-molybdenum cofactor. *eLife* **4**, (2015).

177. Lee, C. C., Hu, Y. & Ribbe, M. W. Catalytic reduction of CN^- , CO, and CO_2 by nitrogenase cofactors in lanthanide-driven reactions. *Angew. Chem., Int. Ed. Engl.* **54**, 1219–1222 (2015).

178. Stoll, S. & Schweiger, A. EasySpin, a comprehensive software package for spectral simulation and analysis in EPR. *J. Magn. Reson.* **178**, 42–55 (2006).

179. Danyal, K., Dean, D. R., Hoffman, B. M. & Seefeldt, L. C. Electron transfer within nitrogenase: evidence for a deficit-spending mechanism. *Biochemistry* **50**, 9255–9263 (2011).

180. Hiller, C., Lee, C. C., Stiebritz, M., Rettberg, L. & Hu, Y. Strategies towards capturing nitrogenase substrates and intermediates via controlled alteration of electron fluxes. *Chemistry - A European Journal* (2018). doi:10.1002/chem.201803735

181. Schilter, D., Camara, J. M., Huynh, M. T., Hammes-Schiffer, S. & Rauchfuss, T. B. Hydrogenase enzymes and their synthetic models: the role of metal hydrides. *Chem. Rev.* **116**, 8693–8749 (2016).

182. Mühlenhoff, U. *et al.* Compartmentalization of iron between mitochondria and the cytosol and its regulation. *Eur. J. Cell Biol.* **94**, 292–308 (2015).

183. O'Brien, E. *et al.* The [4Fe4S] cluster of human DNA primase functions as a redox switch using DNA charge transport. *Science* **355**, (2017).

184. Mettert, E. L. & Kiley, P. J. Fe–S proteins that regulate gene expression. *Biochim. Biophys. Acta* **1853**, 1284–1293 (2015).

185. Rees, D. C. *et al.* Structural basis of biological nitrogen fixation. *Philos. Trans. R. Soc. London, Ser. A* **363**, 971–984 (2005).

186. Rees, D. C. & Howard, J. B. The interface between the biological and inorganic worlds: iron-sulfur metalloclusters. *Science* **300**, 929–931 (2003).

187. Jeoung, J.-H., Fesseler, J., Goetzl, S. & Dobbek, H. Carbon monoxide. Toxic gas and fuel for anaerobes and aerobes: carbon monoxide dehydrogenases. in *The Metal-Driven Biogeochemistry of Gaseous Compounds in the Environment* (eds. Kroneck, P. M. H. & Torres, M. E. S.) **14**, 37–69 (Springer Netherlands, 2014).

188. Kung, Y. & Drennan, C. L. A role for nickel-iron cofactors in biological carbon monoxide and carbon dioxide utilization. *Curr. Opin. Chem. Biol.* **15**, 276–283 (2011).

189. Can, M., Armstrong, F. A. & Ragsdale, S. W. Structure, function, and mechanism of the nickel metalloenzymes, CO dehydrogenase, and acetyl-CoA synthase. *Chem. Rev.* **114**, 4149–4174 (2014).

190. Mayhew, S. G. The redox potential of dithionite and SO_2^- from equilibrium reactions with flavodoxins, methyl viologen and hydrogen plus hydrogenase. *Eur. J. Biochem.* **85**, 535–547 (1978).

191. Averill, B. A., Herskovitz, T., Holm, R. H. & Ibers, J. A. Synthetic analogs of the active sites of iron-sulfur proteins. II. Synthesis and structure of the tetra[mercapto-.*mu.*$_3$-sulfido-iron] clusters, $[Fe_4S_4(SR)_4]^{2-}$. *J. Am. Chem. Soc.* **95**, 3523–3534 (1973).

192. Barclay, J. E., Davies, S. C., Evans, D. J., Hughes, D. L. & Longhurst, S. Lattice effects in the Mössbauer spectra of salts of $[Fe_4S_4\{S(CH_2)_nOH\}_4]^{2-}$. Crystal structures of $[PPh_4]_2[Fe_4S_4\{S(CH_2)_nOH\}_4]$ (n=2, 3 and 4). *Inorg. Chim. Acta* **291**, 101–108 (1999).

193. Sickerman, N. S., Hu, Y. & Ribbe, M. W. Activation of CO_2 by vanadium nitrogenase. *Chemistry - An Asian Journal* **12**, 1985–1996 (2017).

194. Proskurowski, G. *et al.* Abiogenic hydrocarbon production at Lost City Hydrothermal Field. *Science* **319**, 604–607 (2008).

195. McDermott, J. M., Seewald, J. S., German, C. R. & Sylva, S. P. Pathways for abiotic organic synthesis at submarine hydrothermal fields. *Proc. Natl. Acad. Sci. U.S.A.* **112**, 7668–7672 (2015).

196. Novikov, Y. & Copley, S. D. Reactivity landscape of pyruvate under simulated hydrothermal vent conditions. *Proc. Natl. Acad. Sci. U.S.A.* **110**, 13283–13288 (2013).

197. Roldan, A. *et al.* Bio-inspired CO_2 conversion by iron sulfide catalysts under sustainable conditions. *Chemical Communications* **51**, 7501–7504 (2015).

198. Huber, C. & Wächtershäuser, G. Activated acetic acid by carbon fixation on (Fe,Ni)S under primordial conditions. *Science* **276**, 245–247 (1997).

199. Scheidler, C., Sobotta, J., Eisenreich, W., Wächtershäuser, G. & Huber, C. Unsaturated $C_{3,5,7,9}$-monocarboxylic acids by aqueous, one-pot carbon fixation: possible relevance for the origin of life. *Scientific Reports* **6**, (2016).

200. Huber, C. & Wächtershäuser, G. α-hydroxy and α-amino acids under possible Hadean, volcanic origin-of-life conditions. *Science* **314**, 630–632 (2006).

201. Huber, C. & Wächtershäuser, G. Peptides by activation of amino acids with CO on (Ni,Fe)S surfaces: implications for the origin of life. *Science* **281**, 670–672 (1998).

202. Roslev, P., Iversen, N. & Henriksen, K. Oxidation and assimilation of atmospheric methane by soil methane oxidizers. *Appl. Environ. Microbiol.* **63**, 874–880 (1997).

203. Coleman, N. V. & Spain, J. C. Distribution of the coenzyme M pathway of epoxide metabolism among ethene- and vinyl chloride-degrading mycobacterium strains. *Applied and Environmental Microbiology* **69**, 6041–6046 (2003).

204. Saba, S. *et al.* A simple and efficient one-step protocol for the preparation of alkyl-substituted ammonium tetrafluoroborate and hexafluorophosphate salts. *Journal of Fluorine Chemistry* **153**, 168–171 (2013).

205. Evans, W. J. *et al.* Solution synthesis and crystallographic characterization of the divalent organosamarium complexes $(C_5Me_5)_2Sm(THF)_2$ and $[(C_5Me_5)Sm(.mu.-I)(THF)_2]_2$. *Journal of the American Chemical Society* **107**, 941–946 (1985).

206. Schaftenaar, G. & Noordik, J. H. Molden: a pre- and post-processing program for molecular and electronic structures. *J. Comput. Aided Mol. Des.* **14**, 123–134 (2000).

207. Klamt, A. & Schüürmann, G. COSMO: a new approach to dielectric screening in solvents with explicit expressions for the screening energy and its gradient. *J. Chem. Soc., Perkin Trans. 2* 799–805 (1993). doi:10.1039/P29930000799

208. Tao, J., Perdew, J. P., Staroverov, V. N. & Scuseria, G. E. Climbing the density functional ladder: nonempirical meta-generalized gradient approximation designed for molecules and solids. *Phys. Rev. Lett.* **91**, 146401 (2003).

209. Schäfer, A., Huber, C. & Ahlrichs, R. Fully optimized contracted Gaussian basis sets of triple zeta valence quality for atoms Li to Kr. *J. Chem. Phys.* **100**, 5829–5835 (1994).

210. Weigend, F. & Ahlrichs, R. Balanced basis sets of split valence, triple zeta valence and quadruple zeta valence quality for H to Rn: design and assessment of accuracy. *Phys. Chem. Chem. Phys.* **7**, 3297 (2005).

211. Eichkorn, K., Weigend, F., Treutler, O. & Ahlrichs, R. Auxiliary basis sets for main row atoms and transition metals and their use to approximate Coulomb potentials. *Theor. Chem. Acc.* **97**, 119–124 (1997).

212. Weigend, F. Accurate Coulomb-fitting basis sets for H to Rn. *Phys. Chem. Chem. Phys.* **8**, 1057–1065 (2006).

213. Noodleman, L. Valence bond description of antiferromagnetic coupling in transition metal dimers. *J. Chem. Phys.* **74**, 5737–5743 (1981).

214. Noodleman, L., Post, D. & Baerends, E. J. Symmetry breaking and ionization from symmetry equivalent inner shells and lone pairs in Xα theory. *Chem. Phys.* **64**, 159–166 (1982).

215. Noodleman, L., Peng, C. Y., Case, D. A. & Mouesca, J.-M. Orbital interactions, electron delocalization and spin coupling in iron-sulfur clusters. *Coordin. Chem. Rev.* **144**, 199–244 (1995).

216. Noodleman, L., Han Du, W.-G., Fee, J. A., Götz, A. W. & Walker, R. C. Linking chemical electron-proton transfer to proton pumping in cytochrome c oxidase: broken-symmetry DFT exploration of intermediates along the catalytic reaction pathway of the iron-copper dinuclear complex. *Inorg. Chem.* **53**, 6458–6472 (2014).

217. Torres, R. A., Lovell, T., Noodleman, L. & Case, D. A. Density functional and reduction potential calculations of Fe_4S_4 clusters. *J. Am. Chem. Soc.* **125**, 1923–1936 (2003).

218. Tissandier, M. D. *et al.* The proton's absolute aqueous enthalpy and Gibbs free energy of solvation from cluster-ion solvation data. *J. Phys. Chem. A* **102**, 7787–7794 (1998).

219. Lee, C. C., Hu, Y. & Ribbe, M. W. ATP-independent formation of hydrocarbons catalyzed by isolated nitrogenase cofactors. *Angew. Chem., Int. Ed. Engl.* **51**, 1947–1949, S1947/1-S1947/3 (2012).

220. Venkateswara Rao, P. & Holm, R. H. Synthetic analogues of the active sites of iron-sulfur proteins. *Chem. Rev.* **104**, 527–559 (2004).

221. Lee, S. C. & Holm, R. H. The clusters of nitrogenase: synthetic methodology in the construction of weak-field clusters. *Chem. Rev. (Washington, DC, U. S.)* **104**, 1135–1157 (2004).

222. Ohta, S. & Ohki, Y. Impact of ligands and media on the structure and properties of biological and biomimetic iron-sulfur clusters. *Coordination Chemistry Reviews* **338**, 207–225 (2017).

223. McMillan, R. S., Renaud, J., Reynolds, J. G. & Holm, R. H. Biologically related iron—sulfur clusters as reaction centers. Reduction of acetylene to ethylene in systems based on $[Fe_4S_4(SR)_4]^{3-}$. *Journal of Inorganic Biochemistry* **11**, 213–227 (1979).

224. Coucouvanis, D. *et al.* The catalytic reduction of hydrazine to ammonia by the $MoFe_3S_4$ cubanes and implications regarding the function of nitrogenase. Evidence for direct involvement of the molybdenum atom in substrate reduction. *Journal of the American Chemical Society* **115**, 12193–12194 (1993).

225. Malinak, S. M., Demadis, K. D. & Coucouvanis, D. Catalytic reduction of hydrazine to ammonia by the VFe_3S_4 cubanes. Further evidence for the direct involvement of the heterometal in the reduction of nitrogenase substrates and possible relevance to the vanadium nitrogenases. *Journal of the American Chemical Society* **117**, 3126–3133 (1995).

226. Komeda, N., Nagao, H., Matsui, T., Adachi, G. & Tanaka, K. Electrochemical carbon dioxide fixation to thioesters catalyzed by molybdenum-iron-sulfur cluster $[Mo_2Fe_6S_8(SEt)_9]^{3-}$. *Journal of the American Chemical Society* **114**, 3625–3630 (1992).

227. Christou, G., Holm, R. H., Sabat, M. & Ibers, J. A. A hexanuclear iron-sulfide-thiolate cluster: assembly and properties of $[Fe_6S_9(S\text{-}tert\text{-}C_4H_9)_2]^{4-}$ containing three types of bridging sulfur atoms. *Journal of the American Chemical Society* **103**, 6269–6271 (1981).

228. Sickerman, N. S. *et al.* Reduction of C_1 substrates to hydrocarbons by the homometallic precursor and synthetic mimic of the nitrogenase cofactor. *Journal of the American Chemical Society* **139**, 603–606 (2017).

229. Wächtershäuser, G. On the chemistry and evolution of the pioneer organism. *Chem. Biodivers.* **4**, 584–602 (2007).

230. Glikson, A. Y. Milestones in the evolution of the atmosphere with reference to climate change. *Australian Journal of Earth Sciences* **55**, 125–139 (2008).

231. Rebelein, J. G., Lee, C. C., Hu, Y. & Ribbe, M. W. The *in vivo* hydrocarbon formation by vanadium nitrogenase follows a secondary metabolic pathway. *Nature Communications* **7**, 13641 (2016).

232. Lu, X.-B., Ren, W.-M. & Wu, G.-P. CO_2 copolymers from epoxides: catalyst activity, product selectivity, and stereochemistry control. *Accounts of Chemical Research* **45**, 1721–1735 (2012).

233. Martín, C., Fiorani, G. & Kleij, A. W. Recent advances in the catalytic preparation of cyclic organic carbonates. *ACS Catalysis* **5**, 1353–1370 (2015).

234. Wu, X.-F. *et al.* Transition-metal-catalyzed carbonylation reactions of olefins and alkynes: a personal account. *Accounts of Chemical Research* **47**, 1041–1053 (2014).

235. Shima, T. & Hou, Z. Hydrogenation of carbon monoxide by tetranuclear rare earth metal polyhydrido complexes. Selective formation of ethylene and isolation of well-defined polyoxo rare earth metal clusters. *Journal of the American Chemical Society* **128**, 8124–8125 (2006).

236. Dry, M. E. The Fischer–Tropsch process: 1950–2000. *Catalysis Today* **71**, 227–241 (2002).

237. Zhang, Q., Cheng, K., Kang, J., Deng, W. & Wang, Y. Fischer-Tropsch catalysts for the production of hydrocarbon fuels with high selectivity. *ChemSusChem* **7**, 1251–1264 (2014).

238. Khodakov, A. Y., Chu, W. & Fongarland, P. Advances in the development of novel cobalt Fischer−Tropsch catalysts for synthesis of long-chain hydrocarbons and clean fuels. *Chemical Reviews* **107**, 1692–1744 (2007).

239. Kortlever, R., Shen, J., Schouten, K. J. P., Calle-Vallejo, F. & Koper, M. T. M. Catalysts and reaction pathways for the electrochemical reduction of carbon dioxide. *The Journal of Physical Chemistry Letters* **6**, 4073–4082 (2015).

240. Zhu, D. D., Liu, J. L. & Qiao, S. Z. Recent advances in inorganic heterogeneous electrocatalysts for reduction of carbon dioxide. *Adv. Mater. Weinheim* **28**, 3423–3452 (2016).

241. Stiebritz, M. T. *et al.* Ambient conversion of CO_2 to hydrocarbons by biogenic and synthetic $[Fe_4S_4]$ clusters. *Nat. Catal.* **1**, 444–451 (2018).